Karlsruher Institut für Technologie

First-Order Electroweak Phase Transitions Beyond the Standard Model and Gravitational Waves

Zur Erlangung des akademischen Grades eines

Doktors der Naturwissenschaften

von der KIT-Fakultät für Physik

des Karlsruher Instituts für Technologie

genehmigte

Dissertation

von

M.Sc. Lisa Biermann

aus Bühlertal

Referentin: Prof. Dr. M. M. Mühlleitner
Korreferent: Prof. Dr. T. Schwetz-Mangold

Tag der mündlichen Prüfung: 26. Juli 2024

Abstract

The Standard Model of Particle Physics (SM) explains particle masses via the spontaneous breaking of the electroweak symmetry by the ground state of the scalar Higgs potential. In the early universe at high temperatures, the electroweak symmetry in the SM is restored and the universe is in a vacuum in which all particles are massless. Today, at low temperature, the electroweak vacuum expectation value of the ground state breaks the electroweak symmetry and the universe has massive particles. The experimental observation of a Higgs boson confirms the realization of a fundamental scalar sector in nature. All collider data agrees with the minimal scalar sector of the SM within theoretical and experimental uncertainties. However, cosmological observations, in particular the excess of matter over antimatter and the existence of non-baryonic dark matter, cannot be explained by the SM. Therefore, this strongly suggests the presence of physics beyond the SM (BSM). Extensions of the scalar sector of the SM provide a promising avenue for studying BSM physics, as not only the minimal scalar sector of the SM, but also BSM extensions of the scalar sector can reproduce all experimental collider data. Additionally, BSM scalar sector extensions can incorporate mechanisms to produce a matter–antimatter asymmetry, and can as well contain dark matter candidates. The matter–antimatter asymmetry can be dynamically generated through electroweak baryogenesis (EWBG) if the three Sakharov conditions are fulfilled. These are the existence of baryon number violation, violation of the charge conjugation ($\mathcal{C}$) and charge-conjugation and parity ($\mathcal{CP}$) symmetry, as well as departure from thermal equilibrium. In EWBG, a matter–antimatter asymmetry is produced through a combination of $\mathcal{CP}$-violating processes and sphaleron-mediated baryon number violating processes. The excess of matter is then conserved by the departure from thermal equilibrium which is realized through a strong first-order electroweak phase transition (EWPT) from the electroweak symmetric, false vacuum at high temperatures to the electroweak broken, true vacuum at low temperatures. While sphaleron-mediated processes in the SM can violate the baryon number, the SM does not have enough $\mathcal{CP}$ violation, neither does it predict a strong first-order EWPT. Therefore, BSM extensions are required to enable a strong first-order EWPT as well as to provide additional sources of $\mathcal{CP}$ violation. In addition to providing the departure from thermal equilibrium which is necessary for EWBG, first-order EWPTs also source a stochastic gravitational wave (GW) background that could be detectable at GW observatories in the near future.

In this thesis, we connect the parameter space for first-order EWPTs for selected BSM models to collider observables and to their potential to source gravitational waves to which future GW observatories might become sensitive. Further, we show that the models under investigation provide intermediate temperature regions with spontaneous breaking of the electromagnetic symmetry or additional sources of $\mathcal{CP}$ violation, as well as dark matter.

Zusammenfassung

Das Standardmodell der Teilchenphysik (SM) erklärt Teilchenmassen über den Mechanismus der spontanen Brechung der elektroschwachen Symmetrie durch den Grundzustand des skalaren Higgspotentials. Im frühen Universum, bei hohen Temperaturen, ist die elektroschwache Symmetrie des Standardmodells exakt und das Universum befindet sich in einem Grundzustand, in welchem alle Teilchen masselos sind. Heute, bei niedriger Temperatur, bricht der Vakuumerwartungswert des Grundzustandes die elektroschwache Symmetrie, und das Universum befindet sich in einem Grundzustand, in welchem Teilchen massebehaftet sind. Die experimentelle Entdeckung eines Higgs-Bosons bestätigt, dass ein fundamentaler skalarer Sektor in der Natur realisiert ist. Alle Daten von Beschleunigerexperimenten stimmen innerhalb theoretischer und experimenteller Unsicherheitsgrenzen mit den Theorievorhersagen des minimalen Skalarsektors des SM überein. Kosmologische Beobachtungen, wie der Überschuss von Materie gegenüber Antimaterie, oder die Existenz von nicht-baryonischer Dunkler Materie, können jedoch nicht mit dem SM erklärt werden und bilden damit eine deutliche Evidenz für Physik jenseits des Standardmodells (BSM). Erweiterungen des Skalarsektors des SM erklären, genau wie der minimale Skalarsektor des SM, die Daten der Beschleunigerexperimente. Sie können jedoch zusätzlich Mechanismen enthalten, um den Materieüberschuss, sowie Dunkle Materie zu erklären. Die Materie–Antimaterie Asymmetry kann durch elektroschwache Baryogenese (EWBG) dynamisch erzeugt werden, wenn die drei Sakharov Bedingungen erfüllt sind. Diese sind die Existenz von Baryonenzahl-verletzenden Prozessen, Verletzung der Ladungskonjugation- ($\mathcal{C}$) und Ladungskonjugations- und Paritäts-Symmetrie ($\mathcal{CP}$), sowie Abweichung vom thermischen Gleichgewicht. In EWBG wird durch eine Kombination von $\mathcal{CP}$-verletzenden Prozessen und von Baryonenzahl-verletzenden Sphaleron-Prozessen ein Materieüberschuss erzeugt. Der Materieüberschuss wird dann anschließend durch einen starken elektroschwachen Phasenübergang erster Ordnung zwischen dem elektroschwachsymmetrischen falschen Grundzustand bei hohen Temperaturen zu dem elektroschwach-gebrochenen wahren Grundzustand bei niedrigen Temperaturen erhalten. Während Sphaleron-Prozesse im SM die Baryonenzahl verletzen können, hat das SM jedoch nicht genügend $\mathcal{CP}$-Verletzung und sagt außerdem keinen starken elektroschwachen Phasenübergang erster Ordnung voraus. BSM-Erweiterungen sind somit notwendig, um einen starken elektroschwachen Phasenübergang erster Ordnung, sowie zusätzliche $\mathcal{CP}$-Verletzung zu ermöglichen. Zusätzlich zur Bereitstellung einer Abweichung vom thermischen Gleichgewicht, welche eine notwendige Bedingung für erfolgreiche EWBG ist, sind elektroschwache Phasenübergänge erster Ordnung auch Quellen für einen stochastischen Gravitationswellenhintergrund, welcher von zukünftigen Gravitationswellendetektoren gemessen werden könnte.

In dieser Arbeit stellen wir eine Verbindung her zwischen dem Parameterraum spezieller BSM-Modelle, welcher elektroschwache Phasenübergänge erster Ordnung erlaubt, und Observablen an Beschleunigerexperimenten, sowie zu erzeugten Gravitationswellen, für die zukünftige Gravitationswellendetektoren empfindlich sein können. Außerdem können die untersuchten BSM-Modelle spontan die elektromagnetische Symmetrie in zwischenzeitlichen Temperaturregionen brechen, zusätzliche Quellen für $\mathcal{CP}$-Verletzung haben, sowie Kandidaten für Dunkle Materie enthalten.

Publication List

Part of the work presented in this thesis has been published in the following articles.

Journal publications

- Anisha, Duarte Azevedo, Lisa Biermann, Christoph Englert, Margarete Mühlleitner, “Effective 2HDM Yukawa interactions and a strong first-order electroweak phase transition”, In: JHEP **02**, 045 (2024), [arXiv:2311.06353 [**hep-ph**]].
- Mayumi Aoki, Lisa Biermann, Christoph Borschensky, Igor Ivanov, Margarete Mühlleitner, Hiroto Shibuya, “Intermediate charge-breaking phases and symmetry non-restoration in the 2-Higgs-Doublet Model”, In: JHEP **02**, 232 (2024), [arXiv:2308.04141 [**hep-ph**]].
- Lisa Biermann, Margarete Mühlleitner and Jonas Müller, “Electroweak phase transition in a dark sector with CP violation”, In: Eur. Phys. J. C **83**, no.5, 439 (2023), [arXiv:2204.13425 [**hep-ph**]].
- Anisha, Lisa Biermann, Christoph Englert and Margarete Mühlleitner, “Two Higgs doublets, effective interactions and a strong first-order electroweak phase transition”, In: JHEP **08**, 091 (2022), [arXiv:2204.06966 [**hep-ph**]].

Preprints

- Philipp Basler, Lisa Biermann, Margarete Mühlleitner, Jonas Müller, Rui Santos, João Viana, “BSMPT v3 A Tool for Phase Transitions and Primordial Gravitational Waves in Extended Higgs Sectors”, [arXiv:2404.19037 [**hep-ph**]].

Conference proceedings

- Lisa Biermann, Margarete Mühlleitner and Jonas Müller, “‘CP in the Dark’ and a Strong First-Order Electroweak Phase Transition”, In: Proceedings of the 8th Symposium on Prospects in the Physics of Discrete Symmetries, [arXiv:2301.09004 [**hep-ph**]].

List of Abbreviations

2HDM	Two-Higgs-Doublet Model
ATLAS	A Toroidal LHC Apparatus
BAU	Baryon asymmetry of the universe
BBN	Big Bang nucleosynthesis
BBO	Big Bang Observer
BP	Benchmark point
BR	Branching ratio
BSM	Beyond the Standard Model
CB	Charge-breaking
CE	Cosmic Explorer
CKM	Cabibbo–Kobayashi–Maskawa
CMB	Cosmic microwave background
CMS	Compact Muon Solenoid
CP	Charge-conjugation and parity
CT	Counterterm
CW	Coleman–Weinberg
DECIGO	DECi-hertz Interferometer Gravitational Wave Observatory
DM	Dark matter
EDM	Electric dipole moment
EFT	Effective field theory
ET	Einstein Telescope
EW	Electroweak
EWBG	Electroweak baryogenesis
EWPT	Electroweak phase transition
EWSR	Electroweak symmetry restoration
FCNC	Flavour-changing neutral current
GW	Gravitational wave
IPTA	International Pulsar Timing Array
IR	Infrared
KAGRA	Kamioka Gravitational Wave Detector
LEP	Large Electron–Positron Collider
LHC	Large Hadron Collider
LIGO	Laser Interferometer Gravitational-Wave Observatory
LISA	Laser Interferometer Space Antenna
LO	Leading order
N2HDM	Next-to-Minimal Two-Higgs-Doublet Model
NLO	Next-to-leading order
OS	On-shell
PT	Phase transition
QCD	Quantum chromodynamics
RGE	Renormalization group equations
SM	Standard Model
SNR	Signal-to-noise ratio
UV	Ultraviolet
VEV	Vacuum expectation value
WC	Wilson coefficient
WIMP	Weakly interacting massive particle

Contents

CHAPTER 1

INTRODUCTION

The Standard Model of Particle Physics (SM) currently gives the best understanding of the high-energy, or small-scale, universe made up of massive particles and their interactions [1–12]. It describes the particle content of the universe based on symmetries, split into the categories of fermions, i.e. quarks and leptons, as matter particles and bosons as force carriers. Particle masses are generated through spontaneous symmetry breaking in the Higgs mechanism [13–16]. The ground state of the SM Higgs potential breaks the electroweak symmetry spontaneously and is invariant under the electromagnetic symmetry, rendering the photon massless. The Higgs mechanism further predicts a scalar boson, the *Higgs boson h*. The experimental observation of a scalar boson consistent with the Higgs boson predicted by the SM was first reported in 2012 [17, 18]. Since then increasingly precise measurements have substantiated its SM-like properties. The ATLAS and CMS collaboration have independently measured a scalar boson of mass $m_h = 125\,\mathrm{GeV}$, that is even under charge conjugation parity ($\mathcal{CP}$) symmetry. It is observed in multiple final states [19, 20]. The observations are consistent with theoretical predictions for coupling strengths and production probabilities calculated with the SM within experimental and theoretical uncertainties.

The SM, however, cannot be the underlying theory of nature. Besides its lack of an explanation for gravity as the fourth fundamental force of nature, there are experimental observations that the SM cannot explain. These are of cosmological nature [21], e.g. dark energy, dark matter, the matter–antimatter asymmetry, or concern particle physics, like e.g. neutrino masses [22–24], the flavour puzzle [25], or the hierarchy problem [26–29]. The SM was established based on a multitude of independent collider experiments and can be interpreted as a low-energy approximation of an underlying theory that manifests itself at higher energies beyond the reach of current collider experiments.

Extensions of the SM scalar sector represent a promising portal to explore physics beyond the SM (BSM) and to explain at least some of the open questions of the SM. The measured mass of the observed Higgs boson adds the last missing theoretical piece to the Standard Model. However, further experimental efforts are needed in order to precisely determine the shape of the scalar potential, independently of the Higgs boson mass, to test the SM assumption of a minimal scalar sector. These efforts include direct measurements of the Higgs boson self-interaction. Current experimental data does not exclude more complicated scalar sectors that allow for a rich BSM phenomenology, while containing an SM-like Higgs boson.

One promising possibility in BSM scalar sectors is a first-order electroweak phase transition (EWPT). At high temperatures in the early universe, the electroweak symmetry, which is spontaneously broken by the ground state of the scalar potential today, can be restored. In the SM the restoration of the electroweak symmetry takes place via a smooth cross-over [30, 31]. However, with BSM-extended scalar sectors, it is also possible, and allowed by experimental data, to restore the spontaneously broken electroweak symmetry via a first-order EWPT. In a first-order EWPT, a false vacuum of the scalar potential decays by transitions to a barrier-separated true vacuum. The temperature at which both vacua are degenerate is the *critical temperature*, T_c.

A first-order EWPT in the early universe is theoretically motivated because the matter–antimatter asymmetry of our universe can be explained if a strong first-order EWPT appears together with additional violation of the $\mathcal{CP}$ symmetry and baryon number violating processes [32–34]. There are direct consequences on observable signatures, i.e. promising connections to collider signatures, see e.g. [35–38]. Furthermore, a first-order EWPT sources a stochastic gravitational wave (GW) background [39–45]. First evidence for a stochastic GW background was published in 2023 [46–50]. The signal is found to be compatible with a range of sources, including first-order EWPTs [47]. The observation of a stochastic GW background exclusively sourced by a first-order EWPT would be a clear evidence for BSM physics. Therefore, the theoretical possibility of first-order EWPTs provides a link between cosmology and collider physics.

In this thesis, we extend the SM scalar sector to provide mechanisms to generate a first-order EWPT as well as dark matter within experimental bounds. We link the parameter space that allows for first-order EWPTs to collider signatures, dark matter observables, and future GW measurements. This way, we aim to shed light both on the true nature of underlying physics and on the evolution of the early universe. More specifically, this thesis is organized in two parts. In the first part we study prerequisites for a first-order EWPT. For this, we parametrize the strength of a first-order EWPT via the coordinate of the electroweak vacuum expectation value (VEV) $\overline{\omega}_{\text{EW}}$ at the critical temperature T_c divided by critical temperature, $\xi_c = \overline{\omega}_{\text{EW}}(T_c)/T_c$, and define a first-order EWPT to be strong, if $\xi_c \gtrsim 1$. We then investigate the relation between strong first-order EWPTs in the dimension-six extended Two-Higgs-Doublet Model (2HDM) and collider signatures. The existence of a critical temperature is, however, only a prerequisite for a first-order EWPT. To determine whether a first-order EWPT takes place in the early universe or not, we need a calculation of vacuum transition rates and the derivation of characteristic temperatures that takes into account the expansion rate of the universe. In the second part of this thesis, we perform these calculations and find completing first-order EWPTs in a 2HDM with intermediate electromagnetic charge breaking as well as with gravitational waves sourced by it. Additionally, we investigate and show the ability of the model ‘CP in the Dark’ to allow for first-order EWPTs, to source observable gravitational waves, to explain dark matter and to provide additional $\mathcal{CP}$ violation.

This thesis is structured as follows. First, we describe the SM and general BSM scalar sector extensions in Chapter 2. We give a short overview of the early universe in Chapter 3. In the first part of this thesis, we then discuss prerequisites for a first-order EWPT in the early universe. We describe the finite-temperature ground state of the scalar potential by the one-loop effective potential in Chapter 4. We provide an overview of the computer code framework that was used in the context of this thesis in Chapter 5. In Chapter 6, we discuss dimension-six operators added to a 2HDM that can promote a first-order EWPT with $\xi_c < 1$ to a strong first-order EWPT with $\xi_c \gtrsim 1$. For such operators, we draw relations to signatures at collider experiments. We implemented the calculation of the vacuum transition rate and the derivation of characteristic temperatures for first-order EWPTs, as well as the derivation of the GW spectrum that is sourced by first-order EWPTs, in the new public code `BSMPTv3` as a part of this thesis. We present it in detail in Chapter 7. We further review the derivation of the transition rates and the characteristic temperatures for a first-order EWPT in Chapter 8. In Chapter 9 we describe how a stochastic GW background is sourced by first-order EWPTs. In Chapter 10 we discuss EWPTs in a 2HDM with intermediate phases that violate the electromagnetic symmetry. In Chapter 11 we investigate first-order EWPTs and gravitational waves in the model 'CP in the Dark'. We furthermore discuss dark matter and $\mathcal{CP}$ violation within the model, as well as possible phase histories. We summarize and conclude in Chapter 12.

CHAPTER 2

The Standard Model and Scalar Sector Extensions

The Standard Model of Particle Physics (SM) [1–4] has been developed based on a strong interplay between theory and experiment. No other theory so far is in better agreement with experimental findings for small-scale interactions. In this chapter we summarize the SM; for a review, consult e.g. Ref. [51]. We follow the conventions of Ref. [52].

The SM is postulated as a renormalizable [5–9] non-Abelian spontaneously broken [10–12] gauge theory with a Lagrangian which is locally gauge invariant under the symmetry group

$$SU(3)_C \times SU(2)_L \times U(1)_Y \,. \tag{2.1}$$

The gauge group of quantum chromodynamics (QCD) is $SU(3)_C$ with conserved colour charge (C). The strong force is mediated by eight colour-neutral gauge fields, the gluons G^a_μ, and acts on colour triplets of quarks $\{u, d, c, s, t, b\}$ and their corresponding antiquarks. The gauge group $SU(2)_L \times U(1)_Y$ describes the unification of the weak and electromagnetic force. The electroweak (EW) force is associated with the weak isospin through its third component I^z_W for $SU(2)_L$ and the weak hypercharge Y_W for $U(1)_Y$ and is mediated by four gauge bosons, $\{W_1, W_2, W_3, B\}$. As a *chiral* theory, the EW force acts on left-handed fermion doublets, i.e. quarks Q_L and leptons L_L, and right-handed fermion singlets, i.e. quarks u_R, d_R and leptons l_R, which are defined in Table 2.1. There are three fermion families for quarks and leptons each. The respective upper (lower) component of the $SU(2)_L$ left-handed quark doublets of the three families define the *up-type (down-type)* quarks. The leptons are the electron e, the muon μ and the tau τ as well as the three neutrinos $\{\nu_e,\, \nu_\mu,\, \nu_\tau\}$. The Higgs field Φ is a scalar, colour-neutral, $SU(2)_L$ doublet field with $Y_W = +1/2$. The field content of the SM is summarized in Table 2.1. The SM Lagrangian reads ($a \in \{1, \dots, 8\}$, $i \in \{1, 2, 3\}$)

$$\begin{aligned}
\mathcal{L}_{\text{SM}} = &-\frac{1}{4} G^a_{\mu\nu} G^{a\mu\nu} - \frac{1}{4} W^i_{\mu\nu} W^{i\mu\nu} - \frac{1}{4} B_{\mu\nu} B^{\mu\nu} \\
&+ i\,\overline{Q}_L \not{D} Q_L + i\,\overline{L}_L \not{D} L_L + i\,\overline{u}_R \not{D} u_R + i\,\overline{d}_R \not{D} d_R + i\,\overline{l}_R \not{D} l_R \\
&+ (D_\mu \Phi)^\dagger (D^\mu \Phi) + \mu^2 |\Phi|^2 - \lambda |\Phi|^4 + \Big[-\overline{Q}'_L \hat{Y}_u \widetilde{\Phi}\, u'_R - \overline{Q}'_L \hat{Y}_d \Phi\, d'_R - \overline{L}_L \hat{Y}_l \tilde{\Phi}\, l_R + \text{h.c.} \Big] \\
&+ \mathcal{L}_{\text{ghost}} + \mathcal{L}_{\text{fix}} \,.
\end{aligned} \tag{2.2}$$

Summation over repeated indices is implied, following the Einstein sum convention. We denote the contraction with a Dirac matrix γ^μ in the Feynman slash notation, $\not{D} \equiv \gamma^\mu D_\mu$. Local gauge invariance is enforced through the definition of the covariant derivative,

$$\begin{aligned}
D_\mu\, Q_L &= \Big[\partial_\mu + \underbrace{i\, g_S\, T^a\, G^a_\mu}_{SU(3)_C} + \underbrace{i\, g\, T^i\, W^i_\mu}_{SU(2)_L} + \underbrace{i\, g'\, Y_W\, B_\mu}_{U(1)_Y}\Big]\, Q_L\,, \\
D_\mu\, L_L &= \Big[\partial_\mu + i\, g\, T^i\, W^i_\mu + i\, g'\, Y_W\, B_\mu\Big]\, L_L\,, \\
D_\mu\, q_R &= \Big[\partial_\mu + i\, g_S\, T^a\, G^a_\mu + i\, g'\, Y_W\, B_\mu\Big]\, q_R\,, \\
D_\mu\, l_R &= \Big[\partial_\mu + i\, g'\, Y_W\, B_\mu\Big]\, l_R\,, \\
D_\mu\, \Phi &= \Big[\partial_\mu + i\, g\, T^i\, W^i_\mu + i\, g'\, Y_W\, B_\mu\Big]\, \Phi\,,
\end{aligned} \tag{2.3}$$

where we denoted the right-handed up-type and down-type quarks by $q_R = \{u_R,\, d_R\}$. The $T^a = \lambda^a/2$ are the generators of the $SU(3)_C$ written in terms of the Gell–Mann matrices λ_a with $a \in \{1, \ldots, 8\}$. The generators of the $SU(2)_L$, $T^i = \sigma^i/2$, are written in terms of the Pauli matrices σ^i with $i \in \{1, 2, 3\}$. The coupling strengths w.r.t. the gauge groups are denoted by g_S, g and g', respectively. The Lagrangian in Eq. (2.2) includes kinetic terms for the gauge bosons,[1] the kinetic terms for the fermions $\{Q_L,\, L_L,\, u_R,\, d_R,\, l_R\}$, as well as terms involving the Higgs field Φ that we will discuss in more detail below. The ghost and gauge fixing terms, $\mathcal{L}_{\text{ghost}}$ and $\mathcal{L}_{\text{fix}}$, are required for theoretical completeness [53].

Both the gauge bosons that mediate the weak force and the fermions are massive,[2] however, explicit mass terms are not allowed in the SM Lagrangian, because they would violate the gauge symmetry. In the Englert–Brout–Higgs–Guralnik–Hagen–Kibble mechanism [13–16], abbreviated as *Higgs* mechanism, gauge boson and fermion masses are generated in a gauge-invariant way via the introduction of a scalar sector with a scalar Higgs field Φ which has a non-vanishing vacuum expectation value (VEV) that breaks the $SU(2)_L \times U(1)_Y$ gauge symmetry spontaneously. Furthermore, the Higgs mechanism predicts a scalar Higgs boson h that couples to fermions (gauge bosons) proportional to their mass (squared mass), as will be derived below. The existence of such a scalar boson is required to restore unitarity of the weak interaction.[3] In the Higgs mechanism, the electroweak subgroup of the SM gauge group in Eq. (2.1) is spontaneously broken down to a $U(1)_{\text{EM}}$,

$$SU(2)_L \times U(1)_Y \to U(1)_{\text{EM}}\,, \tag{2.4}$$

with conserved electromagnetic charge Q_{EM} given by the Gell–Mann–Nishijima formula,

$$Q_{\text{EM}} = I^z_W + Y_W\,. \tag{2.5}$$

The Higgs mechanism extends the theory by the scalar potential

$$V(\Phi) \equiv -\mu^2|\Phi|^2 + \lambda|\Phi|^4\,, \text{ with } \mu^2 > 0 \text{ and } \lambda > 0\,, \tag{2.6}$$

---

[1] A field strength tensor is defined as $F_{\mu\nu} = \frac{i}{g}[D^\mu,\, D^\nu]$ with generic coupling constant g. For an Abelian gauge theory, e.g. $U(1)_Y$, it follows $B_{\mu\nu} = \partial_\mu B_\nu - \partial_\nu B_\mu$. Non-Abelian gauge theories, e.g. $SU(2)_L$ and $SU(3)_C$, have $W^i_{\mu\nu} = \partial_\mu W^i_\nu - \partial_\nu W^i_\mu - g\,\epsilon^{ijk} W^j_\mu W^k_\nu$ and $G^a_{\mu\nu} = \partial_\mu G^a_\nu - \partial_\nu G^a_\mu - g_S\, f^{abc} G^b_\mu G^c_\nu$, respectively. The ϵ^{ijk} and f^{abc} are the respective structure constants.

[2] Neutrinos are massless in the SM. However, from observations [22–24] we know that neutrinos have a mass. An upper limit on the neutrino mass is derived from e.g. the KATRIN experiment [54], as well as from cosmological probes, cf. Chapter 3. A discussion of BSM sources for neutrino masses is beyond the scope of this thesis.

[3] Without an SM-like Higgs boson, the cross section of longitudinal W boson scattering diverges for high centre-of-mass energies. Unitarity of the S matrix, i.e. probability conservation, is restored through the introduction of a neutral scalar particle that couples to the W boson proportional to the W mass squared. The additional diagrams with this neutral scalar particle then cancel those diagrams that show the unphysical high-energy behaviour. The existence of an SM-like Higgs boson therefore is not just a consequence of the Higgs mechanism that consistently explains gauge boson and fermion masses, but is required to restore unitarity.

Field	Spin	$(SU(3)_C,\, SU(2)_L)$	$\{I_W^z,\, Y_W\}$
$G^a_\mu,\ a \in \{1, \dots, 8\}$	1	$(\mathbf{8},\, \mathbf{1})$	$\{0,\, 0\}$
$W^i_\mu,\ i \in \{1, 2, 3\}$	1	$(\mathbf{1},\, \mathbf{3})$	$Y_W = 0$, see caption
B^μ	1	$(\mathbf{1},\, \mathbf{1})$	$\{0,\, 0\}$
$\Phi = \begin{pmatrix} \phi^+ \\ \phi^0 \end{pmatrix}$	0	$(\mathbf{1},\, \mathbf{2})$	$\left\{ \begin{pmatrix} +1/2 \\ -1/2 \end{pmatrix},\, +1/2 \right\}$
$Q_L = \left\{ \begin{pmatrix} u_L \\ d_L \end{pmatrix}, \begin{pmatrix} c_L \\ s_L \end{pmatrix}, \begin{pmatrix} t_L \\ b_L \end{pmatrix} \right\}$	1/2	$(\mathbf{3},\, \mathbf{2})$	$\left\{ \begin{pmatrix} +1/2 \\ -1/2 \end{pmatrix},\, +1/6 \right\}$
$u_R = \{u_R, c_R, t_R\}$	1/2	$(\mathbf{3},\, \mathbf{1})$	$\{0,\, +2/3\}$
$d_R = \{d_R, s_R, b_R\}$	1/2	$(\mathbf{3},\, \mathbf{1})$	$\{0,\, -1/3\}$
$L_L = \left\{ \begin{pmatrix} \nu_{e_L} \\ e_L \end{pmatrix}, \begin{pmatrix} \nu_{\mu_L} \\ \mu_L \end{pmatrix}, \begin{pmatrix} \nu_{\tau_L} \\ \tau_L \end{pmatrix} \right\}$	1/2	$(\mathbf{1},\, \mathbf{2})$	$\left\{ \begin{pmatrix} +1/2 \\ -1/2 \end{pmatrix},\, -1/2 \right\}$
$l_R = \{e_R, \mu_R, \tau_R\}$	1/2	$(\mathbf{1},\, \mathbf{1})$	$\{0,\, -1\}$

Table 2.1.: Fields of the Standard Model. Fields with integer spin follow Bose–Einstein statistics, fields with spin 1/2 follow Fermi–Dirac Statistics. The gauge group representation is given in the third column, respectively. Gluons, G^a_μ, are octets ($\mathbf{8}$) under $SU(3)_C$ and singlets ($\mathbf{1}$) under $SU(2)_L$. The third component of the weak isospin is denoted by I^z_W, the weak hypercharge by Y_W. The values for Y_W are given in the convention of Eq. (2.5). The electroweak gauge bosons W^i_μ are singlets ($\mathbf{1}$) under $SU(3)_C$ and triplets ($\mathbf{3}$) under $SU(2)_L$. The electroweak gauge boson B_μ is a singlet both under $SU(3)_C$ and under $SU(2)_L$. Eigenstates w.r.t. the weak isospin are $\{W^+_\mu, W^-_\mu, W^3_\mu\}$, with $W^\pm_\mu = \frac{1}{\sqrt{2}}\left(W^1_\mu \mp i W^2_\mu\right)$ and eigenvalues $I^z_W(W^\pm_\mu) = \pm 1$ and $I^z_W(W^3_\mu) = 0$. The scalar Higgs field Φ is a doublet ($\mathbf{2}$) under $SU(2)_L$. The left-handed fermions, i.e. quarks Q_L and leptons L_L, are doublets, the right-handed fermions, i.e. quarks u_R, d_R and leptons l_R, are singlets under $SU(2)_L$. The quarks are charged under $SU(3)_C$ and transform as triplets.

with a complex scalar $SU(2)_L$ doublet field

$$\Phi = \begin{pmatrix} \phi^+ \\ \phi^0 \end{pmatrix} , \quad \text{with} \quad \begin{cases} I^z_W(\phi^+) = +1/2, \quad Y_W(\phi^+) = +1/2 & \Rightarrow Q_{\text{EM}}(\phi^+) = +1 \\ I^z_W(\phi^0) = -1/2, \quad Y_W(\phi^0) = +1/2 & \Rightarrow Q_{\text{EM}}(\phi^0) = 0 \end{cases} . \tag{2.7}$$

The Higgs field Φ has a non-vanishing EW VEV v_{EW} that in unitary gauge can be rotated to

$$\Phi = \frac{1}{\sqrt{2}} \begin{pmatrix} 0 \\ h + v_{\text{EW}} \end{pmatrix} , \tag{2.8}$$

with h denoting fluctuations around the EW VEV corresponding to the SM Higgs boson. In unitary gauge, three degrees of freedom of the Higgs field are absorbed into the longitudinal degrees of freedom of the massive electroweak gauge bosons,

$$\mathcal{L}_{\text{SM}} \supset (D_\mu \Phi)(D^\mu \Phi) = \left(m_W^2 W_\mu^+ W^{\mu -} + \frac{1}{2} m_Z^2 Z_\mu Z^\mu \right) + \dots , \tag{2.9}$$

where we have identified the mass eigenstates

$$W_\mu^\pm = \frac{1}{\sqrt{2}} \left(W_\mu^1 \mp i W_\mu^2 \right) , \tag{2.10}$$

$$Z_\mu = \cos\theta_W \, W_\mu^3 - \sin\theta_W \, B_\mu , \tag{2.11}$$

$$A_\mu = \sin\theta_W \, W_\mu^3 + \cos\theta_W \, B_\mu , \tag{2.12}$$

with the Weinberg angle θ_W,

$$\cos\theta_W = \frac{g}{\sqrt{g^2 + g'^2}} , \quad \sin\theta_W = \frac{g'}{\sqrt{g^2 + g'^2}} . \tag{2.13}$$

The masses of the $W^\pm$ and Z bosons and the photon γ, which is associated with the field A_μ, are

$$m_W = \frac{1}{2} \, g \, v_{\text{EW}} , \quad m_Z = \frac{m_W}{\cos\theta_W} , \quad m_\gamma = 0 . \tag{2.14}$$

The value of the EW VEV v_{EW} can be derived from the Fermi constant G_F as

$$G_F = \frac{g^2}{4\sqrt{2}\, m_W^2} = \frac{1}{\sqrt{2}\, v_{\text{EW}}^2} \quad \Rightarrow \quad v_{\text{EW}} = \sqrt{\frac{1}{\sqrt{2} G_F}} \simeq 246.22 \, \text{GeV} . \tag{2.15}$$

Furthermore, in unitary gauge, with $2\mu^2 = 2\lambda \, v_{\text{EW}}^2 \equiv m_h^2$, the scalar potential simplifies to

$$V(\Phi) = -\frac{m_h^2}{2} h^2 + \frac{\lambda_{hhh}}{3!} h^3 + \frac{\lambda_{hhhh}}{4!} h^4 + \text{const.} , \tag{2.16}$$

which defines the tree-level Higgs boson trilinear and quartic self-couplings as

$$\lambda_{hhh} = \frac{3 \, m_h^2}{v_{\text{EW}}} , \quad \lambda_{hhhh} = \frac{3 \, m_h^2}{v_{\text{EW}}^2} . \tag{2.17}$$

The SM Higgs potential therefore is completely determined by the electroweak VEV v_{EW} through Eq. (2.15) and the SM Higgs boson mass m_h. The Higgs field and the fermion sector are coupled in the *Yukawa* sector

$$\mathcal{L}_{\text{SM}} \supset \mathcal{L}_{\text{Yukawa}} \equiv -\overline{Q}'_L \hat{Y}_u \widetilde{\Phi} \, u'_R - \overline{Q}'_L \hat{Y}_d \Phi \, d'_R - \overline{L}_L \hat{Y}_l \tilde{\Phi} \, l_R + \text{h.c.} , \tag{2.18}$$

where $\widetilde{\Phi} \equiv i\sigma^2\Phi^*$ and $\hat{Y}_u$, $\hat{Y}_d$ and $\hat{Y}_l$ are complex Yukawa coupling matrices for the up-type quarks, down-type quarks and leptons, respectively. $\hat{Y}_l$ can be chosen diagonal without loss of generality. Consequently, the *interaction eigenstates* of the leptons are equivalent to their *mass eigenstates*.[4] The derivation of the mass eigenstates in the quark sector requires a diagonalization of both $\hat{Y}_u$ and $\hat{Y}_d$. We perform rotations with unitary matrices U and D, i.e. $U^\dagger U = UU^\dagger = 1$ and $D^\dagger D = DD^\dagger = 1$, to define the quark mass eigenstates, with $\overline{Q}'_L \equiv \left(\overline{u}'_L, \overline{d}'_L\right)$,

$$\overline{u}'_L \equiv \overline{u}_L U^\dagger_L , \quad \overline{d}'_L \equiv \overline{d}_L D^\dagger_L , \quad u'_R \equiv U_R u_R , \quad d'_R \equiv D_R d_R . \tag{2.19}$$

The quark mass matrices M_u and M_d are then given by

$$\frac{v_{\text{EW}}}{\sqrt{2}} U^\dagger_L \hat{Y}_u U_R = M_u = \text{diag}(m_u, m_c, m_t) , \tag{2.20}$$

$$\frac{v_{\text{EW}}}{\sqrt{2}} D^\dagger_L \hat{Y}_d D_R = M_d = \text{diag}(m_d, m_s, m_b) . \tag{2.21}$$

The Yukawa sector is diagonal in the basis defined in Eq. (2.19). The covariant derivative of Eq. (2.3) introduces couplings between quarks and gauge bosons stemming from the kinetic terms, $i\overline{q}\not{D}q$. The γ and Z couplings to quarks are diagonal in the mass basis. However, because the $W^\pm$ couplings mix up-type and down-type quarks, their basis change introduces the Cabibbo–Kobayashi–Maskawa (CKM) matrix [55, 56], defined as $V \equiv U^\dagger_L D_L$, and

$$\mathcal{L}_{\text{SM}} \supset i\overline{Q}'_L \not{D} Q'_L \supset \frac{g}{\sqrt{2}} \overline{u}_L V \gamma^\mu d_L W^+_\mu + \text{h.c.} . \tag{2.22}$$

In 2012, the ATLAS and CMS collaborations reported an observation of a Higgs boson at the Large Hadron Collider (LHC) [17, 18]. Since then the Higgs boson has been studied and has so far been found to agree with the predictions for an SM Higgs boson within experimental and theoretical uncertainties, as summarized in Refs. [19, 20]. The observations are compatible with a $\mathcal{CP}$-even scalar,[5] with SM-like couplings and measured signal strengths compatible with the SM predictions.[6] The mass of the observed Higgs boson is determined as $m_h = [125.09 \pm 0.21(\mathit{stat.}) \pm 0.11(\mathit{syst.})]\,\text{GeV}$ in an official combination of the ATLAS and CMS result after LHC Run 1 [58]. We will use this result for our calculations in the context of this thesis. An average by the Particle Data Group based on recent independent mass measurements by ATLAS and CMS determines the observed Higgs boson mass to be $m_h = (125.27 \pm 0.17)\,\text{GeV}$ [51].

The SM cannot be the complete theory of nature as it does not include gravity, which is the fourth fundamental force present in nature. Further hints towards BSM physics come from its inability to explain experimental data like, e.g. non-zero neutrino masses, dark matter and the matter–antimatter asymmetry of the universe. Concerning the latter two, we will go into more detail in Chapter 3. The scalar sector provides a promising venue to include BSM physics into the successful framework of the SM while matching experimental observations. Besides the mass measurement, an independent measurement of the Higgs boson trilinear and quartic self-couplings is necessary to determine whether the shape of the Higgs potential follows the prediction of the SM, or whether it deviates from it. Current bounds on the trilinear Higgs boson self-coupling, e.g. Ref. [19, 59], still allow for significant deviations from

---

[4] This no longer holds when mass terms for neutrinos are included in a BSM theory.

[5] The possibility of a $\mathcal{CP}$-odd admixture in e.g. the top quark Yukawa coupling of the observed Higgs boson is still allowed by experimental data, as investigated e.g. in Ref. [57].

[6] In the experimental analysis, the production rates that are observed in a specific channel or for a specific final state, are parameterized by signal strengths. A signal strength normalizes the measured cross section multiplied by the branching ratio to the SM prediction.

the SM prediction. Furthermore, extensions of the scalar sector, while being in agreement with the observation of an SM-like Higgs boson, can enable a first-order EWPT as well as incorporate dark matter candidates that produce the observed dark matter relic density. In this thesis we study SM extensions that are in agreement with experimental collider data like the SM is, *but* in addition can allow for first-order EWPTs that might source observable gravitational waves, or can incorporate a candidate for dark matter.

The construction of an extended scalar sector, is constrained by the experimental non-observation of flavour-changing neutral currents (FCNCs) and the measurement of the ρ parameter that is very close to one [51]. At tree-level the ρ parameter can be expressed as [60–62]

$$\rho \equiv \frac{m_W^2}{m_Z^2 \cos^2\theta_W} = \frac{\sum_{i=1}^{n} \left[I_{W,i}\left(I_{W,i}+1\right) - \frac{1}{4} Y_{W,i}^2 \right] v_i}{\sum_{i=1}^{n} \frac{1}{2} Y_{W,i}^2 v_i}, \tag{2.23}$$

where the sums run over weak isospin I_W and weak hypercharge Y_W of all n scalar multiplets with VEVs v_i. The scalar sector can be expanded by any number of $SU(2)_L$ doublets with $I_W = \frac{1}{2}$ and $Y_W = +1$ or $SU(2)_L$-singlets with $I_W = Y_W = 0$, as both fulfil $I_W(I_W+1) = \frac{3}{4} Y_W^2$, leaving the ρ parameter precisely at unity at tree-level.

When extending the scalar sector with additional doublets and singlets, additional $\mathbb{Z}_2$ symmetries are imposed on the model at $T = 0\,\text{GeV}$ in order to prevent FCNCs at tree-level and zero temperature to comply with the strict experimental bounds. However, if a $\mathbb{Z}_2$ symmetry is spontaneously broken by scalar fields developing a VEV, *domain walls* are introduced [63–65], cf. the discussion in [66]. Domain walls are in conflict with observations, as they would dominate the energy density of the universe at some late time [67–69]. In the case of an explicitly or softly[7] broken $\mathbb{Z}_2$ symmetry, domain wall networks are unstable and decay [70].

The two BSM models that are studied in this thesis are the following ones: In Chapters 6 and 10 we focus on a $\mathcal{CP}$-conserving Two-Higgs-Doublet Model (2HDM) that extends the SM scalar sector by one additional scalar $SU(2)_L$ doublet. In Chapter 11 we investigate a Next-To-Minimal Two-Higgs-Doublet Model (N2HDM) where the SM scalar sector is extended by an additional $SU(2)_L$ doublet and a real singlet under $SU(2)_L$.

---

[7] A $\mathbb{Z}_2$ symmetry is softly broken if the $\mathbb{Z}_2$-breaking term comes with a parameter carrying mass dimension.

CHAPTER 3

The Early Universe

We observe an expanding universe, filled with almost perfect black-body background radiation, with visible matter structured into solar systems, galaxies and galaxy clusters. This chapter briefly sketches the cosmological history of the early universe along the lines of the SM of cosmology, the Λ cold dark matter model (ΛCDM), that is experimentally tested e.g. by the space telescopes WMAP [71] and Planck [21]. Reviews on the topic are given in e.g. Refs. [51, 72–75].

The universe is observed to be homogeneous and isotropic on large scales above the size of galaxy superclusters of $\mathcal{O}(10\,\mathrm{Mpc})$ [51, 76]. Not only the matter density of the universe today is on large scales homogeneous, also the *cosmic microwave background* (CMB) which is the almost perfect black-body background radiation with a temperature of $T = (2.7255 \pm 0.0006)\,\mathrm{K}$ [51]. The CMB is made up of free-streaming photons that were produced at the time of last recombination, when the photons dropped out of thermal equilibrium. More on the topic of thermal relics will follow below. The large-scale isotropy and homogeneity of the universe at recombination and today can be explained if there existed an early period of accelerated expansion, called *inflation*, that leads to causal connections on large scales.

Today, the universe is still observed to be expanding, as inferred from e.g. the redshift of photons emitted from visible matter [77]. The *Hubble rate* H describes the expansion rate of the universe, as a function of time t,

$$H(t) = \frac{\dot{a}(t)}{a(t)}\,, \tag{3.1}$$

in terms of a growing scale factor $a(t)$. The *Hubble constant* H_0 defines the Hubble rate today at $T = T_0$. There is an unresolved tension between H_0 determined from indirect measurements, e.g. by fitting ΛCDM to the CMB from which the Planck collaboration obtains $H_0 = (67.49 \pm 0.53)\,\mathrm{kms}^{-1}\mathrm{Mpc}^{-1}$ [21], and from direct measurements, e.g. the measurement of redshifts of stars, which leads to $H_0 = (73.2 \pm 1.3)\,\mathrm{kms}^{-1}\mathrm{Mpc}^{-1}$ [78], cf. e.g. Ref. [79]. Our calculations in the presented work use the result by Planck.

The time evolution of the energy density content of the universe is written in terms of the

Friedmann equation in the form of

$$H(t)^2 + \frac{k}{a(t)^2} = \frac{\rho_{\rm rad}(t) + \rho_{\rm mat}(t) + \rho_\Lambda(t)}{3M_{\rm Pl}^2}\,, \tag{3.2}$$

with the Planck mass $M_{\rm Pl} = (1.220\,890 \pm 0.000\,014) \times 10^{19}$ GeV [80], the curvature k, radiation energy density $\rho_{\rm rad} \propto a^{-4}$, matter energy density $\rho_{\rm mat} \propto a^{-3}$ and vacuum energy density $\rho_\Lambda \propto a^0$. The *critical density* ρ_c is defined by multiplying Eq. (3.2) with $H(t)^{-2}$, cf. Ref. [72],

$$1 + \frac{k}{H(t)^2 a(t)^2} = \frac{\rho_{\rm tot}(t)}{\rho_c(t)}\,,\ \text{with}\ \rho_c(t) = 3H(t)^2 M_{\rm Pl}^2\,. \tag{3.3}$$

Consequently, if the total energy density of the universe, $\rho_{\rm tot} \equiv \rho_{\rm rad} + \rho_{\rm mat} + \rho_\Lambda$, is equal to the critical density, then the universe is flat, i.e. $k = 0$. As the scale factor a grows with time, initially the radiation density $\propto a^{-4}$ dominated the energy density content so that the universe was *radiation dominated.* An earlier time is associated with a higher cosmological redshift z, derived via

$$1 + z = \frac{a_0}{a(t)}\,, \tag{3.4}$$

with a redshift of today at $t = t_0$ of $z_0 = 0$. Radiation domination ended at the point of matter–radiation equality at a cosmological redshift of $z_{\rm eq} = 3411 \pm 48$ [21], before the photons decoupled at $z_{\rm dec} = 1090.30 \pm 0.41$ [21]. Today, the energy density of the universe is dominated by vacuum energy [51].

In the hot early universe, that is the focus of this thesis, all particles were in thermal equilibrium inside a thermal bath, and relativistic particles, i.e. particles for which $m \ll T$, dominated the energy density. Within this thesis, we study EWPTs that we assume to take place in this radiation-dominated epoch. In the following, we review expressions for the energy density and Hubble rate in the radiation-dominated universe that will be used in later calculations. We can express the scale factor as a function of temperature under the assumption of conservation of the entropy density s per comoving volume

$$0 = \frac{d}{dt}\left(sa^3\right) \sim \frac{d}{dt}\left(g_* T^3 a^3\right) \sim \frac{d}{dt}\left(T^3 a^3\right) \quad \Leftrightarrow \quad a \propto T^{-1}\,, \tag{3.5}$$

where we also assumed that during the radiation-dominated epoch the number of effective degrees of freedom, g_*, remains constant.[1] Furthermore, the assumption of entropy conservation can be directly used to relate time and temperature in the radiation-dominated epoch. Assuming again that in the radiation-dominated epoch, $\frac{d}{dt} g_* = 0$, it follows

$$0 = 3T^2 a^2 \left(\frac{dT}{dt} a + T\,\dot a\right) \quad \Leftrightarrow \quad dt = -\frac{dT}{TH(T)}\,. \tag{3.6}$$

The energy density in the radiation-dominated epoch as a function of temperature is

$$\rho_{\rm rad}(T) = \frac{\pi^2}{30} g_* T^4\,. \tag{3.7}$$

We obtain the Hubble rate in the radiation-dominated era, where the total energy density is given by $\rho_{\rm tot} \simeq \rho_{\rm rad}$, using Eq. (3.2), as,

$$H(T) = \sqrt{\frac{\rho_{\rm tot}(T)}{3M_{\rm Pl}^2} - \frac{k}{a(T)^2}} \simeq \sqrt{\frac{\rho_{\rm rad}(T)}{3M_{\rm Pl}^2}} = \frac{\pi}{M_{\rm Pl}}\sqrt{\frac{g_*}{90}}T^2\,. \tag{3.8}$$

---

[1] After the radiation-dominated epoch, the number of effective degrees of freedom g decreases with time and decreasing temperature from $g_* = 106.75$ when all particles are relativistic, to $g_*(T_0) \equiv g_0 \approx 3 - 4$ today, depending on the assumed temperature of neutrino decoupling, when only the photons are still relativistic. For a derivation see e.g. Ref. [81]. Planck measures $g_0 = 3.11^{+0.44}_{-0.43}$, and is consequently deriving upper bounds on the neutrino masses [21].

When particles of mass m are in thermal equilibrium, their interaction rate is larger than the Hubble rate, $\Gamma(T) \gg H(T)$. However, as the universe cools down, the Hubble rate grows and reaches $\Gamma(T_{\text{f.o.}}) = H(T_{\text{f.o.}})$ and for $T < T_{\text{f.o.}}$, $\Gamma(T) \ll H(T)$ and massive particles are decoupled from the thermal plasma. The relic number density of a particle species is determined by the number density at the *freeze-out* temperature $T_{\text{f.o.}}$. The redshift during the expansion of the universe until today then determines the relic number density of the particle species today. For *hot relics*, the freeze-out takes place when $T_{\text{f.o.}} \gg m$, for *cold relics*, the freeze-out takes place in the non-relativistic regime, when $T_{\text{f.o.}} \ll m$.

On small scales, the CMB is observed to have temperature fluctuations of $\delta T/T \sim \mathcal{O}(10^{-5})$ [51]. A spherical Fourier transform of the temperature fluctuations yields the CMB power spectrum which is fitted to the ΛCDM prediction to determine e.g. the energy density parameters Ω, defined as energy density ratios to the critical density ρ_c of Eq. (3.3). These measurements are in agreement with a flat universe with $\Omega_k = 0.001 \pm 0.002$, and an energy content made out of vacuum energy $\Omega_\Lambda = 0.679 \pm 0.001$ and matter $\Omega_{\text{mat}} = 0.3150 \pm 0.0007$, with negligible contribution from radiation, $\Omega_{\text{rad}} = \mathcal{O}(10^{-5})$ [21]. The matter energy density Ω_{mat} is measured to consist of ordinary, baryonic, matter, Ω_b and non-baryonic non-luminous matter, also called *dark matter* (DM), Ω_χ, here written multiplied with the reduced Hubble constant $h = 0.674 \pm 0.005$ [21]

$$\Omega_b h^2 = 0.0224 \pm 0.0002, \tag{3.9}$$

$$\Omega_\chi h^2 = 0.1200 \pm 0.0012\,. \tag{3.10}$$

Consequently, only less than 5 % of the energy density of the universe today is made of baryonic matter and almost 26 % consists of non-baryonic DM. Aside from the peak spectrum inferred from the temperature anisotropies in the CMB, other evidence for DM comes e.g. from galaxy clusters [82] and galaxy rotation curves [83]. Furthermore, DM plays an important role in the formation of structures in the early universe, which can only be explained if the DM is a cold relic to stabilize matter accumulation [84, 85]. No particle of the SM can fully explain the DM relic density.[2] In Chapter 11 we will discuss a BSM model that contains a candidate for dark matter in the form of a *weakly interacting massive particle* (WIMP), which interacts weakly with the SM sector and freezes out in the non-relativistic regime, when $m_\chi \gg T$. The nature of DM is an open question as there is no evidence for DM found at collider searches [86, 87], at direct detection experiments [88–91] and at indirect detection experiments [92]. Consequently, all current experiments searching for DM give rise to exclusion bounds on the parameter space of specific DM models. The exclusion bounds set by direct detection experiments will be illustrated further in Chapter 11 for the model ‘CP in the Dark’.

Another open question is the origin of the matter–antimatter asymmetry, also called *baryon asymmetry* of the universe (BAU). The puzzle is that the difference between the number density of baryons, n_b, and the number density of anti-baryons $n_{\overline{b}}$, often written normalized to the photon number density n_γ, is determined to be non-vanishing [21, 51]

$$\eta \equiv \frac{n_b - \overline{n}_b}{n_\gamma} \simeq \frac{n_b}{n_\gamma} \simeq (6.12 \pm 0.04) \times 10^{-10}\,. \tag{3.11}$$

However, any initial excess of matter over antimatter would be washed out during inflation. Moreover, the causally connected regions after inflation are too small for a mechanism to separate matter and antimatter successfully. An excess of matter over antimatter can be dynamically generated if for a system with initial matter–antimatter symmetry, the Sakharov conditions are satisfied [32]. These are: (1) existence of a baryon number violating process,

---

[2] Neutrinos are part of dark matter, however, they cannot explain the complete relic density, as they constitute *hot* dark matter.

(2) violation of the $\mathcal{C}$ and $\mathcal{CP}$ symmetries, and (3) departure from thermal equilibrium. A mechanism that fulfills all these necessary conditions is *electroweak baryogenesis* (EWBG) [33, 34]. In EWBG, the departure from thermal equilibrium is realized through a *strong* first-order EWPT from a false vacuum, where the electroweak symmetry is exact, to a true vacuum, where it is spontaneously broken. The strong first-order EWPT takes place at a temperature $T < T_c$, where the critical temperature T_c is defined as the temperature at which the true and false vacuum are degenerate. It then proceeds via the formation and expansion of bubbles filled with the true vacuum within a false vacuum plasma. Inside the false vacuum, where the electroweak symmetry is unbroken, sphaleron-mediated baryon- and lepton-number violating processes are in thermal equilibrium [93, 94].[3] $\mathcal{CP}$-violating interactions between plasma and bubble wall create a $\mathcal{CP}$ asymmetry which is transferred into a baryon excess by the sphaleron transitions. Inside the true vacuum, the electroweak symmetry is spontaneously broken, which translates into a damped sphaleron interaction rate. A non-zero BAU is conserved inside the true vacuum bubble, if the sphaleron interactions are sufficiently suppressed [95, 96],

$$\Gamma^{\mathrm{sph}}_{\not{B}+\not{L}} \propto \mathrm{e}^{\frac{-E^{\mathrm{sph}}(T)}{T}}\,, \tag{3.12}$$

that is if the *baryon wash-out* condition [34]

$$\xi_c \equiv \xi(T_c) = \frac{\overline{\omega}^{\mathrm{true}}_{\mathrm{EW}}(T_c)}{T_c} \gtrsim 1\,, \tag{3.13}$$

is fulfilled, defining a strong first-order EWPT. The electroweak VEV of the true vacuum at T_c is denoted by $\overline{\omega}^{\mathrm{true}}_{\mathrm{EW}}(T_c)$. As the SM neither predicts a strong first-order EWPT, nor provides enough $\mathcal{CP}$ violation,[4] BSM physics is required to explain the generation of the matter–antimatter asymmetry of the universe.

In this thesis, we focus specifically on BSM realizations of first-order EWPTs and investigate if they can be of strong first order with $\xi_c > 1$. A strong first-order EWPT could have taken place in the universe after inflation around $T_{\mathrm{EW}} = 100\,\mathrm{GeV}$ [97]. At later times, around $T = \mathcal{O}(100\,\mathrm{MeV})$, the QCD phase transition takes place, where quarks q and gluons form bound states [97].[5] After neutrinos decouple from the thermal bath at $T = \mathcal{O}(1\,\mathrm{MeV})$, the abundances of light nuclei in the universe are produced via Big Bang nucleosynthesis (BBN) [97]. Using the value for the BAU determined from the CMB measurement [21, 71], BBN predicts abundances in agreement with the measured abundances in the universe. This makes BBN the earliest stage in the evolution of the early universe that is probed by current experiments. After BBN comes the recombination stage, when electrons decouple and form electrically neutral hydrogen atoms together with protons. Only then photons can no longer be coupled to the thermal plasma via scattering with the electrons, and therefore decouple and form the CMB [21, 71].

---

[3] This period of electroweak symmetry restoration can also take place in an intermediate stage of the scalar potential evolution. Anything taking place at even higher temperature is then not constrained by EWBG, as the sphaleron processes wash out any remnants of any earlier baryon–antibaryon asymmetry once thermal equilibrium is reached.

[4] The only source for $\mathcal{CP}$ violation in the SM is the complex phase in the CKM matrix.

[5] Due to the non-zero quark masses, lattice gauge theory determines the QCD phase transition to not be of first-order [98]. It is therefore not able to provide a sufficient departure from thermal equilibrium to explain baryogenesis.

Part I.

Prerequisites for a First-Order Electroweak Phase Transition

CHAPTER 4

One-loop Finite-Temperature Effective Potential

Zero-temperature loop corrections as well as finite-temperature effects can have a significant impact on the ground state of the scalar potential [99]. Ideally, we would gain a complete understanding of the scalar potential to all loop orders and at finite temperature by taking into account an infinite number of Feynman diagrams. This is encoded in the effective potential, first described by [100, 101] and later used for theories with spontaneous symmetry breaking [102, 103], at one-loop [104] and higher loop [105] level. For a review consult e.g. Refs. [106, 107]. In the context of this thesis, we work with the effective potential up to next-to-leading order (NLO) in the perturbative expansion, including the resummed higher-loop daisy diagrams that are dominant in the high-temperature expansion, the *one-loop resummed effective potential*.

In Section 4.1 we summarize the derivation of the effective potential at zero temperature. In Section 4.2 we introduce finite temperature field theory. We then formulate the finite-temperature description of the effective potential in Section 4.3. We discuss perturbativity of the finite-temperature effective potential in the high-temperature limit in Section 4.4. Finally, in Section 4.5, we summarize initial conditions for a first-order EWPT.

4.1. Effective Potential at Zero Temperature

Today, at a temperature of $T = 0\,\text{GeV}$, the ground state of the scalar potential receives loop corrections. Because a potential generally contains all non-derivative terms allowed by the symmetries of a theory, the effective potential corresponds to summing all Feynman diagrams with zero external momentum in the diagrammatic approach. The effective potential can also be calculated from the effective action using the background field method which we discuss in the following. We will sketch the derivation of the effective potential for a field theory with one scalar field ϕ along the lines of [104, 105, 108]. In the path integral formalism, the generating functional $Z[J]$ defines the amplitude for a transition from an initial vacuum to a final vacuum under the presence of a source J,

$$Z[J] \equiv \langle 0_{\text{out}} | 0_{\text{in}} \rangle_J = \int \mathcal{D}\phi \exp \left[iS[\phi] + i \int d^4x J(x)\phi(x) \right] , \tag{4.1}$$

where S is the action that is derived from the Lagrangian density $\mathcal{L}$ as

$$S[\phi] = \int d^4x\, \mathcal{L}\{\phi(x)\}\,. \tag{4.2}$$

The Green's functions are derived as functional derivatives,

$$\langle 0_{\text{out}}|\mathcal{T}\{\phi\ldots\phi\}|0_{\text{in}}\rangle = \left(\frac{1}{i}\frac{\delta}{\delta J}\right)^n Z[J]\Big|_{J=0}\,, \tag{4.3}$$

where $\mathcal{T}\{\phi\ldots\phi\}$ is the time-ordered product of n scalar fields ϕ. The generating functional of the connected[1] Green's functions $W[J]$ is defined as

$$W[J] = -i\log Z[J]\,. \tag{4.4}$$

Using Eq. (4.3), we derive the functional derivative of $W[J]$,

$$\phi_c \equiv \frac{\delta W[J]}{\delta J(x)} = \left[\frac{\langle 0_{\text{out}}|\phi(x)|0_{\text{in}}\rangle}{\langle 0_{\text{out}}|0_{\text{in}}\rangle}\right]_J\,. \tag{4.5}$$

In Eq (4.5) we defined the classical background field ϕ_c. It is defined as the VEV in the presence of J. Therefore, ϕ_c takes into account quantum corrections $h_J(x)$ induced through J, and schematically,

$$\phi_c(x) = \phi(x) + h_J(x)\,. \tag{4.6}$$

The effective action is the generating functional of one-particle irreducible[2] Green's functions and is defined via a functional Legendre transformation of $W[J]$,

$$\Gamma[\phi_c] = W[J] - \int d^4x J(x)\phi_c(x)\,. \tag{4.7}$$

Equations (4.5) and (4.7) imply that the variation of the effective action with respect to the classical field yields the external source J [104]

$$\frac{\delta\Gamma[\phi_c]}{\delta\phi_c} = -J\,. \tag{4.8}$$

We expand the effective action in powers of derivatives of the classical background field ϕ_c and obtain

$$\Gamma[\phi_c] = \int d^4x\left[-\underbrace{V_{\text{eff}}(\phi_c)}_{\substack{\textbf{effective}\\ \textbf{potential}}} + \mathcal{O}\left(\partial_\mu\phi_c\right) + \ldots\right]. \tag{4.9}$$

The *effective potential* $V_{\text{eff}}(\phi_c)$ is defined as the zeroth-order term in the derivative expansion of the effective action. An alternative expansion of Γ in powers of ϕ_c yields the following form for the effective potential

$$V_{\text{eff}}(\phi_c) = -\sum_{n=1}^{\infty}\frac{1}{n!}\phi_c^n\Gamma^{(n)}(p=0)\,. \tag{4.10}$$

---

[1] For a connected Feynman diagram, all internal lines are connected. In other words, a connected diagram has no disconnected vacuum loops. Only connected diagrams contribute to the S matrix [109].

[2] Connected Feynman diagrams that cannot be split in two separate Feynman diagrams by cutting one internal line are named one-particle irreducible diagrams [109].

The $\Gamma^{(n)}$ are the one-particle irreducible Green's functions with n external legs, p is the external momentum. We derive the one-loop effective potential $V_{\text{eff}}^{(1)}$ by expanding Eq. (4.10) in terms of the loop order and calculate the Green's function $\Gamma_1^{(1)}$ for the one-loop one-particle irreducible diagrams with up to n external legs as follows,

$$V_{\text{eff}}^{(1)}(\phi_c) \equiv V^{(0)}(\phi_c) + V^{(1)}(\phi_c) = V^{(0)}(\phi_c) - \sum_{n=1}^{\infty} \phi_c^n \Gamma_1^{(n)}(p=0)\,, \tag{4.11}$$

$$= V^{(0)}(\phi_c) + \frac{1}{2}\int \frac{d^4k_E}{(2\pi)^4} \log\left(k_E^2 + m^2(\phi_c)\right)\,. \tag{4.12}$$

To obtain Eq. (4.12), a Wick rotation to the Euclidean momentum was performed,

$$k_E = (ik_0, \boldsymbol{k})\,, \quad k_E^2 = -k_0^2 + \boldsymbol{k}^2 = -k^2\,. \tag{4.13}$$

We denote external momenta with p and loop momenta with k in the following. The field-dependent mass $m^2(\phi_c)$ is defined as

$$m^2(\phi_c) = \frac{d^2V^{(0)}(\phi_c)}{d\phi_c^2}\,. \tag{4.14}$$

The one-loop effective potential derived in Eq. (4.12) is ultraviolet (UV) divergent, i.e. the integral diverges for $k_E \to \infty$. The integral in Eq. (4.12) can be rendered UV finite through dimensional regularization and renormalization in the $\overline{\text{MS}}$ renormalization scheme, cf. e.g. Ref. [106]. The UV-finite one-loop effective potential for a theory with scalars ϕ, gauge bosons V and fermions f reads [110]

$$V^{(1)}(\phi_c) \equiv V_{\text{CW}}(\phi_c) = \frac{1}{64\pi^2}\left(\sum_{i=\phi,V,f}(-1)^{2s_i}(1+2s_i)\, m_i^4(\phi_c)\left[\log\frac{m_i(\phi_c)^2}{\mu^2} - c_i\right]\right)\,, \tag{4.15}$$

summed over all particles with spins s_i and with the renormalization constants

$$c_\phi = c_f = \frac{3}{2},\, c_V = \frac{5}{6}\,, \tag{4.16}$$

and the renormalization scale μ, that we choose to we set to $\mu = v(T = 0\,\text{GeV}) = 246.22\,\text{GeV}$ for the work presented in this thesis. Equation (4.15) defines the Coleman–Weinberg (CW) potential in the Landau gauge.[3]

The shape of the zero-temperature one-loop effective potential around its minima at moderate field values is well described by the CW potential of Eq. (4.15). Therefore in this thesis, we use Eq. (4.15) to study minima in the effective potential. However, we note, that for too large field values, large logarithms spoil the perturbative validity of Eq. (4.15) which can be cured using the renormalization group improved effective potential [116–120].

---

[3] The CW potential is gauge dependent [105], but observables calculated from it have to be gauge independent. The gauge-dependence of the effective potential is further discussed in e.g. Refs. [111–115]. We choose the Landau gauge, where the gauge parameter vanishes $\xi = 0$, to have no ghost contribution and to obtain purely transverse gauge boson propagators.

4.2. Field Theory at Finite Temperature

At finite temperature $T > 0\,\text{GeV}$ the vacuum is a thermal bath. A system that exchanges particles and energy with the thermal bath is described by the finite-temperature partition function $Z(\beta)$ for a *grand canonical ensemble* with $\beta = T^{-1}$, chemical potential μ and particle number operator N,

$$Z(\beta) = \text{Tr}\ \exp^{-\beta(H-\mu N)} \equiv \text{Tr}\ \exp^{\beta \hat{H}}\ . \tag{4.17}$$

Finite-temperature observables are described via *Gibbs averages* using the grand canonical density operator $\rho = Z(\beta)^{-1} \exp^{-\beta \hat{H}}$ as

$$\langle \mathcal{O} \rangle_\beta \equiv \text{Tr}(\mathcal{O}\rho)\,. \tag{4.18}$$

Using cyclicity of this trace, it follows that finite-temperature observables are periodic in

$$it \to it + \beta\,. \tag{4.19}$$

Therefore, while zero-temperature Green's functions have causal boundary conditions at $t = \pm\infty$, finite-temperature Green's functions are periodic in Euclidean time $\tau = it$ with period β. Consequently, the Fourier transform of the Green's functions involves discrete frequencies, the *Matsubara frequencies* [121]. In summary, the following replacements are needed to perform a field theory calculation at finite temperature

$$\begin{gathered} \mathbb{R}^4 \to \mathbb{R}^3 \times S^1\,, \\ \int \frac{d^4k}{(2\pi)^4} \to T \sum_{n\in\mathbb{Z}} \int \frac{d^3k}{(2\pi)^3}\,, \end{gathered} \tag{4.20}$$

where S^1 denotes the one-dimensional sphere and with the Matsubara frequencies with $n \in \mathbb{Z}$ defined as

$$k_0 \equiv \omega_n = \begin{cases} \frac{2n\pi}{\beta} & \text{for bosons} \\ \frac{(2n+1)\pi}{\beta} & \text{for fermions} \end{cases}\,. \tag{4.21}$$

At finite temperature, the time variable is traded for the equilibrium temperature. The bosonic and fermionic momentum space causal two-point Green's functions in finite temperature field theory read, respectively,

$$\mathcal{D}_0(\boldsymbol{k}, \omega_n) = \frac{1}{\omega_n^2 + \boldsymbol{k}^2 + m^2} \equiv \frac{1}{\omega_n^2 + \omega_k^2} \equiv \mathcal{D}_0\,, \tag{4.22}$$

$$\mathcal{D}_{1/2}(\boldsymbol{k}, \omega_n) = \frac{\gamma^0 \omega_n + \boldsymbol{\gamma}\boldsymbol{k} - m}{\omega_n^2 + \omega_k^2}\,, \tag{4.23}$$

where we define $\omega_k^2 = \boldsymbol{k}^2 + m^2$. The indices of the propagators $\mathcal{D}$ correspond to the spin quantum numbers of bosons, $S = 0$, and fermions, $S = 1/2$.

4.3. Effective Potential at Finite Temperature

The one-loop effective potential at finite temperature is derived by applying the replacements of Eqs. (4.20) and (4.21) to the zero-temperature one-loop effective potential defined in Eq. (4.12)

$$V_{\text{eff}}^{(1)} = \frac{1}{2} \int \frac{d^4k}{(2\pi)^4} \log(\omega_k^2) \quad \to \quad V_{\text{eff}}^{(1)} = \frac{T}{2} \sum_{n\in\mathbb{Z}} \int \frac{d^3k}{(2\pi)^3} \log(\omega_k^2 + \omega_n^2)\,. \tag{4.24}$$

The temperature dependence of the finite-temperature one-loop effective potential can be isolated, cf. e.g. Ref. [106],

$$V_{\text{eff}}^{(1)} = \int \frac{d^3k}{(2\pi)^3}\frac{\omega_k}{2} + \underbrace{\frac{1}{\beta}\int \frac{d^3k}{(2\pi)^3}\log\left(1-\mathrm{e}^{-\beta\omega_k}\right)}_{\equiv V_T^{(1)}} . \tag{4.25}$$

The first term of Eq. (4.25) can be rewritten using that [106]

$$-\frac{i}{2}\int\frac{dx}{2\pi}\log(-x^2+\omega_k^2) = \frac{\omega_k}{2} + \text{const.}, \tag{4.26}$$

and we obtain

$$\int \frac{d^3k}{(2\pi)^3}\frac{\omega_k}{2} = -\frac{i}{2}\int\frac{d^4k}{(2\pi)^4}\log(-k_0^2+\omega_k^2) = \frac{1}{2}\int\frac{d^4k_E}{(2\pi)^4}\log(k_E^2+m^2) = V_{\text{CW}}\,, \tag{4.27}$$

where in the last step, we again performed the Wick rotation, $k_0 \to ik_0$, to the Euclidean momentum k_E as defined in Eq. (4.13). Consequently, in Eq. (4.25), we identify the temperature-independent CW potential as the first term and define the temperature-dependent potential $V_T^{(1)}$ as the second term. The temperature-dependent potential $V_T^{(1)}$ for a theory with scalars ϕ, gauge bosons V and fermions f reads [110]

$$V_T^{(1)}(\phi_c,\,T) = \frac{1}{2\pi^2\beta^4}\sum_{i=\phi,V,f}(-1)^{2s_i}(1+2s_i)\,J_{B/F}\left[\beta^2m_i^2(\phi_c)\right] . \tag{4.28}$$

Equation (4.28) is summed over the particle species with spins s_i with $J_{B/F}$ defined as

$$J_{B/F}(x^2) \equiv J_{\mp}(x^2) \equiv \int_0^\infty dk\,k^2\log\left[1\mp\exp\left(-\sqrt{k^2+x^2}\right)\right] . \tag{4.29}$$

The temperature-dependent one-loop effective potential is a function of $x^2 = \beta^2m^2 = m^2/T^2$, the ratio of the eigenvalues of the field-dependent mass matrix and the temperature T. In the limit of $m \ll T$, or $x \to 0$, $J_{B/F}$ can be expanded as [106, 107, 110, 122],

$$\lim_{x\to 0} J_B(x^2) = -\frac{\pi^4}{45} + \frac{\pi^2}{12}x^2 - \frac{\pi}{6}(x^2)^{3/2} - \frac{1}{32}(x^2)^2\log\left[x^2 - c_-\right] + \dots\,, \tag{4.30}$$

$$\lim_{x\to 0} J_F(x^2) = -\frac{7\pi^4}{360} + \frac{\pi^2}{24}x^2 + \frac{1}{32}\left(x^2\right)^2\log\left[x^2 - c_+\right] + \dots\,, \tag{4.31}$$

with $c_+ = 3/2 + 2\log\pi - 2\gamma_{\text{E}}$ and $c_- = c_+ + 2\log 4$, and with the Euler–Mascheroni constant denoted by γ_{E}. The expansion of the bosonic thermal function contains a term which is cubic in x which is absent for fermions.

The finite-temperature effective potential up to one-loop order has the following form

$$V_{\text{eff}}^{(1)}(\phi_c, T) = V^{(0)}(\phi_c) + V_{\text{CW}}(\phi_c) + V_T^{(1)}(\phi_c,\,T)\,. \tag{4.32}$$

It is split into the tree-level potential $V^{(0)}$, the one-loop temperature-independent and $\overline{\text{MS}}$-renormalized potential V_{CW}, defined in Eq. (4.15), and the UV-finite one-loop finite-temperature corrections, $V_T^{(1)}$, defined in Eq. (4.28).

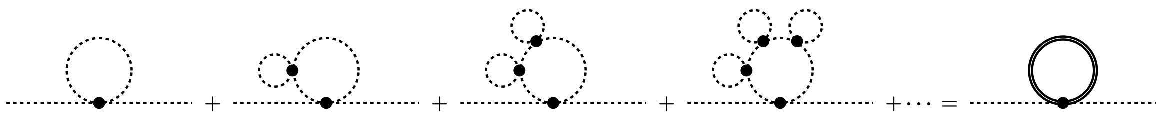

Figure 4.1.: Daisy resummation with a bosonic central loop in ϕ^4 theory. The left-most diagram is the dominant one-loop finite-temperature diagram $\propto \lambda T^2$ that is derived in Eq. (4.34). The other N-loop diagrams on the left side of the equation, that are summed over for $N \to \infty$, are the daisy diagrams with $N-1$ insertions of Π_1 around the bosonic central loop. The result of the daisy resummation is Π_1^{daisy}, see Eq. (4.38), which is illustrated by the diagram on the right side of the equation with the dressed propagator drawn as a solid double line.

4.4. High-Temperature Limit and Resummation

The high-temperature limit of the finite-temperature effective potential gives insights into possible EWPTs in the early universe. The EW symmetry of the SM, $SU(2)_L \times U(1)_Y$, is spontaneously broken to $U(1)_{\text{EM}}$ at low temperatures, as discussed in Chapter 2. From the one-loop effective potential as defined in Eq. (4.32), it can be deduced that the leading field- and temperature-dependent term of $V_T^{(1)}$ is $\propto \phi_c^2 T^2$, which can be seen when inserting Eqs. (4.30) and (4.31) into Eq. (4.28). In the SM, this term comes with a positive prefactor, cf. e.g. Ref. [106] and consequently, at high temperature, the EW symmetry is restored by the temperature corrections [123].

However, the restoration of a symmetry which is broken for the zero-temperature tree-level potential by the loop-level finite-temperature corrections indicates the *breakdown* of perturbativity of the fixed loop-order expansion at finite temperature [122, 124, 125], cf. e.g. Refs. [106, 126] for reviews. The reason for this breakdown is that contributions of higher-order finite temperature diagrams of the form illustrated in Figure 4.1 must not be neglected in the finite-temperature perturbative expansion. Perturbativity of the finite-temperature expansion is restored if in addition to the one-loop finite-temperature diagram, that is illustrated in Figure 4.1 (left), also higher-order finite-temperature diagrams are taken into account through resummation which we will discuss in the following.

Following the lines of [106, 126], we will sketch in the following the procedure of *resummation* for the case of a self-interacting real scalar field ϕ with quartic self-coupling λ. The leading-order (LO) finite-temperature correction stems from the one-loop thermal mass diagram with zero external momentum, $p = 0$, that is illustrated in Figure 4.1 (left) [126]. The amplitude is calculated as follows,

$$\Pi_1(p=0) \propto \lambda T \sum_{n\in\mathbb{Z}} \int \frac{d^3k}{(2\pi)^3} \frac{1}{\omega_k^2 + \omega_n^2} \,. \tag{4.33}$$

The finite-temperature integral in Eq. (4.33) can be split analogously to Eq. (4.25). Taking only the temperature-dependent part into account, this yields

$$\Pi_1(p=0) \propto \lambda \int \frac{d^3k}{(2\pi)^3} \frac{1}{\omega_k} \frac{1}{\mathrm{e}^{\omega_k/T} - 1} \xrightarrow{m \ll T} \propto \lambda \int_0^\infty d|\boldsymbol{k}| \frac{|\boldsymbol{k}|}{\mathrm{e}^{|\boldsymbol{k}|/T} - 1} \propto \lambda T^2 \,. \tag{4.34}$$

In the second-to-last step, the integral is approximated in the high-temperature limit $m \ll T$ and evaluated in spherical coordinates. Numerical prefactors are neglected. Consequently, the dominant one-loop finite-temperature contribution in the limit $m \ll T$ scales $\propto T^2$. It is called *hard thermal loop* in the following.

Higher-order loop diagrams with insertions of hard thermal loops around the central loop are called *daisy diagrams* and are illustrated in Figure 4.1. These diagrams have to be resummed to restore perturbativity at finite temperature, cf. e.g. Ref. [106]. The amplitude of the N-loop *daisy* diagram with $(N-1)$ petals attached to the central loop is, cf. e.g. Ref. [127],

$$\Pi_{N>0}(p=0) \propto \lambda T \sum_{n\in\mathbb{Z}} \int \frac{d^3k}{(2\pi)^3} \left[-\Pi_1\right]^{N-1} \mathcal{D}_0^N \,, \tag{4.35}$$

where the finite-temperature propagator $\mathcal{D}_0$ was defined in Eq. (4.22). However, in the high-temperature limit, defined as $x = m/T \to 0$, the integral of Eq. (4.35) is infrared (IR) divergent, i.e. divergent for $k \to 0$, for the Matsubara zero mode $n = 0$, because

$$\lim_{\substack{\boldsymbol{k}\to 0\\ x\to 0}} \mathcal{D}_0(n=0) = \lim_{\substack{\boldsymbol{k}\to 0\\ x\to 0}} \frac{1}{\boldsymbol{k}^2+m^2} = \lim_{\boldsymbol{k}\to 0} \frac{1}{\boldsymbol{k}^2} \to \infty \,. \tag{4.36}$$

While the individual petal with $N = 1$ is IR-safe in the massless limit, compare Eq. (4.34), the IR divergence of the higher-loop daisy diagrams becomes worse with more petals attached. We find, however, that in the infinite sum of the N-loop daisy diagrams, called *daisy resummation*, the IR-divergence is cured, cf. e.g. Ref. [127],

$$\sum_{N=1}^{\infty} \left[-\Pi_1\right]^{N-1} \mathcal{D}_0^N = \mathcal{D}_0 \sum_{N=0}^{\infty} \left[-\Pi_1\,\mathcal{D}_0\right]^N = \frac{1}{\boldsymbol{k}^2+m^2+\Pi_1} \,. \tag{4.37}$$

Daisy resummation leads to an IR-finite leading thermal self-energy correction in the hard thermal loop approximation, $m \ll T$. The daisy-resummed IR-finite one-loop amplitude is

$$\Pi_1^{\text{daisy}} = \frac{\lambda}{2} T \sum_{n\in\mathbb{Z}} \int \frac{d^3k}{(2\pi)^3} \frac{1}{\omega_n^2+\omega_k^2+\Pi_1} \,. \tag{4.38}$$

In Figure 4.1, we illustrate the derivation of Π_1^{daisy} in terms of Feynman diagrams. As can be seen from Eq. (4.37), performing a daisy resummation is equivalent to shifting the propagator mass by the thermal one-loop self-energy correction Π_1,

$$m^2 \to m^2 + \Pi_1 \,, \tag{4.39}$$

yielding a *dressed* propagator in which the thermal mass, the eigenvalue of Π_1, acts as an IR-regulator. The dressed propagator is illustrated by a solid double line in the Feynman diagram on the right side in Figure 4.1. Π_1 is also called the *Debye mass*. The IR divergence, induced by the bosonic Matsubara zero mode, is a symptom of the loss of perturbativity, not its cause. Perturbative breakdown is caused due to sizable higher-loop temperature corrections that spoil the zero-temperature loop expansion. All-order daisy resummation of the hard thermal loops cures the perturbative breakdown by re-ordering the counting and taking the dominant all-loop temperature correction into account already at one-loop level. Daisy resummation of infinitely many hard thermal loop petal insertions also cures the IR divergence of individual daisy diagrams with $N > 1$ loops. In summary, taking into account leading temperature corrections restores perturbativity, but they have to be resummed to all orders in order to cure the IR divergence that appears in fixed-order finite temperature field theory.

In the following, we will comment on two commonly used resummation methods, the *Parwani* method [125] and the *Arnold–Espinosa* method [122]. In the Parwani method, the replacement $m^2 \to m^2 + \Pi_1$ is done in Eq. (4.32) in both the CW and the temperature-dependent potential for all bosonic Matsubara modes. In the Arnold–Espinosa method, the propagator of the bosonic Matsubara zero mode of the finite-temperature effective potential of Eq. (4.24) is dressed *before* the potential is split into CW and finite-temperature contribution. We will illustrate below, that the Arnold–Espinosa method is equivalent to adding the *ring* potential. In the Arnold–Espinosa method it follows that, cf. Ref. [128],

$$V^{(1)}_{\text{eff, AE}} = \frac{T}{2}\left(\sum_{\substack{n\in\mathbb{Z},\\ n\neq 0}}\int\frac{d^3k}{(2\pi)^3}\log(\omega_k^2+\omega_n^2) + \int\frac{d^3k}{(2\pi)^3}\log(\omega_k^2+\Pi_1)\right) \tag{4.40}$$

$$= \frac{T}{2}\left(\sum_{n\in\mathbb{Z}}\int\frac{d^3k}{(2\pi)^3}\log(\omega_k^2+\omega_n^2) + \int\frac{d^3k}{(2\pi)^3}\left[\log(\omega_k^2+\Pi_1)-\log(\omega_k^2)\right]\right) \tag{4.41}$$

$$= V^{(1)}_{\text{eff}} + \frac{T}{4\pi^2}\int_0^\infty d|\boldsymbol{k}|\boldsymbol{k}^2\left[\log(\boldsymbol{k}^2+m^2+\Pi_1)-\log(\boldsymbol{k}^2+m^2)\right] \tag{4.42}$$

$$= V^{(1)}_{\text{eff}} \underbrace{-\frac{T}{12\,\pi}\left[(m^2+\Pi_1)^{3/2}-(m^2)^{3/2}\right]}_{\equiv V_{\text{ring}}} = V^{(1)}_{\text{eff}} + V_{\text{ring}}\,, \tag{4.43}$$

using that

$$\text{Re}\left[\int_0^\infty dx\,x^2\,\log(x^2+a)\right] = -\frac{\pi}{3}\,a^{3/2} \quad \text{for} \quad a\in\mathbb{R}\,. \tag{4.44}$$

By dressing the bosonic Matsubara zero mode propagator in Eq. (4.24) directly, we recovered the undressed effective potential of Eq. (4.32) and the ring corrections, V_{ring}, which contain all daisy corrections. Moreover, in Eq. (4.43), we derived the cubic term that appears in the high-temperature limit of the bosonic thermal function in Eq. (4.30). Consequently, the Arnold–Espinosa method is equivalent to taking into account one more order in the high-temperature limit of Eq. (4.30). Analogously, the lack of fermionic zero mode also explains the lack of a cubic term in the high-temperature limit of the fermionic thermal functions in Eq. (4.31). For fermions, the non-zero Matsubara frequency already acts as an IR regulator in the massless limit.

In the high-temperature limit, the Parwani and Arnold–Espinoa methods yield different results, even if in the Parwani method also only the bosonic Matsubara zero mode are resummed, as was shown in Ref. [129]. In the Parwani method, the replacement $m^2 \to m^2+\Pi_1$ is applied in the CW and finite-temperature potential of Eq. (4.32). Consequently, the argument x^2 of the temperature-dependent potential in Eq. (4.28) scales as $x^2 = \beta^2\,(m^2+\Pi_1) \propto \beta^2\,(m^2+\lambda T^2)$ which in the high-temperature limit, defined as $m \ll T$ or $x \to 0$, becomes of order $\mathcal{O}(\lambda)$. Therefore, the expansion of Eq. (4.30) is no longer valid. An expansion of the thermal functions for large x, cf. e.g. Ref. [130], then yields the leading difference between the Parwani and Arnold–Espinoa method, as was derived in [129].

In this thesis, we perform daisy resummation following the Arnold–Espinosa method. In this method, applying the high-temperature assumption, the bosonic zero-mode propagator is dressed in the full one-loop finite-temperature potential of Eq. (4.24) directly, and consequently all Debye mass corrections are isolated into the ring potential. The ring potential exactly reproduces the next order in the high-temperature expansion of the bosonic thermal functions of Eq. (4.30). In the Parwani method, the dressing of the bosonic propagators takes place after the undressed one-loop finite temperature potential was split into the CW and the temperature-dependent potential $V_T^{(1)}$, as described above. Therefore, loop orders become mixed inside the CW potential.

4.5. Initial Conditions for an Electroweak Phase Transition

In this thesis, we study the vacuum phase structure of parameter points of BSM models. This section will review our terminology as well as describe some necessary conditions for EWPTs in the early universe.

The term *phase* is used to describe a temperature-dependent minimum configuration in the multi-dimensional field space, meaning a minimum that moves through the field space when the temperature change leads to a deformation of the effective potential. In this thesis, we use the following terminology to describe phases specified by their VEVs:

- *Electroweak (EW) broken phase*: A phase is called an EW broken phase if

  $$\overline{\omega}_{\text{EW}} = \sqrt{\sum_i \langle \phi_i \rangle^2} > 0 \quad \text{with} \quad \phi_i : \text{ real components of the doublet field} \,,$$

  where all VEVs contribute that originate from the scalar $SU(2)_L \times U(1)_Y$ doublet. Our universe today is in an EW broken phase with $v_{\text{EW}} = \overline{\omega}_{\text{EW}}|_{T=0\,\text{GeV}} = 246.22\,\text{GeV}$.
- *EW symmetric phase*: If $\overline{\omega}_{\text{EW}} = 0$, the EW symmetry $SU(2)_L \times U(1)_Y$ is exact and a phase is named EW symmetric.
- *Charge-Breaking (CB) phase*: If a phase develops a non-vanishing VEV of the charged doublet component, $\langle \phi^\pm \rangle \neq 0$, this phase generates non-vanishing mass terms for the photons. This phase is called charge-breaking (CB) phase as it breaks $U(1)_{\text{EM}}$.
- *Neutral phase*: It is experimentally confirmed that $U(1)_{\text{EM}}$ is an unbroken symmetry at $T = 0\,\text{GeV}$, due to the photon being massless and traveling at the speed of light. Our universe today is in an electromagnetically neutral phase with $\langle \phi^\pm \rangle = 0$, that in addition has $v_{\text{EW}} = 246.22\,\text{GeV}$ (EW broken phase), i.e. at $T = 0\,\text{GeV}$ a valid model needs to be in an electromagnetically neutral EW broken phase with $v_{\text{EW}} = 246.22\,\text{GeV}$. On the one hand, EW symmetric phases are implied to be electromagnetically neutral. A CB phase is therefore necessarily also an EW broken phase. On the other hand, an EW broken phase can either be electromagnetically neutral or CB.
- *$\mathcal{CP}$-violating phase*: A process involving a particle violates the charge conjugation and parity ($\mathcal{CP}$) symmetry, if it is not the same for the antiparticle in the mirrored space [131]. In the models discussed in this thesis, $\mathcal{CP}$ violation is parametrized by a non-vanishing relative phase between doublets, cf. Section 6.1 and Chapter 11.[4] If a phase has $\mathcal{CP}$ violation parametrized by such a relative phase between the doublets, it is necessarily also an EW broken phase.
- *Singlet phase*: If a BSM model has an $SU(2)_L \times U(1)_Y$ singlet sector, a singlet phase is realized when any of its real component fields exhibits a non-vanishing VEV. VEVs of singlet fields do not contribute to the EW VEV. If in addition to a non-zero singlet VEV a phase also develops a non-zero EW VEV, the model would be in an EW broken singlet phase.

Today at $T = 0\,\text{GeV}$, our universe is in a neutral EW broken minimum with $v_{\text{EW}} = 246.22\,\text{GeV}$ that belongs to a neutral EW broken phase which evolves with temperature. However, spontaneously broken gauge symmetries can be restored at higher loop order as well as higher temperature [104]. Electroweak symmetry restoration (EWSR) can be realized due to the dominating terms in the high-temperature expansion, $m \ll T$. The universe at

---

[4] In the model discussed in Chapter 11, as we will review, $\mathcal{CP}$ can also be violated in an EW symmetric phase through a different mechanism.

high temperature could therefore have been in a different phase than today, which opens the possibility of an EWPT in the early universe.

As we are mostly interested in EWPTs, we choose the EW VEV as order parameter for the phase transitions studied in the context of this thesis.[5] In general, the phase diagram of two coexisting phases is characterized by three regions [132]. First, a temperature range in which a first-order EWPT can occur. A first-order transition is characterized by a discontinuity of the free energy in the order parameter, the VEV. This range, or line in a phase diagram, terminates with one phase space point at which a second-order EWPT can occur. This transition is continuous in the free energy, but has a discontinuity in the first derivative of the free energy. Beyond this point, no perturbative phase transition is possible anymore. For higher temperatures, the two phases are no longer distinct and the ground state can move smoothly from one to the other. This is called a *smooth cross-over*.

We are interested in model realizations with first-order EWPTs, ideally from an EW symmetric into an EW broken phase as these can serve as the necessary third ingredient for EWBG, as discussed in Chapter 3. First-order EWPTs alone (whether from an EW symmetric into an EW broken minimum or not) are interesting to study, because they source gravitational waves that might be within reach of future detection methods. We will review this in the second part of this thesis.

In order to realize a first-order EWPT, the scalar potential needs to induce a *critical temperature* at which two degenerate minima of the coexisting true and false phase are separated by a potential barrier. A potential barrier can be realized e.g. through a cubic term $\propto -\phi^3$ in the effective potential.

For the SM, the ring corrections of the one-loop effective potential lead to a cubic term that is generated by the W and Z bosons, cf. e.g. Ref. [122]. Therefore, in the one-loop treatment, there exists a small potential barrier between the high-temperature EW symmetric and low-temperature EW broken phase. However, the perturbative treatment at one-loop order does not accurately describe the phase transition in the SM. In non-perturbative lattice studies, the phase diagram of the SM was calculated, for a review see e.g. Ref. [132]. It was found that for an SM Higgs boson mass larger than the W boson mass, $m_h > m_W$, there is neither a first- nor a second-order EWPT in the SM [30]. Furthermore, the endpoint of an EWPT in the SM was tied down to $m_h = 72.4\,\text{GeV}$ [31]. For the experimentally found SM-like Higgs boson with $m_h = 125.09\,\text{GeV}$, there is no phase transition to the EW broken phase in the SM. The SM is in the smooth cross-over regime. A first-order EWPT can only be realized with BSM physics. BSM scalars can add additional terms to the one-loop daisy-resummed effective potential that can induce a first-order EWPT, as discussed in e.g. [126].

---

[5] For a transition between an EW symmetric singlet phase and an EW symmetric phase with zero singlet VEV, the appropriate order parameter would not be the EW, but the singlet VEV.

CHAPTER 5

Software Toolchain

In this thesis, we perform scans and phenomenological analyses in the theoretically and experimentally allowed parameter regions of models with extended scalar sectors. In this chapter we briefly review the codes used to constrain the parameter space of models by applying theoretical and experimental constraints with `ScannerS` [133–137], see Section 5.1, and to calculate first-order phase transitions with `BSMPT`, see Section 5.2.

5.1. ScannerS

The code `ScannerS` [133, 137–139] is used to perform random scans in user-defined parameter regions for models with extended Higgs sectors and checks for theoretical and experimental constraints in order to identify a set of valid points that pass all imposed constraints. Contrary to codes that perform a resource-intensive global model fit to derive a parameter point that fits best with all considered constraints, e.g. [140–144], `ScannerS` performs a *parameter scan* [137]. For this, model-specific points are obtained by generating uniformly distributed random numbers within the user-defined ranges for each of the input parameters of the model. It is then checked whether the random point passes all imposed theoretical and experimental constraints, as will be further detailed below. If so, the random point is returned as a valid point within the allowed parameter region of the model. This parameter scan principle allows for a time-efficient generation of allowed points for BSM models. Using parameter scans, we can generate a set of valid points for a specific model and investigate features of this point sample. This allows us to show that certain features are allowed within the theoretically and experimentally parameter space of a model. The distribution of a point sample generated in a random scan, as outlined above, is a relic of the random seed only and in general no global phenomenological conclusions can be drawn from the shape or the density of point distributions. We will use points generated in parameter scans with `ScannerS` in the following Chapters 6 and 10 for the $\mathcal{CP}$-conserving 2HDM as well as for the model 'CP in the Dark' in Chapter 11.

The theoretical constraints that are checked for ensure that the model is theoretically valid. We perform the following checks on the models that are discussed in the scope of this thesis:

- **Perturbative unitarity**: Using `ScannerS`, we ensure perturbative unitarity in Higgs boson $2 \to 2$ scattering by restricting the eigenvalues of the tree-level $2 \to 2$ scattering matrix, cf. Refs. [136, 145]

$$|\mathcal{M}^i_{2\to 2}| \leq 8\pi\,, \tag{5.1}$$

  which in the high-energy limit translates to an upper bound on functions of the quartic couplings, dependent on the model.

- **Boundedness from below**: A necessary ingredient for absolute stability of the electroweak vacuum is that the tree-level potential tends to positive infinity for large field values. Analytical conditions derived from the requirement of boundedness from below are presented e.g. in [136, 146, 147] for the models discussed in the scope of this thesis.

- **Vacuum stability**: The requirement of boundedness from below just fixes the large-field behaviour of the tree-level potential and the electroweak minimum with $v_{\text{EW}} = 246.22\,\text{GeV}$ could therefore still be a metastable, non-global minimum (as in the SM, see below). In this thesis, we require the one-loop potential to have a global minimum with $v_{\text{EW}} = 246.22\,\text{GeV}$. We do not use the `ScannerS` check for vacuum stability, but check for vacuum stability with `BSMPT`, as will be explained in the following section.

Valid points are furthermore required to meet the following experimental constraints.

- **Electroweak precision data**: Electroweak observables, e.g. the W boson mass, the Z resonance and the electroweak mixing angle, are precisely measured. But they are altered in extended scalar sectors if BSM scalars lead to additional contributions to the gauge boson self-energies. The electroweak one-loop self-energies are combined to a UV-finite set of *oblique parameters* S, T and U [148, 149]. Using `ScannerS` we require the oblique parameters to agree within 2σ with the SM fit [150].

- **Higgs data**: `ScannerS` uses `HiggsSignals` and `HiggsBounds` to check for compatibility with Higgs data, as described in the following. The SM-like Higgs boson predicted by the model is required to comply with the experimentally measured signal rates of the detected Higgs boson, checked using `HiggsSignals` [151–154]. Exclusion bounds from Higgs boson searches at LEP, Tevatron, and LHC are enforced by using `HiggsBounds` [155–161]. `HiggsSignals` and `HiggsBounds` are superseded by `HiggsTools` [162] which we link to `ScannerS` to take into account the most up-to-date Higgs data constraints for our parameter scans. The Higgs data constraints are applied with a 2σ confidence level in a χ^2 fit [137].

- **Flavour constraints**: The flavour observables $\mathcal{R}_b$ [163, 164] and $B \to X_s\gamma$ [165–169] impose constraints on the $m_{H^\pm} - \tan\beta$ plane. Here, $m_{H^\pm}$ denotes the mass of the BSM charged scalar boson and $\tan\beta$ describes the ratio of doublet VEVs.

- **Dark matter data**: For the model with a dark sector that we discuss in Chapter 11, we use `MicrOMEGAs 5.2.7` [170] to ensure that the predicted dark matter relic density $\Omega_{\text{prod}}h^2$ does not exceed the experimental value $\Omega_{\text{exp}}h^2$, $\Omega_{\text{prod}}h^2 \leq \Omega_{\text{exp}}h^2 = 0.1200 \pm 0.0012$ [21] and that the dark matter escapes direct detection at XENON1T [88] to agree with the experimental null result. In Chapter 11 we further discuss the dark matter constraints and also take into account more recent exclusion bounds by spin-independent direct detection experiments [89–91].

- **Electric dipole moments**: For models with $\mathcal{CP}$ violation, electric dipole moment (EDM) constraints by ACME [171] are imposed by `ScannerS`.

5.2. BSMPT

The `C++` package `BSMPT` [66, 110, 172] calculates phase transitions for BSM models with extended scalar sectors and gravitational waves in the newest version, `BSMPTv3` [66]. `BSMPT` is an abbreviation for Beyond the Standard Model Phase Transitions. The code is open-source, continuously maintained and tested and available from

`https://github.com/phbasler/BSMPT`.

The latest version `v3` [66] was developed within the scope of this thesis and will be further reviewed in Chapter 7. Here, we give a overview on the code of `v1` and `v2` which is used for the analysis that will be discussed in Chapter 6.

Since its first version, `BSMPT` provides an implementation of the one-loop-corrected daisy-resummed effective potential at finite temperature in an on-shell (OS) renormalization scheme. The application of the OS scheme allows to use tree-level masses and mixing angles as input parameters for the scan. It is ensured by adding a finite counterterm (CT) potential $V_{\text{CT}}^{\text{finite}}$ to the effective potential defined in Eq. (4.32),

$$\begin{aligned} V_{\texttt{BSMPT}}(\vec{\omega}, T) &\equiv V_{\text{eff}}^{(1)}(\vec{\omega}, T) + V_{\text{CT}}^{\text{finite}}(\vec{\omega})\,, \\ &= V^{(0)}(\vec{\omega}) + V_{\text{CW}}(\vec{\omega}) + V_T^{(1)}(\vec{\omega}, T) + V_{\text{CT}}^{\text{finite}}(\vec{\omega})\,, \end{aligned} \tag{5.2}$$

with the individual terms written in terms of the tree-level coupling tensors in the notation of Ref. [173], as further illustrated in Appendix B or in Ref. [110]. The finite CT potential is constructed by replacing the n_p bare parameters $p_i^{(0)}$ of the tree-level potential, by the renormalized parameters p_i and *finite* CTs δp_i

$$p_i^{(0)} \to p_i + \delta p_i\,. \tag{5.3}$$

In addition, tadpole CTs, δT_k are included that are multiplied by terms linear in the n_v real scalar component fields ϕ_k in which a non-zero VEV ω_k is allowed to develop. The finite CT potential then reads [110, 130, 172, 174, 175]

$$V_{\text{CT}}^{\text{finite}} = \sum_{i=1}^{n_p} \frac{\partial V^{(0)}}{\partial p_i} \delta p_i + \sum_{k=1}^{n_v} \delta T_k (\phi_k + \omega_k)\,. \tag{5.4}$$

The renormalization scheme is defined such that it is ensures that the electroweak tree-level minimum with $v_{\text{EW}} = 246.22\,\text{GeV}$ is still a *local minimum* of the one-loop effective potential and that masses and mixing angles derived from the one-loop mass matrix agree with the tree-level values. In practice this is achieved by applying the CT conditions [128, 130, 176]

$$\frac{\partial}{\partial \phi_i} \left(V_{\text{CW}}(\vec{\omega}) + V_{\text{CT}}^{\text{finite}}(\vec{\omega}) \right) \Big|_{\vec{\omega}=\vec{v}} = 0\,, \tag{5.5a}$$

$$\frac{\partial^2}{\partial \phi_i \phi_j} \left(V_{\text{CW}}(\vec{\omega}) + V_{\text{CT}}^{\text{finite}}(\vec{\omega}) \right) \Big|_{\vec{\omega}=\vec{v}} = 0\,. \tag{5.5b}$$

The first and second derivatives in all scalar field directions are evaluated at the tree-level zero-temperature electroweak minimum $\vec{v}$. The field structure of $V_{\text{CT}}^{\text{finite}}$ needs to include also field combinations that are possibly generated only at one-loop level. Consequently, models e.g. with loop-induced $\mathcal{CP}$ violation require an extension of $V_{\text{CT}}^{\text{finite}}$ beyond the tree-level potential structure, cf. Refs. [177, 178].

In `BSMPT` and all analysis presented in this thesis, we moreover ensure *absolute* vacuum stability. That is, the electroweak minimum with $v_{\text{EW}} = 246.22\,\text{GeV}$ remains not only a local minimum as ensured by the choice of $V_{\mathrm{CT}}^{\mathrm{finite}}$, but also the global minimum of the one-loop effective potential at zero temperature. This choice makes sure that the universe today is in a stable vacuum, however it excludes metastable vacuum configurations, which are experimentally valid as long as the lifetime of the vacuum is sufficiently long, i.e. larger than the lifetime of the universe. Already the vacuum of the SM is metastable as it was found that an extrapolation of its quartic coupling λ to high renormalization scales using the renormalization group equations (RGEs) flips λ to negative values for scales $\gtrsim 10^{10}\,\mathrm{GeV}$ [99, 179–188]. Studies of vacuum stability for extended scalar sector models beyond the SM can be found e.g. in Refs. [189–191].

The first and second version of `BSMPT`, which we use for the analysis in Chapter 6 and the first part of the analysis of Chapter 10, determines the position of the global minimum of the one-loop daisy-resummed effective potential in a temperature range $T \in [0,\, 300]\,\mathrm{GeV}$ and determines the critical temperature T_c. Furthermore, in `BSMPTv1` and `v2`, restoration of the electroweak symmetry latest at $T = 300\,\mathrm{GeV}$ is required, i.e. $\overline{\omega}_{\mathrm{EW}}(300\,\mathrm{GeV}) = 0\,\mathrm{GeV}$. Therefore, `BSMPTv1` and `v2` identify points that are possible candidates for a one-step strong first-order EWPT from a symmetric false to an electroweak broken true phase, that is, if the baryon wash-out condition $\xi_c \gtrsim 1$ is fulfilled, as defined in Eq. (3.13). In Chapter 6 and in the first half of Chapter 10, we study the temperature evolution of the global minimum. Furthermore, in Chapter 6, we determine critical temperatures T_c with $\xi_c = \overline{\omega}_{\mathrm{EW}}(T_c)/T_c$ in the $\mathcal{CP}$-conserving 2HDM and discuss the phenomenological implications associated with these parameter points.

CHAPTER 6

Strong First-Order Electroweak Phase Transitions in the Dimension-Six extended Two-Higgs-Doublet Model

The Two-Higgs-Doublet Model (2HDM) [192, 193] extends the scalar sector of the SM by an additional complex $SU(2)_L \times U(1)_Y$ doublet. In the 2HDM, new degrees of freedom are introduced that can induce a strong first-order EWPTs. Its capability to provide a strong first-order EWPT and the related implications for collider phenomenology have been well studied in e.g. Refs. [130, 175, 177, 194–202]. The 2HDM continues to provide its wide phenomenology in parameter regions that are still allowed by collider searches, cf. e.g. Ref. [203] and that might be in reach of future collider experiments [204].

We focus on the real, or $\mathcal{CP}$-conserving, 2HDM in its type-2 realization. The type-2 2HDM, on the one hand, is particularly compelling as it links the SM to its supersymmetric UV-completion. On the other hand, it is more and more challenged w.r.t. its capability to provide a strong first-order EWPT [130, 175, 201, 205], compared to its type-1 realization. The aim of this chapter is the discussion of an effective field theory (EFT) dimension-six extension for a real type-2 2HDM [206] with regard to its capability to facilitate a strong first-order EWPT within its still allowed parameter space. We characterize the strength of the first-order EWPT at the critical temperature T_c via the ξ_c parameter and define a strong first-order EWPT if $\xi_c \gtrsim 1$, as defined in Eq. (3.13). In the course of this chapter, we consider parameter points of the dimension-four theory that we find to have $\xi_c^{\mathrm{d4}} < 1$. For these points, we investigate the dimension-six dynamics that lift $\xi_c^{\mathrm{d4}} < 1$ to $\xi_c^{\mathrm{d6}} \gtrsim 1$ and study their interplay with collider phenomenology. We limit our study to points that potentially have a one-step first-order EWPT, i.e. we look for critical temperatures in $T \in [0,\, 300]\,\mathrm{GeV}$ and require the restoration of EW symmetry to take place until $T = 300\,\mathrm{GeV}$.

The outline of this chapter is as follows. The $\mathcal{CP}$-conserving 2HDM will be introduced in Section 6.1. In Section 6.2 we study purely scalar dimension-six dynamics and their potential to promote first-order EWPTs to strong first-order EWPTs as well as collider-relevant implications on top quark pair as well as Higgs boson pair production. In Section 6.3 we present our study of the type-2 real 2HDM extended by dimension-six top quark Yukawa couplings. We show, that the top sector still allows for such modifications that can be correlated with a potential strong first-order EWPT. Our results generalize to the type-1 2HDM. The work presented in the following sections was published in [207, 208].

6.1. CP-conserving Two-Higgs-Doublet Model

In the real, or $\mathcal{CP}$-conserving, 2HDM [192] (see e.g. [193] for a review), the SM scalar sector is extended by a second complex $SU(2)_L \times U(1)_Y$ scalar doublet Φ_2,

$$\Phi_1 = \frac{1}{\sqrt{2}} \begin{pmatrix} \rho_1 + i\eta_1 \\ \zeta_1 + i\psi_1 \end{pmatrix}, \Phi_2 = \frac{1}{\sqrt{2}} \begin{pmatrix} \rho_2 + i\eta_2 \\ \zeta_2 + i\psi_2 \end{pmatrix}, \tag{6.1}$$

written in terms of the real scalar fields $\{\rho_i, \eta_i, \zeta_i, \psi_i\}$ with $i = 1, 2$. To avoid FCNCs at tree-level, cf. Chapter 2, a $\mathbb{Z}_2$ symmetry is imposed on the potential under which the doublet fields transform as

$$\Phi_1 \to \Phi_1, \quad \Phi_2 \to -\Phi_2 \,. \tag{6.2}$$

This $\mathbb{Z}_2$ symmetry is furthermore extended to the Yukawa sector, as will be described below. A (soft) $\mathbb{Z}_2$-breaking term $\propto m_{12}^2 \neq 0$ is added to avoid domain-wall domination, as described in Chapter 2. The tree-level potential for the $\mathcal{CP}$-conserving 2HDM with a softly broken $\mathbb{Z}_2$ symmetry is[1]

$$\begin{aligned} V^{(0)}_{\text{2HDM}} = {} & m_{11}^2 |\Phi_1|^2 + m_{22}^2 |\Phi_2|^2 - m_{12}^2 (\Phi_1^\dagger \Phi_2 + \text{h.c.}) + \lambda_1 |\Phi_1|^4 + \lambda_2 |\Phi_2|^4 \\ & + \lambda_3 |\Phi_1|^2 |\Phi_2|^2 + \lambda_4 (\Phi_1^\dagger \Phi_2)(\Phi_2^\dagger \Phi_1) + \frac{\lambda_5}{2} \left[\left(\Phi_1^\dagger \Phi_2 \right)^2 + \text{h.c.} \right] . \end{aligned} \tag{6.3}$$

The assumption of $\mathcal{CP}$ conservation renders all tree-level potential parameters real. Masses are generated via spontaneous symmetry breaking. We choose the general finite-temperature vacuum of the real 2HDM to be

$$\langle \Phi_1 \rangle = \frac{1}{\sqrt{2}} \begin{pmatrix} 0 \\ \overline{\omega}_1 \end{pmatrix}, \quad \langle \Phi_2 \rangle = \frac{1}{\sqrt{2}} \begin{pmatrix} \overline{\omega}_{\text{CB}} \\ \overline{\omega}_2 + i \overline{\omega}_{\text{CP}} \end{pmatrix} . \tag{6.4}$$

The finite-temperature VEVs, i.e. the coordinates of the finite-temperature minimum, are denoted by $\overline{\omega}_i$, $i \in \{\text{CB}, 1, 2, \text{CP}\}$. The $\mathcal{CP}$-violating VEV is rotated to the second doublet and the CB VEV is chosen real without loss of generality [209]. We include a CB, as well as the $\mathcal{CP}$-violating VEV in the finite-temperature vacuum, to be as general as possible. However, in the analysis, we only find points that conserve the $\mathcal{CP}$ symmetry with $\overline{\omega}_{\text{CP}} = 0$. For the analysis in Chapter 6, also the CB VEV is found to be zero, $\overline{\omega}_{\text{CB}} = 0$. The vacuum parametrization aligns with the SM-like zero-temperature vacuum as

$$\{\overline{\omega}_{\text{CB}}, \overline{\omega}_1, \overline{\omega}_2, \overline{\omega}_{\text{CP}}\}\Big|_{T=0\,\text{GeV}} \equiv \{0, v_1, v_2, 0\} \,, \tag{6.5}$$

and

$$246.22\,\text{GeV} = v_{\text{EW}} \equiv \overline{\omega}_{\text{EW}}\big|_{T=0\,\text{GeV}} = \sqrt{\overline{\omega}_{\text{CB}}^2 + \overline{\omega}_1^2 + \overline{\omega}_2^2 + \overline{\omega}_{\text{CP}}^2}\Big|_{T=0\,\text{GeV}} = \sqrt{v_1^2 + v_2^2} \,. \tag{6.6}$$

The ratio of the zero-temperature electroweak VEVs defines

$$\tan\beta \equiv \frac{v_2}{v_1} \,. \tag{6.7}$$

As mentioned above, the $\mathbb{Z}_2$ symmetry is extended to the fermion sector to avoid FCNCs. The right-handed fermion singlets and the Higgs doublets are defined to transform under the $\mathbb{Z}_2$ symmetry, while the left-handed fermion doublets are defined invariant under $\mathbb{Z}_2$. This requirement restricts the right-handed fermions to only couple to one of the two doublets,

---

[1] Hard-breaking terms have the form $\lambda_{6,7}(\Phi_i^\dagger \Phi_i)(\Phi_i^\dagger \Phi_j + \Phi_j^\dagger \Phi_i)$ with $i, j = 1, 2$ and $i \neq j$. We only include soft-breaking via $m_{12}^2 \neq 0$, and no hard-breaking via the choice $\lambda_6 = \lambda_7 = 0$.

	u-type	d-type	leptons
Type 1	Φ_2	Φ_2	Φ_2
Type 2	Φ_2	Φ_1	Φ_1
Lepton-specific	Φ_2	Φ_2	Φ_1
Flipped	Φ_2	Φ_1	Φ_2

Table 6.1.: Yukawa coupling types for a (softly-broken) $\mathbb{Z}_2$ symmetric 2HDM. Noted is the doublet to which the right-handed up-type quarks, down-type quarks and leptons are restricted to couple, respectively.

$\mathcal{O}_6^{111111}$	$(\Phi_1^\dagger\Phi_1)^3$	$\mathcal{O}_6^{222222}$	$(\Phi_2^\dagger\Phi_2)^3$
$\mathcal{O}_6^{111122}$	$(\Phi_1^\dagger\Phi_1)^2(\Phi_2^\dagger\Phi_2)$	$\mathcal{O}_6^{112222}$	$(\Phi_1^\dagger\Phi_1)(\Phi_2^\dagger\Phi_2)^2$
$\mathcal{O}_6^{122111}$	$(\Phi_1^\dagger\Phi_2)(\Phi_2^\dagger\Phi_1)(\Phi_1^\dagger\Phi_1)$	$\mathcal{O}_6^{122122}$	$(\Phi_1^\dagger\Phi_2)(\Phi_2^\dagger\Phi_1)(\Phi_2^\dagger\Phi_2)$
$\mathcal{O}_6^{121211}$	$(\Phi_1^\dagger\Phi_2)^2(\Phi_1^\dagger\Phi_1)$ + h.c.	$\mathcal{O}_6^{121222}$	$(\Phi_1^\dagger\Phi_2)^2(\Phi_2^\dagger\Phi_2)$ + h.c.

Table 6.2.: $\mathbb{Z}_2$ symmetric dimension-six operators of class $\Phi^6_{i,j}$ with $i, j \in \{1, 2\}$.

respectively and consequently introduces four types of Yukawa couplings in the 2HDM that are noted in Table 6.1. The theoretically and experimentally allowed parameter space for the 2HDM depends on its type, cf. e.g. Ref. [210].

The spectrum of scalar particles consists of a light, $\mathcal{CP}$-even neutral Higgs boson h that we choose to be SM-like to comply with experimental data, and a heavy $\mathcal{CP}$-even neutral Higgs boson H, as well as a neutral $\mathcal{CP}$-odd scalar A and a pair of scalars $H^\pm$ charged under $U(1)_{\text{EM}}$.

6.2. Scalar Dimension-Six Extension

An EFT is a bottom-up formulation of BSM physics that is assumed to manifest itself at a higher energy scale Λ. For energies $E < \Lambda$ the high-energy physics is integrated out and its effects are parametrized by higher-dimensional operators, in a power series normalized by powers of Λ. EFTs are non-renormalizable, i.e. cannot be renormalized with a finite set of CTs and instead require a new set of CTs for each loop level. In the first part of this chapter, we extend the scalar potential of the type-2 $\mathcal{CP}$-conserving 2HDM by the purely scalar dimension-six operators listed in Table 6.2 that are part of and follow the convention of the Warsaw 2HDM EFT basis defined in [206]. The dimension-six 2HDM tree-level potential is then given by [211–213]

$$\mathcal{L}_{\text{2HDM-EFT}} \supset \mathcal{L}_{\text{2HDM}} + \sum_i \frac{C_6^i}{\Lambda^2}\mathcal{O}_6^i \quad \Rightarrow \quad V_{\text{d6}}^{(0)} = -\sum_i \frac{C_6^i}{\Lambda^2}\mathcal{O}_6^i\,, \tag{6.8}$$

with the dimension-six scalar operators $\mathcal{O}_6^i$ for all field configurations i listed in Table 6.2 and the dimensionless Wilson coefficients (WCs) C_6^i.

The purely scalar dimension-six operators lead to tree-level and loop-induced shifts of the scalar mass spectrum, that we choose to absorb into the parameters of the theory to ensure that the tree-level mass matrix remains unchanged and also the one-loop mass matrix remains at its tree-level values. For the latter, we use the OS scheme, defined in Section 5.2, as will be illustrated below. We can thus use tree-level scalar masses and mixing angles as input parameters for our parameter scan. In the following, we discuss how to deal with the tree-level and one-loop shifts, respectively.

At tree level, the scalar mass shift induced by the operators of Table 6.2 is absorbed by a redefinition of the (unphysical) Lagrangian parameters λ_i, $i \in \{1, \dots, 5\}$ and m_{12}^2 as $\lambda_i \to \lambda_i + \Delta\lambda_i^{\text{d6}}$ and $m_{12}^2 \to m_{12}^2 + \Delta m_{12}^{2\,\text{d6}}$, where we choose the following redefinition

$$\begin{aligned}
\Delta\lambda_1^{\text{d6}} &= \frac{1}{4\Lambda^2 v_1^2}\left[6C_6^{111111} v_1^4 + (2C_6^{121211} + C_6^{122111}) v_1^2 v_2^2 \right.\\
&\qquad \left. - \{2(C_6^{112222} + C_6^{121222}) + C_6^{122122}) v_2^4\}\right],\\
\Delta\lambda_2^{\text{d6}} &= -\frac{1}{4\Lambda^2 v_2^2}\left[\{2(C_6^{111122} + C_6^{121211}) + C_6^{122111}\} v_1^4 \right.\\
&\qquad \left. - (2C_6^{121222} + C_6^{122122}) v_1^2 v_2^2 - 6C_6^{222222} v_2^4\right],\\
\Delta\lambda_4^{\text{d6}} &= \frac{v_1^2}{\Lambda^2}(C_6^{111122} + C_6^{121211} + C_6^{122111})\\
&\qquad + \frac{v_2^2}{\Lambda^2}(C_6^{112222} + C_6^{121222} + C_6^{122122}),\\
\Delta\lambda_5^{\text{d6}} &= \frac{1}{2\Lambda^2}\left[(2C_6^{111122} + 4C_6^{121211} + C_6^{122111}) v_1^2 \right.\\
&\qquad \left. + (2C_6^{112222} + 4C_6^{121222} + C_6^{122122}) v_2^2\right],\\
\Delta m_{12}^{2\,\text{d6}} &= \frac{v_1 v_2}{2\Lambda^2}\left[\{2(C_6^{111122} + C_6^{121211}) + C_6^{122111}\} v_1^2 \right.\\
&\qquad \left. + \{2(C_6^{112222} + C_6^{121222}) + C_6^{122122}\} v_2^2\right].
\end{aligned} \tag{6.9}$$

These shifts ensure that the dimension-six tree-level scalar mass spectrum is the same as the dimension-four tree-level. Consequently, dimension-six effects are shifted into Higgs boson self-couplings and multi-Higgs boson final states.

As introduced in Section 5.2, at one-loop level and at zero temperature we define the finite CT potential to absorb the NLO vacuum and the mass and mixing angle shifts such that the EW vacuum position as well as the tree-level mass matrix are preserved. The general dimension-six EFT-extended effective potential framework is discussed in detail in Appendix B and we will not go into further detail here. Using Eq. (5.4), we derive $V_{\text{CT}}^{\text{finite}}$ from the tree-level potential extended by $V_{\text{d6}}^{(0)}$ and require Eq. (5.5) to be fulfilled. We find a solution that has the analytical freedom to choose a parametrization where all eight new dimension-six CTs are free parameters. In other words, the degrees of freedom of the dimension-four theory are sufficient to capture all zero-temperature induced one-loop shifts stemming from the CW potential. We choose the free parameters $t, s_i \in \mathbb{R}$ with $i \in \{1, \dots, 8\}$ to be zero, and the finite CTs in that parametrization are given by

$$\begin{aligned}
\delta m_{11}^2 = {}& \frac{1}{2} H_{\zeta_1\zeta_1}^{\text{CW}} + H_{\psi_1\psi_1}^{\text{CW}} - \frac{5}{2} H_{\rho_1\rho_1}^{\text{CW}} + \frac{1}{2}\frac{v_2}{v_1}\left(H_{\zeta_1\zeta_2}^{\text{CW}} - H_{\eta_1\eta_2}^{\text{CW}}\right)\\
& + t v_2^2 - \frac{3v_1^4}{4\Lambda^2} s_1 - \frac{v_1^2 v_2^2}{2\Lambda^2} s_2 - \frac{v_1^2 v_2^2}{\Lambda^2} s_3\\
& - \frac{v_1^2 v_2^2}{\Lambda^2} s_4 - \frac{v_2^4}{4\Lambda^2} s_6 - \frac{3v_2^4}{4\Lambda^2} s_7 - \frac{v_2^4}{2\Lambda^2} s_8,
\end{aligned} \tag{6.10a}$$

$$\begin{aligned}
\delta m_{22}^2 = {}& \frac{1}{2}\left(H_{\zeta_2\zeta_2}^{\text{CW}} - 3H_{\eta_2\eta_2}^{\text{CW}}\right) + \frac{1}{2}\frac{v_1}{v_2}\left(H_{\zeta_1\zeta_2}^{\text{CW}} - H_{\eta_1\eta_2}^{\text{CW}}\right) + \frac{v_1^2}{v_2^2}\left(H_{\psi_1\psi_1}^{\text{CW}} - H_{\rho_1\rho_1}^{\text{CW}}\right)\\
& + t v_1^2 - \frac{v_1^4}{4\Lambda^2} s_2 - \frac{3v_1^4}{4\Lambda^2} s_3 - \frac{v_1^4}{2\Lambda^2} s_4\\
& - \frac{3v_2^4}{4\Lambda^2} s_5 - \frac{v_1^2 v_2^2}{2\Lambda^2} s_6 - \frac{v_1^2 v_2^2}{\Lambda^2} s_7 - \frac{v_1^2 v_2^2}{\Lambda^2} s_8,
\end{aligned} \tag{6.10b}$$

$$\delta m_{12}^2 = H^{\mathrm{CW}}_{\eta_1\eta_2} + \frac{v_1}{v_2}\left(H^{\mathrm{CW}}_{\psi_1\psi_1} - H^{\mathrm{CW}}_{\rho_1\rho_1}\right) + v_1 v_2 t - \frac{v_1^3 v_2}{2\Lambda^2} s_3 - \frac{v_1 v_2^3}{2\Lambda^2} s_7\,, \tag{6.10c}$$

$$\begin{aligned}\delta\lambda_1 = {} & \frac{1}{v_1^2}\left(2H^{\mathrm{CW}}_{\rho_1\rho_1} - H^{\mathrm{CW}}_{\zeta_1\zeta_1} - H^{\mathrm{CW}}_{\psi_1\psi_1}\right) \\ & - \frac{v_2^2}{v_1^2} t + \frac{3v_1^2}{\Lambda^2} s_1 + \frac{v_2^2}{\Lambda^2} s_2 + \frac{3v_2^2}{2\Lambda^2} s_3 + \frac{2v_2^2}{\Lambda^2} s_4 + \frac{v_2^4}{2v_1^2\Lambda^2} s_7\,,\end{aligned} \tag{6.10d}$$

$$\begin{aligned}\delta\lambda_2 = {} & \frac{1}{v_2^2}\left(H^{\mathrm{CW}}_{\eta_2\eta_2} - H^{\mathrm{CW}}_{\zeta_2\zeta_2}\right) + \frac{v_1^2}{v_2^4}\left(H^{\mathrm{CW}}_{\rho_1\rho_1} - H^{\mathrm{CW}}_{\psi_1\psi_1}\right) \\ & - \frac{v_1^2}{v_2^2} t + \frac{v_1^4}{2v_2^2\Lambda^2} s_3 + \frac{3v_2^2}{\Lambda^2} s_5 + \frac{v_1^2}{\Lambda^2} s_6 + \frac{3v_1^2}{2\Lambda^2} s_7 + \frac{2v_1^2}{\Lambda^2} s_8\,,\end{aligned} \tag{6.10e}$$

$$\begin{aligned}\delta\lambda_3 = {} & \frac{1}{v_1 v_2}\left(H^{\mathrm{CW}}_{\eta_1\eta_2} - H^{\mathrm{CW}}_{\zeta_1\zeta_2}\right) + \frac{1}{v_2^2}\left(H^{\mathrm{CW}}_{\rho_1\rho_1} - H^{\mathrm{CW}}_{\psi_1\psi_1}\right) \\ & - t + \frac{v_1^2}{\Lambda^2}\left(s_2 + s_3 + s_4\right) + \frac{v_2^2}{\Lambda^2}\left(s_6 + s_7 + s_8\right)\,,\end{aligned} \tag{6.10f}$$

$$\delta\lambda_4 = t\,, \tag{6.10g}$$

$$\delta\lambda_5 = \frac{2}{v_2^2}\left(H^{\mathrm{CW}}_{\psi_1\psi_1} - H^{\mathrm{CW}}_{\rho_1\rho_1}\right) + t - \frac{v_1^2}{2\Lambda^2} s_3 + \frac{v_1^2}{\Lambda^2} s_4 - \frac{v_2^2}{2\Lambda^2} s_7 + \frac{v_2^2}{\Lambda^2} s_8\,, \tag{6.10h}$$

$$\delta\mathcal{O}_6^{111111} = s_1\,, \tag{6.10i}$$

$$\delta\mathcal{O}_6^{111122} = s_2\,, \tag{6.10j}$$

$$\delta\mathcal{O}_6^{122111} = s_3\,, \tag{6.10k}$$

$$\delta\mathcal{O}_6^{121211} = s_4\,, \tag{6.10l}$$

$$\delta\mathcal{O}_6^{222222} = s_5\,, \tag{6.10m}$$

$$\delta\mathcal{O}_6^{112222} = s_6\,, \tag{6.10n}$$

$$\delta\mathcal{O}_6^{122122} = s_7\,, \tag{6.10o}$$

$$\delta\mathcal{O}_6^{121222} = s_8\,, \tag{6.10p}$$

$$\delta T_1 = H^{\mathrm{CW}}_{\eta_1\eta_2} v_2 + H^{\mathrm{CW}}_{\rho_1\rho_1} v_1 - N^{\mathrm{CW}}_{\zeta_1}\,, \tag{6.10q}$$

$$\delta T_2 = H^{\mathrm{CW}}_{\eta_1\eta_2} v_1 + H^{\mathrm{CW}}_{\eta_2\eta_2} v_2 - N^{\mathrm{CW}}_{\zeta_2}\,, \tag{6.10r}$$

$$\delta T_{\mathrm{CP}} = -N^{\mathrm{CW}}_{\psi_2}\,, \tag{6.10s}$$

$$\delta T_{\mathrm{CB}} = -N^{\mathrm{CW}}_{\rho_2}\,, \tag{6.10t}$$

where we defined $N^{\mathrm{CW}}_{\phi} \equiv \partial_\phi V_{\mathrm{CW}}$ and $H^{\mathrm{CW}}_{\phi_i\phi_j} \equiv \partial_{\phi_i\phi_j} V_{\mathrm{CW}}$.

At non-zero temperature, the dimension-six purely scalar contributions also allow for more diagrams contributing to the finite-temperature scalar self-energy corrections. At dimension four, we perform the resummation of the hard thermal loops taking into account the leading dimension-four one-loop thermal self-energy corrections, as described in Section 4.4. At dimension six, new diagrams emerge and their power counting has to be performed with care. The leading dimension-four scalar Debye mass correction scales $\propto gT^2$, with g denoting a generic coupling constant. We choose to take into account the dimension-six two-loop contribution to the thermal mass, which in the hard-thermal loop assumption scales $\propto g\frac{T^4}{\Lambda^2}$, compare e.g. with Ref. [214].

After discussing the model building of a dimension-six purely-scalar EFT-extended 2HDM, let us now move on to the observed phenomenology. We implement the model discussed above in `ScannerS` and `BSMPT` and perform scans in the theoretically and experimentally allowed parameter space, more details are summarized in Sections 5.1 and 5.2, as well as in Appendix B. First, we consider at a benchmark point with a first-order EWPT at dimension

m_h	m_H	m_A	$m_{H^\pm}$	$\tan\beta$	c_{HVV}	m_{12}^2	T_c^{d4}	$\overline{\omega}_{\text{EW}}(T_c)^{\text{d4}}$	ξ_c^{d4}
125.09	681	855	884	1.362	-0.00459	220945	250.55	226.76	0.91

Table 6.3.: Input parameters of the benchmark point used for Figure 6.1. Unit of m_{12}^2 in GeV^2, $\tan\beta$, c_{HVV}, ξ_c^{d4} are dimensionless, all other units in GeV. c_{HVV} denotes the value of the coupling of H to two gauge bosons V.

m_h [GeV]	m_H [GeV]	m_A [GeV]	$m_{H^\pm}$ [GeV]	$\tan\beta$	c_{HVV}	m_{12}^2 [GeV^2]
125.09	$[130, 3000]$	$[30, 3000]$	$[800, 3000]$	$[0.8, 30]$	$[-0.3, 1.0]$	$[10^{-5}, 10^7]$

Table 6.4.: Scan ranges for the type-2 $\mathcal{CP}$-conserving 2HDM input parameters used for the scan with `ScannerS`. The light $\mathcal{CP}$-even neutral scalar h is the SM-like Higgs boson.

four, $\xi_c^{\text{d4}} = 0.91$, whose parameter values are summarized in Table 6.3. In Figure 6.1, we show the dimension-six first-order EWPT strength ξ_c^{d6} for individual variations of the WCs in the range $\frac{C_6^i}{\Lambda^2} \in [-1,\, 1]\,\text{TeV}^{-2}$ in all eight WC directions. In order for the EFT expansion to be valid, we need to ensure that the dimension-six corrections are small compared to the dimension-four contribution. From Figure 6.1 we deduce that the response in ξ_c^{d6} is to good approximation linear in $\frac{C_6^i}{\Lambda^2}$. Consequently, the introduction of non-linear terms in the EFT scale expansion via e.g. the thermal masses numerically plays an insignificant role. Our EFT expansion is not only valid for small variations of the WCs,[2] but Figure 6.1 also shows that within this WC range it is possible for this benchmark point to strengthen the first-order EWPT to a strong first-order EWPT with $\xi_6^{\text{d6}} \gtrsim 1$ for a moderate choice of C_6^{222222}.

In the following, we discuss whether a dimension-six enhanced first-order EWPT strength can have collider-relevant implications. We choose individual WCs to strengthen the first-order EWPT to $\xi_c^{\text{d6}} \gtrsim 1$ and ensure that the response in ξ_c^{d6} that we calculate with `BSMPT` remains linear when varying $\frac{C_6^i}{\Lambda^2} \in [-1, 1]\,\text{TeV}^{-2}$ for a parameter scan with `ScannerS` in the ranges shown in Table 6.4. In Figure 6.2, we show cross section results for a top quark pair final state $t\bar{t}$ (left) and for SM-like Higgs boson pair production hh (right) for points that yield a dimension-six strong first-order EWPT when varying single WCs. Points with $\xi_c^{\text{d4}} > 0.8$ are highlighted by orange squares. As different directions of WCs do not differ in their phenomenological outcome, they are not distinguished further in the following.

Our parameter sample shows a top quark philic decay of the heavy neutral $\mathcal{CP}$-even Higgs boson H with a branching ratio (BR) $\text{BR}(H \to t\bar{t}) \gtrsim 0.8$. Therefore, the measurement of the $t\bar{t}$ final state would be the prime candidate for an exotic Higgs boson discovery. We show the decay width sensitive (leading-order) interference cross section between $t\bar{t}$ production via a H resonance, $gg \to H \to t\bar{t}$, and the gluon-fusion continuum, $gg \to t\bar{t}$

$$\sigma^{\text{inf}} \sim 2\,\text{Re}\,\{\mathcal{M}(gg \to H \to t\bar{t})\mathcal{M}^*(gg \to t\bar{t})\}\ , \tag{6.11}$$

versus the (leading-order) resonant $gg \to H \to t\bar{t}$ production cross section ratio between dimension-six and dimension-four in Figure 6.2 (left). The size of the resonant modifications scales proportional to $|1-\xi_c^{\text{d4}}|$, i.e. resonant production is amplified or weakened more strongly

---

[2] The operators taken into account here are manifestly momentum independent. Therefore, the scalar amplitudes are not kinematically enhanced. For high energies compared to the particle thresholds, the dominant contribution to the zeroth partial wave scales $\propto \frac{C_6^i}{32\pi}\frac{v^2}{\Lambda^2}$. Consequently, the requirement of perturbativity and unitarity constrains the WCs to $\frac{|C_6^i|}{\Lambda^2} < \mathcal{O}(1) \cdot 32\pi\,\text{TeV}^{-2}$.

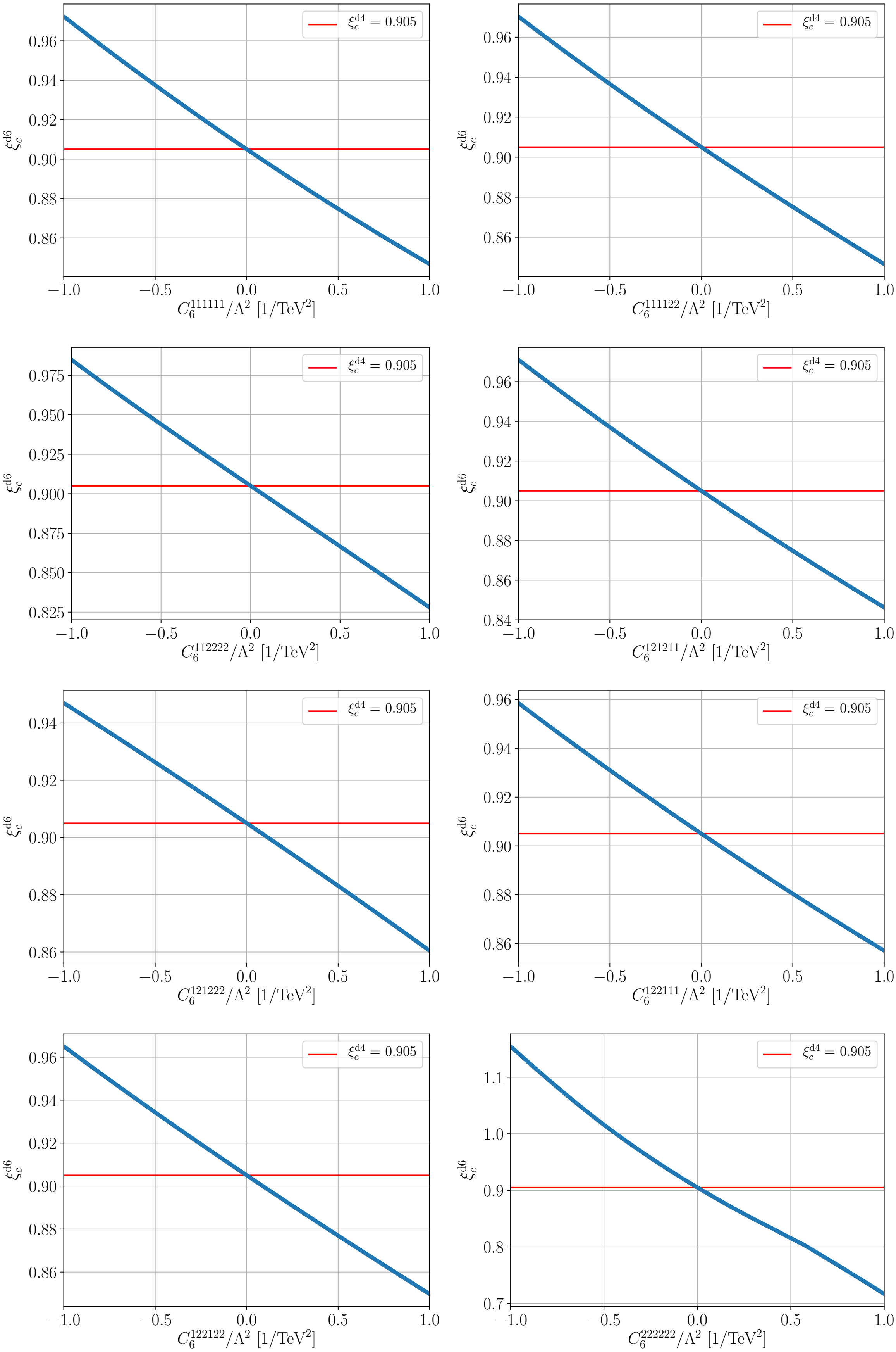

Figure 6.1.: Impact of the variation of individual WCs on the first-order EWPT strength of the benchmark point presented in Table 6.3. Figure published in Ref. [207].

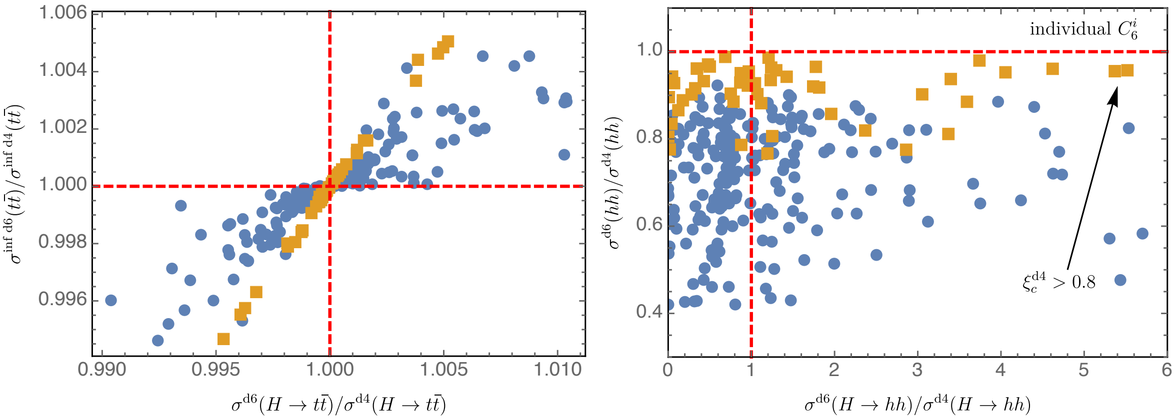

Figure 6.2.: Left: Dimension-six continuum interference cross section versus resonant production cross section into $t\bar{t}$, normalized to the dimension-four value. Right: Dimension-six modifications of the Higgs boson pair production continuum versus resonant production via $gg \to H \to hh$. Blue (orange) circles (squares) yield $\xi_c^{\text{d6}} \simeq 1$ with $\xi_c^{\text{d4}} > 0.3$ ($\xi_c^{\text{d4}} > 0.8$) for individual WCs choices. Figure published in Ref. [207].

in case larger dimension-six modifications are necessary to obtain ξ_c^{d6}. However, these permille level modifications are far beyond the reach of current and near future hadron collider experiments.

As our chosen parametrization shifts the one-loop dimension-six scalar mass spectrum to their tree-level values, EFT effects are shifted to the Higgs boson self-couplings, which are an important input for multi-Higgs boson final states. In Figure 6.2 (right) we display the modification of the Higgs boson pair production continuum, $gg \to hh$, cross section versus the resonance cross section modification, $gg \to H \to hh$. We observe enhancements of the resonance signal up to a factor six due to modifications of λ_{Hhh}. The continuum rate is decreased, we find deviations of $\sigma^{\text{d6}}(hh)/\sigma^{\text{d4}}(hh) \simeq 0.4$ (0.8) for $\xi_c^{\text{d4}} = 0.3$ (0.9). Therefore, we find smaller dimension-six continuum modifications for smaller $|1 - \xi_c^{\text{d4}}|$. The overall observed decrease in the dimension-six continuum cross section for $gg \to hh$ is correlated with an enhancements of the trilinear SM-like Higgs boson coupling λ_{hhh} up to 50 %. This is because the $gg \to hh$ NLO cross section is decreased if the trilinear self-coupling λ_{hhh} becomes enhanced w.r.t. the SM value and a minimal cross section is reached for an enhancement of the trilinear self-coupling by a factor of 2.3 [215, 216].

In the example discussed so far, the heavy Higgs boson H is top quark philic, i.e. decays to $t\bar{t}$ with $\text{BR}(H \to t\bar{t}) \gtrsim 0.8$. Therefore, as mentioned above, $H \to t\bar{t}$ should be the first channel to be sensitive to H. However, the separation of the continuum from the resonance modifications in $t\bar{t}$ require significant experimental efforts, probably out of reach in the near future. On the other hand, modifications are more sizable in the hh final states. Therefore, the hh final state could possibly allow to constrain the size of ξ_c indirectly.

In a second scan we therefore look for points with an enhanced heavy Higgs boson production cross section in the SM-like Higgs pair production channel, so that the OS hh-production and the hh-continuum production are less statistically limited. The result of this scan is displayed in Figure 6.3 (left). The figure illustrates that the more sizable hh signal strengths for this sample are correlated with a larger $|1 - \xi_c^{\text{d4}}|$. In the following, we therefore study uniform modifications of $C_6^i \equiv C$ to achieve $\xi_c^{\text{d6}} \gtrsim 1$ again for the general sample with $\xi_c^{\text{d4}} > 0.3$, as well as for the new Higgs boson philic sample illustrated in Figure 6.3 (left). Our findings are illustrated in Figure 6.3 (right). Similar to Figure 6.2, we see a decrease in the hh continuum and enhancements for resonant production. Large resonant enhancements in the uniform

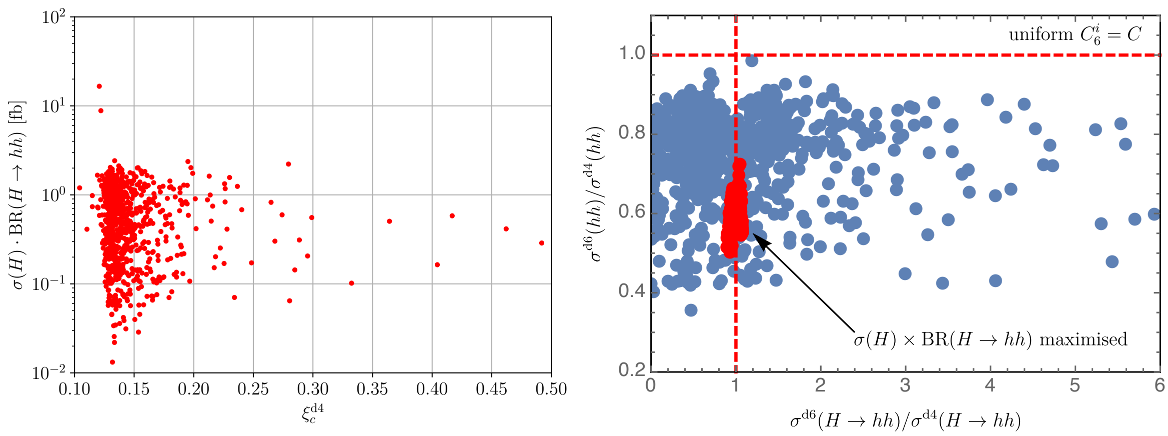

Figure 6.3.: Left: Heavy Higgs boson production cross section in the SM-like Higgs pair production channel versus ξ_c^{d4} for the Higgs boson philic sample. Right: Same figure as Figure 6.2 (right), but now with all WCs $C_6^i \equiv C$ varied uniformly to reach $\xi_c^{\mathrm{d6}} \simeq 1$ (blue points). The Higgs boson philic sample is shown as red points. Figure published in Ref. [207].

dimension-six scan appear for top quark philic points of the old $\xi_c^{\mathrm{d4}} > 0.3$ sample (blue points) where $\sigma^{\mathrm{d4}}(H \to hh)$ is small and $\sigma^{\mathrm{d6}}(H \to hh)/\sigma^{\mathrm{d4}}(H \to hh)$ can grow up to > 3. Yet, they are not correlated with large cross sections. However, we now find resonant enhancements up to a factor of 2.5 for cross sections in the order of fb. The LHC might become sensitive to this range of cross sections in the $b\bar{b}b\bar{b}$ [217–221] and $b\bar{b}\tau\tau$ channels [222–228]. The newly generated Higgs boson philic sample (red points) receives resonance modifications between 5-10 % with continuum modifications up to 50 %.

6.3. Dimension-Six Yukawa Extension

In the second part of this chapter, we analyse effective dimension-six top quark Yukawa interactions in the context of the type-2 $\mathcal{CP}$-conserving 2HDM. The top quark is the heaviest quark of the SM and plays a key role in electroweak physics. It couples to the SM-like Higgs boson via a Yukawa coupling of $\mathcal{O}(1)$. The dominant SM-like Higgs boson production channel is mediated via a top quark loop, therefore the top quark mass can be predicted from the electroweak fit [229]. Also, vacuum stability is closely determined by the value of the top quark mass [185, 230]. We investigate the potential of dimension-six modifications of the interaction between the top quark and the Higgs boson to induce a strong first-order EWPT taking into account theoretical constraints and current experimental limits using `ScannerS` and `BSMPT`. All implied constraints are discussed in Sections 5.1 and 5.2. To this end, we extend the dimension-four Yukawa potential by $\mathcal{CP}$-conserving dimension-six EFT terms [206, 211–213] as

$$\mathcal{L}_{\mathrm{Yuk}}^{\mathrm{EFT}} = \mathcal{L}_{\mathrm{Yuk}}^{\mathrm{dim\text{-}4}} + \sum_i \frac{C_6^i}{\Lambda^2}\mathcal{O}_6^i\,. \tag{6.12}$$

The dimension-six scalar-fermion operators $\mathcal{O}_6^i$ are multiplied by dimensionless WCs C_6^i and normalized to the EFT scale Λ^2. The dimension-six EFT operators $\mathcal{O}_6^i$ concerning the top quark are summarized in Table 6.5.

The introduction of dimension-six top quark Yukawa couplings leads to corrections to the top mass (in general finite-temperature notation with $\overline{\omega}_i \equiv \overline{\omega}_i(T)$) of

$$M_t = \frac{\omega_2}{\sqrt{2}}\left[Y_2^t - \frac{1}{2\Lambda^2}\left(\left(C_{Qt}^{1(12)} + C_{Qt}^{1(21)} + C_{Qt}^{2(11)}\right)\overline{\omega}_1^2 + C_{Qt}^{2(22)}\overline{\omega}_2^2\right)\right]. \tag{6.13}$$

$\mathcal{O}_{Qt}^{1(12)}$	$(\overline{Q}_L\, t_R\, \widetilde{\Phi}_1)(\Phi_1^\dagger \Phi_2)$
$\mathcal{O}_{Qt}^{1(21)}$	$(\overline{Q}_L\, t_R\, \widetilde{\Phi}_1)(\Phi_2^\dagger \Phi_1)$
$\mathcal{O}_{Qt}^{2(11)}$	$(\overline{Q}_L\, t_R\, \widetilde{\Phi}_2)(\Phi_1^\dagger \Phi_1)$
$\mathcal{O}_{Qt}^{2(22)}$	$(\overline{Q}_L\, t_R\, \widetilde{\Phi}_2)(\Phi_2^\dagger \Phi_2)$

Table 6.5.: Dimension-six 2HDM EFT operators of class $\Psi^2\Phi^3$. The Hermitian conjugates for each of these operators are also taken into account. We define $\overline{Q}_L = (\bar{t}_L \;\; \bar{b}_L)$ and $\widetilde{\Phi} = i\sigma^2\Phi^*$.

In order to take the dimension-six top quark mass M_t as input parameter, we shift the dimension-four Yukawa coupling Y^t by

$$Y^t \to \mathcal{Y}^t + \frac{1}{2\Lambda^2}\left(\left(C_{Qt}^{1(12)} + C_{Qt}^{1(21)} + C_{Qt}^{2(11)}\right) v_1^2 + C_{Qt}^{2(22)} v_2^2\right), \tag{6.14}$$

and consequently obtain at $T = 0\,\text{GeV}$

$$M_t = \frac{v_2}{\sqrt{2}}\mathcal{Y}^t\,. \tag{6.15}$$

With this redefinition, we obtain the dimension-four Yukawa interaction of the top quark in the electroweak vacuum at $T = 0\,\text{GeV}$, where $\overline{\omega}_i = v_i$ with $i \in \{1, 2\}$, and the dimension-six effects are shifted into the coupling modifiers between the top quark and the Higgs boson. They are given by

$$\xi_h^t = \frac{\cos\alpha}{\sin\beta} + \frac{v^3}{M_t}\frac{1}{\sqrt{2}\Lambda^2}\left[-C_{Qt}^{2(22)}\cos\alpha\sin^2\beta + \cos\beta\sin\beta\sin\alpha\,\left(C_{Qt}^{1(12)} + C_{Qt}^{1(21)} + C_{Qt}^{2(11)}\right)\right], \tag{6.16}$$

$$\xi_H^t = \frac{\sin\alpha}{\sin\beta} + \frac{v^3}{M_t}\frac{1}{\sqrt{2}\Lambda^2}\left[-C_{Qt}^{2(22)}\sin\alpha\sin^2\beta - \cos\beta\sin\beta\cos\alpha\,\left(C_{Qt}^{1(12)} + C_{Qt}^{1(21)} + C_{Qt}^{2(11)}\right)\right], \tag{6.17}$$

$$\xi_A^t = \cot\beta + \frac{v^3}{M_t}\frac{1}{\sqrt{2}\Lambda^2}\left[\cos\beta\, C_{Qt}^{1(12)}\right]. \tag{6.18}$$

The dimension-four coupling modifiers are recovered in the EFT decoupling limit $\Lambda \to \infty$.

At finite temperature, the dimension-six top quark Yukawa terms introduce new contributions to the thermal masses, cf. Ref. [214, 231], due to modifications of the Yukawa couplings through one-loop corrections and due to new interaction vertices through one- and two-loop corrections. We calculate and include these contributions to be consistent, but note that for our considered parameter choices they do not play a significant role.

It is furthermore convenient to require an OS scheme via Eq. (5.5) to enforce at $T = 0\,\text{GeV}$ an agreement between one-loop and tree-level for the minimum position and the mass matrix. However, in our chosen dimension-six Yukawa-extended effective potential, its temperature-independent one-loop correction, the CW potential, receives dimension-six corrections. While at $T = 0\,\text{GeV}$ the dimension-four CW potential is defined at its tree-level value due to the dimension-four Yukawa shift introduced above, the first and second derivatives receive dimension-six corrections, as further illustrated in Appendix B. Consequently, enforcing Eq. (5.5) with a $V_{\text{CT}}^{\text{finite}}$ that has a dimension-four field structure cannot capture the dimension-six CW shift which is introduced at the level of the derivatives. The reason is that due to the inclusion of these EFT couplings, in the CW potential, the EFT expansion is no longer under analytical control when using a numerical code like `BSMPT`. If we were to perform a linearised

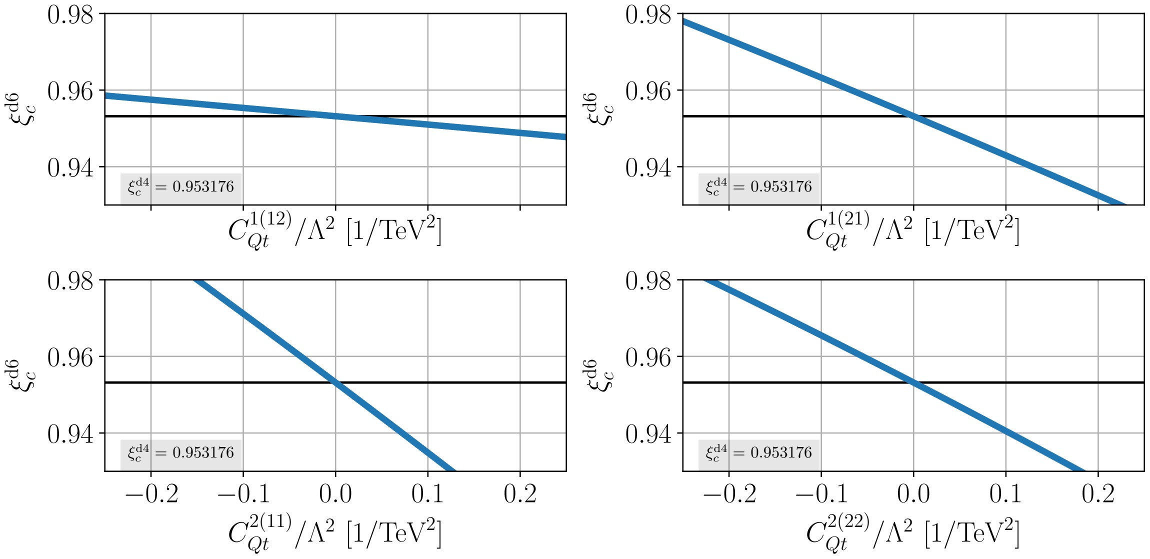

Figure 6.4.: Response in $\xi_c^{\rm d6}$ under individual variation of the four top quark Yukawa dimension-six WCs. The black line denotes the dimension-four $\xi_c^{\rm d4}$ value for the parameter point. The point is detailed in Table 6.6. Figure published in Ref. [208].

expansion in Λ and take into account only the leading-order EFT terms, we could solve Eq. (5.5) analytically. However, in our numerical treatment we are using the full, untruncated top contribution to the effective potential. We emphasize again, that for our considered parameter choices in the perturbative regime, the numerical relics of not using a strictly linear EFT expansion are of subdominant order and do not lead to numerically relevant deviations [208].

We now study the phenomenological impact of varying these dimension-six top quark Yukawa WCs. First, we look at the benchmark point defined in Table 6.6 and vary all four WCs as shown in Figure 6.4. The response in $\xi_c^{\rm d6}$ is linear for all four directions. This illustrates that the formally higher-order non-linear EFT contributions to the effective potential are subleading in the chosen range of WCs. Even though we do not perform an analytical fixed-order EFT-truncation, our studied EFT-extension is under good numerical control.

We now perform a parameter scan in the ranges of Table 6.4 and keep the points for which we find $\xi_c^{\rm d6} \gtrsim 1$ for a variation of individual WCs.[3] Modifications of the top quark Yukawa WCs impact the SM-like signal strengths directly through the Yukawa coupling modifiers. Using `HiggsTools`, we check for agreement with the experimental exclusion limits for BSM Higgs bosons, as well as for agreement of the resulting SM-like Higgs boson signal strengths with the experimentally allowed ranges.[4] This provides strong constraints on the experimentally

---

[3] We check that $\xi_c^{\rm d6} \gtrsim 1$ is realized in the linear response regime. This ensures that our EFT expansion remains under perturbative control.

[4] In Section 5.1 we elaborate in detail on how we use `ScannerS`, `HiggsSignals`, `HiggsBounds` and `HiggsTools`

m_h	m_H	m_A	$m_{H^\pm}$	$\tan\beta$	c_{HVV}	m_{12}^2	$T_c^{\rm d4}$	$\overline{\omega}_{\rm EW}(T_c)^{\rm d4}$	$\xi_c^{\rm d4}$
125.09	683	872	868	1.658	0.00350	205007	226.29	215.69	0.95

Table 6.6.: Input parameters of the benchmark point used for Figure 6.4. Unit of m_{12}^2 in GeV^2, $\tan\beta$, c_{HVV}, $\xi_c^{\rm d4}$ are dimensionless, other units in GeV.

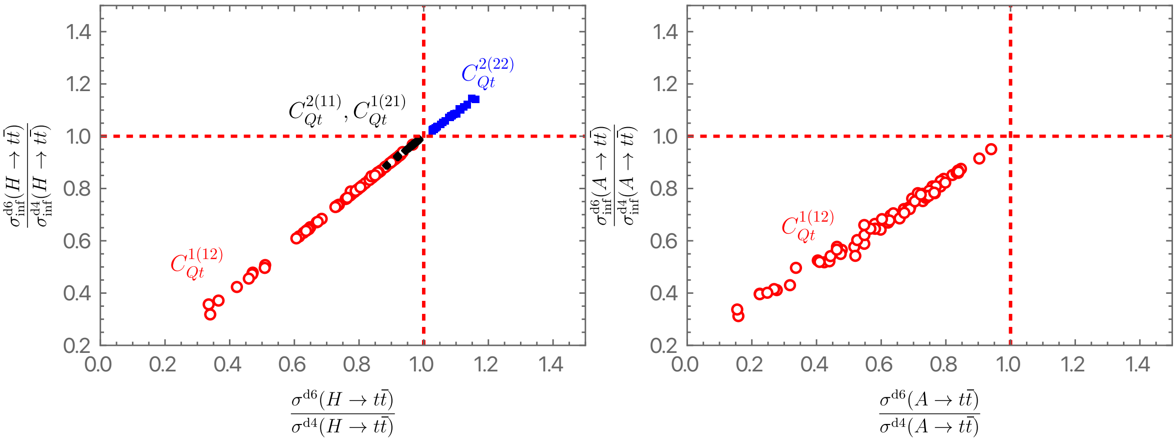

Figure 6.5.: Dimension-six to dimension-four cross section ratios for H (left) and A (right) production via the dominant gluon fusion channel in the $t\bar{t}$ final state. Displayed is the interference cross section (including interference effects from propagating h, H for A production and h propagation for H production) versus the resonance cross section. The points correspond to different operator choices distinguished by different colours to lift points with $0.96 < \xi_c^{\rm d4} < 1$ to $\xi_c^{\rm d6} \simeq 1$. Figure published in Ref. [208].

allowed WC ranges. We find that only $|1-\xi_c^{\rm d4}| \lesssim 0.1$ can be enhanced to $\xi_c^{\rm d6} \gtrsim 1$ while still fulfilling the signal strength constraints. Furthermore, as the measurements identify the measured Higgs boson to be an SM-like Higgs boson, the alignment limit of the 2HDM with $\cos\alpha \simeq \sin\beta$ and $\tan\beta \sim \mathcal{O}(1)$ is favoured. In our conventions, this results in $\sin\alpha < 0$ and relates negative WCs that drive $\xi_c^{\rm d6} \gtrsim 1$ to enhanced coupling modifiers ξ_h^t. For the heavy Higgs boson H, the absolute value of the coupling modifier ξ_H^t is reduced, similarly to ξ_A^t for variations in $C_{Qt}^{1(12)}$.

In Figure 6.5 we show the $gg \to A/H \to t\bar{t}$ cross section ratios for points with individual choices of the WCs to achieve $\xi_c^{\rm d6} \gtrsim 1$ with $0.96 < \xi_c^{\rm d4} < 1$. All WC directions are capable of strengthening the first-order EWPT to a strong first-order EWPT.

The variation of $C_{Qt}^{1(12)}$ shows an interesting feature. We observe strong first-order EWPTs connected with an underabundance of $t\bar{t}$ production in the dominant gluon fusion channels via an H-resonance, Figure 6.5 (left), and an A-resonance, Figure 6.5 (right). The dimension-six heavy Higgs boson phenomenology parametrized by $C_{Qt}^{1(12)}$ is allowed to deviate significantly from its dimension-four prediction due to H and A not being as strictly constrained as h by LHC searches. The WC $C_{Qt}^{2(22)}$, on the other hand, shows an enhancement up to 20 % of only the $H \to t\bar{t}$, but not the $A \to t\bar{t}$ channel. The $A \to t\bar{t}$ channel only receives contributions from $C_{Qt}^{1(12)}$, as can be inferred from the equation of the top-A coupling modifier, Eq. (6.18). The impact and phenomenology of $C_{Qt}^{1(21)}$ and $C_{Qt}^{2(11)}$ is correlated and similar to $C_{Qt}^{1(12)}$, but with a smaller underproduction of resonant H. This aligns with Figure 6.4, where the gradient for $C_{Qt}^{1(21)}$ and $C_{Qt}^{2(11)}$ is steeper than for $C_{Qt}^{1(12)}$, i.e. less dimension-six modifications are necessary to achieve $\xi_c^{\rm d6} \gtrsim 1$ leading to smaller phenomenological impact.

In Figure 6.6 we illustrate the dimension-six modified $pp \to t\bar{t}t\bar{t}$ cross section normalized to the dimension-four value versus the EWPT strength parameter ratio $\xi_c^{\rm d6}/\xi_c^{\rm d4}$. This channel shows the same phenomenological imprint as the $H \to t\bar{t}$ channel depicted in Figure 6.5 (left). Furthermore, the $t\bar{t}t\bar{t}$-channel is of particular interest due to it being more robust

---

(and `MicrOMEGAs` for DM constraints) to limit the parameter space of models to the subspace that agrees with the applied theoretical and experimental constraints.

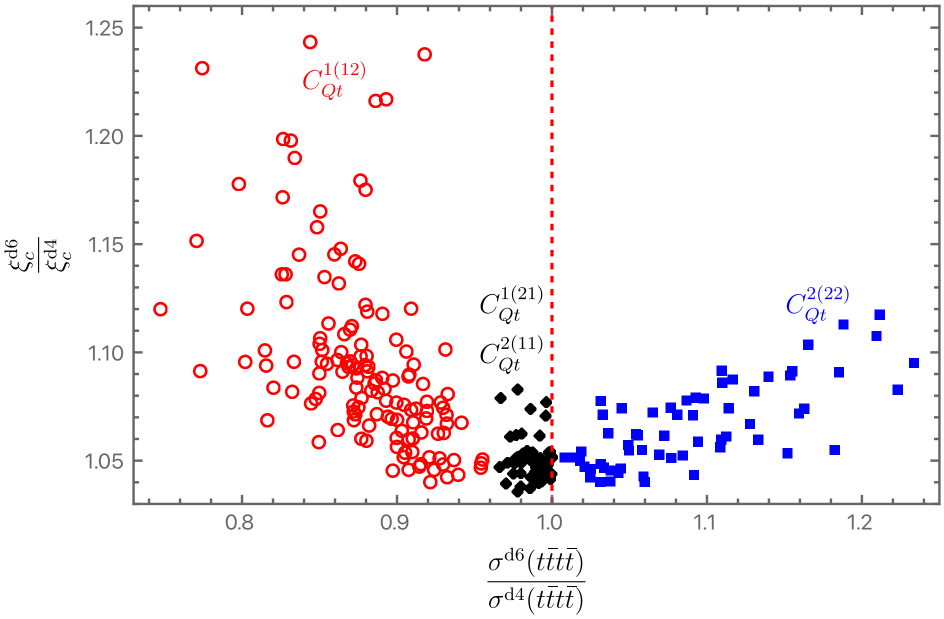

Figure 6.6.: Dimension-six to dimension-four cross section ratios for $t\bar{t}t\bar{t}$-production versus the ratio in the first-order EWPT strength, $\xi_c^{\mathrm{d6}}/\xi_c^{\mathrm{d4}}$. Point sample and colour scheme for the individual dimension-six top quark Yukawa operators are the same as for Figure 6.5. Figure published in Ref. [208].

against signal–background interference [232–238] and might consequently play an important role in observing BSM at particle colliders.

6.4. Conclusions

In this chapter we investigated whether new TeV-scale dynamics can enhance the EWPT strength ξ_c in the type-2 $\mathcal{CP}$-conserving 2HDM to $\xi_c^{\mathrm{d6}} \gtrsim 1$, which defines a strong first-order EWPT. In the first part of this chapter, we considered effective potential extensions with dimension-six purely scalar $\mathcal{CP}$- and $\mathbb{Z}_2$-conserving operators. We found it possible to overcome $|1-\xi_c^{\mathrm{d4}}| > 0$ for WCs in the perturbative range of the EFT. Furthermore, dimension-six strong first-order EWPTs can be correlated to signatures in collider phenomenology. While modifications in the $t\bar{t}$ channel are too small to be measurable in the near future, SM-like Higgs boson pair production is promising. We derived modifications of Higgs boson pair production cross sections, which might be within the reach of LHC in the future. Therefore, it might be possible in the future to derive indirect constraints on the strength ξ_c of an EWPT from Higgs boson pair production measurements at LHC.

In the second part of this chapter, we considered dimension-six top quark Yukawa extensions. We found again that all WCs studied are able to overcome $|1-\xi_c^{\mathrm{d4}}| > 0$, however they are limited to $|1-\xi_c^{\mathrm{d4}}| \simeq 10\,\%$ due to SM-like Higgs boson signal strength modifications. The top quark Yukawa WCs are strongly correlated with phenomenology in the $t\bar{t}$ and $t\bar{t}t\bar{t}$ final states. While being in alignment with the SM-like Higgs boson, the dimension-six modifications lead to characteristic signatures for the heavy BSM scalars H and A, especially a decreased cross section in the direction of $C_{Qt}^{1(12)}$. Therefore, if a strong first-order EWPT is realized via the $C_{Qt}^{1(12)}$ degree of freedom, the LHC BSM sensitivity is *overestimated*. This means, that current constraints on the type-2 2HDM are weakened and the allowed parameter space could widen again.

The condition for strong first-order EWPTs, $\xi_c \gtrsim 1$, that we studied in this first part, is only one of the prerequisites for a first-order EWPT in the early universe. In the second part of this thesis, we will calculate transition rates for first-order EWPTs, as well as gravitational waves sourced by first-order EWPTs. All calculations are implemented in the code `BSMPTv3`, which was developed and released as a part of this thesis and which will be presented in the next chapter.

Part II.

First-Order Electroweak Phase Transitions and Gravitational Waves

CHAPTER 7

BSMPTv3

The presence of a critical temperature is a prerequisite, but not sufficient for a first-order phase transition (PT) to take place and complete.[1] Only by computing the vacuum transition rate and by taking the expansion rate of the universe into account, it can be determined whether a first-order PT to the true vacuum takes place or whether the universe remains trapped in the false vacuum. Furthermore, first-order PTs in the early universe source gravitational waves, possibly within the sensitivity range of future space-bound interferometers. The public code `BSMPTv3` [66], which was developed and published during the scope of this thesis, is the first self-contained open-source code that implements the whole calculation chain starting from a particle physics model to calculating GW spectra sourced by first-order PTs. `BSMPTv3` extends the previous versions of `BSMPT` that were reviewed in Section 5.2, with the ability to trace phases of the effective potential over the whole temperature range in which they exist, to identify and calculate multi-step phase transitions and their characteristic temperatures, phase transition strengths and time scales, as well as other characteristic parameters related to first-order EWPTs. Based on these calculations, `BSMPTv3` calculates the gravitational waves that are produced by first-order EWPTs. Because these new features are implemented in the framework of `BSMPT`, we use the model-independent implementation of the OS-renormalized one-loop daisy-resummed effective potential at finite temperature, cf. Section 5.2. Furthermore, `BSMPT` comes with several models already pre-implemented and also offers an interface to implement user-defined models. `BSMPTv3` adds four new executables to `BSMPT`:

- `MinimaTracer`: Tracing of phases in a user-defined temperature range.
- `CalcTemps`: Calculation of false vacuum decay rates and derivation of the characteristic temperatures of a first-order PT.
- `CalcGW`: Calculation of the GW spectrum sourced by first-order PTs.
- `PotPlotter`: Derivation of user-defined multi-dimensional potential grids in the VEV coordinate space, which are useful for a visualization of the effective potential.

---

[1] Note, that the following considerations apply for generic first-order PTs, of which EWPTs are a special case.

In this chapter we review the new features which were added to `BSMPT` with the release of `BSMPTv3`. The code can be obtained from

`https://github.com/phbasler/BSMPT`.

For a detailed description on how to install `BSMPTv3` and run the new executables with their optional arguments, we refer to Ref. [66].

The new features of `BSMPTv3` are the following:

- **Phase Tracking**: `BSMPTv3` tracks phases in a user-defined temperature interval. Phase tracking is necessary to identify overlaps of phases, i.e. temperature regions in which multiple phases coexist. Between such identified phase overlaps, `BSMPTv3` then calculates first-order PTs, as will be described below. Here, we first describe, how an individual phase is tracked. In the next step presented below, we will elaborate on how `BSMPTv3` handles phase histories with multiple phases.

  A phase exists as long as we can trace its temperature-dependent minimum position, that is as long as it contains a *local* minimum of the effective potential. For a seed point of the phase tracking, we use global minima determined by using a set of gradient-free minimizer routines, cf. [66]. We obtain a more precise position of the initial seed point by the means of the Newton–Raphson method. In this method, the potential shape is approximated locally by a multivariate second-degree polynomial. The polynomial is constructed based on numerically derived first and second derivatives, i.e. the gradient and the Hessian matrix, of the effective potential at the initial seed point. We then iteratively minimize the gradient at the seed point by taking educated steps into the minimum location of the multivariate second-degree polynomial. After a seed point for the tracking is found with that method, we vary the temperature and repeat the procedure to track the phase over the user-defined temperature interval. If the predicted next minimum position is identified to be a saddle point, we decrease the temperature step to converge to the phase endpoint.

  Symmetries of the multi-dimensional effective potential can cause problems for the numerical tracking of phases. `BSMPTv3` deals with *discrete symmetries* and *flat directions* of the effective potential as follows. In `BSMPTv3`, we determine all $\mathbb{Z}_2$ symmetries, also including $\mathbb{Z}_2$ subgroups of gauge symmetries, that the model-specific effective potential exhibits. We then map the seed point to the same ‘principal quadrant’ to ensure that we only track phases which are not related by symmetry transformations, cf. [66]. `BSMPTv3` is additionally able to identify combinations of up to three field directions under which the effective potential is invariant. If such flat directions are found, `BSMPTv3` uses a lower dimensional field space.

- **Multi-Step Phase Tracking**: The multi-dimensional effective potential can exhibit multiple and potentially overlapping phases. We have implemented five multi-step phase tracking modes in `BSMPTv3` that are optimized for different exemplary phase histories. Four of these modes are illustrated in Figure 7.1. The fifth mode combines two of the displayed modes, as we will describe below. By default, the `default` mode, cf. Figure 7.1 (left), is chosen. The `default` mode can track most (multi-step) phase histories, while having the lowest runtime. It assumes the universe to be in the global minimum at the user-defined high temperature. We then trace the high-temperature phase down to $T = 0\,\text{GeV}$. If the phase is found to end, a new global minimum is determined and traced until the global electroweak minimum at $T = 0\,\text{GeV}$ is part of the traced phases.[2]

---

[2] By default, `BSMPTv3` requires absolute vacuum stability, i.e. the zero-temperature global minimum of the one-loop daisy-resummed effective potential at the electroweak minimum with $v_{\text{EW}} = 246.22\,\text{GeV}$, cf. Section 5.2. In `BSMPTv3`, this requirement can optionally be switched off, cf. Ref. [66].

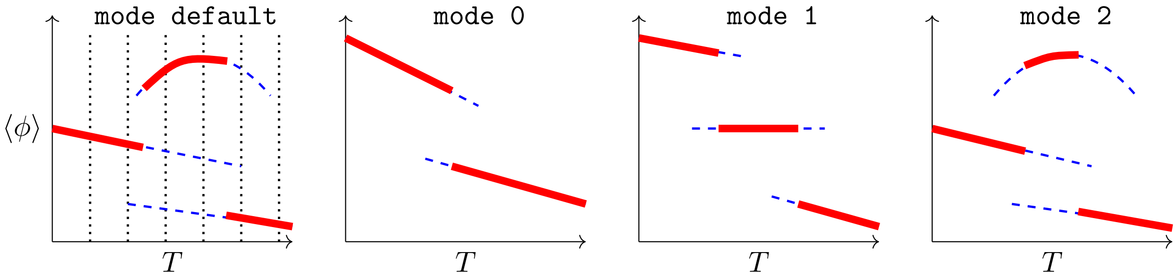

Figure 7.1.: Illustration of the multi-step phase tracking modes (from left to right) `default`, `0`, `1`, `2` for the exemplary type of phase history, for which the respective mode is optimized for. Displayed are the phases with the generic VEV coordinate $\langle\phi\rangle$ as function of the temperature T. Thick red lines mark the temperature region, in which the phase contains the global minimum. Regions, in which the phase only contains a non-global minimum are marked by thinner dashed blue lines. The vertical dotted lines in the leftmost figure illustrate the seed point grid which is used in the `default` mode, cf. text for details. Figure published in Ref. [66].

The `default` mode then checks if the global minima found at an equidistant temperature grid are already part of the traced phases, and if not, adds the newly found phases. This mode can be fine-tuned by the user, through increasing the number of points in the grid. The other modes are specialized for certain types of phase histories, cf. Figure 7.1. For example, `mode 0` only looks for one-step first-order PTs by tracing the low-temperature and the high-temperature global minimum and reporting a valid candidate point, if a phase overlap is identified. It additionally requires that at the phase endpoints, the global minimum is contained within the respective other phase. The other modes, `mode 1` and `mode 2`, can deal with multi-step phase histories. The former enforces that at least one phase is found for each temperature while requiring that the global minimum at the phase endpoints is part of the traced phases. Therefore, `mode 1` is optimized to deal with phase histories that have overlaps of exactly two phases at a time, cf. Figure 7.1. The latter, `mode 2`, works similar to `mode 1`, but for each phase it keeps track how long the phase contains the global minimum. If a phase no longer contains the global minimum, a new phase is tracked using the new global minimum as seed point. With a sufficient grid size, the `default` mode gives the same result as `mode 2`, while being significantly faster. The fifth mode automatizes the choice between `mode 1` and `mode 2`. The multi-step phase tracking modes are described in more detail in Ref. [66].

- **Electroweak Symmetry Restoration**: We derive whether the electroweak symmetry is restored at high temperature. In the high-temperature limit the eigenvalues of the Hessian matrix of the one-loop daisy-corrected effective potential become field independent and are used by `BSMPTv3` to determine the high-temperature shape of the potential. We refer to Ref. [66] for more details.

- **Bounce Solution**: Based on the results of the multi-step phase tracking, `BSMPTv3` identifies temperature regions in which pairs of phases coexist. For each found phase pair, we then calculate the decay rate of the false vacuum. This rate can be written in terms of the *bounce solution*, that is the solution to a second-order differential equation. The derivation of the vacuum decay rate and the algorithm used by `BSMPTv3` to determine the bounce solution will be discussed in detail in Section 8.1.

- **Characteristic Temperatures**: We derive the critical temperature T_c for each phase pair as the temperature at which false and true minimum are degenerate. The possibility of a first-order PT opens for temperatures $T < T_c$. If a false vacuum decay rate can be calculated, `BSMPTv3` derives the nucleation, percolation and completion temperature. These temperatures are calculated by taking into account the false vacuum decay rate, as well as the Hubble rate, that parametrizes the expansion of the universe. The characteristic temperatures of a first-order PT are discussed in detail in Section 8.2. For the calculation of the GW spectrum, as well as the characteristic parameters that will be discussed below, `BSMPTv3` by default assumes the transition temperature T_* of the first-order PT to be equal to the percolation temperature. This choice can be optionally modified by the user.

- **Transition History**: `BSMTPv3` reports on the transition history, based on the calculation of completion temperatures for the found phase pairs. Starting from the initial false phase which is assumed to contain the global minimum at the user-defined high temperature, `BSMPTv3` checks all found phase pairs and identifies the highest found completion temperature for a PT from the initial false phase to a true phase. This true phase is then the new false phase for a possible next transition, for which the search for a completion temperature is repeated. The code then reports on the transition history, i.e. which first-order PTs take place and which phases are populated.

- **Characteristic Parameters**: A first-order PT releases vacuum energy into the false vacuum plasma in front of the bubble wall. This process sources gravitational waves, as we will in detail discuss in Chapter 9. In `BSMPTv3`, we calculate the strength of the PT α at the transition temperature T_*, which is directly related to the released vacuum energy density. The vacuum energy density is converted into kinetic energy of the plasma. This process is parametrized by an efficiency factor κ that defines the kinetic energy fraction K in terms of α. The bubble wall velocity v_w is taken as an input parameter in `BSMPTv3`. The timescale of the PT is determined from the bounce solution. We review all the characteristic parameters, as well as their derivations, that were implemented in `BSMPTv3`, in Section 9.1

- **Gravitational Wave Spectrum**: Gravitational waves are sourced through the breaking of the spherical symmetry by a first-order PT at the transition temperature T_* in the early universe, as will be reviewed in Chapter 9. The spectrum of the gravitational waves is parametrized as a function of the above mentioned characteristic parameters of a first-order PT. With `BSMPT`, we calculate the peak frequency and peak amplitude of two sources of gravitational waves, i.e. plasma sound waves and plasma turbulence. In Section 9.4, we discuss in detail the parametrization of the GW spectrum for both cases in the notation used in `BSMPTv3`.

- **Signal-to-Noise Ratio**: Gravitational waves sourced by first-order PTs can have peak frequencies within the sensitivity of the future space-bound interferometer LISA. As a measure for detectability of the calculated gravitational waves at LISA, we provide in `BSMPTv3` the calculation of the signal-to-noise ratio (SNR). We describe this calculation, as well as give an overview on the experimental search program for gravitational waves, in Section 9.5.

In Ref. [66], we present a comparison with the widely-used code `CosmoTransitions` [239]. We will summarize the results of this comparison in the following. `CosmoTransitions` derives the bounce solution, as well as critical temperatures and nucleation temperatures via an approximation.[3] We find overall good agreement for the critical and (approximate) nucleation temperatures, for a parameter sample of the $\mathcal{CP}$-conserving 2HDM, cf. Section 6.1.

---

[3] In `CosmoTransitions`, the nucleation temperature is determined as the temperature T_n for which the bounce solution at T_n divided by T_n is ~ 140, cf. Ref. [239].

The mean (median) relative differences in the critical temperature are 0.07 % (0.003 %). For the nucleation temperature, derived via the approximation used by `CosmoTransitions`, we find mean and median relative differences below 1 %.[4] While being in good agreement for the determined temperatures, `BSMPTv3` is observed to be significantly faster than `CosmoTransitions`. `BSMPTv3` can be up to 10^3 faster with a mean (median) runtime of 4.15 min (3.47 min). `CosmoTransitions` is observed to have a mean (median) runtime of 41.46 min (5.61 min) for the parameter sample.[5] We moreover find `BSMPTv3` to be able to calculate multi-step phase transitions for cases in which `CosmoTransitions` fails, cf. Ref. [66].

The subsequent chapters contain an in-depth review of the derivations and the implementation in `BSMPTv3` of the false vacuum decay rate, cf. Chapter 8, and of GW spectra sourced by first-order EWPTs, cf. Chapter 9. The code `BSMPTv3` is used in the phenomenological analysis presented in the second part of Chapter 10, as well as in Chapter 11.

---

[4] We also find, that $\mathcal{O}(1\,\%)$ changes in the nucleation temperature can have $\mathcal{O}(10\,\%)$ effects on $\xi_n \equiv \overline{\omega}_{\text{EW}}(T_n)/T_n$, defined analogously to Eq. (3.13), for cases where the minimum position changes significantly in small temperature ranges.

[5] The runtimes are measured by running the codes on a mixture of `Intel Xeon` and `AMD EPYC` processors with `Python 3.6.15` for `CosmoTransitions`.

CHAPTER 8

Phase Transitions in the Early Universe

So far, we discussed critical temperatures in an effective potential at which two degenerate minima exist. These are one low-temperature minimum that evolves to be the electroweak broken minimum today at $T = 0\,\mathrm{GeV}$ and one high-temperature minimum that restores the EW symmetry. Having a minimum constellation with a critical temperature is a requirement for a first-order PT.[1] It does not ensure, however, that the PT actually takes place. For this, the transition rate has to be determined. We will present this calculation in Section 8.1. A first-order PT proceeds via bubble nucleation and expansion. Bubble expansion then competes against the expansion of the universe and from the interplay between transition rate and Hubble rate, we derive in Section 8.2 temperatures which are characteristic for first-order EWPTs.

8.1. Calculation of Vacuum Decay Rates

In this section we elaborate on how transition rates between vacua are calculated. We review the zero-temperature derivation of Refs. [240, 241] adapting to their language of false and true vacua and then generalize to finite temperature along the lines of Refs. [242, 243].

We consider the following minima constellation, illustrated in Figure 8.1: The potential has two barrier-separated minima, one being the non-global *false* minimum at ϕ_{false}, the other one the global *true* minimum at ϕ_{true}, with $V(\phi_{\text{false}}, T) > V(\phi_{\text{true}}, T)$. Classically, both minima are stable ground states. However, quantum mechanical tunnelling leads to the decay of the false vacuum. Therefore, the false vacuum is *metastable*. At finite temperature, in addition to quantum mechanical tunnelling, the energy of the thermal bath can directly lift particles over the potential barrier.

In summary, a transition between two barrier-separated minima, from the false to the true vacuum, can take place in three ways in a finite-temperature quantum field theory:

1. Zero-temperature **tunnelling** through the barrier (Figure 8.1 left).
2. Finite-temperature **tunnelling** through the barrier (Figure 8.1 middle).

---

[1] Note, that the following considerations apply for generic first-order PTs, of which the EWPT is a special case.

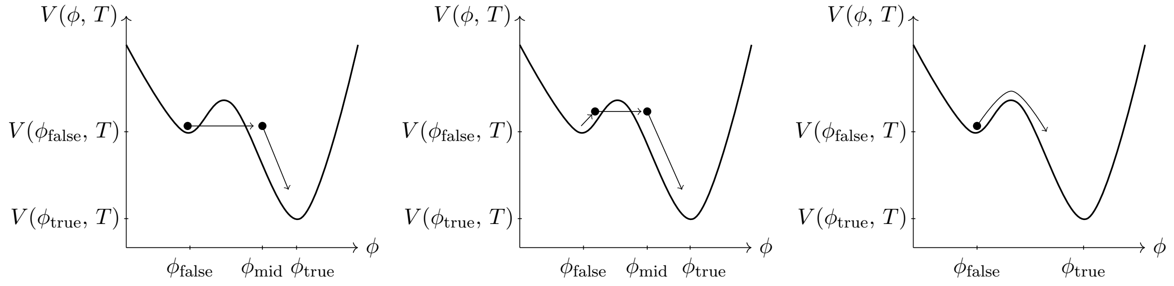

Figure 8.1.: One-dimensional potential projection $V = V(\phi, T)$ with a false (metastable) vacuum at $\phi = \phi_{\text{false}}$ and a true (stable) vacuum at $\phi = \phi_{\text{true}}$. On the left, we show false vacuum decay via zero-temperature tunnelling. In the middle, at finite temperature, the tunnelling takes place after thermal excitation of the particle. On the right, the particle is directly lifted over the barrier by energy induced from the photon bath.

3. **Thermal fluctuations** over the barrier (Figure 8.1 right).

In the following, we derive the transition rate normalized to unit volume for the transition between the false and the true vacuum.

At zero temperature, a particle in the potential at ϕ_{false} can tunnel through the barrier and appear at rest on its other side at ϕ_{mid}, at the same potential energy, after which it classically rolls down into the true vacuum. We will sketch the derivation of the zero-temperature false vacuum decay rate in the following for one-dimensional quantum mechanics and then generalize our findings to quantum field theory.

The one-dimensional quantum mechanical amplitude of the particle going from x_i at $t_i = -\frac{\mathcal{T}}{2}$ to x_f at $t_f = \frac{\mathcal{T}}{2}$ described by a Hamiltonian H can be expressed by a path integral with normalization factor N as [241],

$$\left\langle x_f \,\middle|\, \mathrm{e}^{-iH\mathcal{T}} \,\middle|\, x_i \right\rangle = N \int_{x_i}^{x_f} [dx]\, \mathrm{e}^{iS[x]} \,, \tag{8.1}$$

where we defined $\mathcal{T}$ as the duration of the transition. The left side of Eq. (8.1) can be expanded in a complete set of eigenstates with $H|n\rangle = E_n|n\rangle$,

$$\left\langle x_f \,\middle|\, \mathrm{e}^{-iH\mathcal{T}} \,\middle|\, x_i \right\rangle = \sum_n \mathrm{e}^{-E_n\mathcal{T}} \langle x_f|n\rangle\langle n|x_i\rangle \,. \tag{8.2}$$

From this expansion, it becomes apparent that in the limit $\mathcal{T} \to \infty$ the leading contribution stems from the ground state with $n = 0$, we have

$$\left\langle x_f \,\middle|\, \mathrm{e}^{-iH\mathcal{T}} \,\middle|\, x_i \right\rangle \approx \mathrm{e}^{-E_0\mathcal{T}} \langle x_f|0\rangle\langle 0|x_i\rangle \,. \tag{8.3}$$

The path integral on the right-hand side of Eq. (8.1) is a weighted sum over all paths that respect the boundary conditions, $x\left(-\frac{\mathcal{T}}{2}\right) = x_i$ and $x\left(\frac{\mathcal{T}}{2}\right) = x_f$. Performing a *Wick rotation* to $\tau = it$ we obtain

$$iS[x] = i\int_{t_i}^{t_f} dt \left[\frac{1}{2}\left(\frac{\partial x}{\partial t}\right)^2 - V(x)\right] = -\int_{\tau_i}^{\tau_f} d\tau \left[\frac{1}{2}\left(\frac{\partial x}{\partial \tau}\right)^2 + V(x)\right] \equiv -S_E[x] \,. \tag{8.4}$$

The Euclidean action S_E in Eq. (8.4) corresponds to a particle moving in an *inverted* potential, $-V$. Consequently,

$$\mathrm{e}^{-E_0\mathcal{T}} \langle x_f|0\rangle\langle 0|x_i\rangle = N \int_{x_i}^{x_f} [dx]\, \mathrm{e}^{-S_E[x]} \,. \tag{8.5}$$

Using the method of steepest decent, the Euclidean action S_E can be semi-classically expanded around its extremum B as $S_E \approx B + \delta S_E$. The path integral on the right-hand side of Eq. (8.5) can then be approximated as, cf. Ref. [244],

$$\int_{x_i}^{x_f} [dx]\, \mathrm{e}^{-S_E[x]} \approx \left(\int_{x_i}^{x_f} [dx]\, \mathrm{e}^{-\delta S_E[x]} \right) \mathrm{e}^{-B} \equiv C\, \mathrm{e}^{-B} \,. \tag{8.6}$$

The *bounce action* B is the action of a stationary path $\overline{x}$ which satisfies the equations of motion for a classical particle in a potential $-V$,

$$\frac{\delta S_E}{\delta \overline{x}} \approx \frac{\delta B}{\delta \overline{x}} = -\frac{d^2 \overline{x}}{d\tau^2} + \frac{dV(\overline{x})}{d\overline{x}} = 0 \,. \tag{8.7}$$

We will qualitatively discuss solutions $\overline{x}(\tau)$ of Eq. (8.7) in two cases:

1. If $x_i = x_f = x_{\text{true}}$, only $\overline{x} = x_{\text{true}}$ can satisfy the boundary conditions. The particle is in a bound state with the ground state energy of a harmonic oscillator [241].
2. If $x_i = x_f = x_{\text{false}}$, there exists another solution in which the particle starts at $x_i = x_{\text{false}}$, rolls down the well and up the barrier (in $-V$) until it reaches a turning point from which it *bounces* back and ends at rest at $x_f = x_{\text{false}}$. In the limit of $\mathcal{T} \to \infty$ this solution is called *bounce solution*.

For the first case, the bounce action is zero, $B = 0$ [241]. Therefore only the second case can give rise to a non-zero decay rate of the false vacuum, as we will describe below. We assume $x_i = x_f = x_{\text{false}}$ in the following and simplify Eq. (8.5) to

$$\mathrm{e}^{-E_0 \mathcal{T}} |\phi_0(x_{\text{false}})|^2 = C\, \mathrm{e}^{-B} \,, \tag{8.8}$$

where ϕ_0 is the wave function of the ground state.

For the derivation of the prefactor C we refer to Ref. [241] and will here only quote the result. C is calculated as Gaussian integral over second-order variations of the Euclidean action, as the first-order variations vanish in the expansion around the extremum. Furthermore, the right-hand side of Eq. (8.8) has to be generalized to n bounces of the particle in between $x_i = x_{\text{false}}$ and $x_f = x_{\text{false}}$. Equation (8.8) is finally simplified (using the notation adapted from Ref. [244]) to [241]

$$\mathrm{e}^{-E_0 \mathcal{T}} |\phi_0(x_{\text{false}})|^2 = \left[\det\left(-\partial_\tau^2 + V''(\overline{x}) \right) \right]^{-1/2} \mathrm{e}^{A \mathrm{e}^{-B} \mathcal{T}} \,, \tag{8.9}$$

with $\partial_\tau^2 \equiv \partial^2/\partial\tau^2$, $V''(\overline{x}) \equiv d^2/d\overline{x}^2\, V(\overline{x})$ and

$$A = \left(\frac{B}{2\pi} \right)^{1/2} \left| \frac{\det'\left(-\partial_\tau^2 + V''(\overline{x}) \right)}{\det\left(-\partial_\tau^2 + \omega^2 \right)} \right|^{-1/2} \,. \tag{8.10}$$

The notation $\det'$ indicates that the determinant is calculated leaving out the zero eigenvalue, and we defined $V''(x_{\text{false}}) \equiv \omega^2$. The false vacuum $\phi_0(x_{\text{false}})$ in Equation (8.9) is an unstable quantum mechanical state associated with a decay rate Γ, that is defined via

$$|\phi_0(x_{\text{false}})|^2 \propto \mathrm{e}^{2\, \mathrm{Im}\,(E_0) t} \equiv \mathrm{e}^{-\Gamma t} \quad \Rightarrow \quad \Gamma = -2\, \mathrm{Im}(E_0) \,. \tag{8.11}$$

It was shown in Ref. [241] that the ground state energy E_0 including n bounces is

$$E_0 = -K \mathrm{e}^{-B} + c \,, \tag{8.12}$$

where the constant c is a real number and therefore,

$$\Gamma = 2\, \mathrm{Im}(K)\, \mathrm{e}^{-B} \,. \tag{8.13}$$

A non-zero imaginary part of the ground state energy is sourced by the right-hand side of Eq. (8.9), and by inserting Eq. (8.12) into (8.9) and separating real and imaginary parts, we extract

$$\mathrm{Im}\,(K) = \frac{1}{2}\left(\frac{B}{2\pi}\right)^{1/2} \left|\frac{\det'(-\partial_\tau^2 + V''(\bar{x}))}{\det(-\partial_\tau^2 + \omega^2)}\right|^{-1/2} . \tag{8.14}$$

The decay rate of the false vacuum is

$$\Gamma = 2\,\mathrm{Im}\,(K)\,\mathrm{e}^{-B} = \left(\frac{B}{2\pi}\right)^{1/2} \left|\frac{\det'(-\partial_\tau^2 + V''(\bar{x}))}{\det(-\partial_\tau^2 + \omega^2)}\right|^{-1/2} \mathrm{e}^{-B} . \tag{8.15}$$

The generalization from one-dimensional quantum mechanics to quantum field theory is [241]

$$\frac{\Gamma}{V} = \frac{B^2}{4\pi^2} \left|\frac{\det'(-\partial^2 + V''(\phi))}{\det(-\partial^2 + V''(\phi_{\text{false}}))}\right|^{-1/2} \mathrm{e}^{-B} . \tag{8.16}$$

In Eq. (8.16), the false vacuum decay rate is normalized to a three-dimensional volume. In zero-temperature quantum field theory, the bounce action B is an $O(4)$-symmetric function [241], that we will denote by $B \equiv S_4$ in the following.

Going to finite temperature via the replacement of Eqs. (4.20) and (4.21) in the four-dimensional Euclidean space path formalism equals a summation over paths periodic in Euclidean time with period $\beta = T^{-1}$. The free energy F of the false vacuum is found to develop an imaginary part that relates to the tunnelling rate. Using the techniques of Boltzmann averaging we derive [245–247],

$$\Gamma = -2\,\mathrm{Im}\,[F(\beta)] \qquad \text{for} \quad \beta^{-1} \ll \Delta V_{\text{barrier}} , \tag{8.17}$$

$$\Gamma = -\frac{\omega\beta}{\pi}\,\mathrm{Im}\,[F(\beta)] \quad \text{for} \quad \Delta V_{\text{barrier}} \ll \beta^{-1} . \tag{8.18}$$

For temperatures above the barrier height $\Delta V_{\text{barrier}}$, the bounce action has a negative eigenvalue λ_- and $\omega = \sqrt{-\lambda_-}$ [247]. Both solutions agree for $T_0 = \beta_0^{-1} \equiv \frac{\omega}{2\pi}$. For temperatures $T \lesssim T_0$, Eq. (8.17) describes Boltzmann-averaged thermal tunnelling through the potential barrier, cf. Figure 8.1 (middle). For $T \gtrsim T_0$, Eq. (8.18) describes thermal fluctuations over the barrier, cf. Figure 8.1 (right). Both regimes have a decay rate induced by a non-vanishing imaginary part from the finite-temperature path integral periodic in Euclidean time β. For $\beta \to \infty$, $T \to 0$, one obtains the zero-temperature vacuum decay rate dependent on the $O(4)$-symmetric bounce action. For $\beta \to 0$, $T \to \infty$, the periodicity approaches zero and the solutions become independent of Euclidean time. Consequently, the bounce action B is three-dimensional in this limit [242, 243, 248],

$$B \equiv \beta S_3 = \frac{S_3}{T} . \tag{8.19}$$

Bubbles in zero-temperature field theory are $O(4)$-symmetric, bubbles in finite temperature field theory are $O(3)$-symmetric. The tunnelling rate per unit volume then has contributions of the form

$$\left.\frac{\Gamma}{V}\right|_{T=0\,\text{GeV}} = |A|\,\mathrm{e}^{-S_4} \quad \text{and} \quad \left.\frac{\Gamma}{V}\right|_{T>0\,\text{GeV}} = A(T)\,\mathrm{e}^{-S_3/T} , \tag{8.20}$$

with prefactors analogous to the prefactor of e^{-B} in Eq. (8.16). As the prefactors require the analytically notoriously difficult calculation of functional determinants, they are often approximated by their relevant dimensional scaling under the assumption that their precise form is only a subleading contribution. This, however, might not always hold, as discussed in Ref. [249]. Approximating the functional determinants by dimensional analysis yields [244]

$$A \simeq R_0^{-4} \left(\frac{S_4}{2\pi}\right)^2 \quad \text{and} \quad A(T) \simeq T^4 \left(\frac{S_3}{2\pi T}\right)^{3/2} , \tag{8.21}$$

with the critical bubble radius R_0. Consequently, finite-temperature tunnelling and thermal fluctuations across the potential barrier are assumed to contribute with the same prefactor.

Qualitatively, the metastable false vacuum decays via bubble nucleation, expansion and collision until one bubble contains the whole universe. Initial seed bubbles are constantly nucleated due to thermal fluctuations. The free energy 'cost' of bubble formation is defined as

$$\Delta F(R) = \underbrace{-\frac{4\pi}{3} R^3 \, \Delta E}_{\text{volume energy}} + \underbrace{4\pi R^2 \, \sigma(T)}_{\text{surface energy}} , \tag{8.22}$$

for $T \lesssim T_c$ and with the surface tension $\sigma(T)$. For a growing bubble, the bubble radius R increases and consequently, the surface energy term in Eq. (8.22) increases $\propto R^2$ and the volume energy term in Eq. (8.22) decreases $\propto -R^3$. A nucleated bubble grows if the cost in surface tension is overcompensated by a gain in volume energy and consequently, the expansion reduces the total energy. The radius R_0, for which $\Delta F(R > R_0) < 0$ is named the *critical bubble radius* and defined as [240, 250, 251]

$$\left.\frac{d\Delta F(R)}{dR}\right|_{R=R_0} = 0 \, . \tag{8.23}$$

The bounce action B is in general determined numerically. In the following, we will describe the approach used in `BSMPTv3` [66]. We neglect the contribution of the zero-temperature solution, because for PTs at finite temperature, the finite-temperature rate yields the dominant contribution to the false vacuum decay rate. Therefore, using Eqs. (8.20) and (8.21), we write the finite-temperature false vacuum decay rate per unit volume as

$$\Gamma(T) \simeq T^4 \left(\frac{S_3}{2\pi T}\right)^{3/2} \mathrm{e}^{-S_3/T} \, . \tag{8.24}$$

In quantum field theory, the Euclidean action S_E has the following form

$$S_E = \int d\tau d^3x \left[\frac{1}{2}\left(\partial_\mu \vec{\phi}\right)\left(\partial^\mu \vec{\phi}\right) + V(\vec{\phi})\right] . \tag{8.25}$$

We change variables to $\rho = \sqrt{\tau^2 + |\vec{x}|^2}$ and derive the finite-temperature bounce action S_3 as

$$S_3(T) = 4\pi \int_0^\infty d\rho \, \rho^2 \left[\frac{1}{2}\left(\frac{d\vec{\phi}}{d\rho}\right)^2 + V(\vec{\phi})\right] . \tag{8.26}$$

The path $\vec{\phi}$ is a solution to the Euler–Lagrange equations

$$\frac{d^2\vec{\phi}}{d\rho^2} + \frac{2}{\rho}\frac{d\vec{\phi}}{d\rho} = \nabla V(\vec{\phi}) \, , \tag{8.27}$$

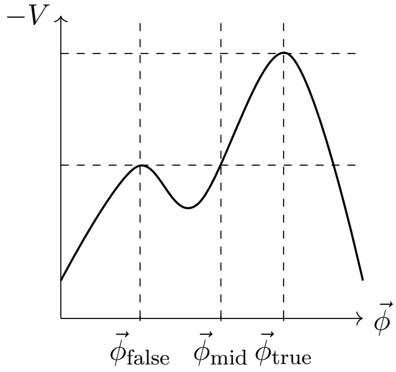

Figure 8.2.: Bounce solution derivation in the upturned potential with false vacuum at $\vec{\phi}_{\text{false}}$ and true vacuum at $\vec{\phi}_{\text{true}}$. The value $\vec{\phi}_{\text{mid}}$ marks the field value where a particle has the same potential energy as a particle resting at $\vec{\phi}_{\text{false}}$.

with the boundary conditions

$$\vec{\phi}(\rho)\Big|_{\rho\to\infty} = \vec{\phi}_{\text{false}}\,, \quad \frac{d\vec{\phi}}{d\rho}\Big|_{\rho=0} = 0\,. \tag{8.28}$$

The boundary conditions ensure that far away from the bubble filled with the true vacuum, at $\rho \to \infty$, the universe is in the false vacuum, $\vec{\phi} = \phi_{\text{false}}$ and, without loss of generality, at $\rho = 0$ the transition to the true vacuum takes place. At $\rho = 0$ a particle moving in the upturned potential $-V$ is at rest at ϕ_0. Coleman proved the existence of a solution to Eqs. (8.27) and (8.28) along the following lines [240]. The problem is illustrated in Figure 8.2. Knowing that the drag term leads to energy dissipation, because

$$\frac{d}{d\rho}\left[\frac{1}{2}\left(\frac{d\phi}{d\rho}\right)^2 - V(\phi)\right] = -\frac{2}{\rho}\left(\frac{d\phi}{d\rho}\right)^2 \leq 0\,, \tag{8.29}$$

we conclude that if $\phi_{\text{false}} < \phi_0 < \phi_{\text{mid}}$ in Figure 8.2, the particle *undershoots* as it cannot reach ϕ_{false} for $\rho \to \infty$. If on the other hand, $\phi_0 \sim \phi_{\text{true}}$, the particle is too energetic for the drag term to compensate and the particle *overshoots* ϕ_{false}. Continuity then requires the existence of a ϕ_0 and therefore a bounce solution that fulfills the Euler–Lagrange equation with the specified boundary conditions.

Except for $\rho = 0$, where we implement an analytical solution, we solve the Euler–Lagrange equation (8.27) numerically in `BSMPTv3` using the iterative method of *path deformation*. In this method, an initial guess path is deformed by perpendicular forces that originate from the potential until convergence to a solution of Eq. (8.27) is obtained as described in [66]. This method was developed and implemented first by [239, 252, 253]. With `BSMPTv3` we then obtain the finite-temperature transition rate as a function of temperature using Eq. (8.24).

8.2. Characteristic Temperatures

First-order PTs from a high-temperature false vacuum to a low-temperature true vacuum are associated with a set of characteristic temperature scales that will be discussed in the following.

At the *critical temperature* T_c, the free energy of the false vacuum equals the free energy of the true vacuum. Both vacua are degenerate and separated by a barrier. For the following discussion, we assume the case of only two barrier-separated phases coexisting for temperatures below the critical temperature and the true minimum to be lower than the false minimum for $T < T_c$. Quantum mechanical tunnelling becomes possible for temperatures $T < T_c$. In case the potential barrier does not exist down to $T = 0\,\mathrm{GeV}$, the false vacuum will decay, either through the quantum mechanical and thermal processes discussed above while the barrier still exists, or through classical processes after the barrier has disappeared. If the barrier however continues to exist down to $T = 0\,\mathrm{GeV}$, there exists the possibility of vacuum trapping, cf. e.g. Refs. [129, 202, 254]. In the case of vacuum trapping, neither tunnelling, nor thermal fluctuations seed enough fast growing true vacuum bubbles that overcome the expansion of the universe, and the universe remains trapped in the false vacuum down to $T = 0\,\mathrm{GeV}$.

The *nucleation* temperature T_n relates the false vacuum decay rate to the expansion rate of the universe. At $T = T_n$ one true-vacuum bubble is nucleated per Hubble volume and per Hubble time, i.e. the false vacuum decay rate as defined in Eq. (8.24) matches the inverse Hubble volume times inverse Hubble time

$$\frac{\Gamma(T_n)}{H^4(T_n)} \equiv 1. \tag{8.30}$$

The evolution of a first-order PT for $T < T_c$ can be quantified by the fraction of the universe which remains in the false vacuum and the fraction which transitioned into the true vacuum, respectively. The false vacuum fraction equation [255, 256], in chemical physics also known as Johnson–Mehl–Avrami–Kolmogorov equation [257–261], was first formulated as

$$P_f(t) = \exp\left(-\kappa(t)\right), \tag{8.31}$$

with the time-dependent fraction of the universe that is in the false vacuum, P_f, parametrized by an exponential decay width the time-dependent exponent κ that is a measure of the volume of the universe which is filled with the true vacuum. Taking into account that true-vacuum bubbles are nucleated by a decay of the false vacuum with rate $\Gamma(t)$, that is calculated via Eq. (8.24), with the scale factor of the universe $a(t)$, cf. Chapter 3, κ can be calculated as

$$\kappa(t) = -\int_{t_c}^{t} dt'\, \frac{a(t')^3}{a(t)^3}\, \Gamma(t')\, V(t', t). \tag{8.32}$$

The integration goes from the critical time t_c, when the transition starts at T_c, to the time $t > t_c$ where the false vacuum fraction is to be calculated. The integrand $\Gamma(t')\, V(t', t)$ describes the true-bubble volume $V(t', t)$ of a bubble nucleated at t' and measured at t, weighted with its probability for nucleation, $\Gamma(t')$. Assuming a vanishing initial bubble radius [262, 263] as well as a constant terminal wall velocity v_w during the false vacuum decay period, the true vacuum bubble volume is further estimated as [248, 264]

$$V(t', t) = \frac{4\pi}{3} \left(v_w \int_{t'}^{t} dt''\, \frac{a(t)}{a(t'')} \right)^3. \tag{8.33}$$

In Section 8.1 we derived the false vacuum decay rate as a function of the temperature. Assuming the radiation-dominated epoch to last during the PT (an assumption that necessarily breaks down for long-lasting, *supercooled*, transitions), we can relate time and temperature via the assumption of adiabatic expansion of the universe, i.e. assuming that the entropy density s per comoving volume is conserved, as derived in Eq. (3.6). The temperature-dependent true-bubble volume is then written as

$$V(T', T) = \frac{4\pi}{3} \left(\frac{v_w}{T} \int_{T}^{T'} dT''\, \frac{dT''}{H(T'')} \right)^3, \tag{8.34}$$

and the temperature-dependent false vacuum fraction is finally derived as [264]

$$P_f(T) = \exp\left[-\frac{4\pi}{3} v_w^3 \int_T^{T_c} dT' \frac{\Gamma(T')}{T'^4 H(T')} \left(\int_T^{T'} \frac{dT''}{H(T'')}\right)^3\right]. \tag{8.35}$$

Using $P_f(T)$, we will define the percolation and completion temperature. The *percolation temperature* T_p is defined as the temperature where 29 % of the universe has transitioned into the true vacuum while 71 % is still in the false vacuum, i.e.

$$P_f(T_p) \equiv 0.71. \tag{8.36}$$

At this false vacuum fraction a universe-wide true-vacuum bubble cluster has formed and the universe is set to end up in the true vacuum [265–269]. Analogously, a first-order PT is complete when only 1 % of the universe is left in the false vacuum, defining the *completion temperature* T_f as

$$P_f(T_f) \equiv 0.01. \tag{8.37}$$

In the following Chapter 9, we review how gravitational waves are sourced by first-order PTs. For this, we assume that the *transition temperature* T_* of the first-order PT is equal to the percolation temperature,[2]

$$T_* \equiv T_p\,. \tag{8.38}$$

The derivation of all mentioned characteristic temperatures is implemented in the public code `BSMPTv3`. The false vacuum fractions P_f at the percolation and completion temperature, as well as the transition temperature can be chosen by the user, as further described in Ref. [66].

---

[2] If the transition is not fast, e.g. in case $T_p \ll T_n$, the predicted GW signal can change significantly depending on the transition temperature chosen for the calculation, e.g. in that case between the choice $T_* = T_p$ or the choice $T_* = T_n$, respectively [270].

CHAPTER 9

Gravitational Waves sourced by Phase Transitions

First-order PTs[1] in the early universe source an isotropic, stochastic *gravitational wave (GW) background*. Plasma interactions during the expansion of the nucleated true vacuum bubbles as well as bubble collisions break the spherical symmetry implying a perturbation of the spacetime metric. As the origin of the metric perturbation is stochastic, and the locations of the source are homogeneously spread across the universe, the induced gravitational waves are expected to constitute an isotropic, stochastic background.[2]

This chapter summarizes the derivation of the characteristic parameters of first-order PTs in Section 9.1 and their impact on the generated gravitational wave in Section 9.4. We give a brief review of the physics behind gravitational waves in Section 9.2. The gravitational wave is sourced by the PT at the transition temperature T_*, and its spectrum is then redshifted to today, as we will describe in Section 9.3. A first-order PT is only one possible source of a stochastic GW background. Other possible sources are supermassive black hole binaries, cosmic strings and domain walls, see e.g. Refs. [47, 48] and references within. In Section 9.5 we give a brief overview of on-going and planned experimental efforts to measure a stochastic GW background and identify its origin.

9.1. Characteristic Parameters of a First-Order Phase Transition

The spectrum of the gravitational wave can be parametrized by a set of characteristic parameters that will be briefly reviewed in this section.

First, we take a thermodynamic viewpoint on an early universe PT that is assumed to take place at a transition temperature T_*. The effective potential can be related to the free energy density $\mathcal{F}$ and the thermodynamic pressure p by

$$V_{\text{eff}} = \mathcal{F} = -p\,. \tag{9.1}$$

---

[1] The derivations presented in this chapter apply for general first-order PTs, of which the EWPT is a special case.

[2] The GW background created by PTs is, similarly to the CMB, also sensitive to primordial density fluctuations and therefore also expected to have anisotropies, as discussed in Ref. [271]. See Ref. [49] for a recent experimental study by the NANOGrav collaboration.

For detailed reviews consult e.g. Refs. [107, 127, 244, 272]. In a first-order PT the released vacuum energy is transferred to the plasma and into kinetic and gradient energy of the scalar fields in the bubble wall [273]. In scenarios in which the friction between the expanding bubble wall and the surrounding plasma leads to a terminal wall velocity v_w, the latter two scalar field contributions are negligible. They can play a dominant role in cases in which friction is negligible and the bubble wall acceleration is not slowed down significantly, called *run-away*, which takes place for long transition durations during which the universe cools down significantly and the plasma is sufficiently diluted, called *supercooled* transitions [274–276].

In this thesis, as well as in the code `BSMPTv3`, we focus on scenarios with terminal wall velocities where the scalar field contribution can be neglected. In the following Section 9.4 this assumption then leads to the conclusion that only two (sound waves and turbulence) out of the three possible GW contributions sourced by a first-order PT play a role. The scalar field contribution can source gravitational waves through spherical symmetry breaking in bubble collisions, whose emission compared to the other contributions is limited to a short timescale while the other contributions are enhanced by a factor of the timescale of the PT.

Assuming that the plasma behaves as a perfect relativistic fluid [273], its energy-momentum tensor is given as

$$T_{\mu\nu}^{\text{plasma}} = \omega u_\mu u_\nu - g_{\mu\nu} p \,, \tag{9.2}$$

with the enthalpy density ω, the fluid four velocity defined as

$$u^\mu = \gamma(1,\, \vec{v}) = \frac{(1,\, \vec{v})}{\sqrt{1-|\vec{v}|^2}} \,, \tag{9.3}$$

and the pressure $p = -V_{\text{eff}}$, as defined in Eq. (9.1). The enthalpy density ω is defined as

$$\omega = T\frac{\partial p}{\partial T} = -T\frac{\partial V_{\text{eff}}}{\partial T} \,. \tag{9.4}$$

The trace of the energy-momentum tensor then defines the *trace anomaly* θ

$$\theta \equiv \frac{1}{4} T_{\mu\nu}^{\text{plasma}} g^{\mu\nu} = \frac{\omega}{4} - p = V_{\text{eff}} - \frac{T}{4}\frac{\partial V_{\text{eff}}}{\partial T} \,. \tag{9.5}$$

The *strength* of the PT α at the transition temperature T_* is defined as the released vacuum energy density ρ_{vac} normalized to the value of the radiation energy density ρ_{rad} as defined in Eq. (3.7),

$$\alpha \equiv \frac{\rho_{\text{vac}}(T_*)}{\rho_{\text{rad}}(T_*)} \,. \tag{9.6}$$

We choose to parametrize ρ_{vac} by the difference in the trace anomaly and normalize to the enthalpy density ω to define α,[3] where we use that for a relativistic fluid $\omega = \frac{4}{3}\rho_{\text{rad}}$ [278]

$$\alpha \equiv \frac{4\Delta\theta(T_*)}{3\,\omega(T_*)} = \frac{1}{\rho_{\text{rad}}(T_*)}\left[\theta_{\text{false}}(T_*) - \theta_{\text{true}}(T_*)\right] = \frac{1}{\rho_{\text{rad}}(T_*)}\left[\Delta V_{\text{eff}} - \frac{T}{4}\Delta\frac{\partial V_{\text{eff}}}{\partial T}\right] \,. \tag{9.7}$$

During a first-order PT, the vacuum energy density ρ_{vac} is released into the plasma and, as discussed above, is converted mostly to kinetic energy if a terminal wall velocity v_w is reached. The *kinetic energy fraction* K describes the kinetic plasma energy density ρ_{kin} normalized to the total plasma energy density ρ_{tot},

$$K \equiv \frac{\rho_{\text{kin}}(T_*)}{\rho_{\text{tot}}(T_*)} \,, \tag{9.8}$$

---

[3] Alternative conventions for defining α use the energy density or pressure difference [244, 273, 277].

where the energy densities are evaluated at the transition temperature T_*. While the pressure difference $\Delta p = -\Delta V_{\text{eff}} = V_{\text{eff}}^{\text{true}} - V_{\text{eff}}^{\text{false}} < 0$ drives the expansion of the true-vacuum bubbles, their expansion is slowed down by friction with the plasma until a terminal wall velocity v_w is reached, for the cases considered here. The requirement of energy-momentum conservation at the bubble wall then leads to a set of hydrodynamic equations. In a simplified treatment, K is determined from the solutions of these equations for one isolated bubble. In [41] the *bag equation of state* is assumed, where the symmetric and broken phase are described as relativistic plasmas that differ in their number of relativistic degrees of freedom. Following this assumption, the speed of sound in the symmetric and broken phase is $c_s = 1/\sqrt{3}$. The strength of the PT, α, and K are expressed via the definition of an efficiency factor κ that defines how efficient the conversion of liberated vacuum energy to kinetic plasma energy is [41, 273]

$$\kappa = \frac{\rho_{\text{kin}}(T_*)}{\epsilon} \quad \Rightarrow \quad K = \frac{\kappa\epsilon}{\rho_{\text{tot}}(T_*)} \quad \text{and} \quad \alpha = \frac{\epsilon}{\rho_{\text{rad}}(T_*)} \,. \tag{9.9}$$

The *bag constant* ϵ can be related to the released vacuum energy, $\epsilon \simeq \rho_{\text{vac}}$,

$$K \equiv \kappa \frac{\epsilon}{\rho_{\text{tot}}} \simeq \kappa \frac{\rho_{\text{vac}}}{\rho_{\text{rad}} + \rho_{\text{vac}}} = \frac{\kappa\alpha}{1+\alpha} \,, \tag{9.10}$$

where we used that the total plasma energy is given by the energy density of radiation and the vacuum energy density that is released into the plasma during the first-order PT, $\rho_{\text{tot}} = \rho_{\text{rad}} + \rho_{\text{vac}}$. The *bubble wall velocity* v_w, in the non run-away case, can also be determined from solving the hydrodynamic equations, in more detail by solving coupled scalar field equations of motion and Boltzmann equations for the different bubble expansion modes, by usually assuming a model-dependent ansatz for the bubble wall profile and particle distribution functions. This highly non-trivial task of solving the hydrodynamic equations for the complete set of hydrodynamic parameters has seen progress, e.g. through Refs. [41, 273, 279–300], but so far no model-independent general treatment has been established. In `BSMPTv3` the wall velocity v_w is an input parameter. We choose

$$v_w = 0.95 \,, \tag{9.11}$$

for the analysis below in Chapter 10 and Chapter 11. The efficiency factor κ is determined in `BSMPTv3` as a function of α and v_w by using the numerical fit result of [273].[4]

Another characteristic parameter of a first-order PT that impacts the spectrum of sourced gravitational waves is the duration of the PT. Assuming a fast enough transition so that the bounce action can be linearly expanded in time t as

$$\frac{B(t)}{T(t)} \approx \frac{S_3(t_*)}{T(t_*)} - \beta(t - t_*), \tag{9.12}$$

and using Eq. (3.6), the temperature-dependent transition rate is proportional to

$$\Gamma(T) \propto \exp\left[-\frac{S_3(T_*)}{T_*} - \frac{\beta}{H_* T_*}(T - T_*)\right] . \tag{9.13}$$

---

[4] This method of taking α as the trace anomaly difference in Eq. (9.7) and determining K from the fit of [273] implicitly assumes the bag model, as explained above. In [301] the authors compared different methods to derive κ. The authors find that our chosen method leads to the smallest numerical deviations from the more sophisticated model presented in [285] compared to other estimations of α in Eq. (9.10). Still, deviations of up to 50 % in K are found for our chosen method in [301], which call for a more complete treatment beyond assuming the bag equation of state, by e.g. also taking into account the full temperature dependence of the speed of sound, $c_s^2 = \frac{dp}{dT} / \frac{d\rho}{dT}$.

The *inverse timescale* of the first-order PT is then given by

$$\frac{\beta}{H_*} = T_* \frac{d}{dT}\left(\frac{S_3(T)}{T}\right)\Bigg|_{T=T_*}\,, \tag{9.14}$$

where H_* is the Hubble parameter at the transition temperature, derived via Eq. (3.8). As pointed out in Ref. [302], α and $\frac{\beta}{H_*}$ are correlated. Because

$$\alpha \propto \Delta V_{\text{eff}} \quad \text{and} \quad \frac{\beta}{H_*} \sim \frac{S_3}{T} \sim \frac{1}{\sqrt{\Delta V_{\text{eff}}}}\,, \tag{9.15}$$

larger α are correlated with smaller inverse timescales $\frac{\beta}{H_*}$, i.e. longer durations of the first-order PT.

The derivation of the characteristic parameters of a first-order PT, i.e. the strength α via Eq. (9.7), the kinetic energy fraction K via Eq. (9.10), as well as the inverse duration of the PT β/H_* via Eq. (9.14), was implemented in the public code `BSMPTv3`. For the wall velocity we assume Eq. (9.11) in the context of this thesis. Details on the usage of `BSMPTv3`, e.g. the selection of different assumptions for v_w, can be found in Ref. [66].

9.2. Gravitational Waves

The *Einstein field equations* [303] connect the curvature of spacetime (parametrized by the Ricci curvature tensor $R_{\mu\nu}$ and its trace, the Ricci curvature R, that both solely depend on the spacetime metric $g_{\mu\nu}$) to the energy-momentum tensor $T_{\mu\nu}$ via the gravitational constant G,

$$R_{\mu\nu} - \frac{1}{2} R g_{\mu\nu} = 8\pi G T_{\mu\nu}\,. \tag{9.16}$$

If the spacetime metric $g_{\mu\nu}$ is expressed as the flat-spacetime metric $\eta_{\mu\nu}$ with a perturbation $h_{\mu\nu}$ added, i.e.

$$g_{\mu\nu} \equiv \eta_{\mu\nu} + \epsilon h_{\mu\nu} \quad \text{with} \quad \epsilon \ll 1\,, \tag{9.17}$$

then Eq. (9.16) can be simplified to the form of a wave equation for $h_{\mu\nu}$ [304], in Lorenz gauge and transverse-traceless gauge[5] written as (following the lines of e.g. [305])

$$\Box h_{\mu\nu} = -16\pi G T_{\mu\nu}\,. \tag{9.18}$$

If there are no sources, i.e. $T_{\mu\nu} = 0$, the solution to Eq. (9.18) is a plane wave,

$$h_{\mu\nu} = C_{\mu\nu} \mathrm{e}^{ik_\sigma x^\sigma}\,, \tag{9.19}$$

with $k^2 = 0$, i.e. the wave propagates at the speed of light. This *gravitational wave* is described by three parameters: Its frequency f and two polarizations, C_+ and $C_\times$. In the case of C_+, the xy-space is periodically deformed parallel to the axes in a '+'-shape, while for the $C_\times$-case the deformation is diagonal [305].

After the initial derivation of gravitational waves from perturbations of the flat-spacetime metric, their existence was deduced also for perturbations of the Friedmann–Lemaître–Robertson–Walker metric which parametrizes an isotropic, homogeneous, expanding universe in general relativity [306–314].

---

[5] In transverse-traceless gauge, the perturbation $h_{\mu\nu}$ is traceless and $k_\mu h^{\mu\nu} = 0$ [305].

The solution for the metric perturbation in the presence of sources with $T_{\mu\nu} \neq 0$ can be derived as [305]

$$h_{\mu\nu} = \frac{2G}{3R}\ddot{Q}\,, \tag{9.20}$$

with R, the distance between source and observer. The gravitational wave therefore depends on Q, the quadrupole moment of the energy density of the source, which is defined via a volume integral over the T^{00}-component of the energy-momentum tensor. Spherical symmetry breaking during first-order PTs leads to $\ddot{Q} \neq 0$ and sources an isotropic, stochastic GW background that be characterized by a GW power spectrum as we will see in the following. The GW energy density is related to the metric perturbations via [315, 316]

$$\rho_{\text{GW}} = \frac{1}{32\pi G}\langle \dot{h}_{\mu\nu}\dot{h}^{\mu\nu}\rangle = \int d\log f\,\frac{d\rho_{\text{GW}}}{d\log f} \equiv \rho_c \int d\log f\,\Omega_{\text{GW}}(f)\,, \tag{9.21}$$

where in the last step, we defined the GW amplitude Ω_{GW} as a function of the GW frequency f as [41, 302, 315, 317–320]

$$\Omega_{\text{GW}}(f) \equiv \frac{1}{\rho_c}\frac{d\rho_{\text{GW}}}{d\log f}\,, \tag{9.22}$$

with the critical density today, defined via Eq. (3.3). We comment on the GW power spectra for different sources during a first-order PT in Section 9.4. In the following Section 9.3, we first discuss the redshift of the GW spectrum from its time of production at $T = T_*$ to today at $T = T_0 \ll T_*$.

9.3. Gravitational Wave Parameters Today

With gravitation being the weakest of all known interactions, gravitons already decouple from thermal equilibrium at energies below the Planck mass M_{Pl} as [321]

$$\left(\frac{\Gamma_G}{H}\right) \sim \left(\frac{n\,\sigma|v|}{T^2/M_{\text{Pl}}}\right) \sim \left(\frac{T^3\cdot(T^2/M_{\text{Pl}}^4)\cdot 1}{T^2/M_{\text{Pl}}}\right) \sim \left(\frac{T}{M_{\text{Pl}}}\right)^3\,, \tag{9.23}$$

where we used the Hubble rate in the radiation dominated era $H(T) \sim T^2/M_{\text{Pl}}$, compare Eq. (3.8), and assumed for the cross section that it scales similar to the weak interaction cross section $\sigma \sim G^2T^2 = T^2/M_{\text{Pl}}^4$. Therefore, gravitational waves produced by PTs at $T_* \ll M_{\text{Pl}}$ are immediately decoupled. Their characteristic parameters become redshifted until today, but aside from the redshift, they still encode the conditions of their production. Assuming an adiabatic expansion of the universe, the scale factor at the transition a_* versus the scale factor today a_0 is [41, 322], cf. Chapter 3,

$$\frac{a_*}{a_0} = \left(\frac{g_0}{g_*}\right)^{1/3}\left(\frac{T_0}{T_*}\right)\,. \tag{9.24}$$

A frequency redshifts with a factor (a_*/a_0). The amplitude scales like an energy density over the critical density and therefore changes like $(a_*/a_0)^4$ (redshift of the energy density) divided by $(H_*/H_0)^2$ (redshift of the critical density). The GW frequency f_0 of today, as well as the GW amplitude $\Omega_{\text{GW},0}$ of today are then derived from the frequency and amplitude at the transition temperature, assuming radiation domination and thermal equilibrium at $T = T_*$, as [41]

$$f_0 = f_*\left(\frac{a_*}{a_0}\right) = 1.65\times 10^{-5}\,\text{Hz}\left(\frac{g_*}{100}\right)^{\frac{1}{6}}\left(\frac{T_*}{100\,\text{GeV}}\right)\frac{f_*}{H_*}\,, \tag{9.25}$$

$$\Omega_{\text{GW},0} = \Omega_{\text{GW},*}\left(\frac{a_*}{a_0}\right)^4\left(\frac{H_0}{H_*}\right)^2 = 1.67\times 10^{-5}\,h^{-2}\left(\frac{100}{g_*}\right)^{\frac{1}{3}}\Omega_{\text{GW},*}\,. \tag{9.26}$$

9.4. First-Order Phase Transition Sources of Gravitational Waves

The GW power spectrum of Eq. (9.22) sourced by first-order PTs can be split into three contributions [277]

$$h^2\Omega_{\mathrm{GW}}(f) = h^2\Omega_{\mathrm{Coll}}(f) + h^2\Omega_{\mathrm{SW}}(f) + h^2\Omega_{\mathrm{Turb}}(f) \simeq h^2\Omega_{\mathrm{SW}}(f) + h^2\Omega_{\mathrm{Turb}}(f)\,. \tag{9.27}$$

As already motivated in Section 9.1, we will in this thesis focus on scenarios, with sufficient friction between the bubble wall and the plasma in which a terminal wall velocity v_w is reached. In such scenarios, the plasma sound waves (SW) [39–41] and turbulence in the plasma (Turb) [43] yield the bulk of the GW energy density and gravitational waves from collisions (Coll), cf. e.g. Refs. [42, 44, 45], can be neglected.

The GW power spectrum can be parametrized by the peak amplitude Ω^{peak} of the power spectrum multiplied by spectral functions that depend on the peak frequency f^{peak} [323]

$$h^2\Omega_{\mathrm{GW}}(f) \simeq h^2\Omega^{\mathrm{peak}}_{\mathrm{SW}} \left(\frac{4}{7}\right)^{-\frac{7}{2}} \left(\frac{f}{f^{\mathrm{peak}}_{\mathrm{SW}}}\right)^3 \left[1 + \frac{3}{4}\left(\frac{f}{f^{\mathrm{peak}}_{\mathrm{SW}}}\right)^2\right]^{-\frac{7}{2}} \tag{9.28}$$

$$+ h^2\Omega^{\mathrm{peak}}_{\mathrm{Turb}} \left(\frac{\left(f/f^{\mathrm{peak}}_{\mathrm{Turb}}\right)^3}{\left(1 + f/f^{\mathrm{peak}}_{\mathrm{Turb}}\right)^{11/3} (1 + 8\pi f/H_*)}\right), \tag{9.29}$$

The frequency and amplitude of the peak of the sound wave spectrum are parametrized semi-analytically by the results of a numerical hydrodynamic lattice simulation [277, 324, 325],

$$f^{\mathrm{peak}}_{\mathrm{SW}} = 26 \times 10^{-6} \left(\frac{1}{H_* R}\right) \left(\frac{T_*}{100\,\mathrm{GeV}}\right) \left(\frac{g_*}{100}\right)^{\frac{1}{6}} \mathrm{Hz}\,, \tag{9.30}$$

$$h^2\Omega^{\mathrm{peak}}_{\mathrm{SW}} = 2.061\; h^2 F_{\mathrm{gw},0} \widetilde{\Omega}_{\mathrm{gw}} \frac{2}{\sqrt{3}} (H_* R)^2 K_{\mathrm{SW}}^{\frac{3}{2}} \quad \text{for} \quad \mathrm{H}_*\tau_{\mathrm{sh}} = \frac{2}{\sqrt{3}} \frac{\mathrm{H}_*\mathrm{R}}{\mathrm{K}_{\mathrm{SW}}^{1/2}} < 1\,, \tag{9.31}$$

$$h^2\Omega^{\mathrm{peak}}_{\mathrm{SW}} = 2.061\; h^2 F_{\mathrm{gw},0} \widetilde{\Omega}_{\mathrm{gw}} (H_* R) K_{\mathrm{SW}}^{2} \quad \text{for} \quad \mathrm{H}_*\tau_{\mathrm{sh}} = \frac{2}{\sqrt{3}} \frac{\mathrm{H}_*\mathrm{R}}{\mathrm{K}_{\mathrm{SW}}^{1/2}} \simeq 1\,, \tag{9.32}$$

$$F_{\mathrm{gw},0} = \Omega_{\mathrm{rad}} \left(\frac{h_0}{h_*}\right)^{\frac{4}{3}} \frac{g_*}{g_0} \approx (3.57 \pm 0.05) \times 10^{-5} \left(\frac{100}{h_*}\right)^{\frac{1}{3}}, \tag{9.33}$$

with the fluid turnover or shock formation time τ_{sh}, $\widetilde{\Omega}_{\mathrm{gw}} = 0.012$ and the effective entropy degrees of freedom at the transition temperature, h_*, and today at T_0, h_0. We assume that $h_* \approx g_*$ and $h_0 \approx g_0$. The kinetic energy fraction for sound waves K_{SW} is defined following Eq. (9.10) with the efficiency factor κ_{SW} derived in Ref. [273], as discussed in Section 9.1. The mean bubble separation R is defined by

$$H_* R = \frac{H_*}{\beta} (8\pi)^{\frac{1}{3}} \max\left(v_w, c_s\right)\,. \tag{9.34}$$

The speed of sound is denoted by $c_s = 1/\sqrt{3}$, see Section 9.1 for a discussion. Numerical fits of the turbulence GW spectrum yield the peak frequency and amplitude [43]

$$f^{\mathrm{peak}}_{\mathrm{Turb}} = 7.909 \times 10^{-5} \left(\frac{1}{H_* R}\right) \left(\frac{T_*}{100\,\mathrm{GeV}}\right) \left(\frac{g_*}{100}\right)^{\frac{1}{6}} \mathrm{Hz}\,, \tag{9.35}$$

$$h^2\Omega^{\mathrm{peak}}_{\mathrm{Turb}} = 1.144 \times 10^{-4} \left(\frac{100}{g_*}\right)^{\frac{1}{3}} (H_* R) K_{\mathrm{Turb}}^{\frac{3}{2}}\,, \tag{9.36}$$

with the kinetic energy fraction K_{Turb} defined as in Eq. (9.10) with the efficiency factor

$$\kappa_{\mathrm{Turb}} \equiv 0.1\, \kappa_{\mathrm{SW}} \,. \tag{9.37}$$

All above mentioned GW spectrum formula in terms of the characteristic parameters, that were defined in Section 9.1, were implemented in the public code `BSMPTv3` [66].

9.5. Experimental Search Program

The experimental measurement of the stochastic GW background enables a pioneering view on the early universe. In this section we want to briefly summarize some ongoing search programs, their different strategies and obtained results. In Figure 9.1 the sensitivities of some of the below-mentioned detectors are visualized.

In 2015, a gravitational wave, `GW150914`, was detected for the first time by a correlated measurement at both sites of the Laser Interferometer Gravitational-Wave Observatory (LIGO) by the Virgo and LIGO collaborations [326], confirming the prediction of gravitational waves in general relativity.[6] Since 2015, many more gravitational waves of different origins were detected using data correlations of Virgo (Italy) and LIGO (US). Their results of their first three runs are categorized in a set of Gravitational-Wave Transient Catalogs [327–329], also together with the underground interferometer Kamioka Gravitational Wave Detector (KAGRA) [330–333] (Japan), and also joint with GEO600 [334–338] (Germany). The next generation of ground-based GW observatories that are panned, are the Einstein Telescope (ET) in Europe [339] and the Cosmic Explorer (CE) in the US [340].

The setup of the (under)ground-based GW detectors follows the principles of a Michelson interferometer. A laser beam is reflected at the end-points of two same-size orthogonal arms with lengths $\mathcal{O}(\mathrm{km})$. A passing gravitational wave induces a length difference of the arms proportional to its amplitude that is then measured as a phase difference of the two laser beams. This detector type is most sensitive in the Hz–kHz frequency band.

In order to go to lower frequencies of order mHz, the order of frequencies of a stochastic GW background emitted e.g. in gravitational waves of first-order electroweak PTs, longer arm lengths are required. They are planned to be realized by a set of space-based interferometers. The first one planned to be launched is the Laser Interferometer Space Antenna (LISA) [341–344] by NASA and ESA. LISA is planned to launch in 2035 and will be operating as a Michelson interferometer with three spacecrafts organized in an equilateral triangle with arms of a length of $2.5 \times 10^6\,\mathrm{km}$. Its mission is planned to be supported by e.g. the DECi-hertz Interferometer Gravitational wave Observatory (DECIGO) [345]. As a future successor to LISA, the Big Band Observer (BBO) [346], is planned.

The first evidence of a stochastic GW background in the nHz-frequency range was published in 2023 by the pulsar-timing array experiment NANOGrav (North American Nanohertz Observatory for Gravitational Waves) [46–50] as part of the collaboration of the International Pulsar Timing Array (IPTA) [347] consisting of the European Pulsar Timing Array together with the Indian Pulsar Timing Array [348] and the Parkes Pulsar Timing Array [349]. The measured GW background can be explained by astronomical sources such as supermassive black hole binaries [48], but also by cosmological sources including e.g. domain walls and first-order PTs, as presented in Ref. [47]. In pulsar-timing array experiments, pulsars, rotating neutron stars that emit jets of electromagnetic radiation, are used as reference clocks

---

[6] Moreover, `GW150914` agrees with the theoretical prediction for the GW emission by a binary black hole merger. Its observation is also the first-ever observation of a binary black hole merger event [326].

and gravitational waves are inferred from deviations in their pulse arrival times, based on the works of e.g. Refs. [350–352].

In this thesis, we investigate gravitational waves sourced by first-order PTs that constitute a stochastic GW background with peak frequencies in the mHz range. Therefore, the space-based interferometer experiments will be most sensitive to their spectra. In the following, we will focus on the detection potential for gravitational waves sourced by first-order PTs of LISA, as it is not only the first-to-be launched space-based experiment, but also, compared to the other experiments, has the highest expected sensitivity in the mHz-range, as illustrated in Fig 9.1. The detection potential of LISA of a predicted gravitational wave is characterized by the signal-to-noise ratio (SNR). The SNR is a measure for the detectability of a GW signal with amplitude $h^2\Omega_{\text{GW}}$ given an experimental sensitivity $h^2\Omega_{\text{Sens}}$ in a frequency range $f_{\text{min}} \leq f \leq f_{\text{max}}$, to which the experiment is sensitive, given a data acquisition time $\mathcal{T}$,

$$\text{SNR}(\mathcal{T}) = \sqrt{\mathcal{T} \int_{f_{\text{min}}}^{f_{\text{max}}} \mathrm{d}f \left[\frac{h^2\Omega_{\text{GW}}(f)}{h^2\Omega_{\text{Sens}}(f)}\right]^2} \,. \tag{9.38}$$

Given the expected data acquisition time of LISA of 4 yrs with a minimum duty cycle of 75 % [353], we take $\mathcal{T} = 4\,\text{yrs} \cdot 75\,\% = 3\,\text{yrs}$ for the calculation of the SNR implemented in `BSMPTv3`.[7] The sensitivity of LISA is written as a function of the power spectral density $S_h(f)$, given by the mission requirements [277, 353, 354], as

$$\Omega_{\text{Sens}}(f) = \frac{4\pi^2}{3H_0^2} f^3 S_h(f) \,. \tag{9.39}$$

As described further in Chapter 3, we take the value measured by Planck for the Hubble constant of today $H_0 = (67.4 \pm 0.5)\,\text{km/s/Mpc}$ [21]. A GW signal is within sensitivity of LISA, if $\text{SNR} > 1$. However, in order for it to be detectable independent of a potentially underestimated experimental noise, we consider it to be detectable if it gives rise to $\text{SNR} > 10$.

---

[7] The result obtained for the SNR with `BSMPTv3` which assumes $\mathcal{T} = 3\,\text{years}$ can be rescaled to obtain any value of $\mathcal{T}$ by $\text{SNR}(\mathcal{T}) = \sqrt{\frac{\mathcal{T}}{3}}\text{SNR}(3\,\text{yrs})$.

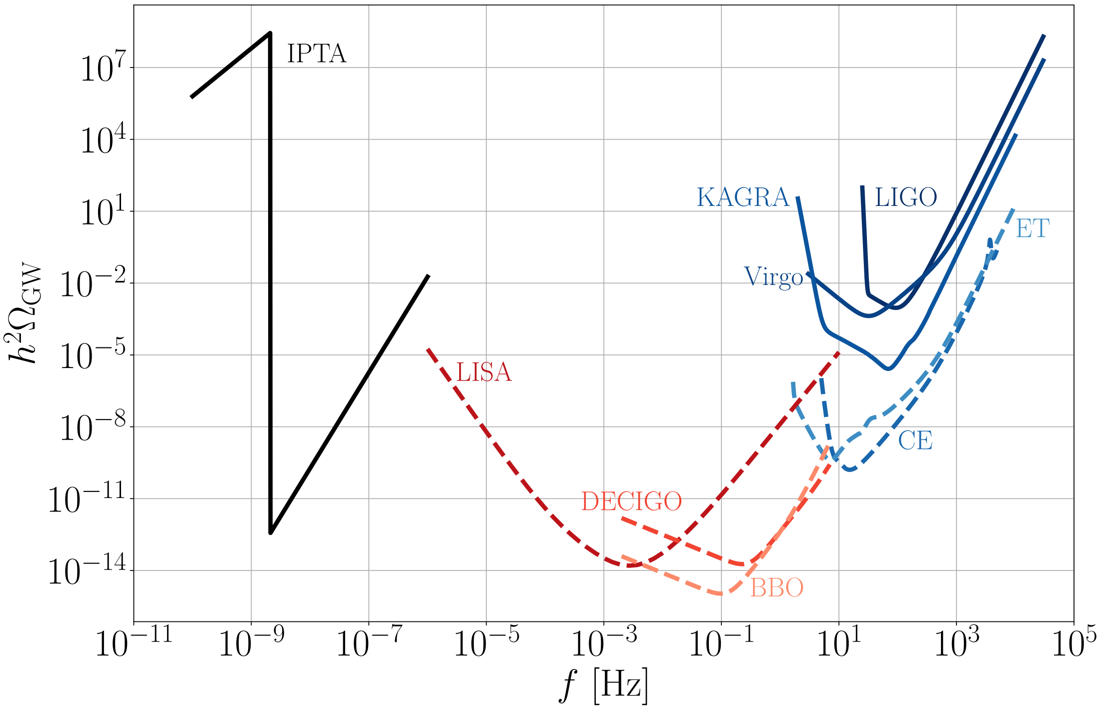

Figure 9.1.: Gravitational wave detector sensitivity curves in the GW amplitude versus GW frequency plane. The sensitivity of the pulsar-timing array experiment is depicted with a black curve, the sensitivities of space-bound interferometers are displayed with red and the sensitivities of ground-based experiments with blue curves, respectively. Solid lines are currently operating experiments, dashed lines are planned experiments. All experiments are further described in the text. This figure uses data provided by Refs. [315, 355], and the latest data for the LISA sensitivity curve from Refs. [277, 325, 356].

CHAPTER 10

Charge-Breaking Phase Transitions in the Two-Higgs-Doublet Model

The origin of cosmic magnetic fields is still an open question [357–359] and aside from plasma turbulence, which leads to magneto-hydrodynamic turbulence, during a first-order PT [43, 360, 361] also an intermediate period of electromagnetic charge violation could provide a production mechanism. Models with extended scalar sectors can exhibit complicated multi-step phase transition histories, cf. e.g. Refs. [209, 362–370]. In the following, we will discuss transition histories with several phases. The nomenclature for phases depending on their characteristic features is summarized in Sec 4.5. An interesting multi-step transition history with an intermediate *charge-breaking* (CB) phase in a BSM model can proceed via the following steps

$$\underbrace{\overline{\omega}_{\text{EW}} = 0, \overline{\omega}_{\text{CB}} = 0}_{\substack{\text{EW symmetric,}\\ \text{neutral phase}}} \xrightarrow{T \searrow} \underbrace{\overline{\omega}_{\text{EW}} \neq 0, \overline{\omega}_{\text{CB}} \neq 0}_{\substack{\text{EW broken,}\\ \textbf{CB phase}}} \xrightarrow{T \searrow} \underbrace{\overline{\omega}_{\text{EW}} \neq 0, \overline{\omega}_{\text{CB}} = 0}_{\substack{\text{EW broken,}\\ \text{neutral phase}}} . \tag{10.1}$$

In a CB phase, the $U(1)_{\text{EM}}$ is broken by the VEVs, i.e. for the $\mathcal{CP}$-conserving 2HDM in our notation outlined in Section 6.1, this corresponds to $\overline{\omega}_{\text{CB}} \neq 0$. Consequently, the electromagnetic gauge boson, the photon, becomes massive and electric charge is no longer conserved, leading e.g. to mixing between the formerly charged leptons and neutrinos.

The 2HDM is the simplest possible BSM model that allows for intermediate CB phases. The real 2HDM allows for CB, neutral $\mathcal{CP}$-violating, and neutral $\mathcal{CP}$-conserving vacua. Because both, the CB and the $\mathcal{CP}$-violating VEV contribute to the EW VEV, defined in Eq. (6.6), the EW symmetry is broken if one of them is non-zero. At zero temperature, it was shown that an existing neutral $\mathcal{CP}$-conserving electroweak broken vacuum must always be a global minimum [371, 372], rendering any additionally existing CB or $\mathcal{CP}$-violating minima non-global. Although theoretically in a 2HDM, a lower, neutral $\mathcal{CP}$-conserving electroweak broken vacuum with $v_{\text{EW}} \neq 246\,\text{GeV}$ can exist [373–375], its existence is ruled out as discussed by Refs. [376, 377] when taking into account LHC bounds. At finite temperature, a vastly diverse landscape of minima of the scalar potential can evolve.

In Section 10.1, we briefly summarize the results of our work in Ref. [378] on intermediate CB minima in the type-1, $\mathcal{CP}$-conserving 2HDM as introduced in Section 6.1. Furthermore, in Section 10.2 and 10.3 we go beyond the study of Ref. [378] by calculating EWPTs with intermediate CB phases, using `BSMPTv3`. We focus on a study of EWPTs for two exemplary benchmark points with CB phases in Section 10.2. This study with `BSMPTv3` was presented in Ref. [66]. We conclude this chapter in Section 10.3 with an analysis of the EWPTs of the full sample of points that exhibit intermediate CB phases generated for Ref. [378], using `BSMPTv3`. We furthermore present calculated SNRs for first-order EWPTs with intermediate CB phases.

10.1. Charge-Breaking Phases in the Two-Higgs-Doublet Model

Using an approximation for the high-temperature behaviour, in which the temperature corrections are absorbed into modified quadratic mass parameters of the tree-level potential, $m_{ii}^2 \to m_{ii}^2 + c_i T^2$ with $i \in \{1, 2\}$, the authors of Refs. [209, 379] showed that transition histories involving intermediate CB phases are possible in the 2HDM. Based on CB seed points generated via the high-temperature approximation, we extended the study of Refs. [209, 379] in Ref. [378] by showing that parameter regions that allow for global intermediate CB minima exist also beyond the high-temperature approximation in the finite-temperature effective potential with one-loop corrections and daisy resummation. We check for agreement with theoretical and experimental constraints using `ScannerS`, as detailed in Section 5.1, and further require zero-temperature absolute vacuum stability at NLO using `BSMPTv2`, as described in Section 5.2. We then calculate the temperature evolution of the global minimum for the valid points with `BSMPTv2`. We find theoretically and experimentally valid points with intermediate CB phases for scenarios with large scalar quartic couplings, $4 \lesssim |\lambda_{\text{max}}| \lesssim 8$, and low charged Higgs boson masses, $m_{H^\pm} \lesssim 210\,\text{GeV}$. Experimental constraints for the type-1 2HDM, on the one hand, limit the allowed range for charged scalar masses for which intermediate CB minima appear to $100\,\text{GeV} \lesssim m_{H^\pm}$. Here, we find that using the one-loop resummed effective potential helps fulfilling the lower bound on the charged scalar mass, as the full one-loop treatment allows intermediate CB minima up to $m_{H^\pm} \lesssim 210\,\text{GeV}$, while the high-temperature approximation can only realize CB phases with $m_{H^\pm} \lesssim 100\,\text{GeV}$, which is ruled out by experiment. However, this consequently means that type-2 2HDM parameter points are ruled out w.r.t. the ability to generate an intermediate CB minimum, as here the experimental lower limit on the charged scalar mass is above 800 GeV [166–169]. On the other hand, large quartic scalar couplings are in conflict with electroweak symmetry restoration at high temperatures. We find no intermediate CB point that is experimentally valid and has high-temperature electroweak symmetry restoration. We find, however, experimentally valid intermediate CB points with a period of intermediate EWSR. Any EWSR period followed by a strong first-order EWPT can possibly yield the initial conditions for successful EWBG, cf. Chapter 3.

On the side of collider phenomenology, the parameter space of intermediate CB points can be probed for in decays of the heavy Higgs boson. As most intermediate CB points of our sample are characterized by $\lambda_4 \approx \lambda_5$, the $\mathcal{CP}$-odd neutral scalar mass m_A and the charged scalar mass $m_{H^\pm}$ are almost degenerate, while the heavy $\mathcal{CP}$-even neutral mass m_H is heavier by $\sim 100\,\text{GeV}$. This mass spectrum favours decays of a H into a scalar boson plus vector boson pair, $H \to AZ$ or $H \to H^\pm W^\mp$. Experimental searches for AZ, cf. e.g. Refs. [380, 381], and searches for $H^\pm W^\mp$ could therefore specifically test this parameter space.

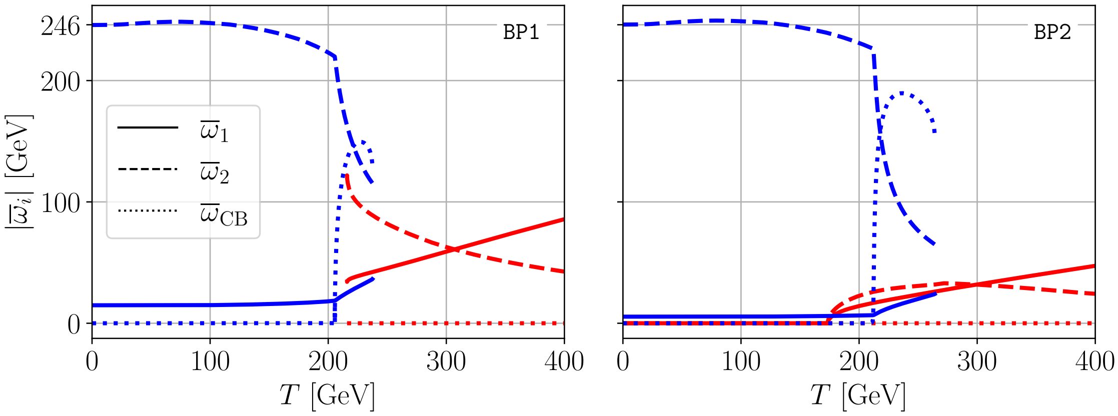

Figure 10.1.: Phases for BP1 (left) and BP2 (right) tracked with `BSMPTv3` in the temperature range $T \in [0, 400]$ GeV. The high-temperature phase is coloured in red, the low-temperature phase in blue. Coordinates of $\overline{\omega}_1$ are marked by solid lines, $\overline{\omega}_2$ by dashed lines and $\overline{\omega}_{\text{CB}}$ by dotted lines. The vacuum coordinate of the $\mathcal{CP}$-violating VEV is zero for the whole temperature range for both points, $\overline{\omega}_{\text{CP}} = 0$. The low-temperature phase contains a continuous transition between the intermediate CB phase and the low-temperature neutral phase.

10.2. Phase Transition Analysis for Benchmark Points

Having shown the existence of global CB minima in the one-loop and daisy-resummed effective potential at finite temperatures for the type-1, $\mathcal{CP}$-conserving 2HDM with a softly-broken $\mathbb{Z}_2$ symmetry, we will discuss in the following whether such CB minima can play a role in the transition history of the early universe. Using `BSMPTv3`, cf. Chapter 7, we will therefore investigate whether first-order EWPTs from a neutral to a CB phase (or vice-versa) can take place in the early universe. For this we consider two benchmark points that were already studied in detail in Ref. [378]. These are benchmark point BP1, defined as

$$\begin{aligned}\text{BP1:} \quad & \text{type} = 1\,,\ \lambda_1 = 6.931\,,\ \lambda_2 = 0.263\,,\ \lambda_3 = 1.287\,,\ \lambda_4 = 4.772\,,\ \lambda_5 = 4.728\,,\\ & m_{12}^2 = 1.893 \times 10^4\,\text{GeV}^2\,,\ \tan\beta = 16.578\,, \end{aligned} \tag{10.2}$$

and benchmark point BP2, given by

$$\begin{aligned}\text{BP2:} \quad & \text{type} = 1\,,\ \lambda_1 = 6.846\,,\ \lambda_2 = 0.259\,,\ \lambda_3 = 1.466\,,\ \lambda_4 = 4.498\,,\ \lambda_5 = 4.450\,,\\ & m_{12}^2 = 6.630 \times 10^3\,\text{GeV}^2\,,\ \tan\beta = 45.320\,. \end{aligned} \tag{10.3}$$

We trace all phases for these points using the code `BSMPTv3` and find a phase structure in agreement with the global minimum evolution that we found using `BSMPTv2` [378], as presented in Ref. [66]. In Figure 10.1, we illustrate the result of the phase tracing. For both points, we find a neutral high-temperature phase with $\overline{\omega}_1 \neq 0$ and $\overline{\omega}_2 \neq 0$ (red lines). We furthermore find an intermediate CB phase (blue dotted line) that transitions continuously to the electroweak broken neutral phase that leads to the electroweak minimum at $T = 0$ GeV. We then calculate the bounce solution and characteristic temperature scales for the overlap between the neutral phase at high temperature and the CB phase at low temperature for both points. We find for both of them valid first-order EWPTs. For BP1 we find $T_c = 226.3$ GeV and T_n, T_p and T_f close together around 223 GeV. This corresponds to a first-order EWPT from $\overline{\omega}_{\text{CB}}^{\text{false}} = 0$ GeV to $\overline{\omega}_{\text{CB}}^{\text{true}} = 148$ GeV. The first-order EWPT of BP1 therefore spontaneously violates the $U(1)_{\text{EM}}$ symmetry. This symmetry is then restored around 200 GeV. For BP2 we find $T_c = 231.0$ GeV, $T_n = 203.5$ GeV, $T_p = 199.0$ GeV and $T_f = 198.4$ GeV. While

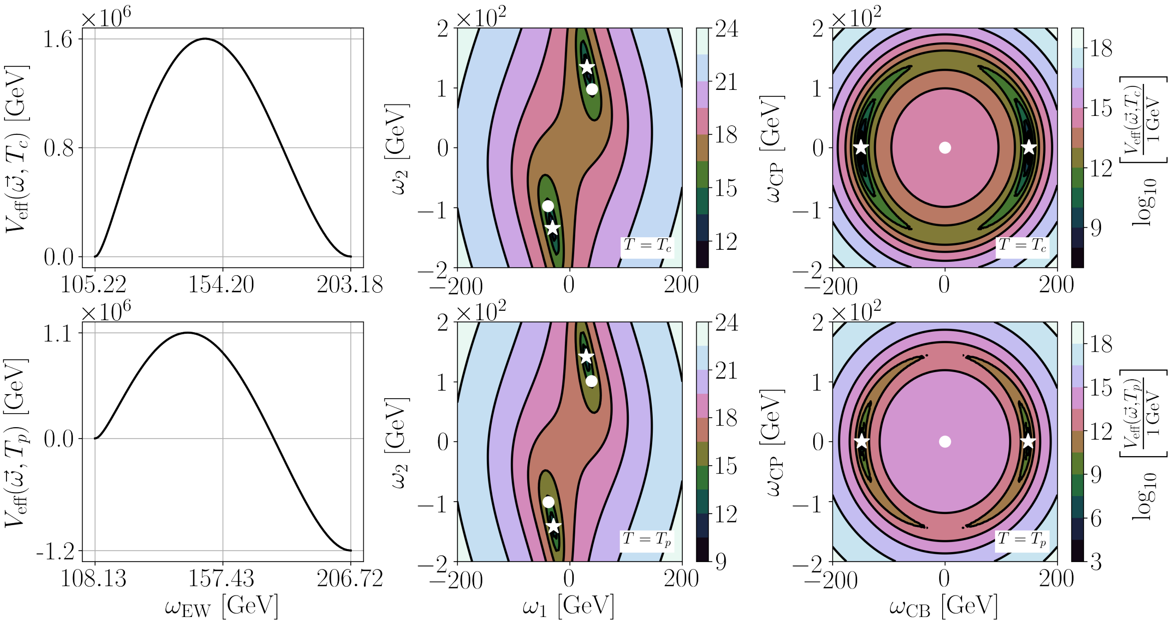

Figure 10.2.: Potential contours for BP1 defined in Eq. (10.2), at the critical temperature T_c (top row) and at the percolation temperature T_p (bottom row). In the left column, one-dimensional slices from the false to the true vacuum versus the coordinate of the electroweak VEV ω_{EW} are illustrated. In the middle column we show the two-dimensional contours in the $(\zeta_1, \zeta_2) \equiv (\omega_1, \omega_2)$-plane, in the right column we show the two-dimensional contours in the $(\rho_2, \psi_2) \equiv (\omega_{\text{CB}}, \omega_{\text{CP}})$-plane, respectively. Field directions not displayed are set to the coordinates of the true minimum. The false (true) minimum is illustrated with a white dot (asterisk). Figure published in Ref. [66].

at T_c the electromagnetic symmetry is violated in the true phase with $\overline{\omega}_{\text{CB}}^{\text{true}} = 188.3\,\text{GeV}$, at T_n, T_p and T_f we find $\overline{\omega}_{\text{CB}}^{\text{true}} = 0\,\text{GeV}$. The true minimum therefore transitions to the neutral phase before the first-order EWPT in BP2 takes place. Consequently, even though a global CB minimum exists in an intermediate temperature region for BP2, no significant fraction of the universe will transition into it and the CB phase cannot leave an imprint on the cosmological history.

In Figures 10.2 (for BP1) and 10.3 (for BP2) we illustrate potential contours for both points at the critical (top row) and percolation temperature (bottom row). In the respective left columns of the figures, we illustrate the degeneracy of true and false minima at $T = T_c$ and the lower true minimum at $T = T_p$. The middle columns display the two-dimensional potential contours in the $(\zeta_1, \zeta_2) \equiv (\omega_1, \omega_2)$-plane. The position of the false (true) minima are marked with a white dot (asterisk). For BP1 and BP2, the false and true minima at T_c and T_p are close together, in accordance with Figure 10.1. In the respective right-most columns, we show two-dimensional potential contours in the $(\rho_2, \psi_2) \equiv (\omega_{\text{CB}}, \omega_{\text{CP}})$-plane. As both points are characterized by $\lambda_4 \approx \lambda_5$, the potential is almost invariant under change of $(\omega_{\text{CB}}^2 + \omega_{\text{CP}}^2)$. At the critical temperature, the near degeneracy of λ_4 and λ_5 leads to a minimum in the $(\omega_{\text{CB}}, \omega_{\text{CP}})$-plane in form of a slightly dented ring in favour of $\overline{\omega}_{\text{CB}} \neq 0$ for both points, while $\overline{\omega}_{\text{CP}} = 0\,\text{GeV}$ for the whole temperature range. At the percolation temperature, this ring still exists for BP1, and the true minimum lies at $\overline{\omega}_{\text{CB}} \neq 0$. For BP2, the ring has contracted onto $\overline{\omega}_{\text{CP}} = \overline{\omega}_{\text{CB}} = 0$ and consequently, the true phase is no longer a CB phase.

To conclude, intermediate CB minima are possible in a type-1, $\mathcal{CP}$-conserving 2HDM with a softly-broken $\mathbb{Z}_2$ symmetry. The analysis of the benchmark points, however, shows that a detailed calculation of transition rates between false and true phases is inevitable to be able

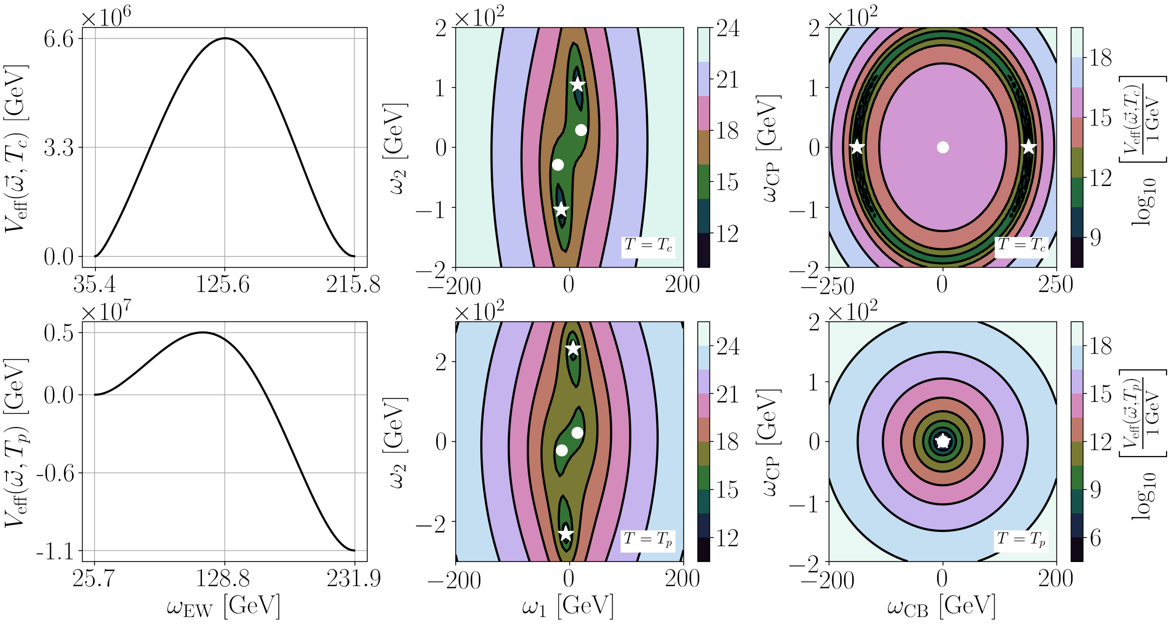

Figure 10.3.: Potential contours for BP2 defined in Eq. (10.3), with the same panels as in Figure 10.2. Figure published in Ref. [66].

to judge if an intermediate CB phase is populated by a significant vacuum fraction during the temperature evolution of the universe.

10.3. Phase Transition Analysis for Point Sample

After looking at these two benchmark points in detail, we perform a calculation of the first-order EWPTs with `BSMPTv3` for the complete point sample of Ref. [378], for which the existence of finite-temperature global CB minima was found with `BSMPTv2`.[1] For each point of the sample, we trace its minima in the range $T \in [0, 1]\,\text{TeV}$, identify overlaps between phases and calculate transition rates for overlaps. For first-order EWPTs, we then derive the characteristic temperatures and the GW spectrum and evaluate the SNR for a three-year data acquisition period at the LISA experiment.

In Figure 10.4 we illustrate the results. We show all points that are confirmed to have an intermediate CB phase with the new phase identification and tracing algorithms of `BSMPTv3` as magenta stars in the two-dimensional plane spanned by the absolute value of the maximal quartic coupling $|\lambda_{\rm max}|$ versus the value of the charged scalar mass $m_{H^\pm}$. The results obtained with `BSMPTv3` are in accordance with the overall results that were obtained by the global minimum search performed with `BSMPTv2` for Ref. [378]. We confirm finding points with intermediate CB phases for $4.8 \lesssim |\lambda_{\rm max}| \lesssim 8$ and $130\,\text{GeV} \lesssim m_{H^\pm} \lesssim 210\,\text{GeV}$.

In Figure 10.4 (top), we display by coloured dots the points for which we find completing first-order EWPTs in addition to an intermediate CB phase. These points have $6.4 \lesssim |\lambda_{\rm max}| \lesssim 7.7$ and $130\,\text{GeV} \lesssim m_{H^\pm} \lesssim 190\,\text{GeV}$, and, as a subset of the magenta points, align with the results of Ref. [378]. The coloured dots have a completing first-order EWPT from a neutral false phase to a CB true phase with a value of $|\overline{\omega}_{\rm CB}^{\rm true}(T_f)| > 0$ of the true phase indicated by the colour code. The transition history of the points illustrated by the coloured dots is therefore similar to the one of BP1. The black squares are points with an intermediate CB true phase that, however, transitions to a neutral true phase before the first-order EWPT

---

[1] Details on `BSMPT` and the differences between its versions can be found in Section 5.2 and in Chapter 7.

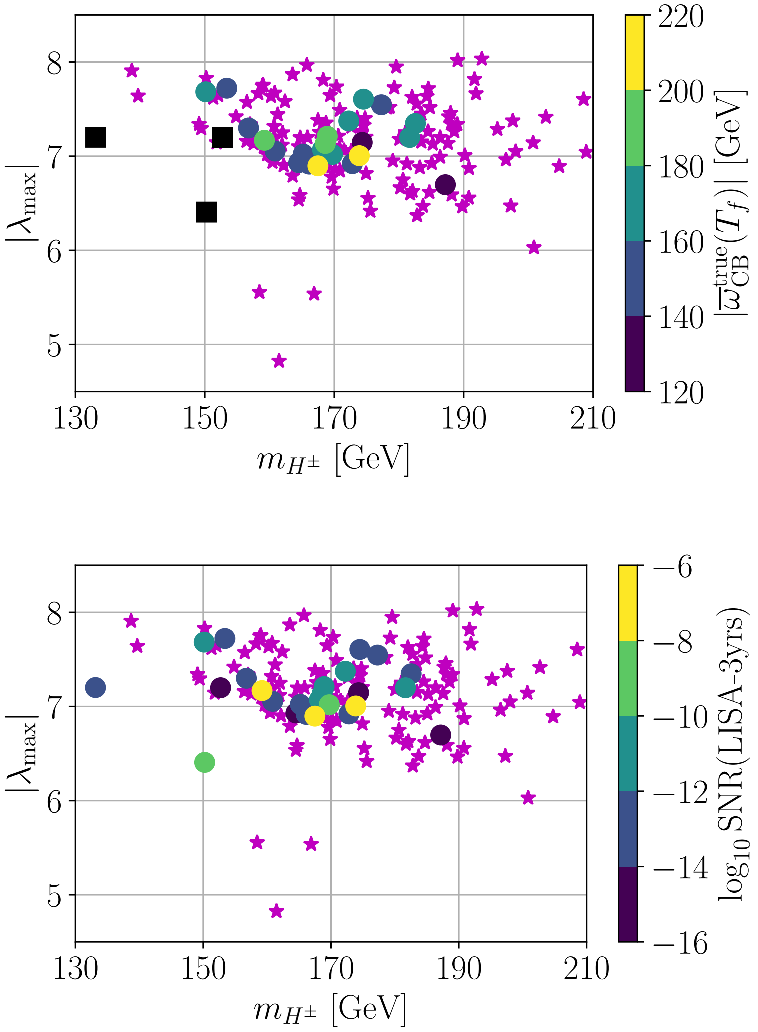

Figure 10.4.: Results of the EWPT calculation for the CB sample generated in Ref. [378] using `BSMPTv3`. Displayed as magenta stars are points where we identify intermediate CB phases in the parameter plane spanned by the maximal absolute quartic coupling $|\lambda_{\mathrm{max}}|$ versus the charged scalar mass $m_{H^\pm}$. The coloured points that are displayed on top of the magenta stars indicate points for which in addition to an intermediate CB phase we find completing first-order EWPTs. The colour of the overlaying points indicates the size of $\overline{\varpi}_{\mathrm{CB}}^{\mathrm{true}}(T_f)$ of the true vacuum (top) as well as the SNR at LISA with a three-year data acquisition period (bottom), calculated assuming radiation domination. The black squares in the top figure mark points for which $|\overline{\varpi}_{\mathrm{CB}}^{\mathrm{true}}(T_f)| < 1\,\mathrm{GeV}$ and therefore the $U(1)_{\mathrm{EM}}$ is already restored when the first-order EWPT completes.

from a neutral false phase takes place, i.e. they show transition histories similar to the one of BP2. Therefore, in the full CB-point sample, we find versions of the transition history of BP1 and BP2. However, only histories similar to BP1, in Figure 10.4 displayed by the coloured dots, can potentially imprint their CB properties on the cosmological history of the universe.

With `BSMPTv3` we furthermore calculate the SNR at LISA with a three-year data acquisition period for gravitational waves sourced by first-order EWPTs. Under the assumption that the universe is radiation-dominated at the percolation temperature,[2] we calculate $10^{-16} < \text{SNR(LISA-3yrs)} < 10^{-6}$ for the points for which we find first-order EWPTs with an intermediate CB phase. In Figure 10.4 (bottom), we show the SNR at LISA as colour code of these points. Due to $\text{SNR(LISA-3yrs)} < 10^{-6}$, gravitational waves of the displayed points will escape detection at LISA.

10.4. Conclusions

In this chapter we showed the possibility of first-order EWPT with intermediate CB in a type-1, $\mathcal{CP}$-conserving 2HDM with a softly-broken $\mathbb{Z}_2$ symmetry. We found first-order EWPTs from a neutral to a CB phase that transitions continuously at a lower temperature into the neutral phase of today. We furthermore calculated the gravitational waves associated with such CB first-order EWPTs. The SNRs that we identified for the first-order EWPT points of our CB sample are too low to be in the sensitivity range of LISA. However, we note that this may be merely a result of our sparse point sample and that no general phenomenological statement can be drawn from this observation. Moreover, even in our sparse CB first-order EWPT point sample, we found SNRs spanning over ten orders of magnitude, with larger $|\overline{\omega}_{\text{CB}}^{\text{true}}(T_f)|$ correlated with higher SNRs. This clearly shows the potential of gravitational waves being amplified by strong first-order EWPTs. As the size of $|\overline{\omega}_{\text{CB}}^{\text{true}}(T_f)| > 0$ directly drives the strength of the first-order EWPT, a more detailed parameter scan in the discussed parameter regions might well reveal strong first-order EWPTs with spontaneous CB that source gravitational waves which are in the detectable range of future space-bound interferometers, such as LISA.

We further note, that the impact of the CB phase on the energy density of the universe adds to the existing theoretical uncertainties of the GW calculation, consisting of e.g. the determination of the wall velocity. A consistent treatment of the change in the energy density content of the universe during a first-order EWPT into a CB phase would be desirable, and is left for future work. The presented SNRs already illustrate the potential of first-order EWPTs into CB phases to also source gravitational waves with large ranges of possible SNRs.

---

[2] The first-order EWPTs that are under investigation here, take place from a neutral false phase to a CB true phase at the percolation temperature $T_* = T_p$, where 71 % of the universe is still in the false radiation-dominated phase.

CHAPTER 11

Phase Transitions in 'CP in the Dark'

In this chapter we discuss a specific N2HDM extension of the SM, named 'CP in the Dark' [178, 382–384]. We focus on its ability to facilitate a one-step first-order EWPT and source gravitational waves. We furthermore show the possible transition histories. The characteristic feature of this model is the possibility of $\mathcal{CP}$ violation that is not in tension with the EDM bounds [171], as will be elaborated below, as its $\mathcal{CP}$ violation resides in the dark sector. $\mathcal{CP}$ violation in the dark sector has also been studied in the literature, e.g. for a 2HDM plus real singlet and real triplet field in Refs. [385, 386], named *partially secluded* $\mathcal{CP}$ violation, where the authors showed that the BAU can be generated and transferred to the EW broken phase of today in a two-step PT.

The model 'CP in the Dark' has a scalar sector extended by an additional doublet Φ_2 and a real singlet Φ_S with an imposed $\mathbb{Z}_2$ symmetry,

$$\Phi_1 \to \Phi_1\,, \quad \Phi_2 \to -\Phi_2\,, \quad \Phi_S \to -\Phi_S\,. \tag{11.1}$$

The fermion fields are assumed to be invariant under the $\mathbb{Z}_2$ symmetry. Therefore, only the first doublet Φ_1 couples to fermions, the Yukawa sector is identical to the SM Yukawa sector, and tree-level FCNCs are prohibited. The $SU(2)_L \times U(1)_Y$ and $\mathbb{Z}_2$-invariant tree-level potential of 'CP in the Dark' reads

$$\begin{aligned} V^{(0)} \;=\; & m_{11}^2|\Phi_1|^2 + m_{22}^2|\Phi_2|^2 + \frac{m_S^2}{2}\Phi_S^2 + \left(A\Phi_1^\dagger\Phi_2\Phi_S + A^*\Phi_2^\dagger\Phi_1\Phi_S\right) \\ & + \frac{\lambda_1}{2}|\Phi_1|^4 + \frac{\lambda_2}{2}|\Phi_2|^4 + \lambda_3|\Phi_1|^2|\Phi_2|^2 + \lambda_4|\Phi_1^\dagger\Phi_2|^2 + \frac{\lambda_5}{2}[(\Phi_1^\dagger\Phi_2)^2 + (\Phi_2^\dagger\Phi_1)^2] \\ & + \frac{\lambda_6}{4}\Phi_S^4 + \frac{\lambda_7}{2}|\Phi_1|^2\Phi_S^2 + \frac{\lambda_8}{2}|\Phi_2|^2\Phi_S^2\,. \end{aligned} \tag{11.2}$$

While λ_5 can be chosen real without loss of generality, by absorbing its complex phase into a redefinition of the doublets, the trilinear coupling A is in general complex. The finite-temperature vacuum structure is defined by taking into account the neutral $\mathcal{CP}$-even doublet and singlet VEVs, $\overline{\omega}_{1,2}$ and $\overline{\omega}_S$, respectively, as well as the $\mathcal{CP}$-violating ($\overline{\omega}_{\text{CP}}$) and the charge-breaking ($\overline{\omega}_{\text{CB}}$) VEV

$$\Phi_1 = \frac{1}{\sqrt{2}}\begin{pmatrix}\rho_1 + i\eta_1 \\ \zeta_1 + \overline{\omega}_1 + i\Psi_1\end{pmatrix}, \; \Phi_2 = \frac{1}{\sqrt{2}}\begin{pmatrix}\rho_2 + \overline{\omega}_{\text{CB}} + i\eta_2 \\ \zeta_2 + \overline{\omega}_2 + i(\Psi_2 + \overline{\omega}_{\text{CP}})\end{pmatrix}, \; \Phi_S = \zeta_S + \overline{\omega}_S\,, \tag{11.3}$$

introducing the charged $\mathcal{CP}$-even fields ρ_i, charged $\mathcal{CP}$-odd fields η_i, neutral $\mathcal{CP}$-even fields ζ_i, ζ_S and neutral $\mathcal{CP}$-odd fields Ψ_i $(i = 1, 2)$. To be as general as possible, we allow for $\overline{\omega}_{\text{CB}}$, find however, that numerically, $\overline{\omega}_{\text{CB}}$ is zero for all parameter points discussed below. The zero-temperature minimum conserves the $\mathbb{Z}_2$ symmetry,

$$\langle\Phi_1\rangle|_{T=0\,\text{GeV}} = \frac{1}{\sqrt{2}}\begin{pmatrix}0\\ v_1\end{pmatrix}, \; \langle\Phi_2\rangle|_{T=0\,\text{GeV}} = \frac{1}{\sqrt{2}}\begin{pmatrix}0\\ 0\end{pmatrix}, \; \langle\Phi_S\rangle|_{T=0\,\text{GeV}} = 0\,, \tag{11.4}$$

with

$$\overline{\omega}_1\big|_{T=0\,\text{GeV}} \equiv v_1 \equiv v_{\text{EW}} = 246\,\text{GeV}\,. \tag{11.5}$$

Therefore, at $T = 0\,\text{GeV}$, there is a conserved quantum number, named *dark charge*, associated with the exact $\mathbb{Z}_2$ symmetry. The first doublet is SM-like with dark charge +1. Its neutral $\mathcal{CP}$-even mass eigenstate is the SM-like Higgs boson h. The second doublet and real singlet form a *dark sector* with dark charge −1. The neutral fields ζ_2, Ψ_2 and ζ_S mix with a mixing matrix given by

$$M_N^2 = \begin{pmatrix} m_{22}^2 + \frac{v_1^2}{2}\lambda_{345} & 0 & \text{Re}\,(A)v_1 \\ 0 & m_{22}^2 + \frac{v_1^2}{2}\overline{\lambda}_{345} & -\text{Im}\,(A)v_1 \\ \text{Re}\,(A)v_1 & -\text{Im}\,(A)v_1 & m_S^2 + \frac{v_1^2}{2}\lambda_7 \end{pmatrix}, \tag{11.6}$$

where $\lambda_{345} \equiv \lambda_3 + \lambda_4 + \lambda_5$ and $\overline{\lambda}_{345} \equiv \lambda_3 + \lambda_4 - \lambda_5$. The mass eigenstates are derived via diagonalization with a rotation matrix R that is parametrized in terms of three mixing angles α_i, $i = 1, 2, 3$,

$$R = \begin{pmatrix} c_{\alpha_1}c_{\alpha_2} & s_{\alpha_1}c_{\alpha_2} & s_{\alpha_2} \\ -(c_{\alpha_1}s_{\alpha_2}s_{\alpha_3} + s_{\alpha_1}c_{\alpha_3}) & c_{\alpha_1}c_{\alpha_3} - s_{\alpha_1}s_{\alpha_2}s_{\alpha_3} & c_{\alpha_2}s_{\alpha_3} \\ -c_{\alpha_1}s_{\alpha_2}c_{\alpha_3} + s_{\alpha_1}s_{\alpha_3} & -(c_{\alpha_1}s_{\alpha_3} + s_{\alpha_1}s_{\alpha_2}c_{\alpha_3}) & c_{\alpha_2}c_{\alpha_3} \end{pmatrix}, \tag{11.7}$$

so that

$$\text{diag}(m_{h_1}^2, m_{h_2}^2, m_{h_3}^2) = R M_N^2 R^T\,. \tag{11.8}$$

By convention, the masses are ordered, $m_{h_1} < m_{h_2} < m_{h_3}$. The dark sector consists of a pair of dark charged scalars $H^\pm$ and three neutral dark scalars h_i, $i \in \{1, 2, 3\}$. The lightest neutral dark scalar, h_1, is a stable dark matter candidate.

The model 'CP in the Dark' exhibits *explicit* $\mathcal{CP}$ violation in the dark sector [382]. Under $\mathcal{CP}$, the complex scalar doublets and the real scalar singlet transform as

$$\Phi_1(t,\vec{x}) \xrightarrow{\mathcal{CP}} \Phi_1^*(t,-\vec{x}), \quad \Phi_2(t,\vec{x}) \xrightarrow{\mathcal{CP}} \Phi_2^*(t,-\vec{x}), \quad \Phi_S(t,\vec{x}) \xrightarrow{\mathcal{CP}} \Phi_S(t,-\vec{x}), \tag{11.9}$$

and the tree-level potential is invariant except for the trilinear term $\propto A$ that transforms as

$$\begin{aligned} T \equiv \left(A\Phi_1^\dagger\Phi_2 + A^*\Phi_2^\dagger\Phi_1\right)\Phi_S &\xrightarrow{\mathcal{CP}} \left(A\Phi_1^T\Phi_2^* + A^*\Phi_2^T\Phi_1^*\right)\Phi_S \\ &= \left(A^*\Phi_1^\dagger\Phi_2 + A\Phi_2^\dagger\Phi_1\right)\Phi_S \\ &\Rightarrow \quad T \xrightarrow{\mathcal{CP}} T \quad \text{if} \quad A = A^*. \end{aligned} \tag{11.10}$$

Therefore, if $\text{Im}\,(A) \neq 0$, the tree-level potential is not invariant under the $\mathcal{CP}$ transformation defined in Eq. (11.9). However, the vacuum after spontaneous symmetry breaking at $T = 0\,\text{GeV}$, defined in Eq. (11.4), is invariant under $\mathcal{CP}$. Therefore, $\mathcal{CP}$ is not spontaneously, but *explicitly* broken in case $\text{Im}\,(A) \neq 0$ [382]. Moreover, the dark neutral scalars h_i, $(i = 1, 2, 3)$,

m_h	$m_{h_{i,j}}$	$m_{H^\pm}$	α_i	λ_2	λ_6	λ_8	m_{22}^2	m_S^2
125.09	$[1, 10^3]$	$[65, 10^3]$	$\left[-\frac{\pi}{2}, \frac{\pi}{2}\right]$	$[0, 9]$	$[0, 17]$	$[-26, 26]$	$[0, 10^6]$	$[0, 10^6]$

Table 11.1.: Ranges for the input parameters used for the scan with `ScannerS`. Units of the masses m_h, m_{h_i}, $m_{H^\pm}$ are in GeV, the units of the mass-squared parameters m_{22}^2, m_S^2 are in GeV^2, all other parameters are dimensionless. The chosen ranges for the dark scalar masses are further discussed in the text.

are mixtures of the $\mathcal{CP}$-even and $\mathcal{CP}$-odd neutral dark fields in case $\text{Im}\,(A) \neq 0$, as can be seen from Eq. (11.6). This shows that the explicit $\mathcal{CP}$ violation is in the dark sector. Because the dark sector does not couple directly to fermions, this explicit $\mathcal{CP}$ violation in the dark sector is not constrained by the stringent EDM constraints. As the dark charged scalar does not couple to fermions, the B-physics bounds, compare Section 5.1, are fulfilled. Its mass is furthermore not constrained by the direct LEP bound of $m_{H^\pm} > 90\,\text{GeV}$, because this constraint assumes an exclusive decay of $H^\pm$ into fermions [382].

The neutral $\mathcal{CP}$-mixed dark scalars h_i couple to the Z boson, in a Zh_ih_j vertex with $i \neq j$ [382], and to neutral scalars, e.g. in vertices with the SM-like Higgs boson, hh_ih_j and the neutral Goldstone boson, $G^0h_ih_j$, $i,j \in \{1,2,3\}$. Loop effects can therefore transfer $\mathcal{CP}$ violation from the dark to the visible sector. In Ref. [382] the impact of explicit $\mathcal{CP}$ violation on anomalous triple gauge boson vertices was studied in detail. The possibility of loop-induced $\mathcal{CP}$ violation furthermore requires an extension of the finite CT potential, introduced for our OS renormalization, cf. Section 5.2, beyond the field combinations appearing in the tree-level potential. One additional CT needs to be introduced, which parametrizes the additional $\mathcal{CP}$-violating structure, as was discussed in detail in Ref. [178].

In the following, we discuss results for 'CP in the Dark' for a random parameter scan[1] performed with `ScannerS` and `BSMPTv3` in the input parameter ranges of Tab 11.1. With `ScannerS` and `BSMPT`, we ensure that our points today at $T = 0\,\text{GeV}$ lie within the theoretically and experimentally allowed parameter space, as discussed in detail in Section 5.1.

Let us add a remark on the compatibility with the LHC Higgs data in this context. The only decays of h into SM particles that are influenced by dark sector contributions are the decays into a pair of photons γ, as well as the decay into $Z\gamma$, stemming from a loop with the dark charged scalar $H^\pm$. Therefore, the $h \to \gamma\gamma$ and $h \to Z\gamma$ branching ratio can be modified w.r.t. the SM prediction. The mass of the dark charged scalar $H^\pm$ is chosen to vary between 65 GeV and 1 TeV to eliminate the possibility of $h \to H^+H^-$ decays. We furthermore allow a range of $1\,\text{GeV} \leq m_{h_i} \leq 1\,\text{TeV}$ for the dark neutral scalar masses.[2] This allows for decays of the SM-like Higgs boson h into h_ih_j when $m_{h_i} + m_{h_j} < m_h$, with $i,j \in \{1,2,3\}$. When such new dark decay channels open up, all branching ratios of h into SM particles are reduced w.r.t. the SM prediction. With `ScannerS`, using `HiggsTools`, as described in Section 5.1, we take into account all Higgs data constraints.

In our earlier analysis [178, 383] of 'CP in the Dark' with `BSMPTv2`, cf. Section 5.2, we found points that allow for a strong first-order EWPT, $\xi_c \gtrsim 1$. The analysis presented in this chapter goes beyond this earlier analysis by calculating first-order EWPTs and gravitational waves with `BSMPTv3`, cf. Chapter 7. For the parameter points, that we find to be valid using `ScannerS` as described above, we look exclusively for completing[3] one-step first-order EWPTs

---

[1] The seed point distribution for the scan is random, therefore the point density in the scatter plots has no physical meaning.

[2] In the scan of [382] the masses of h_k $(k = 1, 2, 3)$ were constrained to be above 70 GeV which ruled out $h \to h_ih_j$ decays, with $i, j = \{1, 2, 3\}$. Consequently, all h branching ratios, except for $h \to \gamma\gamma$ were SM-like.

[3] For a completing transition, there exists a completion temperature that we can calculate as defined in Eq. (8.37).

in a temperature range $T \in [0,\, 300]$ GeV with `BSMPTv3`. We require absolute vacuum stability, i.e. that the NLO zero-temperature global minimum lies at the position of the EW tree-level vacuum $v_{\text{EW}} = 246.22\,\text{GeV}$. We also choose to only take into account points with $T_c > T_{\text{EW}} = 100\,\text{GeV}$, cf. Chapter 3, to not include points in the analysis that depart too far from the high-temperature approximation, c.f. Chapter 4. We furthermore enforce EWSR in the false phase at the critical temperature by requiring that $\overline{\omega}_{\text{EW}}^{\text{false}}(T_c) = 0$. Consequently, sphaleron-mediated transitions are in thermal equilibrium in the false phase, which ensures one necessary condition for electroweak baryogenesis, as discussed in Chapter 3. For the computation of the GW signals, we assume the EWPT to take place at a transition temperature equal to the percolation temperature

$$T_* = T_p \,, \tag{11.11}$$

see Section 8.2. We define the ξ-parameter at the critical temperature, ξ_c, as in Eq. (3.13) and at the percolation temperature, ξ_p, analogously,

$$\xi_p \equiv \xi(T_p) = \frac{\overline{\omega}_{\text{EW}}^{\text{true}}(T_p)}{T_p} \,, \tag{11.12}$$

with

$$\overline{\omega}_{\text{EW}} \equiv \sqrt{\overline{\omega}_1^2 + \overline{\omega_2}^2 + \overline{\omega}_{\text{CP}}^2 + \overline{\omega}_{\text{CB}}^2} \,. \tag{11.13}$$

The superscripts $\overline{\omega}^{\text{true}}$ and $\overline{\omega}^{\text{false}}$ label the VEVs of the true and false phase, respectively.

In Section 11.1 we discuss the generated point sample with a one-step first-order EWPT with respect to the expected SNR at LISA. In Section 11.2, we show DM observables, e.g. the direct detection cross section and DM relic density for the point sample and comment on the impact of the latest experimental direct detection exclusion bounds. We present a detailed discussion of the observed different phase histories in Section 11.3 and conclude in Section 11.4.

11.1. First-Order Phase Transitions and Gravitational Waves

In agreement with our earlier studies [178, 383, 384] using `BSMPTv2`, we find that 'CP in the Dark' allows for strong first-order EWPTs. Moreover, we find completing strong first-order EWPTs with $\xi_p \gtrsim 1$ across the allowed mass region $m_{H^\pm} > m_{h_1}$, as illustrated in Figure 11.1 (left).[4]

Furthermore, we derive the acoustic and turbulence GW spectrum sourced by the first-order EWPTs and calculate the corresponding SNR at LISA with a three-year data acquisition period. Figure 11.1 (right) shows the point sample in the $m_{h_1} - m_{H^\pm}$-plane, colour coded with the value of the SNR. We find strong first-order EWPTs with up to SNR(LISA-3yrs) = 17.11 and points with SNR > 10 scattered across the allowed $m_{h_1} - m_{H^\pm}$-region. Only the strongest first-order EWPTs with $\xi_p > 3.2$ lead to a value of SNR > 1, as illustrated by Figure 11.2. Here, we show ξ_p versus ξ_c for the allowed point sample, colour coded corresponding to the SNR. All points with SNR > 1 are strong first-order EWPT points with $1.3 \lesssim \xi_c < \xi_p$, as $T_p < T_c$.

In Figure 11.3, we show peak amplitude and peak frequency values of the GW spectrum, colour coded corresponding to the value of the SNR at LISA with a three-years data acquisition period. From the figure, we see that, as expected, points with SNR > 1 lie above

---

[4] The mass hierarchy $m_{H^\pm} > m_{h_1}$ stems from the requirement that h_1 is the lightest stable state in order to have a neutral DM candidate.

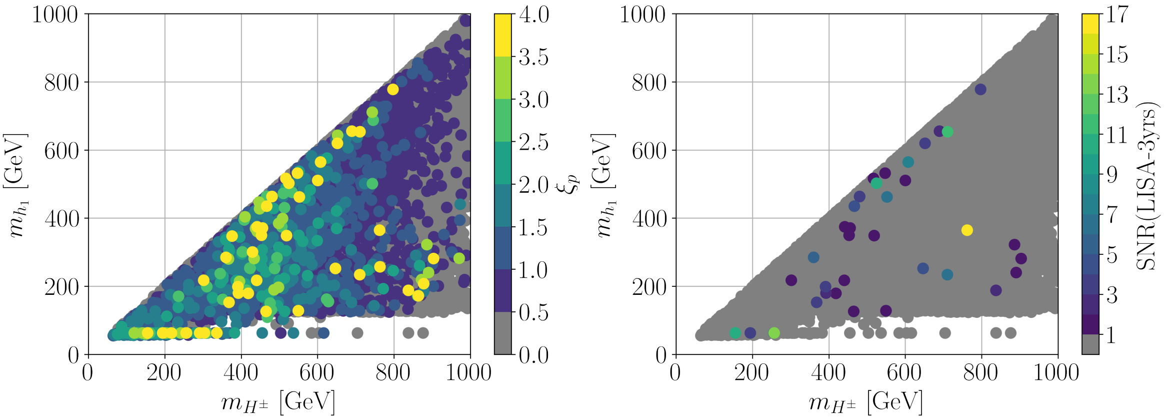

Figure 11.1.: Scatter plot in the $m_{h_1} - m_{H^\pm}$-plane for the parameter sample generated in the ranges of Table 11.1 with applied the constraints from `ScannerS` and `BSMPT`, cf. text for details. Left: Colour code denotes ξ_p. Points with $\xi_p < 0.5$ are coloured in grey. Right: Colour code corresponds to the value of the SNR of the gravitational waves sourced by the first-order EWPTs in sound waves and turbulence measured at LISA with a three-years data acquisition period. The grey points have an SNR < 1 and therefore escape detection at LISA.

the LISA sensitivity curve, shown as the dashed grey line. For this figure, we exceptionally take into account only the sound-wave contribution to the GW signal. We find that gravitational waves sourced by turbulence only play a subdominant role for our points, which we will elaborate on in the following. After the period, during which sound waves are sourced, turbulence is sourced by non-linearities in the plasma. In particular, strong transitions with long durations and therefore possible supercooling are expected to lead to an early start of the turbulent regime [244, 323–325, 387]. However, in our point sample we maximally find $\alpha \lesssim 0.3$, with α defined as in Eq. (9.7). Using the categorization of [388], this corresponds to the regime of mild supercooling.[5] This is compatible with the observed $\mathcal{O}(10\,\text{GeV})$ differences between nucleation and percolation temperature, $T_n - T_p$, for points with SNR > 1. Our point sample is therefore characterized by comparably short durations of the first-order EWPTs, that are primarily in the acoustic regime, in which the bulk of the vacuum energy is emitted as sound waves. The SNR is therefore dominantly given by the sound wave contribution. Based on these observations, we assume that the first-order EWPTs of the point sample take place fast enough to ensure that our assumption of a terminal bubble wall velocity holds.

---

[5] We find $1.01 < \text{SNR(LISA-3yrs)} < 4.14$ for $\alpha < 0.1$ (slight supercooling) and $1.98 < \text{SNR(LISA-3yrs)} < 17.11$ for $0.1 < \alpha < 0.5$ (mild supercooling), according to the classification of supercooling by the PT strength α of Ref. [388].

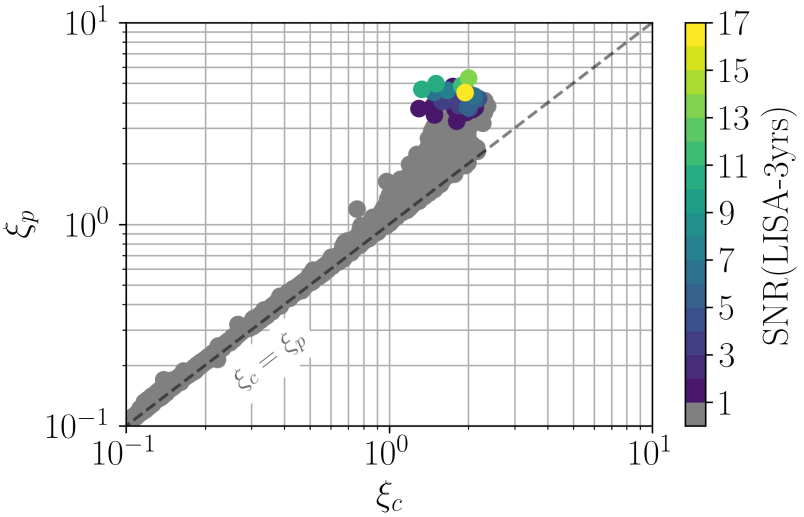

Figure 11.2.: ξ_p versus ξ_c. The colour indicates the SNR for gravitational waves produced via sound waves and turbulence at LISA after a three-year data acquisition period. Points with SNR < 1 are coloured in grey.

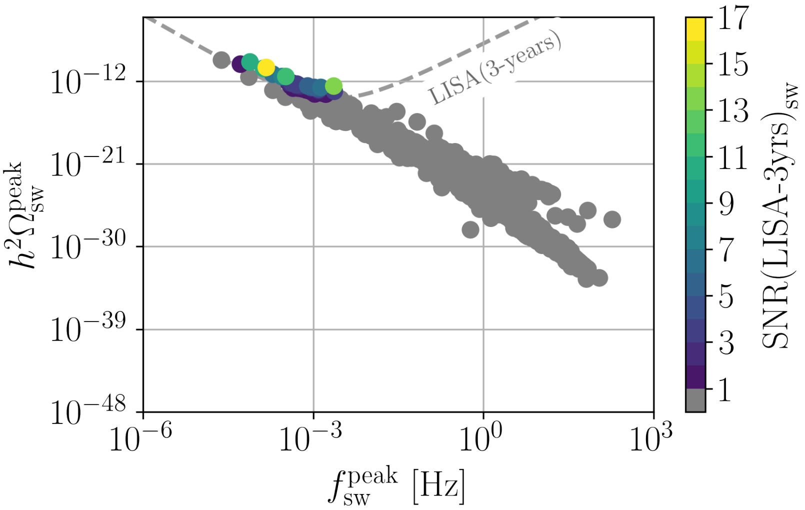

Figure 11.3.: Sound-wave GW peak amplitude versus peak frequency. The colour code shows the SNR calculated from the sound-wave contribution only. Grey points have SNR < 1. The dashed grey line marks the sensitivity curve of the LISA experiment taken from Refs. [277, 325, 356], cf. Section 9.5.

11.2. Dark Matter Observables

The model features a WIMP as a DM candidate, given by h_1. In this section we show how the obtained sample of strong first-order EWPT points matches the DM constraints from the measured relic density and direct detection experiments. In Figure 11.4 (left column) we show the freeze-out relic density $\Omega_{\text{prod}}h^2$ for the DM, which is given by h_1 calculated with `MicrOMEGAs`, versus m_{h_1} for all allowed parameter points coloured by ξ_p (top), as well as their corresponding value of the SNR (bottom) for the resulting GW spectrum at LISA with a three-year data acquisition period. Using `ScannerS` and `MicrOMEGAs`, as described in Section 5.1, only (under)abundant points with a DM relic density of $\Omega_{\text{prod}}h^2 \leq \Omega_{\text{exp}}h^2 = 0.1200 \pm 0.0012$ [21] are retained.[6] We find strong first-order EWPTs with $\xi_p > 1$ within the 1σ error bands of the measured relic density. For the points with SNR > 1 we find at most $\Omega_{\text{prod}}h^2 = 0.08$, which is slightly underabundant w.r.t. to the experimental result. The underabundance does not rule out these points, it just raises the need of additional DM candidates to saturate the measured relic density. Consequently, a strong first-order EWPT and observable gravitational waves are compatible with the observed DM relic density. Parameter points with a strong first-order EWPTs can even saturate the measured DM relic density. The latter conclusion was reached already in Ref. [178], based on only the `BSMPTv2` analysis.

In Figure 11.4 (right column) we show the effective spin-independent direct detection cross section $f_{\chi\chi} \cdot \sigma$ versus the DM mass m_{h_1} for the allowed parameter points coloured again according to their value of ξ_p (top), as well as SNR value (bottom). The effective cross section is calculated by rescaling the cross section σ with

$$f_{\chi\chi} \equiv \frac{\Omega_{\text{prod}}h^2}{\Omega_{\text{exp}}h^2}\,, \tag{11.14}$$

to account for underabundance $\Omega_{\text{prod}}h^2 \leq \Omega_{\text{exp}}h^2$, cf. Refs. [389, 390]. The null result of direct detection experiments [88–91] constrains the dark sector of BSM models such that the allowed interaction of the dark sector with the SM-like sector is more and more suppressed. Applying the constraints of `ScannerS` using `MicrOMEGAs`, points that have $f_{\chi\chi} \cdot \sigma$ above the exclusion limit measured in 2018 by XENON1T [88] are discarded. Since 2018, updated exclusion limits were published by the PandaX collaboration in 2021 [89], by LUX-ZEPLIN (LZ) in 2022 [90] and by XENONnT in 2023 [91]. We show all mentioned exclusion limits in Figure 11.4 (right column). The parameter space is most constrained by the LZ exclusion limit. An application of the LZ exclusion limit on our parameter points would remove a slice of the parameter space including points with SNR > 10. We still find strong first-order EWPT points, however, with SNR > 10 and $\xi_p > 1$ below the LZ exclusion limit. Such points are furthermore found to be above the neutrino floor, below which elastic coherent neutrino-nucleus scattering becomes undistinguishable from the dark matter signal [391]. Consequently, the requirement of escaping detection at current direct detection experiments is compatible with points that have a strong first-order EWPT with $\xi_p > 1$ as well as with an SNR > 10.

Figure 11.5 shows the effective direct detection cross section $f_{\chi\chi} \cdot \sigma$ versus the DM mass m_{h_1} for the allowed point sample, with the colour code indicating the corresponding DM abundance ratio, $0 \leq \Omega_{\text{prod}}h^2/\Omega_{\text{exp}}h^2 \leq 1$. From the figure, we can deduce that $\Omega_{\text{prod}} \simeq \Omega_{\text{exp}} \simeq 1$ is found for low, as well as for high DM masses m_{h_1}.[7] In addition, the requirement of escaping direct detection is compatible with saturating the measured DM relic density.

---

[6] The most precise value of the DM relic density is derived from CMB data collected by the Planck satellite [21], from which the CMB anisotropy power spectrum is obtained. The values of the baryonic and DM relic densities are then directly derived by fitting the CMB anisotropy power spectrum assuming the ΛCDM model.

[7] The high density of points with $\Omega_{\text{prod}}/\Omega_{\text{exp}} \simeq 1$ for large m_{h_1} is a relic of the random seed of the scan, cf. Section 5.1. We also find points that saturate the DM relic abundance for lower m_{h_1}, cf. Figure 11.5.

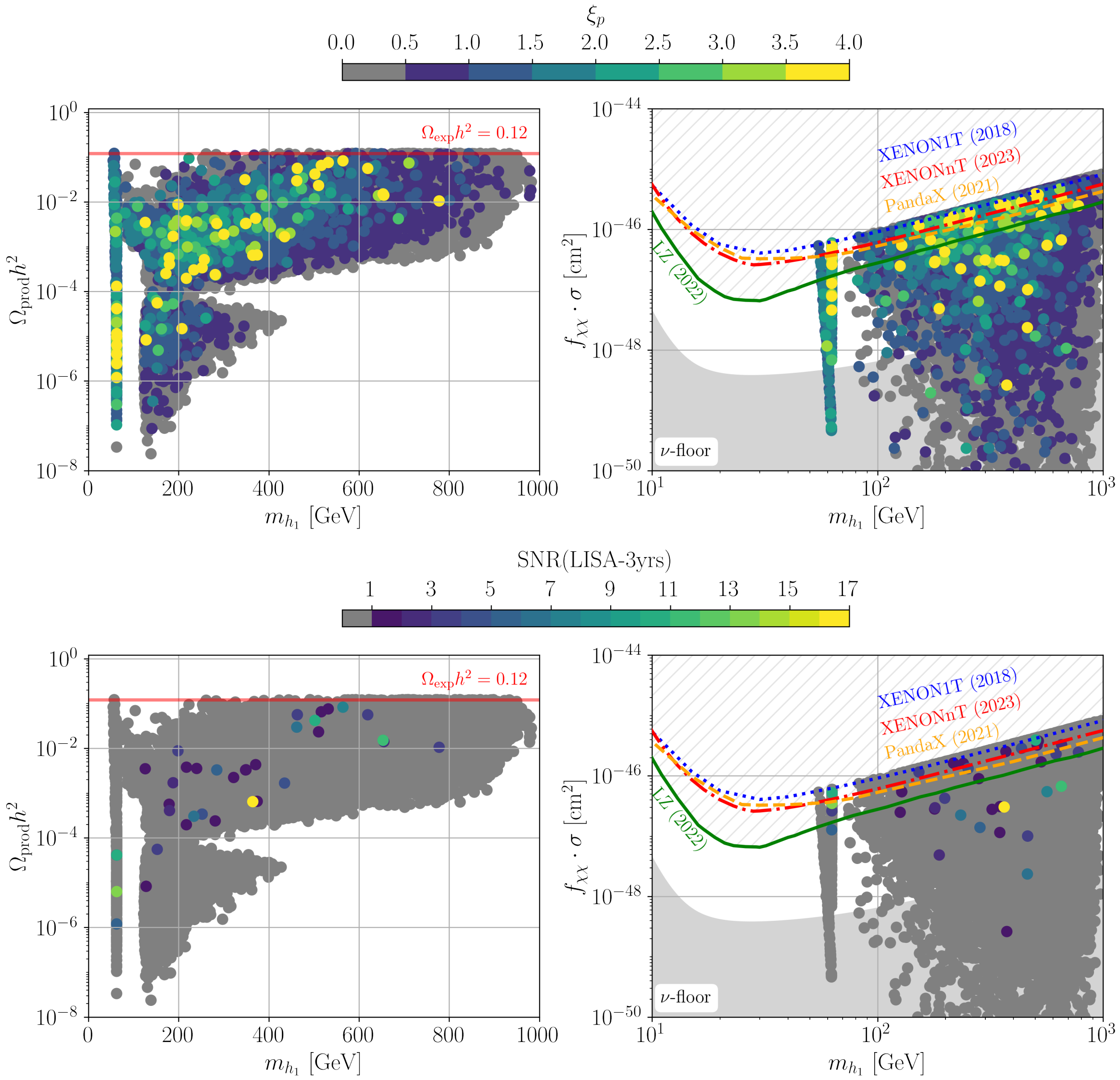

Figure 11.4.: Left column: Relic density versus DM mass m_{h_1} for the allowed parameter points. The red line marks the experimental central value of $\Omega_{\rm exp}h^2 = 0.12$ [21]. Right column: Effective spin-independent direct detection cross section versus DM mass m_{h_1} for the allowed parameter points. The light grey area is the neutrino floor, below which WIMP DM cross sections become indistinguishable from coherent elastic neutrino scattering with the nucleus [391]. The coloured lines illustrate exclusion limits by XENON1T (dotted blue line) [88], XENONnT (dash-dotted red line) [91], PandaX (dashed orange line) [89] and LZ (solid green line) [90]. The parameters space that is excluded by LZ is hatched. The colour code of the top row indicates the value of ξ_p and the colour code in the bottom row indicates the SNR for gravitational waves produced via sound waves and turbulence at LISA after a three-year data acquisition period. Points with $\xi_p < 0.5$ or SNR < 1 are displayed in grey, respectively.

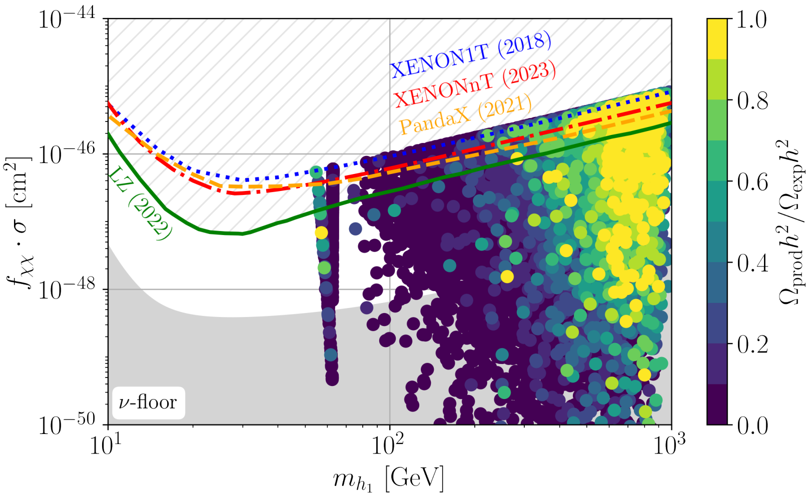

Figure 11.5.: Same figure as Figure 11.4 (right), but points are colour coded by the value of the calculated relic density $\Omega_{\text{prod}} h^2$ normalized to the experimental central value $\Omega_{\text{exp}} h^2 = 0.12$ [21].

11.3. Phase Histories

We now look in more detail at the different possible phase histories that we find to allow for a one-step first-order EWPT while requiring the restoration of the electroweak symmetry in the false phase at T_c as well as absolute vacuum stability at $T = 0\,\text{GeV}$. In [178] we found points with a strong first-order EWPT with two different temperature evolutions of the global minimum. In the first one, only the SM-like finite-temperature VEV participates, $|\overline{\omega_1}| > 0$, while the dark VEV coordinates of the global minimum are zero across the whole temperature range. In the second one, additionally the dark VEV coordinates of the global minimum are non-zero (excluding $\overline{\omega}_{\text{CB}}$ which is found to be zero for $T \in [0, 300]\,\text{GeV}$) in intermediate temperature-ranges.

Using `BSMPTv3`, we go beyond a global minimum analysis and trace the five-dimensional local minima positions of the high- and the low-temperature phase over the temperature range in which they exist within $T \in [0, 300]\,\text{GeV}$. This does not only allow for a calculation of the transition rates between false and true phases and the deduction of characteristic temperatures and GW parameters as already discussed above, but also gives more insight into the possible phase patterns.

Our study confirms the observation presented in Refs. [178] and further details the possible phase histories by categorizing them into four cases. Phase histories for exemplary benchmark points for each category are shown in Figure 11.6 and will be further discussed below. The benchmark points are given in Appendix A. Each row of the figure corresponds to one benchmark point. The columns (from left to right) illustrate the temperature evolution of the false, high-temperature, phase (red dashed line) and the true, low-temperature, phase (blue solid line) of one of the five VEV coordinates $\{\overline{\omega}_1, \overline{\omega}_2, \overline{\omega}_{\text{CP}}, \overline{\omega}_S, \overline{\omega}_{\text{CB}}\}$, respectively. We find the following four categories:

1. For points of the first category, only the SM-like neutral $\mathcal{CP}$-even doublet VEV $\overline{\omega}_1$ participates in the first-order EWPT and is non-zero for the low-temperature EW broken phase. In the high-temperature phase, all VEVs are zero at T_c. Therefore, the $\mathbb{Z}_2$ symmetry is exact in the false and in the true phase and the EW symmetry is broken spontaneously by $\overline{\omega}_1$. In short, the phase history associated with the first category is:

$$\begin{array}{c}\text{EW symmetric and}\\ \mathbb{Z}_2\text{-symmetric phase}\end{array} \xrightarrow{\textbf{1st-order EWPT}} \begin{array}{c}\text{EW broken and}\\ \mathbb{Z}_2\text{-symmetric phase}\end{array} .$$

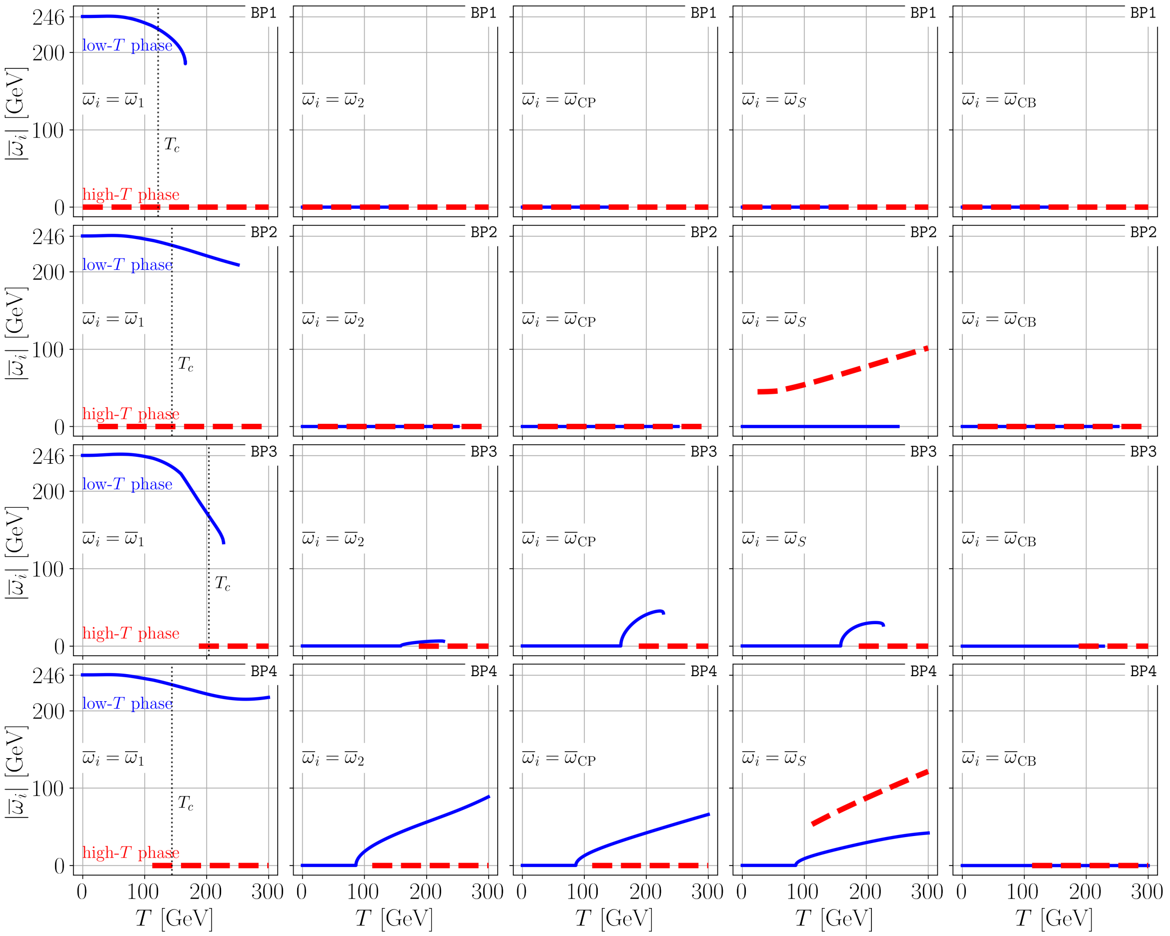

Figure 11.6.: Four benchmark points exemplary for the four categories of found phase histories that can yield a first-order EWPT with EWSR at T_c, illustrated in all five VEV coordinates. The columns (from left to right) show the temperature evolution of the high-temperature phase (red dashed line) and the low-temperature phase (blue solid line) in the five coordinates $\{\overline{\omega}_1, \overline{\omega}_2, \overline{\omega}_{\text{CP}}, \overline{\omega}_S, \overline{\omega}_{\text{CB}}\}$, respectively, versus the temperature $T \in [0, 300]$ GeV. The rows correspond to one benchmark point, respectively. The critical temperature T_c is marked as a vertical dashed line in the leftmost column. The benchmark points are given in Appendix A. The second and fourth benchmark points are taken from Figure 5 (and Table 2 and Table 3) of Ref. [178].

2. For points of the second category, the high-temperature phase has a non-zero dark singlet VEV coordinate at T_c. Consequently, the $\mathbb{Z}_2$ symmetry is broken[8] at T_c in the false phase. The first-order EWPT spontaneously breaks the EW symmetry and restores $\mathbb{Z}_2$. All dark VEVs are zero in the low-temperature phase and the phase history for the second category is:

$$\begin{array}{l}\text{EW symmetric}\\ \mathbb{Z}_2\text{-broken}\\ \text{singlet phase}\end{array} \xrightarrow{\textbf{1st-order EWPT}} \begin{array}{l}\text{EW broken and}\\ \mathbb{Z}_2\text{-symmetric phase}\end{array} .$$

   We comment on the high-temperature behaviour for $T > T_c$ of the potential for 'CP in the Dark' further below, but already note here that any domains that exist at high temperature merge at the first-order EWPT with the EW broken phase in which, by definition, the $\mathbb{Z}_2$ symmetry is exact. The benchmark point BP2 displayed in Figure 11.6 is taken from Figure 5(a) (and Table 2 and Table 3) of Ref. [178].

3. Points of the third category have an exact $\mathbb{Z}_2$ symmetry at T_c in the false phase and a first-order EWPT into a phase with non-zero dark VEVs, with the exception of $|\overline{\omega}_{\mathrm{CB}}|$, which is found to be zero in the whole temperature range. Consequently, the EW symmetry and the $\mathbb{Z}_2$ symmetry are spontaneously broken through the first-order EWPT. The point then transitions continuously into the EW broken, $\mathbb{Z}_2$-symmetric low-temperature phase:

$$\begin{array}{l}\text{EW symmetric and}\\ \mathbb{Z}_2\text{-symmetric phase}\end{array} \xrightarrow{\textbf{1st-order EWPT}} \begin{array}{l}\text{EW broken and}\\ \mathbb{Z}_2\text{-broken phase}\end{array} \longrightarrow \begin{array}{l}\text{EW broken and}\\ \mathbb{Z}_2\text{-symmetric phase}\end{array} .$$

   In this transition history, as the $\mathbb{Z}_2$ symmetry is spontaneously broken in an intermediate temperature range, domain walls are created. The domain walls decay when the $\mathbb{Z}_2$ symmetry is restored in the EW broken, $\mathbb{Z}_2$-symmetric low-temperature phase. However, their existence in an intermediate temperature range could influence the energy density of the universe, which might raise the need to apply additional constraints on such points, cf. Chapter 2. A detailed discussion of domain walls within this model is left for future work.

4. The fourth category contains points with non-zero dark VEVs in the low-temperature phase similarly to third category, but in addition the high-temperature phase has $|\overline{\omega}_S^{\mathrm{false}}(T_c)| > 0$ similar to points of the second category. Consequently, the $\mathbb{Z}_2$ symmetry is already broken in the false phase and the first-order EWPT spontaneously breaks the EW symmetry. The EW broken and $\mathbb{Z}_2$-broken intermediate phase then transitions continuously into the EW broken, $\mathbb{Z}_2$-symmetric phase in which the universe is in today. The transition history for the fourth category is:

$$\begin{array}{l}\text{EW symmetric}\\ \mathbb{Z}_2\text{-broken}\\ \text{singlet phase}\end{array} \xrightarrow{\textbf{1st-order EWPT}} \begin{array}{l}\text{EW broken and}\\ \mathbb{Z}_2\text{-broken phase}\end{array} \longrightarrow \begin{array}{l}\text{EW broken and}\\ \mathbb{Z}_2\text{-symmetric phase}\end{array} .$$

   The benchmark point BP4 displayed in Figure 11.6 is taken from Figure 5(b) (and Table 2 and Table 3) of Ref. [178].

All points of our generated sample have explicit $\mathcal{CP}$ violation with $\mathrm{Im}\,(A) \neq 0$. However, we also find the possibility of first-order EWPTs with $|\overline{\omega}_{\mathrm{CP}}^{\mathrm{true}}(T_p)| > 0$ in transition histories similar to the ones of BP3 and BP4 as discussed above. These points therefore have a source of *additional* $\mathcal{CP}$ *violation* through $|\overline{\omega}_{\mathrm{CP}}| > 0$ at finite temperature. If $\mathrm{Im}\,(A) = 0$, and a non-vanishing $\mathcal{CP}$-violating VEV $\overline{\omega}_{\mathrm{CP}}$ is generated, this would correspond to *spontaneous* $\mathcal{CP}$ violation.[9] The additional $\mathcal{CP}$ violation through $|\overline{\omega}_{\mathrm{CP}}| > 0$ is accompanied by the violation

---

[8] The $\mathbb{Z}_2$ symmetry, as defined in Eq. (11.1), is broken if any of the dark fields acquires a non-zero VEV at finite temperature.

[9] The possibility of spontaneous $\mathcal{CP}$ violation was first discussed by Lee in Ref. [192], and for example in Ref. [392] spontaneous $\mathcal{CP}$ violation was studied for a softly-broken $\mathbb{Z}_2$ symmetric 2HDM with an additional pseudoscalar singlet field. For this model, the authors discussed that there might be a promising link to EWBG.

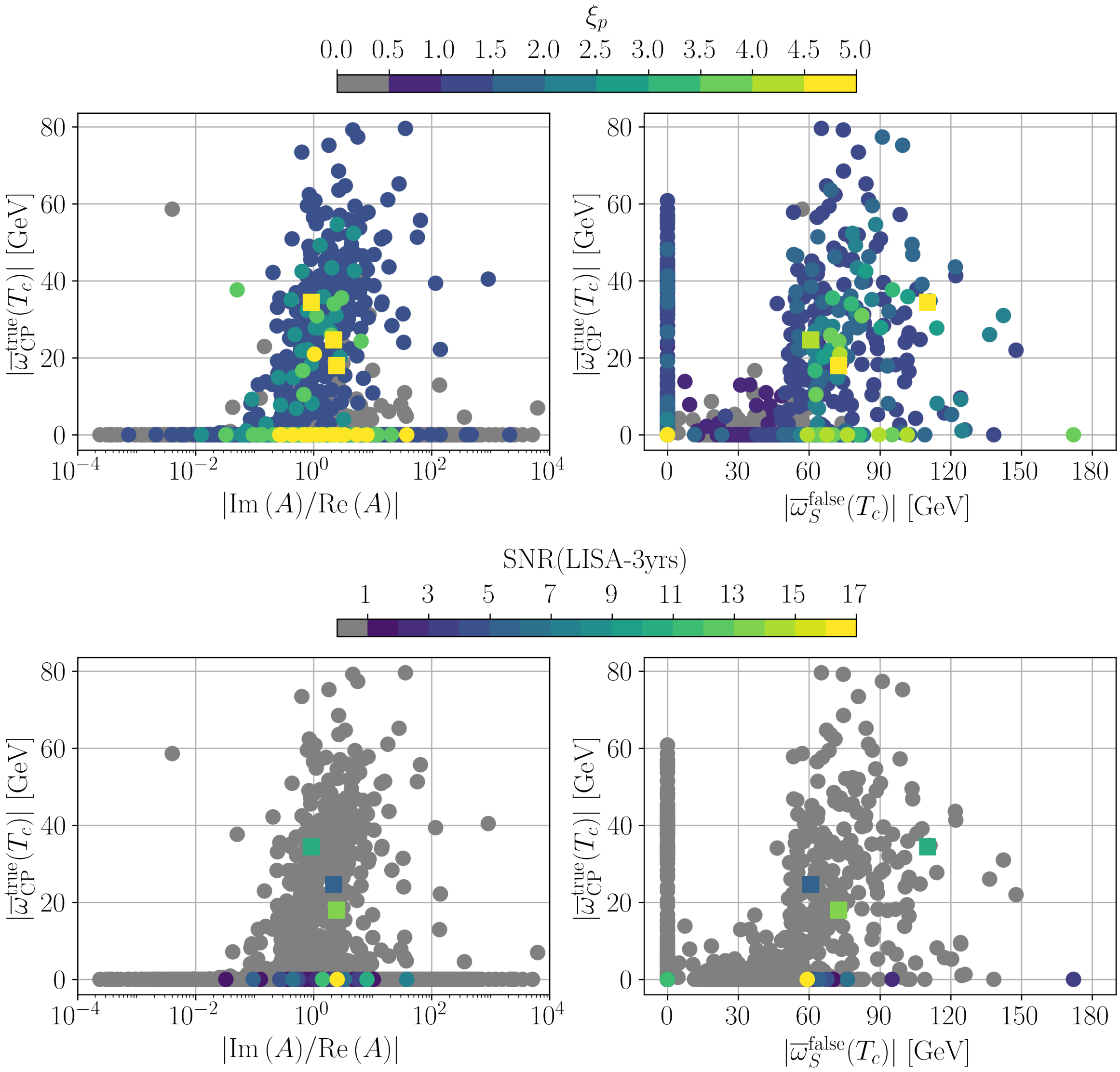

Figure 11.7.: Left column: $\mathcal{CP}$-violating VEV coordinate of the true phase at the critical temperature versus the imaginary part the trilinear scalar potential parameter A normalized to its real part for the generated point sample. The colour indicates the value of ξ_p (top) as well as the SNR for gravitational waves produced via sound waves and turbulence at LISA after a three-year data acquisition period (bottom). Dots indicate points for which $\overline{\omega}_{\rm CP}^{\rm true}$ is either zero or non-zero both at the critical temperature T_c and at the completion temperature T_f. Squares indicate points for which only $|\overline{\omega}_{\rm CP}^{\rm true}(T_c)| > 0$, but $\overline{\omega}_{\rm CP}^{\rm true}(T_n) = \overline{\omega}_{\rm CP}^{\rm true}(T_p) = \overline{\omega}_{\rm CP}^{\rm true}(T_f) = 0$. Right column: $\mathcal{CP}$-violating VEV coordinate of the true phase, $|\overline{\omega}_{\rm CP}^{\rm true}(T_c)|$, versus the singlet VEV coordinate of the false phase, $|\overline{\omega}_{S}^{\rm false}(T_c)|$ at the critical temperature T_c for the generated point sample. The colour code is the same as for the rows in the left column, respectively.

of the $\mathbb{Z}_2$ symmetry of Eq. (11.1). We find that if $|\overline{\omega}_{\mathrm{CP}}| > 0$, the SM-like neutral scalar mixes with the former dark neutral $\mathcal{CP}$-mixed scalars. The possibility of non-zero $|\overline{\omega}_{\mathrm{CP}}|$ at finite temperature is a great opportunity for EWBG: It may allow for sufficiently large $\mathcal{CP}$ violation, that can be transferred to the visible sector, without being in conflict with the strict EDM bounds. A more detailed study of EWBG within 'CP in the Dark' is left for future work.

In the following, we compare the EWPT strength, ξ_p, and the SNR for points with and without additional $\mathcal{CP}$ violation at finite temperature. In Figure 11.7 (left column) the $\mathcal{CP}$-violating VEV coordinate of the true phase is displayed versus the tree-level parameter that parametrizes explicit $\mathcal{CP}$ violation in the model, the value of $\mathrm{Im}\,(A)$ normalized to its real part, $\mathrm{Re}\,(A)$ for the whole allowed first-order EWPT data sample. The points are colour coded by the value of ξ_p (top row) as well as the size of the SNR at LISA with a three-year data acquisition period (bottom row). The dots represent all points for which $|\overline{\omega}_{\mathrm{CP}}^{\mathrm{true}}|$ is zero, respectively non-zero, at both the critical temperature and at the completion temperature. The squares mark points for which only $|\overline{\omega}_{\mathrm{CP}}^{\mathrm{true}}(T_c)| > 0$, but $\overline{\omega}_{\mathrm{CP}}^{\mathrm{true}}(T_n) = \overline{\omega}_{\mathrm{CP}}^{\mathrm{true}}(T_p) = \overline{\omega}_{\mathrm{CP}}^{\mathrm{true}}(T_f) = 0$. Consequently, for the points displayed as squares, the true phase, which has at T_c a non-zero $\mathcal{CP}$-violating VEV coordinate, $|\overline{\omega}_{\mathrm{CP}}(T_c)| > 0$, transitions continuously into a phase with $\overline{\omega}_{\mathrm{CP}}^{\mathrm{true}} = 0$, before the first-order EWPT takes place.

We find strong first-order EWPT points with additional $\mathcal{CP}$ violation at finite temperature, cf. Figure 11.7 (top row). We also find $|\overline{\omega}_{\mathrm{CP}}^{\mathrm{true}}(T_c)| > 0$ for SNR(LISA-3yrs) > 10, cf. Figure 11.7 (bottom row), however, only for the points displayed as squares. The latter points are all found to be characterized by $m_{h_1} \approx m_h/2$. This does *not* mean that an SNR(LISA-3yrs) > 10 together with non-zero $\mathcal{CP}$-violating VEV coordinate at the transition temperature, $|\overline{\omega}_{\mathrm{CP}}^{\mathrm{true}}(T_p)| > 0$, is impossible in 'CP in the Dark', just that this feature is not part of the generated random sample. The generated random sample clearly shows the possibility of additional $\mathcal{CP}$ violation through $|\overline{\omega}_{\mathrm{CP}}^{\mathrm{true}}| > 0$ for valid first-order EWPTs. A more dedicated scan could reveal valid parameter regions that source detectable gravitational waves from a first-order EWPT into a true phase with an additional source of $\mathcal{CP}$ violation at finite temperature.

In Figure 11.7 (right column) we show the allowed sample in the two-dimensional plane spanned by $|\overline{\omega}_{\mathrm{CP}}^{\mathrm{true}}(T_c)|$ versus $|\overline{\omega}_{S}^{\mathrm{false}}(T_c)|$, again colour coded by the value of ξ_p (top) and SNR(LISA-3yrs) (bottom). This figure illustrates the relation between the benchmark phase histories, cf. Figure 11.6, and the first-order EWPT strength as well as the detectability of the sourced gravitational wave. The points of the first category have $\overline{\omega}_{\mathrm{CP}}^{\mathrm{true}}(T_c) = \overline{\omega}_{S}^{\mathrm{false}}(T_c) = 0$ and are located in the left bottom corner of the figures, respectively. Our random sample for these points has a maximal SNR(LISA-3yrs) of 11, so within detectable ranges at LISA. For points of the second category with $\overline{\omega}_{\mathrm{CP}}^{\mathrm{true}}(T_c) = 0$, but $|\overline{\omega}_{S}^{\mathrm{false}}(T_c)| > 0$, we also observe SNR(LISA-3yrs) > 10 for points with the largest found ξ_p. Points of the third category, where $\mathbb{Z}_2$ is spontaneously broken at T_c, by an intermediate phase with $|\overline{\omega}_{\mathrm{CP}}| > 0$, are found to allow for $\xi_p > 1$, but are not found to have an SNR(LISA-3yrs) > 1. Again, this is just a feature of the randomly generated points and not necessarily a global feature of the model. For points of the fourth category with intermediate $|\overline{\omega}_{\mathrm{CP}}| > 0$ and already broken $\mathbb{Z}_2$ symmetry in the high-temperature phase, we find points with SNR(LISA-3yrs) > 10, but as already discussed above, these have no additional $\mathcal{CP}$ violation any more at temperatures where the first-order EWPT takes place.

Let us add a few remarks on the found high-temperature behaviour of these points. We find high-temperature EWSR and $\mathbb{Z}_2$ conservation for $2\,\%$ of the points of the full sample, using the symmetry restoration check implemented in `BSMPTv3`, cf. Chapter 7.[10] These points have a maximal $\xi_p = 2.4$ as well as a maximal SNR(LISA-3yrs) $= \mathcal{O}(10^{-3})$. The remaining bulk of the parameter sample has either non-restoration of the EW symmetry, a broken $\mathbb{Z}_2$ symmetry, or both combined, in the high-temperature limit. In the first case, the dark fields have zero VEV, but $|\overline{\omega}_1| > 0$, which breaks the EW symmetry, but leaves the $\mathbb{Z}_2$ symmetry exact. In the second case, all doublet VEVs are zero, i.e. the EW symmetry is restored, but the dark singlet acquires a non-zero VEV which breaks the $\mathbb{Z}_2$ symmetry. The third case includes points for which at least one of the dark doublet fields acquires a VEV, or the dark singlet and the SM-like doublet acquire a VEV, as well as combinations of the two. We note, that these cases of non-restoration of the EW symmetry or the $\mathbb{Z}_2$ symmetry can be accompanied with minima at large field values. While our approach is under good numerical control for high temperatures, large field values break perturbativity and a complete RGE treatment of the effective potential is necessary to consistently handle such situations, cf. Section 4.1.

11.4. Conclusions

In this chapter we studied an N2HDM-like model, 'CP in the Dark'. We analysed its parameter space allowed by theory and experiment in detail and found that it allows for points with a strong first-order EWPT, whose associated GW signal is within the sensitivity of the future space-bound interferometer LISA. Furthermore, we identified regions of the parameter space in which valid strong first-order EWPT points can abundantly predict dark matter while escaping direct detection. We showed that the latter can also be true for points with an SNR above ten. Therefore, a measurement of the stochastic GW background can shed light on parameter regions beyond the sensitivity of current and future direct detection experiments. In a detailed study of the possible phase histories that induce first-order EWPTs, from an EW symmetric false phase to an EW broken true phase, we identified cases with and without additional $\mathcal{CP}$ violation at finite temperature. We argued that this makes the model a promising candidate for EWBG. A dedicated analysis of possible portals for the transfer of $\mathcal{CP}$ violation to the SM-like Higgs couplings to fermions at finite temperature is left for a future study.

---

[10] The EW symmetry is restored, if all doublet VEVs are zero. The $\mathbb{Z}_2$ symmetry, defined in Eq. (11.1), is exact, if all VEVs of the second doublet and the singlet are zero.

CHAPTER 12

Final Conclusions and Outlook

Nature has realized a fundamental scalar sector that is described by a Higgs potential in the SM. The ground state of the Higgs potential breaks the EW symmetry of the SM spontaneously and is further associated with a scalar Higgs boson which determines the experimental phenomenology today, e.g. through masses and couplings of the SM particles. While the masses are input parameters of the SM, couplings of SM particles to the observed Higgs boson are measured to agree with the SM predictions within experimental and theoretical uncertainty bounds. The observed Higgs boson behaves SM-like. However, more data is needed to resolve the shape of the scalar potential independently from the Higgs boson mass measurement to receive more insight in the nature of the scalar sector.

While the postulated minimal SM scalar sector can accommodate for all observations made at colliders, there are strong cosmological hints that the SM is not the complete underlying theory of nature, e.g. the observed matter excess over antimatter in the universe and dark matter. The former can be generated dynamically through EWBG, given that all three Sakharov conditions are fulfilled. These are the existence of baryon number violation, $\mathcal{C}$ and $\mathcal{CP}$ violation, as well as departure from thermal equilibrium. Baryon number violating processes are possible in the SM through sphaleron-mediated transitions. In EWBG the departure from thermal equilibrium is realized through a strong first-order EWPT from a high-temperature EW symmetric false phase, where the sphaleron processes are in thermal equilibrium, to a low-temperature true phase which spontaneously breaks the EW symmetry and agrees with the SM Higgs ground state at zero temperature. The strong first-order EWPT conserves the matter–antimatter asymmetry, that was generated in the false phase by the interplay of $\mathcal{CP}$ violation with baryon number violation in the sphaleron transitions. Even though the EW symmetry is restored at high temperatures in the SM, this restoration takes place via a smooth cross-over that does not provide the departure from thermal equilibrium that is required in EWBG. Furthermore, the SM does not offer enough $\mathcal{CP}$ violation. Also, the explanation of dark matter necessitates an extension of the SM.

Within current experimental bounds, the SM scalar sector can be extended to accommodate (strong) first-order EWPTs and dark matter, as well as additional $\mathcal{CP}$ violation. First-order EWPTs are a particularly promising tool, as they can connect collider signatures with gravitational waves. If our universe underwent a first-order EWPT during the early phase of its existence, such a violent transition sourced a stochastic GW background. Through future space-bound experiments, we might be able to observe a stochastic GW background sourced by first-order EWPTs. If so, then this is a clear signal of BSM physics. The parameter configurations of this BSM physics leading to observable gravitational waves may imply interesting phenomenology that can be investigated at present and future colliders.

In this thesis, we studied two promising extensions of the SM scalar sector. In Chapters 6 and 10, we investigated the $\mathcal{CP}$-conserving 2HDM that extends the SM scalar sector by an additional complex $SU(2)_L$ doublet. In Chapter 11, we presented an extension by an additional $SU(2)_L$ doublet and a real $SU(2)_L$ singlet. This model, named 'CP in the Dark', has $\mathcal{CP}$ violation in its dark sector at zero temperature.

In Chapter 6, we investigated dimension-six enhanced strong first-order EWPTs, characterized through the ratio of the EW VEV at the critical temperature over the critical temperature, $\xi_c = \overline{\omega}_{\text{EW}}(T_c)/T_c \gtrsim 1$ in a 2HDM. We find that, purely scalar dimension-six modifications as well as top quark Yukawa dimension-six modifications can enable $\xi_c^{\text{d6}} \gtrsim 1$ for points with $\xi_c^{\text{d4}} < 1$, i.e. no strong first-order EWPT in the 2HDM without dimension-six extensions. The purely scalar dimension-six modifications lead to enhancements of the Higgs boson pair production cross section within the sensitivity range of future colliders. The top quark Yukawa modifications can be correlated to the phenomenology of heavy Higgs states in top quark final states. Overall, this analysis illustrates the connection between the strength of a first-order EWPT parametrized by ξ_c and parameter spaces that could be probed at present and future collider experiments.

However, only a calculation of false vacuum decay rates and the calculation of characteristic temperatures, which takes into account the expansion rate of the universe, can determine whether a first-order EWPT in the early universe takes place. Furthermore, a first-order EWPT releases vacuum energy into the surrounding plasma, which is a source for gravitational waves. These calculations have been implemented in the public code `BSMTPv3`, which was presented in Chapter 7. The code `BSMPTv3` was developed and published during the course of this work.

In Chapter 10, we showed that at finite temperature and in the description of the one-loop daisy-resummed effective potential, the possibility of intermediate electromagnetic CB phases exists. Using `BSMPTv3`, we find valid first-order EWPTs from an electromagnetically neutral to a CB phase, where consequently the electromagnetic charge is spontaneously broken. Such CB phases are then found to continuously transition to the electromagnetically neutral, but EW broken minimum in which the universe manifests itself today. First-order EWPTs into CB true phases were further related to a GW background. The associated SNRs for a measurement of this background at the future space-bound interferometer LISA, are found to be below the estimated sensitivity.

In Chapter 11 the model 'CP in the Dark' was studied with `BSMPTv3` w.r.t. its ability to enable first-order EWPTs and explain dark matter. We find wide ranges of the parameter space to be able to source strong first-order EWPTs in agreement with theoretical and experimental constraints. Furthermore, the dark matter candidate h_1 can saturate the experimentally measured relic density as well as escape direct detection. In correlation to strong first-order EWPTs, 'CP in the Dark' is found to be able to source gravitational waves that will lead to detectable signals at LISA, with SNR > 10. We also investigated different phase histories that allow for a one-step first-order EWPT from an EW symmetric false to an EW broken true phase. In addition to the explicit $\mathcal{CP}$ violation that is in the dark sector at zero temperature, at finite temperature, phase histories are possible that allow for additional $\mathcal{CP}$ violation via the generation of a non-zero complex phase between the scalar doublets, which is parametrized by a non-zero $\mathcal{CP}$-violating VEV coordinate. Together with a strong first-order EWPT, the additional $\mathcal{CP}$ violation makes 'CP in the Dark' a promising model to be studied further in the context of the generation of the matter–antimatter asymmetry in the early universe.

Based on the presented findings, there are numerous directions that can be pursued in the future. For 'CP in the Dark' a calculation of the baryon asymmetry based on the present initial conditions could reveal if the additional $\mathcal{CP}$ violation can be successfully transferred to the visible sector and lead to the generation of enough matter excess that is then conserved in a strong first-order EWPT. Additionally, a future analysis on domain walls in this model might reveal the necessity of additional constraints on the parameter space. Moreover, a more complete understanding of the composition of the universe during a CB phase in the 2HDM could shed light on how such a phase in detail could influence the cosmological history. Finally, the presented study is based on the assumption that the one-loop daisy-resummed effective potential yields a perturbatively valid description of the physics at temperatures around the EWPT. This assumption could be replaced by an EFT-motivated approach with a careful consideration of all relevant scales. Additionally, the presented derivation of a GW signal from a first-order EWPT relies on assumptions, e.g. of the energy density content of the universe and of a simplified solution to the set of hydrodynamic equations and relies on numerical fits for the GW spectrum. While this approach allowed us to estimate the potential of the presented models to generate an observable GW background through first-order EWPTs, any step of the calculation could be refined with more precise calculations and approaches that may become available in the future.

In summary, we outlined several BSM avenues that agree with experimental collider data and moreover fill in shortcomings of the SM. The presented BSM scenarios allow for a first-order EWPT. The search for a first-order EWPT is especially interesting, as it provides a link between collider physics and early universe cosmology. With the upcoming experimental program of space-bound interferometers, the study of first-order EWPTs presents exciting avenues for possible groundbreaking discoveries. New physics might just be 'around the corner' and the observation of a first-order EWPT, e.g. through the GW background, would then be a clear evidence for it.

Acknowledgements

I would like to express my most sincere gratitude to Prof. Dr. Milada M. Mühlleitner for providing me the opportunity to work on and learn about many fascinating and inspiring topics, for her continuous invaluable guidance, support and encouragement, for countless always valuable discussions, feedback and advice at all stages of this work and for supporting my participation in several conferences, workshops, and summer schools. I also thank Prof. Dr. T. Schwetz-Mangold for being the second reviewer of this thesis.

Furthermore, I would like to thank everyone that I was able to work together with during this time, and from whom I was honoured to have learnt and continue to learn a lot: Anisha, Mayumi Aoki, Duarte Azevedo, Philipp Basler, Christoph Borschensky, Christoph Englert, Pedro Gabriel, Igor Ivanov, Jonas Müller, Rui Santos, Hiroto Shibuya, and João Viana. In particular, I would like to express my thanks to João, with whom the development of `BSMPTv3` was not only enjoyable but also a most rewarding experience. Also, thanks to Philipp and Jonas for always providing advice on `BSMPT`. Many thanks to Thomas Biekötter for countless discussions from which I have learnt and continue to learn a lot. Thanks to my PhD colleagues that became friends, Felix Egle, Pedro Gabriel, Johann Plotnikov, Karim Elyaouti, Kateryna Radchenko, Francesco Costa, and many more for this fantastic journey together. Also, thanks to Jannis Lang and Vitaly Magerya for being the best office mates I could have hoped for. Thanks also to Thomas Biekötter, Christoph Borschensky, Martin Lang, Vitaly Magerya, and Heike Herber for providing detailed feedback on the written form of this thesis. Thanks to all members of the Institute for Theoretical Physics, who have always had time to discuss physics and have made work an additionally enjoyable experience. Furthermore, thanks to all my IT admin colleagues, Sowmiya Balan, Marco Bonetti, Manuel Egner, Martin Gabelmann, Marius Höfer, Martin Lang, Fabian Lange, Vitaly Magerya, Jonas Matuszak, and Augustin Vestner for keeping our IT infrastructure up and running.

Finally, thanks a lot to Vitaly for being by my side. My biggest thanks goes to Heike and Bernd for their unconditional support and for encouraging me to always be curious. Thank you for everything!

APPENDIX A

Benchmark Points of 'CP in the Dark'

In Table A.1 we provide the input parameters of the four benchmark points BP1–BP4 shown in Figure 11.6 in Chapter 11. In Table A.2 we give the corresponding mass spectra, as well as the critical temperatures T_c and the VEVs of the true vacuum at T_c together with the derived values of ξ_c using Eq. 3.13.

point	m_{22}^2 [GeV^2]	m_S^2 [GeV^2]	Re (A) [GeV]	Im (A) [GeV]	λ_2	
BP1	529 186.148	356 345.493	476.542	−678.778	4.299	
BP2	96 703.414	32 442.949	159.627	−325.391	3.532	
BP3	34 330.331	206 553.473	142.797	814.968	4.679	
BP4	65 258.809	36 279.847	279.502	−326.645	3.660	
point	λ_3	λ_4	λ_5	λ_6	λ_7	λ_8
BP1	−0.782	0.572	0.071	1.053	16.810	−2.093
BP2	−0.796	0.787	−0.055	10.446	7.596	4.683
BP3	2.779	3.093	0.840	10.188	1.243	−4.563
BP4	−0.821	0.220	−0.371	4.715	7.760	14.781

Table A.1.: Input parameters for the benchmark points of Figure 11.6. We set $v_1 = 246.22\,\text{GeV}$ and $m_h = 125.09\,\text{GeV}$. The quartic coupling λ_1 is fixed through $m_h^2 = \lambda_1 v_1^2$ to $\lambda_1 \simeq 0.258$. Also, m_{11}^2 follows from the minimum condition, $m_{11}^2 + \frac{1}{2}\lambda_1 v_1^2 = 0$, to be $m_{11}^2 \simeq -7824\,\text{GeV}^2$ [382].

point	$m_{H^\pm}$	m_{h_1}	m_{h_2}	m_{h_3}	T_c	$\overline{\omega}^{\text{true}}_{\text{EW}}(T_c)$
BP1	710.979	653.473	723.595	980.264	121.96	230.06
BP2	269.386	241.718	308.943	549.265	144.45	234.08
BP3	344.358	102.422	486.105	649.695	204.04	175.41
BP4	200.940	62.680	218.700	560.206	191.38	233.12
point	ξ_c	$\lvert\overline{\omega}^{\text{true}}_{\text{CB}}(T_c)\rvert$	$\lvert\overline{\omega}^{\text{true}}_{1}(T_c)\rvert$	$\lvert\overline{\omega}^{\text{true}}_{2}(T_c)\rvert$	$\lvert\overline{\omega}^{\text{true}}_{\text{CP}}(T_c)\rvert$	$\lvert\overline{\omega}^{\text{true}}_{S}(T_c)\rvert$
BP1	1.89	0	230.06	0	0	0
BP2	1.62	0	234.08	0	0	0
BP3	0.85	0	167.65	5.89	41.83	29.64
BP4	1.22	0	223.42	53.25	39.91	27.97

Table A.2.: Masses, critical temperature and critical VEV, ξ_c, and individual VEVs at T_c of the four benchmark points of Figure 11.6 calculated with `BSMPTv3`. ξ_c is dimensionless, all other units are in GeV. VEV coordinate values $|\overline{\omega}_i| < 10^{-5}$ are numerically zero and set to zero in the table.

APPENDIX B

One-loop Dimension-Six Effective Potential

For the implementation in `BSMPT`, the one-loop daisy-resummed effective potential at finite temperature is constructed in terms of coupling tensors following the notation presented in Ref. [173]. This notation has to be extended when dimension-six EFT terms are included. In this chapter we summarize these extensions in the notation of Ref. [173]. The presented formula were implemented in `BSMPT` for the calculation presented in Chapter 6. We review the tensor notation for a dimension-four Lagrangian in Section B.1 following the conventions of Ref. [110] and generalize the notation to dimension six in Section B.2.

B.1. Tensor Notation for the Four-Dimensional Effective Potential

The one-loop daisy-resummed effective potential at finite temperature is constructed in terms of the tree-level scalar coupling tensors, L^i, L^{ij}, L^{ijk}, L^{ijkl}, the tree-level Yukawa tensor Y^{IJk} and the gauge boson scalar coupling tensor G^{abij}. The Lagrangian is written in terms of tensors multiplied with real scalar component fields Φ_i, fermion fields Ψ_I and electroweak gauge boson fields $A_{a\mu}$ following the notation of Ref. [173]. Terms that do not contribute to the effective potential, i.e. that do not involve scalar fields, as well as derivative terms $\propto \partial_\mu \Phi_i$, are therefore not considered. The Lagrangian is given by

$$\begin{aligned} -\mathcal{L} = & \underbrace{L^i\Phi_i + \frac{1}{2!}L^{ij}\Phi_i\Phi_j + \frac{1}{3!}L^{ijk}\Phi_i\Phi_j\Phi_k + \frac{1}{4!}L^{ijkl}\Phi_i\Phi_j\Phi_k\Phi_l}_{-\mathcal{L}_S} \\ & + \underbrace{\frac{1}{2}Y^{IJk}\Psi_I\Psi_J\phi_k + \text{c.c.}}_{-\mathcal{L}_F} + \underbrace{\frac{1}{4}G^{abij}A_{a\mu}A_b^\mu\Phi_i\Phi_j}_{-\mathcal{L}_G} \, . \end{aligned} \tag{B.1}$$

The indices i, j, k, l run over the number of real scalar component fields, N_0, the indices I, J run over the number of fermion fields, $N_{1/2}$, and the indices a, b run over the number of electroweak gauge boson fields, N_1. We sum over repeated indices following the Einstein sum convention. The daisy-corrected one-loop effective potential at finite temperature can be expressed in terms of these tensors for the four-dimensional renormalizable Lagrangian.

After spontaneous electroweak symmetry breaking, the scalar fields Φ_i are expanded around their VEVs ω_i, $\Phi_i = \phi_i + \overline{\omega}_i$, and the Lagrangian can be written as

$$\begin{aligned}
-\mathcal{L}_S &= \Lambda + \Lambda^{i}_{(S)}\phi_i + \frac{1}{2}\Lambda^{ij}_{(S)}\phi_i\phi_j + \frac{1}{3!}\Lambda^{ijk}_{(S)}\phi_i\phi_j\phi_k + \frac{1}{4!}\Lambda^{ijkl}_{(S)}\phi_i\phi_j\phi_k\phi_l\,, \\
-\mathcal{L}_F &= \frac{1}{2}M^{IJ}\Psi_I\Psi_J + \frac{1}{2}Y^{IJk}\Psi_I\Psi_J\phi_k + \text{c.c.}\,, \\
-\mathcal{L}_G &= \frac{1}{2}\Lambda^{ab}_{(G)}A_{a\mu}A^{\mu}_{b} + \frac{1}{2}\Lambda^{abi}_{(G)}A_{a\mu}A^{\mu}_{b}\phi_i + \frac{1}{4}\Lambda^{abij}_{(G)}A_{a\mu}A^{\mu}_{b}\phi_i\phi_j\,.
\end{aligned} \tag{B.2}$$

The Λ tensors are defined as

$$\Lambda \equiv V^{(0)}(\overline{\omega}_i) = L^{i}\overline{\omega}_i + \frac{1}{2!}L^{ij}\overline{\omega}_i\overline{\omega}_j + \frac{1}{3!}L^{ijk}\overline{\omega}_i\overline{\omega}_j\overline{\omega}_k + \frac{1}{4!}L^{ijkl}\overline{\omega}_i\overline{\omega}_j\overline{\omega}_k\overline{\omega}_l\,, \tag{B.3a}$$

$$\Lambda^{i}_{(S)} \equiv L^{i} + L^{ij}\overline{\omega}_j + \frac{1}{2!}L^{ijk}\overline{\omega}_j\overline{\omega}_k + \frac{1}{3!}L^{ijkl}\overline{\omega}_j\overline{\omega}_k\overline{\omega}_l\,, \tag{B.3b}$$

$$\Lambda^{ij}_{(S)} \equiv L^{ij} + L^{ijk}\overline{\omega}_k + \frac{1}{2!}L^{ijkl}\overline{\omega}_k\overline{\omega}_l\,, \tag{B.3c}$$

$$\Lambda^{ijk}_{(S)} \equiv L^{ijk} + L^{ijkl}\overline{\omega}_l\,, \tag{B.3d}$$

$$\Lambda^{ijkl}_{(S)} \equiv L^{ijkl}\,, \tag{B.3e}$$

$$\Lambda^{ab}_{(G)} \equiv \frac{1}{2!}G^{abij}\overline{\omega}_i\overline{\omega}_j\,, \tag{B.3f}$$

$$\Lambda^{abi}_{(G)} \equiv G^{abij}\overline{\omega}_j\,, \tag{B.3g}$$

$$\Lambda^{abij}_{(G)} \equiv G^{abij}\,, \tag{B.3h}$$

$$\Lambda^{IJ}_{(F)} \equiv M^{*IL}M^{J}_{L}\,, \quad M^{IJ} \equiv Y^{IJk}\overline{\omega}_k\,. \tag{B.3i}$$

The tensors $\Lambda^{ij}_{(S)}$, $\Lambda^{IJ}_{(F)}$ and $\Lambda^{ab}_{(G)}$ are the tree-level mass matrices for the scalars, fermions and electroweak gauge bosons, respectively. The CW and the temperature-dependent potential in terms of these tensors read

$$V_{\text{CW}} = \frac{\epsilon}{4}\sum_{X=S,G,F}(-1)^{2s_X}(1+2s_X)\,\text{Tr}\left[\left(\Lambda^{xy}_{(X)}\right)^2\left(\log\left(\frac{\Lambda^{xy}_{(X)}}{\mu^2}\right) - k_X\right)\right]\,, \tag{B.4}$$

$$V_T^{(1)} = \sum_{X=S,G,F}(-1)^{2s_X}(1+2s_X)\frac{T^4}{2\pi^2}J_{\pm}\left(\frac{\Lambda^{xy}_{(X)}}{T^2}\right)\,, \tag{B.5}$$

with $\epsilon = \frac{1}{(4\pi)^2}$ and $xy \in \{ij, ab, IJ\}$, $X \in \{S, G, F\}$. The CW potential is given in Landau gauge and in the $\overline{\text{MS}}$ scheme, with the renormalization constant k_X

$$k_X = \begin{cases} \frac{5}{6}, & \text{for gauge bosons} \\ \frac{3}{2}, & \text{otherwise} \end{cases}\,. \tag{B.6}$$

Resummation is performed following the Arnold–Espinosa method, as described in Section 4.4 by adding a ring potential of the form

$$V_{\text{ring}} = -\frac{T}{12\pi}\left[\sum_{i=1}^{N_0}\left(\left(\overline{m}_i^2\right)^{3/2} - \left(m_i^2\right)^{3/2}\right) + \sum_{a=1}^{N_1}\left(\left(\overline{m}_a^2\right)^{3/2} - \left(m_a^2\right)^{3/2}\right)\right]\,, \tag{B.7}$$

with m_k^2, $\overline{m}_k^2$ denoting the eigenvalues of $\Lambda^{xy}_{(X)}$ and $\Lambda^{xy}_{(X)} + \Pi^{xy}_{(X)}$, respectively, and with $xy \in ij, ab$ and $X \in \{S, G\}$. The bosonic thermal masses $\Pi^{xy}_{(X)}$ are calculated from their leading hard-thermal loop contribution, which is expressed in the tensor notation as illustrated in Ref. [110].

B.2. Dimension-Six Extension of the Tensor Notation

In Chapter 6, we discuss an extension of the tree-level scalar and Yukawa Lagrangian by dimension-six operators. Following the tensor notation of Ref. [173], we will in the following denote the purely scalar dimension-six operators by L^{ijklmn} and the scalar-fermion dimension-six operators by Y^{IJklm} with i, j, k, l, m, n going up to N_0. The dimension-six tensors are divided by the EFT scale Λ^{-2} and the dimension-six scalar and Yukawa tree-level Lagrangians before spontaneous electroweak symmetry breaking read

$$\begin{aligned} -\mathcal{L}_S &= L^i\Phi_i + \frac{1}{2!}L^{ij}\Phi_i\Phi_j + \frac{1}{3!}L^{ijk}\Phi_i\Phi_j\Phi_k + \frac{1}{4!}L^{ijkl}\Phi_i\Phi_j\Phi_k\Phi_l \\ &\quad + \frac{1}{6!}\frac{L^{ijklmn}}{\Lambda^2}\Phi_i\Phi_j\Phi_k\Phi_l\Phi_m\Phi_n\,, \end{aligned} \tag{B.8a}$$

$$-\mathcal{L}_F = \frac{1}{2}Y^{IJk}\psi_I\psi_J\Phi_k + \frac{1}{2\cdot 3!}\frac{Y^{IJklm}}{\Lambda^2}\psi_I\psi_J\Phi_k\Phi_l\Phi_m + \text{c.c.}\,. \tag{B.8b}$$

After spontaneous electroweak symmetry breaking, the scalar Lagrangian is again written in the Λ basis, which at dimension six is extended by $\Lambda^{ijklm}_{(S)}$ and $\Lambda^{ijklmn}_{(S)}$, which are defined analogously to Eq. (B.2)

$$\begin{aligned} -\mathcal{L}_S &= \Lambda + \Lambda^i_{(S)}\phi_i + \frac{1}{2!}\Lambda^{ij}_{(S)}\phi_i\phi_j + \frac{1}{3!}\Lambda^{ijk}_{(S)}\phi_i\phi_j\phi_k + \frac{1}{4!}\Lambda^{ijkl}_{(S)}\phi_i\phi_j\phi_k\phi_l \\ &\quad + \frac{1}{5!}\Lambda^{ijklm}_{(S)}\phi_i\phi_j\phi_k\phi_l\phi_m + \frac{1}{6!}\Lambda^{ijklmn}_{(S)}\phi_i\phi_j\phi_k\phi_l\phi_m\phi_n\,, \end{aligned} \tag{B.9a}$$

The dimension-six Λ tensors are defined analogously to Eq. (B.3) as

$$\begin{aligned} \Lambda = V^{(0)}(\overline{\omega}_i) &= L^i\overline{\omega}_i + \frac{1}{2!}L^{ij}\overline{\omega}_i\overline{\omega}_j + \frac{1}{3!}L^{ijk}\overline{\omega}_i\overline{\omega}_j\overline{\omega}_k + \frac{1}{4!}L^{ijkl}\overline{\omega}_i\overline{\omega}_j\overline{\omega}_k\overline{\omega}_l \\ &\quad + \frac{1}{6!}\frac{L^{ijklmn}}{\Lambda^2}\overline{\omega}_i\overline{\omega}_j\overline{\omega}_k\overline{\omega}_l\overline{\omega}_m\overline{\omega}_n\,, \end{aligned} \tag{B.10a}$$

$$\Lambda^i_{(S)} = L^i + L^{ij}\overline{\omega}_j + \frac{1}{2!}L^{ijk}\overline{\omega}_j\overline{\omega}_k + \frac{1}{3!}L^{ijkl}\overline{\omega}_j\overline{\omega}_k\overline{\omega}_l + \frac{1}{5!}\frac{L^{ijklmn}}{\Lambda^2}\overline{\omega}_j\overline{\omega}_k\overline{\omega}_l\overline{\omega}_m\overline{\omega}_n\,, \tag{B.10b}$$

$$\Lambda^{ij}_{(S)} = L^{ij} + L^{ijk}\overline{\omega}_k + \frac{1}{2!}L^{ijkl}\overline{\omega}_k\overline{\omega}_l + \frac{1}{4!}\frac{L^{ijklmn}}{\Lambda^2}\overline{\omega}_k\overline{\omega}_l\overline{\omega}_m\overline{\omega}_n\,, \tag{B.10c}$$

$$\Lambda^{ijk}_{(S)} = L^{ijk} + L^{ijkl}\overline{\omega}_l + \frac{1}{3!}\frac{L^{ijklmn}}{\Lambda^2}\overline{\omega}_l\overline{\omega}_m\overline{\omega}_n\,, \tag{B.10d}$$

$$\Lambda^{ijkl}_{(S)} = L^{ijkl} + \frac{1}{2}\frac{L^{ijklmn}}{\Lambda^2}\overline{\omega}_m\overline{\omega}_n\,, \tag{B.10e}$$

$$\Lambda^{ijklm}_{(S)} = \frac{L^{ijklmn}}{\Lambda^2}\overline{\omega}_n\,, \tag{B.10f}$$

$$\Lambda^{ijklmn}_{(S)} = \frac{L^{ijklmn}}{\Lambda^2}\,. \tag{B.10g}$$

The dimension-six fermion mass matrix extended by terms $\propto Y^{IJklm}$ reads

$$M^{IJ} = Y^{IJk}\overline{\omega}_k + \frac{1}{3!}\frac{Y^{IJklm}}{\Lambda^2}\overline{\omega}_k\overline{\omega}_l\overline{\omega}_m\,. \tag{B.11}$$

We choose to take into account leading dimension-six coupling tensor L^{ijklmn} and Y^{IJklm} contributions to the thermal masses, as described further in Chapter 6.

As already detailed in Section 6.3, we absorb the dimension-six shift of the fermion mass matrix into a redefinition of the dimension-four Yukawa coupling in order to take the tree-level fermion masses as input values. In the tensor notation, this corresponds to a redefinition of the form of

$$M^{IJ} = Y^{IJk}_{\text{corr}}\overline{\omega}_k + \frac{1}{3!}\frac{Y^{IJklm}}{\Lambda^2}\overline{\omega}_k\overline{\omega}_l\overline{\omega}_m \quad \text{with} \quad Y^{IJk}_{\text{corr}} = Y^{IJk} - \frac{1}{3!}\frac{Y^{IJklm}}{\Lambda^2}v_l v_m\,, \tag{B.12}$$

with $\overline{\omega}_i\big|_{T=0\,\text{GeV}} = v_i$. This coupling redefinition fixes the zero-temperature fermion masses to

$$M^{IJ}\Big|_{T=0\,\text{GeV}} = Y^{IJk}v_k\,. \tag{B.13}$$

This redefinition of the dimension-four Yukawa coupling shifts dimension-six effects into couplings between scalars and fermions. In Ref. [173] it was shown, using the tensor notation, that the first and second derivatives of the CW potential depend only on the mass matrices as well as the trilinear and quartic couplings, which receive corrections from the dimension-six EFT expansion.[1] The dimension-six corrected trilinear fermion-scalar coupling reads

$$\lambda^{IJi}_{(F)} \equiv \partial^i\,\Lambda^{IJ}_{(F)} = \partial^i\,\left(M^{*IL}M^J_L\right) \tag{B.14a}$$

$$= \left(Y^{*ILi}_{\text{corr}} + \frac{1}{2}\frac{Y^{*ILikl}}{\Lambda^2}\overline{\omega}_k\overline{\omega}_l\right)M^J_L + M^{*IL}\left(Y^{Ji}_{\text{corr},\,L} + \frac{1}{2}\frac{Y^{Jimn}_L}{\Lambda^2}\overline{\omega}_m\overline{\omega}_n\right)\,, \tag{B.14b}$$

which gives a dimension-six contribution to the zero-temperature trilinear coupling of the form

$$\begin{aligned}\lambda^{IJi}_{(F)}\big|_{T=0\,\text{GeV}} = {} & \left(Y^{*ILi}Y^{Jk}_L + Y^{*ILk}Y^{Ji}_L\right)v_k \\ & + \frac{1}{3\Lambda^2}\left(Y^{*ILilm}Y^{Jk}_L + Y^{*ILk}Y^{Jilm}_L\right)v_k v_l v_m\,.\end{aligned} \tag{B.15}$$

Analogously, the dimension-six corrected fermion-scalar quartic coupling reads

$$\begin{aligned}\lambda^{IJij}_{(F)} \equiv \partial^i\partial^j\,\Lambda^{IJ}_{(F)} = {} & \left[Y^{*ILi}_{\text{corr}}Y^{Jj}_{\text{corr},\,L} + \frac{1}{2\Lambda^2}\left(Y^{*ILi}_{\text{corr}}Y^{Jjkl}_L + Y^{*ILikl}Y^{Jj}_{\text{corr},\,L}\right)\overline{\omega}_k\overline{\omega}_l + (i\leftrightarrow j)\right] \\ & + \frac{1}{\Lambda^2}\left(Y^{*ILijk}Y^{Jl}_{\text{corr},\,L} + Y^{*ILk}_{\text{corr}}Y^{Jijl}_L\right)\overline{\omega}_k\overline{\omega}_l + \mathcal{O}(\Lambda^{-4})\,,\end{aligned} \tag{B.16}$$

and

$$\lambda^{IJij}_{(F)}\big|_{T=0\,\text{GeV}} = \left[Y^{*ILi}Y^{Jj}_L + \frac{1}{3\Lambda^2}\left(Y^{*ILi}Y^{Jjkl}_L + Y^{*ILikl}Y^{Jj}_L\right)v_k v_l + (i\leftrightarrow j)\right] \tag{B.17}$$

$$+ \frac{1}{\Lambda^2}\left(Y^{*ILijk}Y^{Jl}_L + Y^{*ILk}Y^{Jijl}_L\right)v_k v_l + \mathcal{O}(\Lambda^{-4})\,. \tag{B.18}$$

The dimension-six corrected trilinear and quartic scalar self-couplings are

$$\lambda^{ijk}_{(S)} \equiv \partial^i\Lambda^{jk}_{(S)} = \Lambda^{ijk}_{(S)}\,, \quad \text{and} \quad \lambda^{ijkl}_{(S)} \equiv \partial^i\partial^j\Lambda^{kl}_{(S)} = \Lambda^{ijkl}_{(S)}\,, \tag{B.19}$$

as defined in Eq. (B.10).

---

[1] The OS-renormalization scheme only requires derivatives of the CW potential up to second order. Therefore, the derivation of Ref. [173] generalizes to dimension six, as only for the third and higher derivatives, the dimension-six coupling structure would generate new quintic and sextic vertices.

References

[1] S. L. Glashow. “Partial Symmetries of Weak Interactions”. In: *Nucl. Phys.* 22 (1961), pp. 579–588. DOI: `10.1016/0029-5582(61)90469-2`.

[2] S. Weinberg. “A Model of Leptons”. In: *Phys. Rev. Lett.* 19 (1967), pp. 1264–1266. DOI: `10.1103/PhysRevLett.19.1264`.

[3] A. Salam. “Weak and Electromagnetic Interactions”. In: *Conf. Proc. C* 680519 (1968), pp. 367–377. DOI: `10.1142/9789812795915_0034`.

[4] S. L. Glashow, J. Iliopoulos, and L. Maiani. “Weak Interactions with Lepton-Hadron Symmetry”. In: *Phys. Rev. D* 2 (1970), pp. 1285–1292. DOI: `10.1103/PhysRevD.2.1285`.

[5] G. ’t Hooft. “Renormalization of Massless Yang-Mills Fields”. In: *Nucl. Phys. B* 33 (1971), pp. 173–199. DOI: `10.1016/0550-3213(71)90395-6`.

[6] J. C. Taylor. “Ward Identities and Charge Renormalization of the Yang-Mills Field”. In: *Nucl. Phys. B* 33 (1971), pp. 436–444. DOI: `10.1016/0550-3213(71)90297-5`.

[7] G. ’t Hooft. “Renormalizable Lagrangians for Massive Yang-Mills Fields”. In: *Nucl. Phys. B* 35 (1971). Ed. by J. C. Taylor, pp. 167–188. DOI: `10.1016/0550-3213(71)90139-8`.

[8] A. A. Slavnov. “Ward Identities in Gauge Theories”. In: *Theor. Math. Phys.* 10 (1972), pp. 99–107. DOI: `10.1007/BF01090719`.

[9] G. ’t Hooft and M. J. G. Veltman. “Combinatorics of gauge fields”. In: *Nucl. Phys. B* 50 (1972), pp. 318–353. DOI: `10.1016/S0550-3213(72)80021-X`.

[10] B. W. Lee and J. Zinn-Justin. “Spontaneously Broken Gauge Symmetries Part 1: Preliminaries”. In: *Phys. Rev. D* 5 (1972), pp. 3121–3137. DOI: `10.1103/PhysRevD.5.3121`.

[11] B. W. Lee and J. Zinn-Justin. “Spontaneously Broken Gauge Symmetries Part 2: Perturbation Theory and Renormalization”. In: *Phys. Rev. D* 5 (1972). [Erratum: Phys.Rev.D 8, 4654 (1973)], pp. 3137–3155. DOI: `10.1103/PhysRevD.5.3137`.

[12] B. W. Lee and J. Zinn-Justin. “Spontaneously Broken Gauge Symmetries Part 3: Equivalence”. In: *Phys. Rev. D* 5 (1972), pp. 3155–3160. DOI: `10.1103/PhysRevD.5.3155`.

[13] P. W. Higgs. “Broken symmetries, massless particles and gauge fields”. In: *Phys. Lett.* 12 (1964), pp. 132–133. DOI: `10.1016/0031-9163(64)91136-9`.

[14] F. Englert and R. Brout. “Broken Symmetry and the Mass of Gauge Vector Mesons”. In: *Phys. Rev. Lett.* 13 (1964). Ed. by J. C. Taylor, pp. 321–323. DOI: `10.1103/PhysRevLett.13.321`.

[15] P. W. Higgs. “Broken Symmetries and the Masses of Gauge Bosons”. In: *Phys. Rev. Lett.* 13 (1964). Ed. by J. C. Taylor, pp. 508–509. DOI: `10.1103/PhysRevLett.13.508`.

[16] G. S. Guralnik, C. R. Hagen, and T. W. B. Kibble. “Global Conservation Laws and Massless Particles”. In: *Phys. Rev. Lett.* 13 (1964). Ed. by J. C. Taylor, pp. 585–587. DOI: `10.1103/PhysRevLett.13.585`.

[17] ATLAS, G. Aad et al. “Observation of a new particle in the search for the Standard Model Higgs boson with the ATLAS detector at the LHC”. In: *Phys. Lett. B* 716 (2012), pp. 1–29. DOI: `10.1016/j.physletb.2012.08.020`. arXiv: `1207.7214 [hep-ex]`.

[18] CMS, S. Chatrchyan et al. “Observation of a New Boson at a Mass of 125 GeV with the CMS Experiment at the LHC”. In: *Phys. Lett. B* 716 (2012), pp. 30–61. DOI: `10.1016/j.physletb.2012.08.021`. arXiv: `1207.7235 [hep-ex]`.

[19] CMS, A. Tumasyan et al. “A portrait of the Higgs boson by the CMS experiment ten years after the discovery.” In: *Nature* 607.7917 (2022). [Erratum: Nature 623, (2023)], pp. 60–68. DOI: `10.1038/s41586-022-04892-x`. arXiv: `2207.00043 [hep-ex]`.

[20] ATLAS, G. Aad et al. “A detailed map of Higgs boson interactions by the ATLAS experiment ten years after the discovery”. In: *Nature* 607.7917 (2022). [Erratum: Nature 612, E24 (2022)], pp. 52–59. DOI: `10.1038/s41586-022-04893-w`. arXiv: `2207.00092 [hep-ex]`.

[21] Planck, N. Aghanim et al. “Planck 2018 results. VI. Cosmological parameters”. In: *Astron. Astrophys.* 641 (2020). [Erratum: Astron.Astrophys. 652, C4 (2021)], A6. DOI: `10.1051/0004-6361/201833910`. arXiv: `1807.06209 [astro-ph.CO]`.

[22] Super-Kamiokande, Y. Fukuda et al. “Evidence for oscillation of atmospheric neutrinos”. In: *Phys. Rev. Lett.* 81 (1998), pp. 1562–1567. DOI: `10.1103/PhysRevLett.81.1562`. arXiv: `hep-ex/9807003`.

[23] SNO, Q. R. Ahmad et al. “Measurement of the rate of $\nu_e + d \to p + p + e^-$ interactions produced by ^{8}B solar neutrinos at the Sudbury Neutrino Observatory”. In: *Phys. Rev. Lett.* 87 (2001), p. 071301. DOI: `10.1103/PhysRevLett.87.071301`. arXiv: `nucl-ex/0106015`.

[24] SNO, Q. R. Ahmad et al. “Direct evidence for neutrino flavor transformation from neutral current interactions in the Sudbury Neutrino Observatory”. In: *Phys. Rev. Lett.* 89 (2002), p. 011301. DOI: `10.1103/PhysRevLett.89.011301`. arXiv: `nucl-ex/0204008`.

[25] F. Feruglio. “Pieces of the Flavour Puzzle”. In: *Eur. Phys. J. C* 75.8 (2015), p. 373. DOI: `10.1140/epjc/s10052-015-3576-5`. arXiv: `1503.04071 [hep-ph]`.

[26] K. G. Wilson. “The Renormalization Group and Strong Interactions”. In: *Phys. Rev. D* 3 (1971), p. 1818. DOI: `10.1103/PhysRevD.3.1818`.

[27] E. Gildener. “Gauge Symmetry Hierarchies”. In: *Phys. Rev. D* 14 (1976), p. 1667. DOI: `10.1103/PhysRevD.14.1667`.

[28] S. Weinberg. “Gauge Hierarchies”. In: *Phys. Lett. B* 82 (1979), pp. 387–391. DOI: `10.1016/0370-2693(79)90248-X`.

[29] G. ’t Hooft, C. Itzykson, A. Jaffe, H. Lehmann, P. K. Mitter, I. M. Singer, and R. Stora, eds. *Recent Developments in Gauge Theories. Proceedings, Nato Advanced Study Institute, Cargese, France, August 26 - September 8, 1979.* Vol. 59. 1980, pp.1–438. DOI: `10.1007/978-1-4684-7571-5`.

[30] K. Kajantie, M. Laine, K. Rummukainen, and M. E. Shaposhnikov. “Is there a hot electroweak phase transition at $m_H \gtrsim m_W$?” In: *Phys. Rev. Lett.* 77 (1996), pp. 2887–2890. DOI: `10.1103/PhysRevLett.77.2887`. arXiv: `hep-ph/9605288`.

[31] F. Csikor, Z. Fodor, and J. Heitger. “Endpoint of the hot electroweak phase transition”. In: *Phys. Rev. Lett.* 82 (1999), pp. 21–24. DOI: `10.1103/PhysRevLett.82.21`. arXiv: `hep-ph/9809291`.

[32] A. D. Sakharov. “Violation of CP Invariance, C asymmetry, and baryon asymmetry of the universe”. In: *Pisma Zh. Eksp. Teor. Fiz.* 5 (1967), pp. 32–35. DOI: `10.1070/PU1991v034n05ABEH002497`.

[33] A. G. Cohen, D. B. Kaplan, and A. E. Nelson. “Progress in electroweak baryogenesis”. In: *Ann. Rev. Nucl. Part. Sci.* 43 (1993), pp. 27–70. DOI: `10.1146/annurev.ns.43.120193.000331`. arXiv: `hep-ph/9302210`.

[34] D. E. Morrissey and M. J. Ramsey-Musolf. “Electroweak baryogenesis”. In: *New J. Phys.* 14 (2012), p. 125003. DOI: `10.1088/1367-2630/14/12/125003`. arXiv: `1206.2942 [hep-ph]`.

[35] L. Niemi, H. H. Patel, M. J. Ramsey-Musolf, T. V. I. Tenkanen, and D. J. Weir. “Electroweak phase transition in the real triplet extension of the SM: Dimensional reduction”. In: *Phys. Rev. D* 100.3 (2019), p. 035002. DOI: `10.1103/PhysRevD.100.035002`. arXiv: `1802.10500 [hep-ph]`.

[36] M. Chala, M. Ramos, and M. Spannowsky. “Gravitational wave and collider probes of a triplet Higgs sector with a low cutoff”. In: *Eur. Phys. J. C* 79.2 (2019), p. 156. DOI: `10.1140/epjc/s10052-019-6655-1`. arXiv: `1812.01901 [hep-ph]`.

[37] O. Gould, J. Kozaczuk, L. Niemi, M. J. Ramsey-Musolf, T. V. I. Tenkanen, and D. J. Weir. “Nonperturbative analysis of the gravitational waves from a first-order electroweak phase transition”. In: *Phys. Rev. D* 100.11 (2019), p. 115024. DOI: `10.1103/PhysRevD.100.115024`. arXiv: `1903.11604 [hep-ph]`.

[38] M. J. Ramsey-Musolf. “The electroweak phase transition: a collider target”. In: *JHEP* 09 (2020), p. 179. DOI: `10.1007/JHEP09(2020)179`. arXiv: `1912.07189 [hep-ph]`.

[39] E. Witten. “Cosmic Separation of Phases”. In: *Phys. Rev. D* 30 (1984), pp. 272–285. DOI: `10.1103/PhysRevD.30.272`.

[40] C. J. Hogan. “Gravitational radiation from cosmological phase transitions”. In: *Mon. Not. Roy. Astron. Soc.* 218.4 (1986), pp. 629–636. DOI: `10.1093/mnras/218.4.629`.

[41] M. Kamionkowski, A. Kosowsky, and M. S. Turner. “Gravitational radiation from first order phase transitions”. In: *Phys. Rev. D* 49 (1994), pp. 2837–2851. DOI: `10.1103/PhysRevD.49.2837`. arXiv: `astro-ph/9310044`.

[42] S. J. Huber and T. Konstandin. “Gravitational Wave Production by Collisions: More Bubbles”. In: *JCAP* 09 (2008), p. 022. DOI: `10.1088/1475-7516/2008/09/022`. arXiv: `0806.1828 [hep-ph]`.

[43] C. Caprini, R. Durrer, and G. Servant. “The stochastic gravitational wave background from turbulence and magnetic fields generated by a first-order phase transition”. In: *JCAP* 12 (2009), p. 024. DOI: `10.1088/1475-7516/2009/12/024`. arXiv: `0909.0622 [astro-ph.CO]`.

[44] D. J. Weir. “Revisiting the envelope approximation: gravitational waves from bubble collisions”. In: *Phys. Rev. D* 93.12 (2016), p. 124037. DOI: `10.1103/PhysRevD.93.124037`. arXiv: `1604.08429 [astro-ph.CO]`.

[45] R. Jinno and M. Takimoto. “Gravitational waves from bubble collisions: An analytic derivation”. In: *Phys. Rev. D* 95.2 (2017), p. 024009. DOI: `10.1103/PhysRevD.95.024009`. arXiv: `1605.01403 [astro-ph.CO]`.

[46] NANOGrav, G. Agazie et al. “The NANOGrav 15 yr Data Set: Evidence for a Gravitational-wave Background”. In: *Astrophys. J. Lett.* 951.1 (2023), p. L8. DOI: `10.3847/2041-8213/acdac6`. arXiv: `2306.16213 [astro-ph.HE]`.

[47] NANOGrav, A. Afzal et al. “The NANOGrav 15 yr Data Set: Search for Signals from New Physics”. In: *Astrophys. J. Lett.* 951.1 (2023), p. L11. DOI: `10.3847/2041-8213/acdc91`. arXiv: `2306.16219 [astro-ph.HE]`.

[48] NANOGrav, G. Agazie et al. “The NANOGrav 15 yr Data Set: Constraints on Supermassive Black Hole Binaries from the Gravitational-wave Background”. In: *Astrophys. J. Lett.* 952.2 (2023), p. L37. DOI: `10.3847/2041-8213/ace18b`. arXiv: `2306.16220 [astro-ph.HE]`.

[49] NANOGrav, G. Agazie et al. “The NANOGrav 15 yr Data Set: Search for Anisotropy in the Gravitational-wave Background”. In: *Astrophys. J. Lett.* 956.1 (2023), p. L3. DOI: `10.3847/2041-8213/acf4fd`. arXiv: `2306.16221 [astro-ph.HE]`.

[50] NANOGrav, G. Agazie et al. “The NANOGrav 15 yr Data Set: Bayesian Limits on Gravitational Waves from Individual Supermassive Black Hole Binaries”. In: *Astrophys. J. Lett.* 951.2 (2023), p. L50. DOI: `10.3847/2041-8213/ace18a`. arXiv: `2306.16222 [astro-ph.HE]`.

[51] Particle Data Group, R. L. Workman et al. “Review of Particle Physics”. In: *PTEP* 2022 (2022), p. 083C01. DOI: `10.1093/ptep/ptac097`.

[52] J. C. Romao and J. P. Silva. “A resource for signs and Feynman diagrams of the Standard Model”. In: *Int. J. Mod. Phys. A* 27 (2012), p. 1230025. DOI: `10.1142/S0217751X12300256`. arXiv: `1209.6213 [hep-ph]`.

[53] L. D. Faddeev and V. N. Popov. “Feynman Diagrams for the Yang-Mills Field”. In: *Phys. Lett. B* 25 (1967). Ed. by J.-P. Hsu and D. Fine, pp. 29–30. DOI: `10.1016/0370-2693(67)90067-6`.

[54] KATRIN, M. Aker et al. “Improved Upper Limit on the Neutrino Mass from a Direct Kinematic Method by KATRIN”. In: *Phys. Rev. Lett.* 123.22 (2019), p. 221802. DOI: `10.1103/PhysRevLett.123.221802`. arXiv: `1909.06048 [hep-ex]`.

[55] N. Cabibbo. “Unitary Symmetry and Leptonic Decays”. In: *Phys. Rev. Lett.* 10 (1963), pp. 531–533. DOI: `10.1103/PhysRevLett.10.531`.

[56] M. Kobayashi and T. Maskawa. “CP Violation in the Renormalizable Theory of Weak Interaction”. In: *Prog. Theor. Phys.* 49 (1973), pp. 652–657. DOI: `10.1143/PTP.49.652`.

[57] H. Bahl, P. Bechtle, S. Heinemeyer, J. Katzy, T. Klingl, K. Peters, M. Saimpert, T. Stefaniak, and G. Weiglein. “Indirect $\mathcal{CP}$ probes of the Higgs-top-quark interaction: current LHC constraints and future opportunities”. In: *JHEP* 11 (2020), p. 127. DOI: `10.1007/JHEP11(2020)127`. arXiv: `2007.08542 [hep-ph]`.

[58] ATLAS, CMS, G. Aad et al. “Combined Measurement of the Higgs Boson Mass in pp Collisions at $\sqrt{s} = 7$ and 8 TeV with the ATLAS and CMS Experiments”. In: *Phys. Rev. Lett.* 114 (2015), p. 191803. DOI: `10.1103/PhysRevLett.114.191803`. arXiv: `1503.07589 [hep-ex]`.

[59] ATLAS, G. Aad et al. “Constraints on the Higgs boson self-coupling from single- and double-Higgs production with the ATLAS detector using pp collisions at s=13 TeV”. In: *Phys. Lett. B* 843 (2023), p. 137745. DOI: `10.1016/j.physletb.2023.137745`. arXiv: `2211.01216 [hep-ex]`.

[60] D. Ross and M. Veltman. “Neutral currents and the Higgs mechanism”. In: *Nuclear Physics B* 95.1 (1975), pp. 135–147. ISSN: 0550-3213. DOI: `10.1016/0550-3213(75)90485-X`.

[61] P. Langacker. “Grand Unified Theories and Proton Decay”. In: *Phys. Rept.* 72 (1981), p. 185. DOI: `10.1016/0370-1573(81)90059-4`.

[62] J. F. Gunion, H. E. Haber, G. L. Kane, and S. Dawson. *The Higgs Hunter’s Guide.* Vol. 80. 2000.

[63] Y. B. Zeldovich, I. Y. Kobzarev, and L. B. Okun. “Cosmological Consequences of the Spontaneous Breakdown of Discrete Symmetry”. In: *Zh. Eksp. Teor. Fiz.* 67 (1974), pp. 3–11.

[64] T. W. B. Kibble. “Topology of Cosmic Domains and Strings”. In: *J. Phys. A* 9 (1976), pp. 1387–1398. DOI: `10.1088/0305-4470/9/8/029`.

[65] W. H. Zurek. “Cosmological Experiments in Superfluid Helium?” In: *Nature* 317 (1985), pp. 505–508. DOI: `10.1038/317505a0`.

[66] P. Basler, L. Biermann, M. Mühlleitner, J. Müller, R. Santos, and J. Viana. “BSMPT v3 A Tool for Phase Transitions and Primordial Gravitational Waves in Extended Higgs Sectors”. In: (Apr. 2024). arXiv: `2404.19037 [hep-ph]`.

[67] W. H. Press, B. S. Ryden, and D. N. Spergel. “Dynamical Evolution of Domain Walls in an Expanding Universe”. In: *Astrophys. J.* 347 (1989), pp. 590–604. DOI: `10.1086/168151`.

[68] S. E. Larsson, S. Sarkar, and P. L. White. “Evading the cosmological domain wall problem”. In: *Phys. Rev. D* 55 (1997), pp. 5129–5135. DOI: `10.1103/PhysRevD.55.5129`. arXiv: `hep-ph/9608319`.

[69] A. Lazanu, C. J. A. P. Martins, and E. P. S. Shellard. “Contribution of domain wall networks to the CMB power spectrum”. In: *Phys. Lett. B* 747 (2015), pp. 426–432. DOI: `10.1016/j.physletb.2015.06.034`. arXiv: `1505.03673 [astro-ph.CO]`.

[70] R. A. Battye, A. Pilaftsis, and D. G. Viatic. “Domain wall constraints on two-Higgs-doublet models with Z_2 symmetry”. In: *Phys. Rev. D* 102 (12 Dec. 2020), p. 123536. DOI: `10.1103/PhysRevD.102.123536`.

[71] WMAP, G. Hinshaw et al. “Nine-Year Wilkinson Microwave Anisotropy Probe (WMAP) Observations: Cosmological Parameter Results”. In: *Astrophys. J. Suppl.* 208 (2013), p. 19. DOI: `10.1088/0067-0049/208/2/19`. arXiv: `1212.5226 [astro-ph.CO]`.

[72] E. W. Kolb and M. S. Turner. *The Early Universe.* Vol. 69. 1990. ISBN: 978-0-201-62674-2. DOI: `10.1201/9780429492860`.

[73] M. Bauer and T. Plehn. *Yet Another Introduction to Dark Matter: The Particle Physics Approach.* Vol. 959. Lecture Notes in Physics. Springer, 2019. DOI: `10.1007/978-3-030-16234-4`. arXiv: `1705.01987 [hep-ph]`.

[74] D. Baumann. “Primordial Cosmology”. In: *PoS* TASI2017 (2018), p. 009. DOI: `10.22323/1.305.0009`. arXiv: `1807.03098 [hep-th]`.

[75] D. Baumann. *Cosmology.* Cambridge University Press, July 2022. ISBN: 978-1-108-93709-2, 978-1-108-83807-8. DOI: `10.1017/9781108937092`.

[76] *SDSS Sloan Digital Sky Survey.* Accessed: 2024-05-26. URL: `https://www.sdss.org/`.

[77] F. Zwicky. “Die Rotverschiebung von extragalaktischen Nebeln”. In: *Helv. Phys. Acta* 6 (1933), pp. 110–127. DOI: `10.1007/s10714-008-0707-4`.

[78] A. G. Riess, S. Casertano, W. Yuan, J. B. Bowers, L. Macri, J. C. Zinn, and D. Scolnic. “Cosmic Distances Calibrated to 1% Precision with Gaia EDR3 Parallaxes and Hubble Space Telescope Photometry of 75 Milky Way Cepheids Confirm Tension with ΛCDM”. In: *Astrophys. J. Lett.* 908.1 (2021), p. L6. DOI: `10.3847/2041-8213/abdbaf`. arXiv: `2012.08534 [astro-ph.CO]`.

[79] E. Di Valentino, O. Mena, S. Pan, L. Visinelli, W. Yang, A. Melchiorri, D. F. Mota, A. G. Riess, and J. Silk. "In the realm of the Hubble tensiona review of solutions". In: *Class. Quant. Grav.* 38.15 (2021), p. 153001. DOI: `10.1088/1361-6382/ac086d`. arXiv: `2103.01183 [astro-ph.CO]`.

[80] CODATA. *Internationally recommended 2018 values of the Fundamental Physical Constants.* Accessed: 2024-05-26. URL: `https://physics.nist.gov/cuu/Constants/index.html`.

[81] L. Husdal. "On Effective Degrees of Freedom in the Early Universe". In: *Galaxies* 4.4 (2016), p. 78. DOI: `10.3390/galaxies4040078`. arXiv: `1609.04979 [astro-ph.CO]`.

[82] F. Zwicky. "On the Masses of Nebulae and of Clusters of Nebulae". In: *Astrophys. J.* 86 (1937), pp. 217–246. DOI: `10.1086/143864`.

[83] V. C. Rubin and W. K. Ford Jr. "Rotation of the Andromeda Nebula from a Spectroscopic Survey of Emission Regions". In: *Astrophys. J.* 159 (1970), pp. 379–403. DOI: `10.1086/150317`.

[84] M. Davis, G. Efstathiou, C. S. Frenk, and S. D. M. White. "The Evolution of Large Scale Structure in a Universe Dominated by Cold Dark Matter". In: *Astrophys. J.* 292 (1985). Ed. by M. A. Srednicki, pp. 371–394. DOI: `10.1086/163168`.

[85] S. Dodelson. "The Real Problem with MOND". In: *Int. J. Mod. Phys. D* 20 (2011), pp. 2749–2753. DOI: `10.1142/S0218271811020561`. arXiv: `1112.1320 [astro-ph.CO]`.

[86] ATLAS, G. Aad et al. "Search for invisible Higgs-boson decays in events with vector-boson fusion signatures using 139 fb^{-1} of proton-proton data recorded by the ATLAS experiment". In: *JHEP* 08 (2022), p. 104. DOI: `10.1007/JHEP08(2022)104`. arXiv: `2202.07953 [hep-ex]`.

[87] CMS, A. Tumasyan et al. "A search for decays of the Higgs boson to invisible particles in events with a top-antitop quark pair or a vector boson in proton-proton collisions at $\sqrt{s} = 13\,\mathrm{TeV}$". In: *Eur. Phys. J. C* 83.10 (2023), p. 933. DOI: `10.1140/epjc/s10052-023-11952-7`. arXiv: `2303.01214 [hep-ex]`.

[88] XENON, E. Aprile et al. "Dark Matter Search Results from a One Ton-Year Exposure of XENON1T". In: *Phys. Rev. Lett.* 121.11 (2018), p. 111302. DOI: `10.1103/PhysRevLett.121.111302`. arXiv: `1805.12562 [astro-ph.CO]`.

[89] PandaX-4T, Y. Meng et al. "Dark Matter Search Results from the PandaX-4T Commissioning Run". In: *Phys. Rev. Lett.* 127.26 (2021), p. 261802. DOI: `10.1103/PhysRevLett.127.261802`. arXiv: `2107.13438 [hep-ex]`.

[90] LZ, J. Aalbers et al. "First Dark Matter Search Results from the LUX-ZEPLIN (LZ) Experiment". In: *Phys. Rev. Lett.* 131.4 (2023), p. 041002. DOI: `10.1103/PhysRevLett.131.041002`. arXiv: `2207.03764 [hep-ex]`.

[91] XENON, E. Aprile et al. "First Dark Matter Search with Nuclear Recoils from the XENONnT Experiment". In: *Phys. Rev. Lett.* 131.4 (2023), p. 041003. DOI: `10.1103/PhysRevLett.131.041003`. arXiv: `2303.14729 [hep-ex]`.

[92] R. K. Leane. "Indirect Detection of Dark Matter in the Galaxy". In: *3rd World Summit on Exploring the Dark Side of the Universe.* 2020, pp. 203–228. arXiv: `2006.00513 [hep-ph]`.

[93] N. S. Manton. "Topology in the Weinberg-Salam Theory". In: *Phys. Rev. D* 28 (1983), p. 2019. DOI: `10.1103/PhysRevD.28.2019`.

[94] F. R. Klinkhamer and N. S. Manton. "A Saddle Point Solution in the Weinberg-Salam Theory". In: *Phys. Rev. D* 30 (1984), p. 2212. DOI: `10.1103/PhysRevD.30.2212`.

[95] V. A. Rubakov and M. E. Shaposhnikov. “Electroweak baryon number nonconservation in the early universe and in high-energy collisions”. In: *Usp. Fiz. Nauk* 166 (1996), pp. 493–537. DOI: `10.1070/PU1996v039n05ABEH000145`. arXiv: `hep-ph/9603208`.

[96] W. Bernreuther. “CP violation and baryogenesis”. In: *Lect. Notes Phys.* 591 (2002), pp. 237–293. arXiv: `hep-ph/0205279`.

[97] V. Rubakov and D. Gorbunov. *Introduction To The Theory Of The Early Universe: Hot Big Bang Theory (Second Edition).* World Scientific Publishing Company, 2017. ISBN: 9789813220058.

[98] R. D. Pisarski and F. Wilczek. “Remarks on the Chiral Phase Transition in Chromodynamics”. In: *Phys. Rev. D* 29 (1984), pp. 338–341. DOI: `10.1103/PhysRevD.29.338`.

[99] M. Sher. “Electroweak Higgs Potentials and Vacuum Stability”. In: *Phys. Rept.* 179 (1989), pp. 273–418. DOI: `10.1016/0370-1573(89)90061-6`.

[100] W. Heisenberg and H. Euler. “Consequences of Dirac’s theory of positrons”. In: *Z. Phys.* 98.11-12 (1936), pp. 714–732. DOI: `10.1007/BF01343663`. arXiv: `physics/0605038`.

[101] J. S. Schwinger. “On gauge invariance and vacuum polarization”. In: *Phys. Rev.* 82 (1951). Ed. by K. A. Milton, pp. 664–679. DOI: `10.1103/PhysRev.82.664`.

[102] J. Goldstone, A. Salam, and S. Weinberg. “Broken Symmetries”. In: *Phys. Rev.* 127 (1962), pp. 965–970. DOI: `10.1103/PhysRev.127.965`.

[103] G. Jona-Lasinio. “Relativistic field theories with symmetry breaking solutions”. In: *Nuovo Cim.* 34 (1964), pp. 1790–1795. DOI: `10.1007/BF02750573`.

[104] S. R. Coleman and E. J. Weinberg. “Radiative Corrections as the Origin of Spontaneous Symmetry Breaking”. In: *Phys. Rev. D* 7 (1973), pp. 1888–1910. DOI: `10.1103/PhysRevD.7.1888`.

[105] R. Jackiw. “Functional evaluation of the effective potential”. In: *Phys. Rev. D* 9 (1974), p. 1686. DOI: `10.1103/PhysRevD.9.1686`.

[106] M. Quiros. “Finite temperature field theory and phase transitions”. In: *ICTP Summer School in High-Energy Physics and Cosmology.* Jan. 1999, pp. 187–259. arXiv: `hep-ph/9901312`.

[107] M. Laine and A. Vuorinen. *Basics of Thermal Field Theory.* Vol. 925. Springer, 2016. DOI: `10.1007/978-3-319-31933-9`. arXiv: `1701.01554 [hep-ph]`.

[108] L. F. Abbott. “Introduction to the Background Field Method”. In: *Acta Phys. Polon. B* 13 (1982), p. 33.

[109] M. E. Peskin and D. V. Schroeder. *An Introduction to quantum field theory.* Reading, USA: Addison-Wesley, 1995. ISBN: 978-0-201-50397-5.

[110] P. Basler and M. Mühlleitner. “BSMPT (Beyond the Standard Model Phase Transitions): A tool for the electroweak phase transition in extended Higgs sectors”. In: *Comput. Phys. Commun.* 237 (2019), pp. 62–85. DOI: `10.1016/j.cpc.2018.11.006`. arXiv: `1803.02846 [hep-ph]`.

[111] L. Dolan and R. Jackiw. “Gauge Invariant Signal for Gauge Symmetry Breaking”. In: *Phys. Rev. D* 9 (1974), p. 2904. DOI: `10.1103/PhysRevD.9.2904`.

[112] I. J. R. Aitchison and C. M. Fraser. “Gauge Invariance and the Effective Potential”. In: *Annals Phys.* 156 (1984), p. 1. DOI: `10.1016/0003-4916(84)90209-4`.

[113] H. H. Patel and M. J. Ramsey-Musolf. “Baryon Washout, Electroweak Phase Transition, and Perturbation Theory”. In: *JHEP* 07 (2011), p. 029. DOI: `10.1007/JHEP07(2011)029`. arXiv: `1101.4665 [hep-ph]`.

[114] C. Wainwright, S. Profumo, and M. J. Ramsey-Musolf. “Gravity Waves from a Cosmological Phase Transition: Gauge Artifacts and Daisy Resummations”. In: *Phys. Rev. D* 84 (2011), p. 023521. DOI: `10.1103/PhysRevD.84.023521`. arXiv: `1104.5487 [hep-ph]`.

[115] M. Garny and T. Konstandin. “On the gauge dependence of vacuum transitions at finite temperature”. In: *JHEP* 07 (2012), p. 189. DOI: `10.1007/JHEP07(2012)189`. arXiv: `1205.3392 [hep-ph]`.

[116] B. M. Kastening. “Renormalization group improvement of the effective potential in massive phi**4 theory”. In: *Phys. Lett. B* 283 (1992), pp. 287–292. DOI: `10.1016/0370-2693(92)90021-U`.

[117] C. Ford, D. R. T. Jones, P. W. Stephenson, and M. B. Einhorn. “The Effective potential and the renormalization group”. In: *Nucl. Phys. B* 395 (1993), pp. 17–34. DOI: `10.1016/0550-3213(93)90206-5`. arXiv: `hep-lat/9210033`.

[118] M. Bando, T. Kugo, N. Maekawa, and H. Nakano. “Improving the effective potential”. In: *Phys. Lett. B* 301 (1993), pp. 83–89. DOI: `10.1016/0370-2693(93)90725-W`. arXiv: `hep-ph/9210228`.

[119] S.-B. Liao and M. Strickland. “Dimensional crossover and effective exponents”. In: *Nucl. Phys. B* 497 (1997), pp. 611–638. DOI: `10.1016/S0550-3213(97)00212-5`. arXiv: `hep-th/9604125`.

[120] H. Nakkagawa and H. Yokota. “RG improvement of the effective potential at finite temperature”. In: *Mod. Phys. Lett. A* 11 (1996), pp. 2259–2269. DOI: `10.1142/S0217732396002253`.

[121] T. Matsubara. “A New approach to quantum statistical mechanics”. In: *Prog. Theor. Phys.* 14 (1955), pp. 351–378. DOI: `10.1143/PTP.14.351`.

[122] P. B. Arnold and O. Espinosa. “The Effective potential and first order phase transitions: Beyond leading-order”. In: *Phys. Rev. D* 47 (1993). [Erratum: Phys.Rev.D 50, 6662 (1994)], p. 3546. DOI: `10.1103/PhysRevD.47.3546`. arXiv: `hep-ph/9212235`.

[123] D. A. Kirzhnits. “Weinberg model in the hot universe”. In: *JETP Lett.* 15 (1972), pp. 529–531.

[124] D. J. Gross, R. D. Pisarski, and L. G. Yaffe. “QCD and Instantons at Finite Temperature”. In: *Rev. Mod. Phys.* 53 (1981), p. 43. DOI: `10.1103/RevModPhys.53.43`.

[125] R. R. Parwani. “Resummation in a hot scalar field theory”. In: *Phys. Rev. D* 45 (1992). [Erratum: Phys.Rev.D 48, 5965 (1993)], p. 4695. DOI: `10.1103/PhysRevD.45.4695`. arXiv: `hep-ph/9204216`.

[126] D. Curtin, P. Meade, and H. Ramani. “Thermal Resummation and Phase Transitions”. In: *Eur. Phys. J. C* 78.9 (2018), p. 787. DOI: `10.1140/epjc/s10052-018-6268-0`. arXiv: `1612.00466 [hep-ph]`.

[127] J. I. Kapusta and C. Gale. *Finite-Temperature Field Theory: Principles and Applications*. 2nd ed. Cambridge Monographs on Mathematical Physics. Cambridge University Press, 2023.

[128] C. Delaunay, C. Grojean, and J. D. Wells. “Dynamics of Non-renormalizable Electroweak Symmetry Breaking”. In: *JHEP* 04 (2008), p. 029. DOI: `10.1088/1126-6708/2008/04/029`. arXiv: `0711.2511 [hep-ph]`.

[129] T. Biekötter, S. Heinemeyer, J. M. No, M. O. Olea, and G. Weiglein. “Fate of electroweak symmetry in the early Universe: Non-restoration and trapped vacua in the N2HDM”. In: *JCAP* 06 (2021), p. 018. DOI: `10.1088/1475-7516/2021/06/018`. arXiv: `2103.12707 [hep-ph]`.

[130] P. Basler, M. Krause, M. Muhlleitner, J. Wittbrodt, and A. Wlotzka. “Strong First Order Electroweak Phase Transition in the CP-Conserving 2HDM Revisited”. In: *JHEP* 02 (2017), p. 121. DOI: `10.1007/JHEP02(2017)121`. arXiv: `1612.04086 [hep-ph]`.

[131] L. D. Landau. “On the Conservation Laws for Weak Interactions”. In: *Nucl. Phys.* 3 (1957). Ed. by D. ter Haar. DOI: `10.1016/b978-0-08-010586-4.50097-3`.

[132] M. Laine and K. Rummukainen. “What’s new with the electroweak phase transition?” In: *Nucl. Phys. B Proc. Suppl.* 73 (1999). Ed. by T. A. DeGrand, C. E. DeTar, R. Sugar, and D. Toussaint, pp. 180–185. DOI: `10.1016/S0920-5632(99)85017-8`. arXiv: `hep-lat/9809045`.

[133] R. Coimbra, M. O. P. Sampaio, and R. Santos. “ScannerS: Constraining the phase diagram of a complex scalar singlet at the LHC”. In: *Eur. Phys. J. C* 73 (2013), p. 2428. DOI: `10.1140/epjc/s10052-013-2428-4`. arXiv: `1301.2599 [hep-ph]`.

[134] P. M. Ferreira, R. Guedes, M. O. P. Sampaio, and R. Santos. “Wrong sign and symmetric limits and non-decoupling in 2HDMs”. In: *JHEP* 12 (2014), p. 067. DOI: `10.1007/JHEP12(2014)067`. arXiv: `1409.6723 [hep-ph]`.

[135] R. Costa, M. Mühlleitner, M. O. P. Sampaio, and R. Santos. “Singlet Extensions of the Standard Model at LHC Run 2: Benchmarks and Comparison with the NMSSM”. In: *JHEP* 06 (2016), p. 034. DOI: `10.1007/JHEP06(2016)034`. arXiv: `1512.05355 [hep-ph]`.

[136] M. Muhlleitner, M. O. P. Sampaio, R. Santos, and J. Wittbrodt. “The N2HDM under Theoretical and Experimental Scrutiny”. In: *JHEP* 03 (2017), p. 094. DOI: `10.1007/JHEP03(2017)094`. arXiv: `1612.01309 [hep-ph]`.

[137] M. Mühlleitner, M. O. P. Sampaio, R. Santos, and J. Wittbrodt. “ScannerS: parameter scans in extended scalar sectors”. In: *Eur. Phys. J. C* 82.3 (2022), p. 198. DOI: `10.1140/epjc/s10052-022-10139-w`. arXiv: `2007.02985 [hep-ph]`.

[138] R. Costa, R. Guedes, M. O. P. Sampaio, and R. Santos. *ScannerS*. 2014. URL: `https://scanners.hepforge.org/`.

[139] J. Wittbrodt, R. Coimbra, M. Sampaio, and R. Santos. *ScannerS v2.0.0*. 2021. URL: `https://gitlab.com/jonaswittbrodt/ScannerS`.

[140] P. Bechtle, K. Desch, and P. Wienemann. “Fittino, a program for determining MSSM parameters from collider observables using an iterative method”. In: *Comput. Phys. Commun.* 174 (2006), pp. 47–70. DOI: `10.1016/j.cpc.2005.09.002`. arXiv: `hep-ph/0412012`.

[141] A. B. Arbuzov, M. Awramik, M. Czakon, A. Freitas, M. W. Grunewald, K. Monig, S. Riemann, and T. Riemann. “ZFITTER: A Semi-analytical program for fermion pair production in e+ e- annihilation, from version 6.21 to version 6.42”. In: *Comput. Phys. Commun.* 174 (2006), pp. 728–758. DOI: `10.1016/j.cpc.2005.12.009`. arXiv: `hep-ph/0507146`.

[142] H. Flacher, M. Goebel, J. Haller, A. Hocker, K. Monig, and J. Stelzer. “Revisiting the Global Electroweak Fit of the Standard Model and Beyond with Gfitter”. In: *Eur. Phys. J. C* 60 (2009). [Erratum: Eur.Phys.J.C 71, 1718 (2011)], pp. 543–583. DOI: `10.1140/epjc/s10052-009-0966-6`. arXiv: `0811.0009 [hep-ph]`.

[143] GAMBIT, P. Athron et al. “GAMBIT: The Global and Modular Beyond-the-Standard-Model Inference Tool”. In: *Eur. Phys. J. C* 77.11 (2017). [Addendum: Eur.Phys.J.C 78, 98 (2018)], p. 784. DOI: `10.1140/epjc/s10052-017-5321-8`. arXiv: `1705.07908 [hep-ph]`.

[144] J. De Blas et al. "`HEPfit`: a code for the combination of indirect and direct constraints on high energy physics models". In: *Eur. Phys. J. C* 80.5 (2020), p. 456. DOI: `10.1140/epjc/s10052-020-7904-z`. arXiv: `1910.14012 [hep-ph]`.

[145] B. W. Lee, C. Quigg, and H. B. Thacker. "Weak Interactions at Very High-Energies: The Role of the Higgs Boson Mass". In: *Phys. Rev. D* 16 (1977), p. 1519. DOI: `10.1103/PhysRevD.16.1519`.

[146] N. G. Deshpande and E. Ma. "Pattern of Symmetry Breaking with Two Higgs Doublets". In: *Phys. Rev. D* 18 (1978), p. 2574. DOI: `10.1103/PhysRevD.18.2574`.

[147] K. G. Klimenko. "On Necessary and Sufficient Conditions for Some Higgs Potentials to Be Bounded From Below". In: *Theor. Math. Phys.* 62 (1985), pp. 58–65. DOI: `10.1007/BF01034825`.

[148] M. E. Peskin and T. Takeuchi. "A New constraint on a strongly interacting Higgs sector". In: *Phys. Rev. Lett.* 65 (1990), pp. 964–967. DOI: `10.1103/PhysRevLett.65.964`.

[149] M. E. Peskin and T. Takeuchi. "Estimation of oblique electroweak corrections". In: *Phys. Rev. D* 46 (1992), pp. 381–409. DOI: `10.1103/PhysRevD.46.381`.

[150] Gfitter Group, M. Baak, J. Cúth, J. Haller, A. Hoecker, R. Kogler, K. Mönig, M. Schott, and J. Stelzer. "The global electroweak fit at NNLO and prospects for the LHC and ILC". In: *Eur. Phys. J. C* 74 (2014), p. 3046. DOI: `10.1140/epjc/s10052-014-3046-5`. arXiv: `1407.3792 [hep-ph]`.

[151] P. Bechtle, S. Heinemeyer, O. Stål, T. Stefaniak, and G. Weiglein. "*HiggsSignals*: Confronting arbitrary Higgs sectors with measurements at the Tevatron and the LHC". In: *Eur. Phys. J. C* 74.2 (2014), p. 2711. DOI: `10.1140/epjc/s10052-013-2711-4`. arXiv: `1305.1933 [hep-ph]`.

[152] O. Stål and T. Stefaniak. "Constraining extended Higgs sectors with HiggsSignals". In: *PoS* EPS-HEP2013 (2013), p. 314. DOI: `10.22323/1.180.0314`. arXiv: `1310.4039 [hep-ph]`.

[153] P. Bechtle, S. Heinemeyer, O. Stål, T. Stefaniak, and G. Weiglein. "Probing the Standard Model with Higgs signal rates from the Tevatron, the LHC and a future ILC". In: *JHEP* 11 (2014), p. 039. DOI: `10.1007/JHEP11(2014)039`. arXiv: `1403.1582 [hep-ph]`.

[154] P. Bechtle, S. Heinemeyer, T. Klingl, T. Stefaniak, G. Weiglein, and J. Wittbrodt. "HiggsSignals-2: Probing new physics with precision Higgs measurements in the LHC 13 TeV era". In: *Eur. Phys. J. C* 81.2 (2021), p. 145. DOI: `10.1140/epjc/s10052-021-08942-y`. arXiv: `2012.09197 [hep-ph]`.

[155] P. Bechtle, O. Brein, S. Heinemeyer, G. Weiglein, and K. E. Williams. "HiggsBounds: Confronting Arbitrary Higgs Sectors with Exclusion Bounds from LEP and the Tevatron". In: *Comput. Phys. Commun.* 181 (2010), pp. 138–167. DOI: `10.1016/j.cpc.2009.09.003`. arXiv: `0811.4169 [hep-ph]`.

[156] P. Bechtle, O. Brein, S. Heinemeyer, G. Weiglein, and K. E. Williams. "HiggsBounds 2.0.0: Confronting Neutral and Charged Higgs Sector Predictions with Exclusion Bounds from LEP and the Tevatron". In: *Comput. Phys. Commun.* 182 (2011), pp. 2605–2631. DOI: `10.1016/j.cpc.2011.07.015`. arXiv: `1102.1898 [hep-ph]`.

[157] P. Bechtle, O. Brein, S. Heinemeyer, O. Stal, T. Stefaniak, G. Weiglein, and K. Williams. "Recent Developments in HiggsBounds and a Preview of HiggsSignals". In: *PoS* CHARGED2012 (2012). Ed. by R. Enberg and A. Ferrari, p. 024. DOI: `10.22323/1.156.0024`. arXiv: `1301.2345 [hep-ph]`.

[158] P. Bechtle, O. Brein, S. Heinemeyer, O. Stål, T. Stefaniak, G. Weiglein, and K. E. Williams. "HiggsBounds – 4: Improved Tests of Extended Higgs Sectors against Exclusion Bounds from LEP, the Tevatron and the LHC". In: *Eur. Phys. J. C* 74.3 (2014), p. 2693. DOI: `10.1140/epjc/s10052-013-2693-2`. arXiv: `1311.0055 [hep-ph]`.

[159] P. Bechtle, S. Heinemeyer, O. Stal, T. Stefaniak, and G. Weiglein. "Applying Exclusion Likelihoods from LHC Searches to Extended Higgs Sectors". In: *Eur. Phys. J. C* 75.9 (2015), p. 421. DOI: `10.1140/epjc/s10052-015-3650-z`. arXiv: `1507.06706 [hep-ph]`.

[160] P. Bechtle, D. Dercks, S. Heinemeyer, T. Klingl, T. Stefaniak, G. Weiglein, and J. Wittbrodt. "HiggsBounds-5: Testing Higgs Sectors in the LHC 13 TeV Era". In: *Eur. Phys. J. C* 80.12 (2020), p. 1211. DOI: `10.1140/epjc/s10052-020-08557-9`. arXiv: `2006.06007 [hep-ph]`.

[161] H. Bahl, V. M. Lozano, T. Stefaniak, and J. Wittbrodt. "Testing exotic scalars with HiggsBounds". In: *Eur. Phys. J. C* 82.7 (2022), p. 584. DOI: `10.1140/epjc/s10052-022-10446-2`. arXiv: `2109.10366 [hep-ph]`.

[162] H. Bahl, T. Biekötter, S. Heinemeyer, C. Li, S. Paasch, G. Weiglein, and J. Wittbrodt. "HiggsTools: BSM scalar phenomenology with new versions of HiggsBounds and HiggsSignals". In: *Comput. Phys. Commun.* 291 (2023), p. 108803. DOI: `10.1016/j.cpc.2023.108803`. arXiv: `2210.09332 [hep-ph]`.

[163] H. E. Haber and H. E. Logan. "Radiative corrections to the Z b anti-b vertex and constraints on extended Higgs sectors". In: *Phys. Rev. D* 62 (2000), p. 015011. DOI: `10.1103/PhysRevD.62.015011`. arXiv: `hep-ph/9909335`.

[164] O. Deschamps, S. Descotes-Genon, S. Monteil, V. Niess, S. T'Jampens, and V. Tisserand. "The Two Higgs Doublet of Type II facing flavour physics data". In: *Phys. Rev. D* 82 (2010), p. 073012. DOI: `10.1103/PhysRevD.82.073012`. arXiv: `0907.5135 [hep-ph]`.

[165] F. Mahmoudi and O. Stal. "Flavor constraints on the two-Higgs-doublet model with general Yukawa couplings". In: *Phys. Rev. D* 81 (2010), p. 035016. DOI: `10.1103/PhysRevD.81.035016`. arXiv: `0907.1791 [hep-ph]`.

[166] T. Hermann, M. Misiak, and M. Steinhauser. "$\bar{B} \to X_s\gamma$ in the Two Higgs Doublet Model up to Next-to-Next-to-Leading Order in QCD". In: *JHEP* 11 (2012), p. 036. DOI: `10.1007/JHEP11(2012)036`. arXiv: `1208.2788 [hep-ph]`.

[167] M. Misiak et al. "Updated NNLO QCD predictions for the weak radiative B-meson decays". In: *Phys. Rev. Lett.* 114.22 (2015), p. 221801. DOI: `10.1103/PhysRevLett.114.221801`. arXiv: `1503.01789 [hep-ph]`.

[168] M. Misiak and M. Steinhauser. "Weak radiative decays of the B meson and bounds on $M_{H^\pm}$ in the Two-Higgs-Doublet Model". In: *Eur. Phys. J. C* 77.3 (2017), p. 201. DOI: `10.1140/epjc/s10052-017-4776-y`. arXiv: `1702.04571 [hep-ph]`.

[169] M. Misiak, A. Rehman, and M. Steinhauser. "Towards $\overline{B} \to X_s\gamma$ at the NNLO in QCD without interpolation in m_c". In: *JHEP* 06 (2020), p. 175. DOI: `10.1007/JHEP06(2020)175`. arXiv: `2002.01548 [hep-ph]`.

[170] G. Belanger, A. Mjallal, and A. Pukhov. "Recasting direct detection limits within micrOMEGAs and implication for non-standard Dark Matter scenarios". In: *Eur. Phys. J. C* 81.3 (2021), p. 239. DOI: `10.1140/epjc/s10052-021-09012-z`. arXiv: `2003.08621 [hep-ph]`.

[171] ACME, V. Andreev et al. "Improved limit on the electric dipole moment of the electron". In: *Nature* 562.7727 (2018), pp. 355–360. DOI: `10.1038/s41586-018-0599-8`.

[172] P. Basler, M. Mühlleitner, and J. Müller. “BSMPT v2 a tool for the electroweak phase transition and the baryon asymmetry of the universe in extended Higgs Sectors”. In: *Comput. Phys. Commun.* 269 (2021), p. 108124. DOI: `10.1016/j.cpc.2021.108124`. arXiv: `2007.01725 [hep-ph]`.

[173] J. E. Camargo-Molina, A. P. Morais, R. Pasechnik, M. O. P. Sampaio, and J. Wessén. “All one-loop scalar vertices in the effective potential approach”. In: *JHEP* 08 (2016), p. 073. DOI: `10.1007/JHEP08(2016)073`. arXiv: `1606.07069 [hep-ph]`.

[174] P. Basler, M. Mühlleitner, and J. Wittbrodt. “The CP-Violating 2HDM in Light of a Strong First Order Electroweak Phase Transition and Implications for Higgs Pair Production”. In: *JHEP* 03 (2018), p. 061. DOI: `10.1007/JHEP03(2018)061`. arXiv: `1711.04097 [hep-ph]`.

[175] P. Basler, M. Mühlleitner, and J. Müller. “Electroweak Phase Transition in Non-Minimal Higgs Sectors”. In: *JHEP* 05 (2020), p. 016. DOI: `10.1007/JHEP05(2020)016`. arXiv: `1912.10477 [hep-ph]`.

[176] G. W. Anderson and L. J. Hall. “The Electroweak phase transition and baryogenesis”. In: *Phys. Rev. D* 45 (1992), pp. 2685–2698. DOI: `10.1103/PhysRevD.45.2685`.

[177] P. Basler, L. Biermann, M. Mühlleitner, and J. Müller. “Electroweak baryogenesis in the CP-violating two-Higgs doublet model”. In: *Eur. Phys. J. C* 83.1 (2023), p. 57. DOI: `10.1140/epjc/s10052-023-11192-9`. arXiv: `2108.03580 [hep-ph]`.

[178] L. Biermann, M. Mühlleitner, and J. Müller. “Electroweak phase transition in a dark sector with CP violation”. In: *Eur. Phys. J. C* 83.5 (2023), p. 439. DOI: `10.1140/epjc/s10052-023-11612-w`. arXiv: `2204.13425 [hep-ph]`.

[179] J. A. Casas, J. R. Espinosa, and M. Quiros. “Improved Higgs mass stability bound in the standard model and implications for supersymmetry”. In: *Phys. Lett. B* 342 (1995), pp. 171–179. DOI: `10.1016/0370-2693(94)01404-Z`. arXiv: `hep-ph/9409458`.

[180] J. R. Espinosa and M. Quiros. “Improved metastability bounds on the standard model Higgs mass”. In: *Phys. Lett. B* 353 (1995), pp. 257–266. DOI: `10.1016/0370-2693(95)00572-3`. arXiv: `hep-ph/9504241`.

[181] G. Isidori, G. Ridolfi, and A. Strumia. “On the metastability of the standard model vacuum”. In: *Nucl. Phys. B* 609 (2001), pp. 387–409. DOI: `10.1016/S0550-3213(01)00302-9`. arXiv: `hep-ph/0104016`.

[182] J. R. Espinosa, G. F. Giudice, and A. Riotto. “Cosmological implications of the Higgs mass measurement”. In: *JCAP* 05 (2008), p. 002. DOI: `10.1088/1475-7516/2008/05/002`. arXiv: `0710.2484 [hep-ph]`.

[183] J. Ellis, J. R. Espinosa, G. F. Giudice, A. Hoecker, and A. Riotto. “The Probable Fate of the Standard Model”. In: *Phys. Lett. B* 679 (2009), pp. 369–375. DOI: `10.1016/j.physletb.2009.07.054`. arXiv: `0906.0954 [hep-ph]`.

[184] F. Bezrukov, M. Y. Kalmykov, B. A. Kniehl, and M. Shaposhnikov. “Higgs Boson Mass and New Physics”. In: *JHEP* 10 (2012). Ed. by G. Moortgat-Pick, p. 140. DOI: `10.1007/JHEP10(2012)140`. arXiv: `1205.2893 [hep-ph]`.

[185] G. Degrassi, S. Di Vita, J. Elias-Miro, J. R. Espinosa, G. F. Giudice, G. Isidori, and A. Strumia. “Higgs mass and vacuum stability in the Standard Model at NNLO”. In: *JHEP* 08 (2012), p. 098. DOI: `10.1007/JHEP08(2012)098`. arXiv: `1205.6497 [hep-ph]`.

[186] K. G. Chetyrkin and M. F. Zoller. “β-function for the Higgs self-interaction in the Standard Model at three-loop level”. In: *JHEP* 04 (2013). [Erratum: JHEP 09, 155 (2013)], p. 091. DOI: `10.1007/JHEP04(2013)091`. arXiv: `1303.2890 [hep-ph]`.

[187] D. Buttazzo, G. Degrassi, P. P. Giardino, G. F. Giudice, F. Sala, A. Salvio, and A. Strumia. “Investigating the near-criticality of the Higgs boson”. In: *JHEP* 12 (2013), p. 089. DOI: `10.1007/JHEP12(2013)089`. arXiv: `1307.3536 [hep-ph]`.

[188] A. Andreassen, W. Frost, and M. D. Schwartz. “Consistent Use of the Standard Model Effective Potential”. In: *Phys. Rev. Lett.* 113.24 (2014), p. 241801. DOI: `10.1103/PhysRevLett.113.241801`. arXiv: `1408.0292 [hep-ph]`.

[189] J. E. Camargo-Molina, B. O’Leary, W. Porod, and F. Staub. “**Vevacious**: A Tool For Finding The Global Minima Of One-Loop Effective Potentials With Many Scalars”. In: *Eur. Phys. J. C* 73.10 (2013), p. 2588. DOI: `10.1140/epjc/s10052-013-2588-2`. arXiv: `1307.1477 [hep-ph]`.

[190] W. G. Hollik, G. Weiglein, and J. Wittbrodt. “Impact of Vacuum Stability Constraints on the Phenomenology of Supersymmetric Models”. In: *JHEP* 03 (2019), p. 109. DOI: `10.1007/JHEP03(2019)109`. arXiv: `1812.04644 [hep-ph]`.

[191] P. M. Ferreira, M. Mühlleitner, R. Santos, G. Weiglein, and J. Wittbrodt. “Vacuum Instabilities in the N2HDM”. In: *JHEP* 09 (2019), p. 006. DOI: `10.1007/JHEP09(2019)006`. arXiv: `1905.10234 [hep-ph]`.

[192] T. D. Lee. “A Theory of Spontaneous T Violation”. In: *Phys. Rev. D* 8 (1973). Ed. by G. Feinberg, pp. 1226–1239. DOI: `10.1103/PhysRevD.8.1226`.

[193] G. C. Branco, P. M. Ferreira, L. Lavoura, M. N. Rebelo, M. Sher, and J. P. Silva. “Theory and phenomenology of two-Higgs-doublet models”. In: *Phys. Rept.* 516 (2012), pp. 1–102. DOI: `10.1016/j.physrep.2012.02.002`. arXiv: `1106.0034 [hep-ph]`.

[194] G. C. Dorsch, S. J. Huber, K. Mimasu, and J. M. No. “Echoes of the Electroweak Phase Transition: Discovering a second Higgs doublet through $A_0 \to ZH_0$”. In: *Phys. Rev. Lett.* 113.21 (2014), p. 211802. DOI: `10.1103/PhysRevLett.113.211802`. arXiv: `1405.5537 [hep-ph]`.

[195] G. C. Dorsch, S. J. Huber, T. Konstandin, and J. M. No. “A Second Higgs Doublet in the Early Universe: Baryogenesis and Gravitational Waves”. In: *JCAP* 05 (2017), p. 052. DOI: `10.1088/1475-7516/2017/05/052`. arXiv: `1611.05874 [hep-ph]`.

[196] G. C. Dorsch, S. J. Huber, K. Mimasu, and J. M. No. “Hierarchical versus degenerate 2HDM: The LHC run 1 legacy at the onset of run 2”. In: *Phys. Rev. D* 93.11 (2016), p. 115033. DOI: `10.1103/PhysRevD.93.115033`. arXiv: `1601.04545 [hep-ph]`.

[197] G. C. Dorsch, S. J. Huber, K. Mimasu, and J. M. No. “The Higgs Vacuum Uplifted: Revisiting the Electroweak Phase Transition with a Second Higgs Doublet”. In: *JHEP* 12 (2017), p. 086. DOI: `10.1007/JHEP12(2017)086`. arXiv: `1705.09186 [hep-ph]`.

[198] D. Gonçalves, A. Kaladharan, and Y. Wu. “Electroweak phase transition in the 2HDM: Collider and gravitational wave complementarity”. In: *Phys. Rev. D* 105.9 (2022), p. 095041. DOI: `10.1103/PhysRevD.105.095041`. arXiv: `2108.05356 [hep-ph]`.

[199] W. Su, A. G. Williams, and M. Zhang. “Strong first order electroweak phase transition in 2HDM confronting future Z & Higgs factories”. In: *JHEP* 04 (2021), p. 219. DOI: `10.1007/JHEP04(2021)219`. arXiv: `2011.04540 [hep-ph]`.

[200] L. Wang. “Inflation, electroweak phase transition, and Higgs searches at the LHC in the two-Higgs-doublet model”. In: *JHEP* 07 (2022), p. 055. DOI: `10.1007/JHEP07(2022)055`. arXiv: `2105.02143 [hep-ph]`.

[201] O. Atkinson, M. Black, A. Lenz, A. Rusov, and J. Wynne. “Cornering the Two Higgs Doublet Model Type II”. In: *JHEP* 04 (2022), p. 172. DOI: `10.1007/JHEP04(2022)172`. arXiv: `2107.05650 [hep-ph]`.

[202] T. Biekötter, S. Heinemeyer, J. M. No, M. O. Olea-Romacho, and G. Weiglein. “The trap in the early Universe: impact on the interplay between gravitational waves and LHC physics in the 2HDM”. In: *JCAP* 03 (2023), p. 031. DOI: `10.1088/1475-7516/2023/03/031`. arXiv: `2208.14466 [hep-ph]`.

[203] ATLAS, G. Aad et al. “ATLAS searches for additional scalars and exotic Higgs boson decays with the LHC Run 2 dataset”. In: (May 2024). arXiv: `2405.04914 [hep-ex]`.

[204] O. Atkinson, M. Black, C. Englert, A. Lenz, A. Rusov, and J. Wynne. “The flavourful present and future of 2HDMs at the collider energy frontier”. In: *JHEP* 11 (2022), p. 139. DOI: `10.1007/JHEP11(2022)139`. arXiv: `2202.08807 [hep-ph]`.

[205] P. Basler, S. Dawson, C. Englert, and M. Mühlleitner. “Showcasing HH production: Benchmarks for the LHC and HL-LHC”. In: *Phys. Rev. D* 99.5 (2019), p. 055048. DOI: `10.1103/PhysRevD.99.055048`. arXiv: `1812.03542 [hep-ph]`.

[206] Anisha, S. Das Bakshi, J. Chakrabortty, and S. Prakash. “Hilbert Series and Plethystics: Paving the path towards 2HDM- and MLRSM-EFT”. In: *JHEP* 09 (2019), p. 035. DOI: `10.1007/JHEP09(2019)035`. arXiv: `1905.11047 [hep-ph]`.

[207] Anisha, L. Biermann, C. Englert, and M. Mühlleitner. “Two Higgs doublets, effective interactions and a strong first-order electroweak phase transition”. In: *JHEP* 08 (2022), p. 091. DOI: `10.1007/JHEP08(2022)091`. arXiv: `2204.06966 [hep-ph]`.

[208] Anisha, D. Azevedo, L. Biermann, C. Englert, and M. Mühlleitner. “Effective 2HDM Yukawa interactions and a strong first-order electroweak phase transition”. In: *JHEP* 02 (2024), p. 045. DOI: `10.1007/JHEP02(2024)045`. arXiv: `2311.06353 [hep-ph]`.

[209] I. F. Ginzburg, I. P. Ivanov, and K. A. Kanishev. “The Evolution of vacuum states and phase transitions in 2HDM during cooling of Universe”. In: *Phys. Rev. D* 81 (2010), p. 085031. DOI: `10.1103/PhysRevD.81.085031`. arXiv: `0911.2383 [hep-ph]`.

[210] H. Abouabid, A. Arhrib, D. Azevedo, J. E. Falaki, P. M. Ferreira, M. Mühlleitner, and R. Santos. “Benchmarking di-Higgs production in various extended Higgs sector models”. In: *JHEP* 09 (2022), p. 011. DOI: `10.1007/JHEP09(2022)011`. arXiv: `2112.12515 [hep-ph]`.

[211] A. Crivellin, M. Ghezzi, and M. Procura. “Effective Field Theory with Two Higgs Doublets”. In: *JHEP* 09 (2016), p. 160. DOI: `10.1007/JHEP09(2016)160`. arXiv: `1608.00975 [hep-ph]`.

[212] S. Karmakar and S. Rakshit. “Higher dimensional operators in 2HDM”. In: *JHEP* 10 (2017), p. 048. DOI: `10.1007/JHEP10(2017)048`. arXiv: `1707.00716 [hep-ph]`.

[213] U. Banerjee, J. Chakrabortty, S. Prakash, and S. U. Rahaman. “Characters and group invariant polynomials of (super)fields: road to Lagrangian”. In: *Eur. Phys. J. C* 80.10 (2020), p. 938. DOI: `10.1140/epjc/s10052-020-8392-x`. arXiv: `2004.12830 [hep-ph]`.

[214] D. Bodeker, L. Fromme, S. J. Huber, and M. Seniuch. “The Baryon asymmetry in the standard model with a low cut-off”. In: *JHEP* 02 (2005), p. 026. DOI: `10.1088/1126-6708/2005/02/026`. arXiv: `hep-ph/0412366`.

[215] J. Baglio, A. Djouadi, R. Gröber, M. M. Mühlleitner, J. Quevillon, and M. Spira. “The measurement of the Higgs self-coupling at the LHC: theoretical status”. In: *JHEP* 04 (2013), p. 151. DOI: `10.1007/JHEP04(2013)151`. arXiv: `1212.5581 [hep-ph]`.

[216] J. Baglio, F. Campanario, S. Glaus, M. Mühlleitner, J. Ronca, M. Spira, and J. Streicher. “Higgs-Pair Production via Gluon Fusion at Hadron Colliders: NLO QCD Corrections”. In: *JHEP* 04 (2020), p. 181. DOI: `10.1007/JHEP04(2020)181`. arXiv: `2003.03227 [hep-ph]`.

[217] D. E. Ferreira de Lima, A. Papaefstathiou, and M. Spannowsky. "Standard model Higgs boson pair production in the $(b\bar{b})(b\bar{b})$ final state". In: *JHEP* 08 (2014), p. 030. DOI: `10.1007/JHEP08(2014)030`. arXiv: `1404.7139 [hep-ph]`.

[218] CMS, A. M. Sirunyan et al. "Search for nonresonant Higgs boson pair production in the $\mathrm{b\bar{b}b\bar{b}}$ final state at $\sqrt{s} = 13$ TeV". In: *JHEP* 04 (2019), p. 112. DOI: `10.1007/JHEP04(2019)112`. arXiv: `1810.11854 [hep-ex]`.

[219] ATLAS, G. Aad et al. "Search for the $HH \to b\bar{b}b\bar{b}$ process via vector-boson fusion production using proton-proton collisions at $\sqrt{s} = 13$ TeV with the ATLAS detector". In: *JHEP* 07 (2020). [Erratum: JHEP 01, 145 (2021), Erratum: JHEP 05, 207 (2021)], p. 108. DOI: `10.1007/JHEP07(2020)108`. arXiv: `2001.05178 [hep-ex]`.

[220] ATLAS, G. Aad et al. "Search for resonant pair production of Higgs bosons in the $b\bar{b}b\bar{b}$ final state using pp collisions at $\sqrt{s} = 13$ TeV with the ATLAS detector". In: *Phys. Rev. D* 105.9 (2022), p. 092002. DOI: `10.1103/PhysRevD.105.092002`. arXiv: `2202.07288 [hep-ex]`.

[221] CMS, A. Tumasyan et al. "Search for Higgs Boson Pair Production in the Four b Quark Final State in Proton-Proton Collisions at s=13 TeV". In: *Phys. Rev. Lett.* 129.8 (2022), p. 081802. DOI: `10.1103/PhysRevLett.129.081802`. arXiv: `2202.09617 [hep-ex]`.

[222] M. J. Dolan, C. Englert, and M. Spannowsky. "Higgs self-coupling measurements at the LHC". In: *JHEP* 10 (2012), p. 112. DOI: `10.1007/JHEP10(2012)112`. arXiv: `1206.5001 [hep-ph]`.

[223] CMS, A. M. Sirunyan et al. "Search for Higgs boson pair production in the $bb\tau\tau$ final state in proton-proton collisions at $\sqrt(s) = 8$ TeV". In: *Phys. Rev. D* 96.7 (2017), p. 072004. DOI: `10.1103/PhysRevD.96.072004`. arXiv: `1707.00350 [hep-ex]`.

[224] CMS, A. M. Sirunyan et al. "Search for Higgs boson pair production in events with two bottom quarks and two tau leptons in protonproton collisions at $\sqrt{s}$ =13TeV". In: *Phys. Lett. B* 778 (2018), pp. 101–127. DOI: `10.1016/j.physletb.2018.01.001`. arXiv: `1707.02909 [hep-ex]`.

[225] CMS, A. M. Sirunyan et al. "Combination of searches for Higgs boson pair production in proton-proton collisions at $\sqrt{s} = 13$ TeV". In: *Phys. Rev. Lett.* 122.12 (2019), p. 121803. DOI: `10.1103/PhysRevLett.122.121803`. arXiv: `1811.09689 [hep-ex]`.

[226] "Search for resonant and non-resonant Higgs boson pair production in the $b\bar{b}\tau^+\tau^-$ decay channel using 13 TeV pp collision data from the ATLAS detector". In: (2021).

[227] "Combination of searches for non-resonant and resonant Higgs boson pair production in the $b\bar{b}\gamma\gamma$, $b\bar{b}\tau^+\tau^-$ and $b\bar{b}b\bar{b}$ decay channels using pp collisions at $\sqrt{s} = 13$ TeV with the ATLAS detector". In: (2021).

[228] ATLAS, G. Aad et al. "Reconstruction and identification of boosted di-τ systems in a search for Higgs boson pairs using 13 TeV proton-proton collision data in ATLAS". In: *JHEP* 11 (2020), p. 163. DOI: `10.1007/JHEP11(2020)163`. arXiv: `2007.14811 [hep-ex]`.

[229] M. Baak, M. Goebel, J. Haller, A. Hoecker, D. Kennedy, R. Kogler, K. Moenig, M. Schott, and J. Stelzer. "The Electroweak Fit of the Standard Model after the Discovery of a New Boson at the LHC". In: *Eur. Phys. J. C* 72 (2012), p. 2205. DOI: `10.1140/epjc/s10052-012-2205-9`. arXiv: `1209.2716 [hep-ph]`.

[230] A. V. Bednyakov, B. A. Kniehl, A. F. Pikelner, and O. L. Veretin. "Stability of the Electroweak Vacuum: Gauge Independence and Advanced Precision". In: *Phys. Rev. Lett.* 115.20 (2015), p. 201802. DOI: `10.1103/PhysRevLett.115.201802`. arXiv: `1507.08833 [hep-ph]`.

[231] D. Croon, O. Gould, P. Schicho, T. V. I. Tenkanen, and G. White. “Theoretical uncertainties for cosmological first-order phase transitions”. In: *JHEP* 04 (2021), p. 055. DOI: `10.1007/JHEP04(2021)055`. arXiv: `2009.10080 [hep-ph]`.

[232] S. Kanemura, H. Yokoya, and Y.-J. Zheng. “Searches for additional Higgs bosons in multi-top-quarks events at the LHC and the International Linear Collider”. In: *Nucl. Phys. B* 898 (2015), pp. 286–300. DOI: `10.1016/j.nuclphysb.2015.07.005`. arXiv: `1505.01089 [hep-ph]`.

[233] E. Alvarez, D. A. Faroughy, J. F. Kamenik, R. Morales, and A. Szynkman. “Four tops for LHC”. In: *Nucl. Phys. B* 915 (2017), pp. 19–43. DOI: `10.1016/j.nuclphysb.2016.11.024`. arXiv: `1611.05032 [hep-ph]`.

[234] E. Alvarez, A. Juste, and R. M. S. Seoane. “Four-top as probe of light top-philic New Physics”. In: *JHEP* 12 (2019), p. 080. DOI: `10.1007/JHEP12(2019)080`. arXiv: `1910.09581 [hep-ph]`.

[235] F. Blekman, F. Déliot, V. Dutta, and E. Usai. “Four-top quark physics at the LHC”. In: *Universe* 8.12 (2022), p. 638. DOI: `10.3390/universe8120638`. arXiv: `2208.04085 [hep-ex]`.

[236] Anisha, O. Atkinson, A. Bhardwaj, C. Englert, W. Naskar, and P. Stylianou. “BSM reach of four-top production at the LHC”. In: *Phys. Rev. D* 108.3 (2023), p. 035001. DOI: `10.1103/PhysRevD.108.035001`. arXiv: `2302.08281 [hep-ph]`.

[237] ATLAS, G. Aad et al. “Observation of four-top-quark production in the multilepton final state with the ATLAS detector”. In: *Eur. Phys. J. C* 83.6 (2023). [Erratum: Eur.Phys.J.C 84, 156 (2024)], p. 496. DOI: `10.1140/epjc/s10052-023-11573-0`. arXiv: `2303.15061 [hep-ex]`.

[238] CMS, A. Hayrapetyan et al. “Observation of four top quark production in proton-proton collisions at s=13TeV”. In: *Phys. Lett. B* 847 (2023), p. 138290. DOI: `10.1016/j.physletb.2023.138290`. arXiv: `2305.13439 [hep-ex]`.

[239] C. L. Wainwright. “CosmoTransitions: Computing Cosmological Phase Transition Temperatures and Bubble Profiles with Multiple Fields”. In: *Comput. Phys. Commun.* 183 (2012), pp. 2006–2013. DOI: `10.1016/j.cpc.2012.04.004`. arXiv: `1109.4189 [hep-ph]`.

[240] S. R. Coleman. “The Fate of the False Vacuum. 1. Semiclassical Theory”. In: *Phys. Rev. D* 15 (1977). [Erratum: Phys.Rev.D 16, 1248 (1977)], pp. 2929–2936. DOI: `10.1103/PhysRevD.16.1248`.

[241] C. G. Callan Jr. and S. R. Coleman. “The Fate of the False Vacuum. 2. First Quantum Corrections”. In: *Phys. Rev. D* 16 (1977), pp. 1762–1768. DOI: `10.1103/PhysRevD.16.1762`.

[242] A. D. Linde. “On the Vacuum Instability and the Higgs Meson Mass”. In: *Phys. Lett. B* 70 (1977), pp. 306–308. DOI: `10.1016/0370-2693(77)90664-5`.

[243] A. D. Linde. “Fate of the False Vacuum at Finite Temperature: Theory and Applications”. In: *Phys. Lett. B* 100 (1981), pp. 37–40. DOI: `10.1016/0370-2693(81)90281-1`.

[244] P. Athron, C. Balázs, A. Fowlie, L. Morris, and L. Wu. “Cosmological phase transitions: From perturbative particle physics to gravitational waves”. In: *Prog. Part. Nucl. Phys.* 135 (2024), p. 104094. DOI: `10.1016/j.ppnp.2023.104094`. arXiv: `2305.02357 [hep-ph]`.

[245] J. S. Langer. “Statistical theory of the decay of metastable states”. In: *Annals Phys.* 54 (1969), pp. 258–275. DOI: `10.1016/0003-4916(69)90153-5`.

[246] J. S. Langer. "Metastable states". In: *Physica* 73.1 (1974), pp. 61–72. DOI: `10.1016/0031-8914(74)90226-2`.

[247] I. Affleck. "Quantum Statistical Metastability". In: *Phys. Rev. Lett.* 46 (1981), p. 388. DOI: `10.1103/PhysRevLett.46.388`.

[248] A. D. Linde. "Decay of the False Vacuum at Finite Temperature". In: *Nucl. Phys. B* 216 (1983). [Erratum: Nucl.Phys.B 223, 544 (1983)], p. 421. DOI: `10.1016/0550-3213(83)90072-X`.

[249] A. Ekstedt, O. Gould, and J. Hirvonen. "BubbleDet: a Python package to compute functional determinants for bubble nucleation". In: *JHEP* 12 (2023), p. 056. DOI: `10.1007/JHEP12(2023)056`. arXiv: `2308.15652 [hep-ph]`.

[250] M. B. Voloshin, I. Y. Kobzarev, and L. B. Okun. "On bubbles in metastable vacuum". In: *Yad. Fiz.* 20.6 (1974), pp. 1229–34. URL: `https://cds.cern.ch/record/411754`.

[251] G. C. Marques and R. O. Ramos. "Phase transitions and formation of bubbles in the early Universe". In: *Phys. Rev. D* 45 (12 June 1992), pp. 4400–4410. DOI: `10.1103/PhysRevD.45.4400`.

[252] J. M. Cline, G. D. Moore, and G. Servant. "Was the electroweak phase transition preceded by a color broken phase?" In: *Phys. Rev. D* 60 (1999), p. 105035. DOI: `10.1103/PhysRevD.60.105035`. arXiv: `hep-ph/9902220`.

[253] R. Apreda, M. Maggiore, A. Nicolis, and A. Riotto. "Gravitational waves from electroweak phase transitions". In: *Nucl. Phys. B* 631 (2002), pp. 342–368. DOI: `10.1016/S0550-3213(02)00264-X`. arXiv: `gr-qc/0107033`.

[254] S. Baum, M. Carena, N. R. Shah, C. E. M. Wagner, and Y. Wang. "Nucleation is more than critical: A case study of the electroweak phase transition in the NMSSM". In: *JHEP* 03 (2021), p. 055. DOI: `10.1007/JHEP03(2021)055`. arXiv: `2009.10743 [hep-ph]`.

[255] A. H. Guth and S. H. H. Tye. "Phase Transitions and Magnetic Monopole Production in the Very Early Universe". In: *Phys. Rev. Lett.* 44 (1980). [Erratum: Phys. Rev. Lett. 44, 963 (1980)], p. 631. DOI: `10.1103/PhysRevLett.44.631`.

[256] A. H. Guth and E. J. Weinberg. "Cosmological Consequences of a First Order Phase Transition in the SU(5) Grand Unified Model". In: *Phys. Rev. D* 23 (1981), p. 876. DOI: `10.1103/PhysRevD.23.876`.

[257] A. Kolmogorov. "On the Statistical Theory of Metal Crystallization". In: *Izv. Akad. Nauk SSSR, Ser. Math* 1 (1937), pp. 335–360.

[258] W. A. Johnson. "Reaction Kinetics in Processes of Nucleation and Growth". In: 1939.

[259] M. Avrami. "Kinetics of Phase Change. I General Theory". In: *The Journal of Chemical Physics* 7.12 (Dec. 1939), pp. 1103–1112. ISSN: 0021-9606. DOI: `10.1063/1.1750380`.

[260] M. Avrami. "Kinetics of Phase Change. II TransformationTime Relations for Random Distribution of Nuclei". In: *The Journal of Chemical Physics* 8.2 (Feb. 1940), pp. 212–224. ISSN: 0021-9606. DOI: `10.1063/1.1750631`.

[261] M. Avrami. "Granulation, Phase Change, and Microstructure Kinetics of Phase Change. III". In: *The Journal of Chemical Physics* 9.2 (Feb. 1941), pp. 177–184. ISSN: 0021-9606. DOI: `10.1063/1.1750872`.

[262] A. Megevand. "Development of the electroweak phase transition and baryogenesis". In: *Int. J. Mod. Phys. D* 9 (2000), pp. 733–756. DOI: `10.1142/S0218271800000724`. arXiv: `hep-ph/0006177`.

[263] A. Megevand and A. D. Sanchez. “Supercooling and phase coexistence in cosmological phase transitions”. In: *Phys. Rev. D* 77 (2008), p. 063519. DOI: `10.1103/PhysRevD.77.063519`. arXiv: `0712.1031 [hep-ph]`.

[264] P. Athron, C. Balázs, and L. Morris. “Supercool subtleties of cosmological phase transitions”. In: *JCAP* 03 (2023), p. 006. DOI: `10.1088/1475-7516/2023/03/006`. arXiv: `2212.07559 [hep-ph]`.

[265] S. R. Broadbent and J. M. Hammersley. “Percolation processes. 1. Crystals and mazes”. In: *Proc. Cambridge Phil. Soc.* 53 (1957), pp. 629–641. DOI: `10.1017/S0305004100032680`.

[266] V. K. Shante and S. Kirkpatrick. “An introduction to percolation theory”. In: *Advances in Physics* 20.85 (1971), pp. 325–357. DOI: `10.1080/00018737100101261`.

[267] A. Hunt, R. Ewing, and B. Ghanbarian. *Percolation Theory for Flow in Porous Media.* Lecture Notes in Physics. Springer International Publishing, 2014. ISBN: 9783319037714.

[268] J. Lin and H. Chen. “Continuum percolation of porous media via random packing of overlapping cube-like particles”. In: *Theoretical and Applied Mechanics Letters* 8.5 (2018), pp. 299–303. ISSN: 2095-0349. DOI: `10.1016/j.taml.2018.05.007`.

[269] M. Li, H. Chen, and J. Lin. “Numerical study for the percolation threshold and transport properties of porous composites comprising non-centrosymmetrical superovoidal pores”. In: *Computer Methods in Applied Mechanics and Engineering* 361 (2020), p. 112815. ISSN: 0045-7825. DOI: `https://doi.org/10.1016/j.cma.2019.112815`.

[270] P. Athron, L. Morris, and Z. Xu. “How robust are gravitational wave predictions from cosmological phase transitions?” In: *JCAP* 05 (2024), p. 075. DOI: `10.1088/1475-7516/2024/05/075`. arXiv: `2309.05474 [hep-ph]`.

[271] M. Geller, A. Hook, R. Sundrum, and Y. Tsai. “Primordial Anisotropies in the Gravitational Wave Background from Cosmological Phase Transitions”. In: *Phys. Rev. Lett.* 121.20 (2018), p. 201303. DOI: `10.1103/PhysRevLett.121.201303`. arXiv: `1803.10780 [hep-ph]`.

[272] M. B. Hindmarsh, M. Lüben, J. Lumma, and M. Pauly. “Phase transitions in the early universe”. In: *SciPost Phys. Lect. Notes* 24 (2021), p. 1. DOI: `10.21468/SciPostPhysLectNotes.24`. arXiv: `2008.09136 [astro-ph.CO]`.

[273] J. R. Espinosa, T. Konstandin, J. M. No, and G. Servant. “Energy Budget of Cosmological First-order Phase Transitions”. In: *JCAP* 06 (2010), p. 028. DOI: `10.1088/1475-7516/2010/06/028`. arXiv: `1004.4187 [hep-ph]`.

[274] J. Ellis, M. Lewicki, J. M. No, and V. Vaskonen. “Gravitational wave energy budget in strongly supercooled phase transitions”. In: *JCAP* 06 (2019), p. 024. DOI: `10.1088/1475-7516/2019/06/024`. arXiv: `1903.09642 [hep-ph]`.

[275] J. Ellis, M. Lewicki, and V. Vaskonen. “Updated predictions for gravitational waves produced in a strongly supercooled phase transition”. In: *JCAP* 11 (2020), p. 020. DOI: `10.1088/1475-7516/2020/11/020`. arXiv: `2007.15586 [astro-ph.CO]`.

[276] M. Lewicki and V. Vaskonen. “Gravitational waves from bubble collisions and fluid motion in strongly supercooled phase transitions”. In: *Eur. Phys. J. C* 83.2 (2023), p. 109. DOI: `10.1140/epjc/s10052-023-11241-3`. arXiv: `2208.11697 [astro-ph.CO]`.

[277] C. Caprini et al. “Detecting gravitational waves from cosmological phase transitions with LISA: an update”. In: *JCAP* 03 (2020), p. 024. DOI: `10.1088/1475-7516/2020/03/024`. arXiv: `1910.13125 [astro-ph.CO]`.

[278] M. Hindmarsh and M. Hijazi. “Gravitational waves from first order cosmological phase transitions in the Sound Shell Model”. In: *JCAP* 12 (2019), p. 062. DOI: `10.1088/1475-7516/2019/12/062`. arXiv: `1909.10040 [astro-ph.CO]`.

[279] P. J. Steinhardt. “Relativistic Detonation Waves and Bubble Growth in False Vacuum 12ay”. In: *Phys. Rev. D* 25 (1982), p. 2074. DOI: `10.1103/PhysRevD.25.2074`.

[280] G. D. Moore and T. Prokopec. “Bubble wall velocity in a first order electroweak phase transition”. In: *Phys. Rev. Lett.* 75 (1995), pp. 777–780. DOI: `10.1103/PhysRevLett.75.777`. arXiv: `hep-ph/9503296`.

[281] G. D. Moore and T. Prokopec. “How fast can the wall move? A Study of the electroweak phase transition dynamics”. In: *Phys. Rev. D* 52 (1995), pp. 7182–7204. DOI: `10.1103/PhysRevD.52.7182`. arXiv: `hep-ph/9506475`.

[282] T. Konstandin, G. Nardini, and I. Rues. “From Boltzmann equations to steady wall velocities”. In: *JCAP* 09 (2014), p. 028. DOI: `10.1088/1475-7516/2014/09/028`. arXiv: `1407.3132 [hep-ph]`.

[283] J. Kozaczuk. “Bubble Expansion and the Viability of Singlet-Driven Electroweak Baryogenesis”. In: *JHEP* 10 (2015), p. 135. DOI: `10.1007/JHEP10(2015)135`. arXiv: `1506.04741 [hep-ph]`.

[284] G. C. Dorsch, S. J. Huber, and T. Konstandin. “Bubble wall velocities in the Standard Model and beyond”. In: *JCAP* 12 (2018), p. 034. DOI: `10.1088/1475-7516/2018/12/034`. arXiv: `1809.04907 [hep-ph]`.

[285] F. Giese, T. Konstandin, and J. van de Vis. “Model-independent energy budget of cosmological first-order phase transitionsA sound argument to go beyond the bag model”. In: *JCAP* 07.07 (2020), p. 057. DOI: `10.1088/1475-7516/2020/07/057`. arXiv: `2004.06995 [astro-ph.CO]`.

[286] M. Barroso Mancha, T. Prokopec, and B. Swiezewska. “Field-theoretic derivation of bubble-wall force”. In: *JHEP* 01 (2021), p. 070. DOI: `10.1007/JHEP01(2021)070`. arXiv: `2005.10875 [hep-th]`.

[287] S. Höche, J. Kozaczuk, A. J. Long, J. Turner, and Y. Wang. “Towards an all-orders calculation of the electroweak bubble wall velocity”. In: *JCAP* 03 (2021), p. 009. DOI: `10.1088/1475-7516/2021/03/009`. arXiv: `2007.10343 [hep-ph]`.

[288] B. Laurent and J. M. Cline. “Fluid equations for fast-moving electroweak bubble walls”. In: *Phys. Rev. D* 102.6 (2020), p. 063516. DOI: `10.1103/PhysRevD.102.063516`. arXiv: `2007.10935 [hep-ph]`.

[289] A. Azatov and M. Vanvlasselaer. “Bubble wall velocity: heavy physics effects”. In: *JCAP* 01 (2021), p. 058. DOI: `10.1088/1475-7516/2021/01/058`. arXiv: `2010.02590 [hep-ph]`.

[290] X. Wang, F. P. Huang, and X. Zhang. “Bubble wall velocity beyond leading-log approximation in electroweak phase transition”. In: (Nov. 2020). arXiv: `2011.12903 [hep-ph]`.

[291] Y. Bea, J. Casalderrey-Solana, T. Giannakopoulos, D. Mateos, M. Sanchez-Garitaonandia, and M. Zilhão. “Bubble wall velocity from holography”. In: *Phys. Rev. D* 104.12 (2021), p. L121903. DOI: `10.1103/PhysRevD.104.L121903`. arXiv: `2104.05708 [hep-th]`.

[292] F. Bigazzi, A. Caddeo, T. Canneti, and A. L. Cotrone. “Bubble wall velocity at strong coupling”. In: *JHEP* 08 (2021), p. 090. DOI: `10.1007/JHEP08(2021)090`. arXiv: `2104.12817 [hep-ph]`.

[293] W.-Y. Ai, B. Garbrecht, and C. Tamarit. “Bubble wall velocities in local equilibrium”. In: *JCAP* 03.03 (2022), p. 015. DOI: `10.1088/1475-7516/2022/03/015`. arXiv: `2109.13710 [hep-ph]`.

[294] M. Lewicki, M. Merchand, and M. Zych. “Electroweak bubble wall expansion: gravitational waves and baryogenesis in Standard Model-like thermal plasma”. In: *JHEP* 02 (2022), p. 017. DOI: `10.1007/JHEP02(2022)017`. arXiv: `2111.02393 [astro-ph.CO]`.

[295] G. C. Dorsch, S. J. Huber, and T. Konstandin. “A sonic boom in bubble wall friction”. In: *JCAP* 04.04 (2022), p. 010. DOI: `10.1088/1475-7516/2022/04/010`. arXiv: `2112.12548 [hep-ph]`.

[296] B. Laurent and J. M. Cline. “First principles determination of bubble wall velocity”. In: *Phys. Rev. D* 106.2 (2022), p. 023501. DOI: `10.1103/PhysRevD.106.023501`. arXiv: `2204.13120 [hep-ph]`.

[297] S. De Curtis, L. Delle Rose, A. Guiggiani, Á. Gil Muyor, and G. Panico. “Collision integrals for cosmological phase transitions”. In: *JHEP* 05 (2023), p. 194. DOI: `10.1007/JHEP05(2023)194`. arXiv: `2303.05846 [hep-ph]`.

[298] T. Krajewski, M. Lewicki, and M. Zych. “Hydrodynamical constraints on the bubble wall velocity”. In: *Phys. Rev. D* 108.10 (2023), p. 103523. DOI: `10.1103/PhysRevD.108.103523`. arXiv: `2303.18216 [astro-ph.CO]`.

[299] M. Sanchez-Garitaonandia and J. van de Vis. “Prediction of the bubble wall velocity for a large jump in degrees of freedom”. In: (Dec. 2023). arXiv: `2312.09964 [hep-ph]`.

[300] T. Krajewski, M. Lewicki, and M. Zych. “Bubble-wall velocity in local thermal equilibrium: hydrodynamical simulations vs analytical treatment”. In: *JHEP* 05 (2024), p. 011. DOI: `10.1007/JHEP05(2024)011`. arXiv: `2402.15408 [astro-ph.CO]`.

[301] F. Giese, T. Konstandin, K. Schmitz, and J. van de Vis. “Model-independent energy budget for LISA”. In: *JCAP* 01 (2021), p. 072. DOI: `10.1088/1475-7516/2021/01/072`. arXiv: `2010.09744 [astro-ph.CO]`.

[302] C. Grojean and G. Servant. “Gravitational Waves from Phase Transitions at the Electroweak Scale and Beyond”. In: *Phys. Rev. D* 75 (2007), p. 043507. DOI: `10.1103/PhysRevD.75.043507`. arXiv: `hep-ph/0607107`.

[303] A. Einstein. “Die Grundlage der allgemeinen Relativitätstheorie”. In: *Annalen Phys.* 49.7 (1916), pp. 769–822. DOI: `10.1002/andp.19163540702`.

[304] A. Einstein. “Näherungsweise Integration der Feldgleichungen der Gravitation”. In: *Sitzungsberichte der Preussischen Akademie der Wissenschaften* (1916), pp. 688–696.

[305] S. M. Carroll. “Lecture notes on general relativity”. In: (Dec. 1997). arXiv: `gr-qc/9712019`.

[306] F. A. E. Pirani. “Invariant formulation of gravitational radiation theory”. In: *Phys. Rev.* 105 (1957), pp. 1089–1099. DOI: `10.1103/PhysRev.105.1089`.

[307] H. Bondi. “Plane gravitational waves in general relativity”. In: *Nature* 179 (1957), pp. 1072–1073. DOI: `10.1038/1791072a0`.

[308] A. Trautman. “Boundary Conditions at Infinity for Physical Theories”. In: *Bull. Acad. Pol. Sci. Ser. Sci. Math. Astron. Phys.* 6.6 (1958), pp. 403–406. arXiv: `1604.03144 [math-ph]`.

[309] A. Trautman. “Radiation and Boundary Conditions in the Theory of Gravitation”. In: *Bull. Acad. Pol. Sci. Ser. Sci. Math. Astron. Phys.* 6.6 (1958), pp. 407–412. arXiv: `1604.03145 [gr-qc]`.

[310] H. Bondi, F. A. E. Pirani, and I. Robinson. “Gravitational waves in general relativity. 3. Exact plane waves”. In: *Proc. Roy. Soc. Lond. A* 251 (1959), pp. 519–533. DOI: `10.1098/rspa.1959.0124`.

[311] R. Penrose. “A spinor approach to general relativity”. In: *Annals of Physics* 10.2 (1960), pp. 171–201. ISSN: 0003-4916. DOI: `10.1016/0003-4916(60)90021-X`.

[312] I. Robinson and A. Trautman. “Spherical Gravitational Waves”. In: *Phys. Rev. Lett.* 4 (1960), pp. 431–432. DOI: `10.1103/PhysRevLett.4.431`.

[313] I. Robinson and A. Trautman. “Some spherical gravitational waves in general relativity”. In: *Proc. Roy. Soc. Lond. A* 265 (1962), pp. 463–473. DOI: `10.1098/rspa.1962.0036`.

[314] A. PETROV. *Einstein Spaces.* Pergamon, 1969. ISBN: 978-0-08-012315-8. DOI: `10.1016/C2013-0-02070-1`.

[315] C. J. Moore, R. H. Cole, and C. P. L. Berry. “Gravitational-wave sensitivity curves”. In: *Class. Quant. Grav.* 32.1 (2015), p. 015014. DOI: `10.1088/0264-9381/32/1/015014`. arXiv: `1408.0740 [gr-qc]`.

[316] N. Benincasa. “Phase transitions and gravitational waves in models of dark matter”. PhD thesis. University of Tartu, 2023.

[317] L. Leitao and A. Megevand. “Gravitational waves from a very strong electroweak phase transition”. In: *JCAP* 05 (2016), p. 037. DOI: `10.1088/1475-7516/2016/05/037`. arXiv: `1512.08962 [astro-ph.CO]`.

[318] C. Caprini and R. Durrer. “Gravitational wave production: A Strong constraint on primordial magnetic fields”. In: *Phys. Rev. D* 65 (2001), p. 023517. DOI: `10.1103/PhysRevD.65.023517`. arXiv: `astro-ph/0106244`.

[319] D. G. Figueroa, M. Hindmarsh, and J. Urrestilla. “Exact Scale-Invariant Background of Gravitational Waves from Cosmic Defects”. In: *Phys. Rev. Lett.* 110.10 (2013), p. 101302. DOI: `10.1103/PhysRevLett.110.101302`. arXiv: `1212.5458 [astro-ph.CO]`.

[320] M. Hindmarsh. “Sound shell model for acoustic gravitational wave production at a first-order phase transition in the early Universe”. In: *Phys. Rev. Lett.* 120.7 (2018), p. 071301. DOI: `10.1103/PhysRevLett.120.071301`. arXiv: `1608.04735 [astro-ph.CO]`.

[321] M. Maggiore. “Gravitational wave experiments and early universe cosmology”. In: *Phys. Rept.* 331 (2000), pp. 283–367. DOI: `10.1016/S0370-1573(99)00102-7`. arXiv: `gr-qc/9909001`.

[322] C. Caprini and D. G. Figueroa. “Cosmological Backgrounds of Gravitational Waves”. In: *Class. Quant. Grav.* 35.16 (2018), p. 163001. DOI: `10.1088/1361-6382/aac608`. arXiv: `1801.04268 [astro-ph.CO]`.

[323] C. Caprini et al. “Science with the space-based interferometer eLISA. II: Gravitational waves from cosmological phase transitions”. In: *JCAP* 04 (2016), p. 001. DOI: `10.1088/1475-7516/2016/04/001`. arXiv: `1512.06239 [astro-ph.CO]`.

[324] M. Hindmarsh, S. J. Huber, K. Rummukainen, and D. J. Weir. “Numerical simulations of acoustically generated gravitational waves at a first order phase transition”. In: *Phys. Rev. D* 92.12 (2015), p. 123009. DOI: `10.1103/PhysRevD.92.123009`. arXiv: `1504.03291 [astro-ph.CO]`.

[325] M. Hindmarsh, S. J. Huber, K. Rummukainen, and D. J. Weir. “Shape of the acoustic gravitational wave power spectrum from a first order phase transition”. In: *Phys. Rev. D* 96.10 (2017). [Erratum: Phys.Rev.D 101, 089902 (2020)], p. 103520. DOI: `10.1103/PhysRevD.96.103520`. arXiv: `1704.05871 [astro-ph.CO]`.

[326] LIGO Scientific, Virgo, B. P. Abbott et al. “Observation of Gravitational Waves from a Binary Black Hole Merger”. In: *Phys. Rev. Lett.* 116.6 (2016), p. 061102. DOI: `10.1103/PhysRevLett.116.061102`. arXiv: `1602.03837 [gr-qc]`.

[327] LIGO Scientific, Virgo, B. P. Abbott et al. “GWTC-1: A Gravitational-Wave Transient Catalog of Compact Binary Mergers Observed by LIGO and Virgo during the First and Second Observing Runs”. In: *Phys. Rev. X* 9.3 (2019), p. 031040. DOI: `10.1103/PhysRevX.9.031040`. arXiv: `1811.12907 [astro-ph.HE]`.

[328] LIGO Scientific, Virgo, R. Abbott et al. “GWTC-2: Compact Binary Coalescences Observed by LIGO and Virgo During the First Half of the Third Observing Run”. In: *Phys. Rev. X* 11 (2021), p. 021053. DOI: `10.1103/PhysRevX.11.021053`. arXiv: `2010.14527 [gr-qc]`.

[329] LIGO Scientific, VIRGO, R. Abbott et al. “GWTC-2.1: Deep extended catalog of compact binary coalescences observed by LIGO and Virgo during the first half of the third observing run”. In: *Phys. Rev. D* 109.2 (2024), p. 022001. DOI: `10.1103/PhysRevD.109.022001`. arXiv: `2108.01045 [gr-qc]`.

[330] KAGRA, K. Somiya. “Detector configuration of KAGRA: The Japanese cryogenic gravitational-wave detector”. In: *Class. Quant. Grav.* 29 (2012). Ed. by M. Hannam, P. Sutton, S. Hild, and C. van den Broeck, p. 124007. DOI: `10.1088/0264-9381/29/12/124007`. arXiv: `1111.7185 [gr-qc]`.

[331] KAGRA, Y. Aso, Y. Michimura, K. Somiya, M. Ando, O. Miyakawa, T.-n. Sekiguchi, D. Tatsumi, and H. Yamamoto. “Interferometer design of the KAGRA gravitational wave detector”. In: *Phys. Rev. D* 88.4 (2013), p. 043007. DOI: `10.1103/PhysRevD.88.043007`. arXiv: `1306.6747 [gr-qc]`.

[332] KAGRA, T. Akutsu et al. “Overview of KAGRA: Detector design and construction history”. In: *PTEP* 2021.5 (2021), 05A101. DOI: `10.1093/ptep/ptaa125`. arXiv: `2005.05574 [physics.ins-det]`.

[333] KAGRA, VIRGO, LIGO Scientific, R. Abbott et al. “GWTC-3: Compact Binary Coalescences Observed by LIGO and Virgo during the Second Part of the Third Observing Run”. In: *Phys. Rev. X* 13.4 (2023), p. 041039. DOI: `10.1103/PhysRevX.13.041039`. arXiv: `2111.03606 [gr-qc]`.

[334] H. Luck et al. “The status of GEO600”. In: *AIP Conf. Proc.* 523.1 (2000). Ed. by S. Meshkov, p. 119. DOI: `10.1063/1.1291849`.

[335] H. Luck et al. “The upgrade of GEO600”. In: *J. Phys. Conf. Ser.* 228 (2010). Ed. by Z. Marka and S. Marka, p. 012012. DOI: `10.1088/1742-6596/228/1/012012`. arXiv: `1004.0339 [gr-qc]`.

[336] C. Affeldt et al. “Advanced techniques in GEO 600”. In: *Class. Quant. Grav.* 31.22 (2014), p. 224002. DOI: `10.1088/0264-9381/31/22/224002`.

[337] K. L. Dooley et al. “GEO 600 and the GEO-HF upgrade program: successes and challenges”. In: *Class. Quant. Grav.* 33 (2016), p. 075009. DOI: `10.1088/0264-9381/33/7/075009`. arXiv: `1510.00317 [physics.ins-det]`.

[338] KAGRA, VIRGO, LIGO Scientific, R. Abbott et al. “First joint observation by the underground gravitational-wave detector KAGRA with GEO 600”. In: *PTEP* 2022.6 (2022), 063F01. DOI: `10.1093/ptep/ptac073`. arXiv: `2203.01270 [gr-qc]`.

[339] M. Punturo et al. “The Einstein Telescope: A third-generation gravitational wave observatory”. In: *Class. Quant. Grav.* 27 (2010). Ed. by F. Ricci, p. 194002. DOI: `10.1088/0264-9381/27/19/194002`.

[340] D. Reitze et al. “Cosmic Explorer: The U.S. Contribution to Gravitational-Wave Astronomy beyond LIGO”. In: *Bull. Am. Astron. Soc.* 51.7 (2019), p. 035. arXiv: `1907.04833 [astro-ph.IM]`.

[341] LISA, W. M. Folkner. “The LISA mission design”. In: *AIP Conf. Proc.* 456.1 (1998). Ed. by W. M. Folkner, pp. 11–16. DOI: `10.1063/1.57401`.

[342] LISA Study Team, K. Danzmann. “LISA mission overview”. In: *Adv. Space Res.* 25 (2000), pp. 1129–1136. DOI: `10.1016/S0273-1177(99)00973-4`.

[343] LISA, P. Amaro-Seoane et al. “Laser Interferometer Space Antenna”. In: (Feb. 2017). arXiv: `1702.00786 [astro-ph.IM]`.

[344] LISA Cosmology Working Group, P. Auclair et al. “Cosmology with the Laser Interferometer Space Antenna”. In: *Living Rev. Rel.* 26.1 (2023), p. 5. DOI: `10.1007/s41114-023-00045-2`. arXiv: `2204.05434 [astro-ph.CO]`.

[345] S. Kawamura et al. “The Japanese space gravitational wave antenna DECIGO”. In: *Class. Quant. Grav.* 23 (2006). Ed. by N. Mio, S125–S132. DOI: `10.1088/0264-9381/23/8/S17`.

[346] G. M. Harry, P. Fritschel, D. A. Shaddock, W. Folkner, and E. S. Phinney. “Laser interferometry for the big bang observer”. In: *Class. Quant. Grav.* 23 (2006). [Erratum: Class.Quant.Grav. 23, 7361 (2006)], pp. 4887–4894. DOI: `10.1088/0264-9381/23/15/008`.

[347] G. Hobbs et al. “The international pulsar timing array project: using pulsars as a gravitational wave detector”. In: *Class. Quant. Grav.* 27 (2010). Ed. by Z. Marka and S. Marka, p. 084013. DOI: `10.1088/0264-9381/27/8/084013`. arXiv: `0911.5206 [astro-ph.SR]`.

[348] EPTA, InPTA:, J. Antoniadis et al. “The second data release from the European Pulsar Timing Array - III. Search for gravitational wave signals”. In: *Astron. Astrophys.* 678 (2023), A50. DOI: `10.1051/0004-6361/202346844`. arXiv: `2306.16214 [astro-ph.HE]`.

[349] D. J. Reardon et al. “Search for an Isotropic Gravitational-wave Background with the Parkes Pulsar Timing Array”. In: *Astrophys. J. Lett.* 951.1 (2023), p. L6. DOI: `10.3847/2041-8213/acdd02`. arXiv: `2306.16215 [astro-ph.HE]`.

[350] M. Sazhin. “Opportunities for detecting ultralong gravitational waves”. In: *Soviet Astronomy* 22 (Jan. 1978), pp. 36–38.

[351] S. L. Detweiler. “Pulsar timing measurements and the search for gravitational waves”. In: *Astrophys. J.* 234 (1979), pp. 1100–1104. DOI: `10.1086/157593`.

[352] R. W. Hellings and G. S. Downs. “Upper limits on the isotropic gravitational radiation background from pulsar timing analysis”. In: *Astrophys. J. Lett.* 265 (1983), pp. L39–L42. DOI: `10.1086/183954`.

[353] G. M. Harry, P. Fritschel, D. A. Shaddock, W. Folkner, and E. S. Phinney. “LISA Science Requirements Document”. In: (). URL: `https://www.cosmos.esa.int/web/lisa/`.

[354] S. Babak, A. Petiteau, and M. Hewitson. “LISA Sensitivity and SNR Calculations”. In: (Aug. 2021). arXiv: `2108.01167 [astro-ph.IM]`.

[355] C. J. Moore, R. H. Cole, and C. P. L. Berry. *Gravitational Wave Sensitivity Curve Plotter*. URL: `https://github.com/robsci/GWplotter`.

[356] D. J. Weir. “PTPlot: a tool for exploring the gravitational wave power spectrum from first-order phase transitions”. Version 1.1.0. In: *Zenodo* (Aug. 2023). DOI: `10.5281/zenodo.8220720`.

[357] L. M. Widrow. “Origin of galactic and extragalactic magnetic fields”. In: *Rev. Mod. Phys.* 74 (2002), pp. 775–823. DOI: `10.1103/RevModPhys.74.775`. arXiv: `astro-ph/0207240`.

[358] R. Durrer and A. Neronov. “Cosmological Magnetic Fields: Their Generation, Evolution and Observation”. In: *Astron. Astrophys. Rev.* 21 (2013), p. 62. DOI: `10.1007/s00159-013-0062-7`. arXiv: `1303.7121 [astro-ph.CO]`.

[359] K. Subramanian. “The origin, evolution and signatures of primordial magnetic fields”. In: *Rept. Prog. Phys.* 79.7 (2016), p. 076901. DOI: `10.1088/0034-4885/79/7/076901`. arXiv: `1504.02311 [astro-ph.CO]`.

[360] T. Kahniashvili, L. Kisslinger, and T. Stevens. “Gravitational Radiation Generated by Magnetic Fields in Cosmological Phase Transitions”. In: *Phys. Rev. D* 81 (2010), p. 023004. DOI: `10.1103/PhysRevD.81.023004`. arXiv: `0905.0643 [astro-ph.CO]`.

[361] P. Binetruy, A. Bohe, C. Caprini, and J.-F. Dufaux. “Cosmological Backgrounds of Gravitational Waves and eLISA/NGO: Phase Transitions, Cosmic Strings and Other Sources”. In: *JCAP* 06 (2012), p. 027. DOI: `10.1088/1475-7516/2012/06/027`. arXiv: `1201.0983 [gr-qc]`.

[362] S. Weinberg. “Gauge and Global Symmetries at High Temperature”. In: *Phys. Rev. D* 9 (1974), pp. 3357–3378. DOI: `10.1103/PhysRevD.9.3357`.

[363] H. H. Patel and M. J. Ramsey-Musolf. “Stepping Into Electroweak Symmetry Breaking: Phase Transitions and Higgs Phenomenology”. In: *Phys. Rev. D* 88 (2013), p. 035013. DOI: `10.1103/PhysRevD.88.035013`. arXiv: `1212.5652 [hep-ph]`.

[364] N. Blinov, J. Kozaczuk, D. E. Morrissey, and C. Tamarit. “Electroweak Baryogenesis from Exotic Electroweak Symmetry Breaking”. In: *Phys. Rev. D* 92.3 (2015), p. 035012. DOI: `10.1103/PhysRevD.92.035012`. arXiv: `1504.05195 [hep-ph]`.

[365] A. P. Morais and R. Pasechnik. “Probing multi-step electroweak phase transition with multi-peaked primordial gravitational waves spectra”. In: *JCAP* 04 (2020), p. 036. DOI: `10.1088/1475-7516/2020/04/036`. arXiv: `1910.00717 [hep-ph]`.

[366] M. Aoki, T. Komatsu, and H. Shibuya. “Possibility of a multi-step electroweak phase transition in the two-Higgs doublet models”. In: *PTEP* 2022.6 (2022), 063B05. DOI: `10.1093/ptep/ptac068`. arXiv: `2106.03439 [hep-ph]`.

[367] N. Benincasa, L. Delle Rose, K. Kannike, and L. Marzola. “Multi-step phase transitions and gravitational waves in the inert doublet model”. In: *JCAP* 12 (2022), p. 025. DOI: `10.1088/1475-7516/2022/12/025`. arXiv: `2205.06669 [hep-ph]`.

[368] H. Shibuya and T. Toma. “Impact of first-order phase transitions on dark matter production in the scotogenic model”. In: *JHEP* 11 (2022), p. 064. DOI: `10.1007/JHEP11(2022)064`. arXiv: `2207.14662 [hep-ph]`.

[369] S. Liu and L. Wang. “Spontaneous CP violation electroweak baryogenesis and gravitational wave through multistep phase transitions”. In: *Phys. Rev. D* 107.11 (2023), p. 115008. DOI: `10.1103/PhysRevD.107.115008`. arXiv: `2302.04639 [hep-ph]`.

[370] M. Aoki and H. Shibuya. “Electroweak baryogenesis between broken phases in multi-step phase transition”. In: *Phys. Lett. B* 843 (2023), p. 138041. DOI: `10.1016/j.physletb.2023.138041`. arXiv: `2302.11551 [hep-ph]`.

[371] P. M. Ferreira, R. Santos, and A. Barroso. “Stability of the tree-level vacuum in two Higgs doublet models against charge or CP spontaneous violation”. In: *Phys. Lett. B* 603 (2004). [Erratum: Phys.Lett.B 629, 114–114 (2005)], pp. 219–229. DOI: `10.1016/j.physletb.2004.10.022`. arXiv: `hep-ph/0406231`.

[372] A. Barroso, P. M. Ferreira, and R. Santos. “Charge and CP symmetry breaking in two Higgs doublet models”. In: *Phys. Lett. B* 632 (2006), pp. 684–687. DOI: `10.1016/j.physletb.2005.11.031`. arXiv: `hep-ph/0507224`.

[373] I. P. Ivanov. “Minkowski space structure of the Higgs potential in 2HDM”. In: *Phys. Rev. D* 75 (2007). [Erratum: Phys.Rev.D 76, 039902 (2007)], p. 035001. DOI: `10.1103/PhysRevD.75.035001`. arXiv: `hep-ph/0609018`.

[374] A. Barroso, P. M. Ferreira, and R. Santos. “Neutral minima in two-Higgs doublet models”. In: *Phys. Lett. B* 652 (2007), pp. 181–193. DOI: `10.1016/j.physletb.2007.07.010`. arXiv: `hep-ph/0702098`.

[375] I. P. Ivanov. “Minkowski space structure of the Higgs potential in 2HDM. II. Minima, symmetries, and topology”. In: *Phys. Rev. D* 77 (2008), p. 015017. DOI: `10.1103/PhysRevD.77.015017`. arXiv: `0710.3490 [hep-ph]`.

[376] A. Barroso, P. M. Ferreira, I. P. Ivanov, R. Santos, and J. P. Silva. “Evading death by vacuum”. In: *Eur. Phys. J. C* 73 (2013), p. 2537. DOI: `10.1140/epjc/s10052-013-2537-0`. arXiv: `1211.6119 [hep-ph]`.

[377] A. Barroso, P. M. Ferreira, I. P. Ivanov, and R. Santos. “Metastability bounds on the two Higgs doublet model”. In: *JHEP* 06 (2013), p. 045. DOI: `10.1007/JHEP06(2013)045`. arXiv: `1303.5098 [hep-ph]`.

[378] M. Aoki, L. Biermann, C. Borschensky, I. P. Ivanov, M. Mühlleitner, and H. Shibuya. “Intermediate charge-breaking phases and symmetry non-restoration in the 2-Higgs-Doublet Model”. In: *JHEP* 02 (2024), p. 232. DOI: `10.1007/JHEP02(2024)232`. arXiv: `2308.04141 [hep-ph]`.

[379] I. P. Ivanov. “Thermal evolution of the ground state of the most general 2HDM”. In: *Acta Phys. Polon. B* 40 (2009), pp. 2789–2807. arXiv: `0812.4984 [hep-ph]`.

[380] CMS, A. M. Sirunyan et al. “Search for new neutral Higgs bosons through the H→ ZA → $\ell^+\ell^-\mathrm{b\bar{b}}$ process in pp collisions at $\sqrt{s} = 13$ TeV”. In: *JHEP* 03 (2020), p. 055. DOI: `10.1007/JHEP03(2020)055`. arXiv: `1911.03781 [hep-ex]`.

[381] ATLAS, G. Aad et al. “Search for a heavy Higgs boson decaying into a Z boson and another heavy Higgs boson in the $\ell\ell bb$ and $\ell\ell WW$ final states in pp collisions at $\sqrt{s} = 13$ TeV with the ATLAS detector”. In: *Eur. Phys. J. C* 81.5 (2021), p. 396. DOI: `10.1140/epjc/s10052-021-09117-5`. arXiv: `2011.05639 [hep-ex]`.

[382] D. Azevedo, P. M. Ferreira, M. M. Muhlleitner, S. Patel, R. Santos, and J. Wittbrodt. “CP in the dark”. In: *JHEP* 11 (2018), p. 091. DOI: `10.1007/JHEP11(2018)091`. arXiv: `1807.10322 [hep-ph]`.

[383] L. Biermann. “Dark Matter Phase Transitions in CP in the Dark”. MA thesis. Institute for Theoretical Physics, Karlsruhe Institut of Technology, 2021.

[384] L. Biermann, M. Mühlleitner, and J. Müller. “‘CP in the Dark’ and a Strong First-Order Electroweak Phase Transition”. In: *8th Symposium on Prospects in the Physics of Discrete Symmetries.* Jan. 2023. arXiv: `2301.09004 [hep-ph]`.

[385] S. Inoue, G. Ovanesyan, and M. J. Ramsey-Musolf. “Two-Step Electroweak Baryogenesis”. In: *Phys. Rev. D* 93 (2016), p. 015013. DOI: `10.1103/PhysRevD.93.015013`. arXiv: `1508.05404 [hep-ph]`.

[386] L. Niemi, M. J. Ramsey-Musolf, T. V. I. Tenkanen, and D. J. Weir. “Thermodynamics of a Two-Step Electroweak Phase Transition”. In: *Phys. Rev. Lett.* 126.17 (2021), p. 171802. DOI: `10.1103/PhysRevLett.126.171802`. arXiv: `2005.11332 [hep-ph]`.

[387] J. Ellis, M. Lewicki, and J. M. No. “On the Maximal Strength of a First-Order Electroweak Phase Transition and its Gravitational Wave Signal”. In: *JCAP* 04 (2019), p. 003. DOI: `10.1088/1475-7516/2019/04/003`. arXiv: `1809.08242 [hep-ph]`.

[388] X. Wang, F. P. Huang, and X. Zhang. “Phase transition dynamics and gravitational wave spectra of strong first-order phase transition in supercooled universe”. In: *JCAP* 05 (2020), p. 045. DOI: `10.1088/1475-7516/2020/05/045`. arXiv: `2003.08892 [hep-ph]`.

[389] I. Engeln, P. Ferreira, M. M. Mühlleitner, R. Santos, and J. Wittbrodt. “The Dark Phases of the N2HDM”. In: *JHEP* 08 (2020), p. 085. DOI: `10.1007/JHEP08(2020)085`. arXiv: `2004.05382 [hep-ph]`.

[390] S. Glaus, M. Mühlleitner, J. Müller, S. Patel, T. Römer, and R. Santos. “Electroweak Corrections in a Pseudo-Nambu Goldstone Dark Matter Model Revisited”. In: *JHEP* 12 (2020), p. 034. DOI: `10.1007/JHEP12(2020)034`. arXiv: `2008.12985 [hep-ph]`.

[391] J. Billard, L. Strigari, and E. Figueroa-Feliciano. “Implication of neutrino backgrounds on the reach of next generation dark matter direct detection experiments”. In: *Phys. Rev. D* 89.2 (2014), p. 023524. DOI: `10.1103/PhysRevD.89.023524`. arXiv: `1307.5458 [hep-ph]`.

[392] S. J. Huber, K. Mimasu, and J. M. No. “Baryogenesis from transitional CP violation in the early Universe”. In: *Phys. Rev. D* 107.7 (2023), p. 075042. DOI: `10.1103/PhysRevD.107.075042`. arXiv: `2208.10512 [hep-ph]`.